NASA/CR—2004–213285

The 2003 NASA Faculty Fellowship Program Research Reports

Program Co-Directors:
S.K. Nash-Stevenson, Marshall Space Flight Center, Marshall Space Flight Center, Alabama

G. Karr, The University of Alabama in Huntsville, Huntsville, Alabama

L.M. Freeman, The University of Alabama, Tuscaloosa, Alabama

J. Bland
Compiler and Editor
Marshall Space Flight Center, Marshall Space Flight Center, Alabama

Prepared for Marshall Space Flight Center
under Contract NAG8–1904

May 2004

The NASA STI Program Office…in Profile

Since its founding, NASA has been dedicated to the advancement of aeronautics and space science. The NASA Scientific and Technical Information (STI) Program Office plays a key part in helping NASA maintain this important role.

The NASA STI Program Office is operated by Langley Research Center, the lead center for NASA's scientific and technical information. The NASA STI Program Office provides access to the NASA STI Database, the largest collection of aeronautical and space science STI in the world. The Program Office is also NASA's institutional mechanism for disseminating the results of its research and development activities. These results are published by NASA in the NASA STI Report Series, which includes the following report types:

- TECHNICAL PUBLICATION. Reports of completed research or a major significant phase of research that present the results of NASA programs and include extensive data or theoretical analysis. Includes compilations of significant scientific and technical data and information deemed to be of continuing reference value. NASA's counterpart of peer-reviewed formal professional papers but has less stringent limitations on manuscript length and extent of graphic presentations.

- TECHNICAL MEMORANDUM. Scientific and technical findings that are preliminary or of specialized interest, e.g., quick release reports, working papers, and bibliographies that contain minimal annotation. Does not contain extensive analysis.

- CONTRACTOR REPORT. Scientific and technical findings by NASA-sponsored contractors and grantees.

- CONFERENCE PUBLICATION. Collected papers from scientific and technical conferences, symposia, seminars, or other meetings sponsored or cosponsored by NASA.

- SPECIAL PUBLICATION. Scientific, technical, or historical information from NASA programs, projects, and mission, often concerned with subjects having substantial public interest.

- TECHNICAL TRANSLATION. English-language translations of foreign scientific and technical material pertinent to NASA's mission.

Specialized services that complement the STI Program Office's diverse offerings include creating custom thesauri, building customized databases, organizing and publishing research results…even providing videos.

For more information about the NASA STI Program Office, see the following:

- Access the NASA STI Program Home Page at ***http://www.sti.nasa.gov***

- E-mail your question via the Internet to help@sti.nasa.gov

- Fax your question to the NASA Access Help Desk at (301) 621–0134

- Telephone the NASA Access Help Desk at (301) 621–0390

- Write to:
  NASA Access Help Desk
  NASA Center for AeroSpace Information
  7121 Standard Drive
  Hanover, MD 21076–1320
  (301)621–0390

NASA/CR—2004–213285

The 2003 NASA Faculty Fellowship Program Research Reports

Program Co-Directors:
S.K. Nash-Stevenson, Marshall Space Flight Center, Marshall Space Flight Center, Alabama

G. Karr, The University of Alabama in Huntsville, Huntsville, Alabama

L.M. Freeman, The University of Alabama, Tuscaloosa, Alabama

J. Bland
Compiler and Editor:
Marshall Space Flight Center, Marshall Space Flight Center, Alabama

Prepared for Marshall Space Flight Center
under Contract NAG8–1904

National Aeronautics and
Space Administration

Marshall Space Flight Center • MSFC, Alabama 35812

May 2004

TRADEMARKS

Trade names and trademarks are used in this report for identification only. This usage does not constitute an official endorsement, either expressed or implied, by the National Aeronautics and Space Administration.

Available from:

NASA Center for AeroSpace Information
7121 Standard Drive
Hanover, MD 21076–1320
(301) 621–0390

National Technical Information Service
5285 Port Royal Road
Springfield, VA 22161
(703) 487–4650

INTRODUCTION

This is the administrative report for the 2003 NASA Faculty Fellowship Program (NFFP) held at the George C. Marshall Space Flight Center (MSFC) for the 39th consecutive year. The NFFP offers science and engineering faculty at U.S. colleges and universities hands-on exposure to NASA's research challenges through summer research residencies and extended research opportunities at participating NASA research Centers. During this program, fellows work closely with NASA colleagues on research challenges important to NASA's strategic enterprises that are of mutual interest to the fellow and the Center. The nominal starting and finishing dates for the 10-week program were May 27 through August 1, 2003. The program was sponsored by NASA Headquarters, Washington, DC, and operated under contract by The University of Alabama in Huntsville. In addition, promotion and applications are managed by the American Society for Engineering Education (ASEE) and assessment is completed by Universities Space Research Association (USRA). This program combines aspects of two successful and long-running NASA programs, the NASA/ASEE Summer Faculty Fellowship Program and the NASA/USRA Joint Venture (JOVE) program. This program was one of ten such programs at nine NASA Centers sponsored and funded by NASA Headquarters.

The primary objectives of the NFFP are to:

- Increase the quality and quantity of research collaborations between NASA and the academic community that contribute to NASA's research objectives;

- Provide research opportunities for college and university faculty that serve to enrich their knowledge base;

- Involve students in cutting-edge science and engineering challenges related to NASA's strategic enterprises, while providing exposure to the methods and practices of real-world research

- Enhance faculty pedagogy and facilitate interdisciplinary networking

- Encourage collaborative research and technology transfer with other Government agencies and the private sector; and

- Establish an effective education and outreach activity to foster greater awareness of this program.

Questions about any report should be addressed to Dr. Gerald Karr, Department of Mechanical and Aerospace Engineering, The University of Alabama in Huntsville, TH-N261, Huntsville, AL 35899. Email: karr@eng.uah.edu

TABLE OF CONTENTS

Mechanical Characterization of a New Material Developed for Radiation Shielding
Felipe Acosta-Costa, University of Puerto Rico-Mayaguez

System Identification of X33 Using Neural Network
Shiv Aggarwal, Embry Riddle Aeronautical University

Realizing the New Mythology Through the Old
Mary Bangs, SUNY Empire State College

Extraction of Iron from Martian Soil by Microwave Processing—A Feasibility Study
Walter Boles, Middle Tennessee State University

Genetic Algorithm Tuned Fuzzy Logic for Gliding Return Trajectories
Bradley Burchett, Rose-Hulman Institute of Technology

Developing a Set of Similarity Rules for Scaling Solar Sail Systems
Stephen Canfield, Tennessee Technological University

Development and Verification of Digital Image Correlation for NDE
Tsuchin Chu, Southern Illinois University

Semi-Automated Acquisition of Flight Software Requirements
Harry Delugach, The University of Alabama in Huntsville

Theta-D Control Technique for Ascent Control of Reusable Launch Vehicles
David Drake, University of Missouri-Rolla

Controls for Reusable Launch Vehicles During Terminal Area Energy Management
Brian Driessen, The University of Alabama in Huntsville

The Matrix Reloaded: Characteristic Matrices for Spherical Shell Photonic Systems
Kirk Fuller, The University of Alabama in Huntsville

Probabilistic Risk Assessment for Hubble Space Telescope End of Mission Conceptual Study
Kye Gilder, U.S. Coast Guard Academy

Analysis of Transfer Functions and Sampling Rate in Propulsion Measurements
Don Gregory, The University of Alabama in Huntsville

A Mathematical Model for Predicting Gas Distribution in a Pack Bed Under Microgravity Conditions
Boyun Guo, University of Louisiana at Lafayette

Rocket and Payload Design, Development, and Launch Initiative
Razi Hassan, Alabama A&M University

Concepts for a Lessons Learned Software System
J. Scott Hawker, University of Alabama

Investigation of Nickel Electrocodeposition with the Aid of Reverse-Pulse Plating
Ryan Hulguin, Austin Peay State University

Initial Assessment of CHEM for RBCC Flow Field Prediction
Ziaul Huque, Prairie View A&M University

Adaptive Inverse Control of X-33 for TAEM Approach/Landing
Leehyun Keel, Tennessee State University

Tensegrity Research for Genetic Algorithm Optimization
Kenneth Kimble, University of Tennessee - Space Institute

MSFC in the Context of Granular Materials Research in Support of the In-Space Fabrication and Repair Initiative
Emir Macari, Louisiana State University

Reverse Engineering with Geomagic Studio 5 and the Polygon Editing Tool Software
Angela Lawson-Macklin, Alabama A&M University

Experiment with the (FAST) FRC Acceleration Space Thruster Experiment
Lionel Macklin, Alabama A&M University

The Testing Designs and Data Analysis of New Composite Material for Radiation Shielding and Structural Carrying Loads
John Martin, Alabama A&M University

Ground-Level Ozone Air Quality Issues and Public Policy Challenges
William McAllister, Alabama A&M University

An Overview of Momentum-Exchange Electrodynamic-Reboost (MXER) Tether Technology
William Miller, Alabama A&M University

Refinement of a Platform to Compute Fourier Transforms
Terrence Mizell, Alabama A&M University

A Novel Approach to Fabricating Sample Containment Assemblies for Microgravity Materials Processing
Amir Mobasher, Alabama A&M University

Solar-Powered Pulsed Gas Lasers for In-Space Fabrication
Ade Odutola, Alabama A&M University

Incorporating Mission Risk in the Concept Selection Process
Madara Ogot, Rutgers University

Emissive Probes
Harold Penn, Alabama A&M University

Design and Fabrication of a Force Measurement Table for FSW Studies
Joseph Querin, Mississippi State University

Development of a Rocket Engine Combustion Chamber Cooling Module for the ROCETS Modeling System
Sivaguru Ravindran, The University of Alabama in Huntsville

Microgravity Educational Research
Carol Denise Richardson, Jacksonville State University

New Hydrophilic, Composite Membranes for Air Removal from Water Coolant Systems
Stephen Ritchie, The University of Alabama

Lightning Detection Efficiency Determinations for Lightning Networks of Limited Scope
John Rompala, University of Wisconsin – Stout

Development of a Fuzzy Logic Controller for Use in the Approach and Landing Portion of Descent
Curtis Schmitt, Rose-Hulman Institute of Technology

Use of Marker Studies to Study Material Flow in the Friction Stir Welding Process
Judy Schneider, Mississippi State University

Design of Experiments and Data Analysis of New Composite Material for Radiation Shielding and Structural Effectiveness
Mohamed Seif, Alabama A&M University

Preliminary Design and Minimum Material Cost Estimates of 1 to 8-Kilometer Height Steel Towers for Electro-Magnetic Launch Assist Systems
Ajay Shanker, University of Florida

Analysis of a Rotating Vapor Compression Distillation System for Urine Purification
Muhammad Sharif, The University of Alabama

Dusty Plasma Sail Feasibility Study
Robert Sheldon, Wheaton College

Graphical User Interface (GUI) Using MATLAB/Simulink for Nuclear Electric Propulsion Simulation Models
Yeu-Sheng Shiue, Christian Brothers University

Structural Dynamics Website in Support of AIAA's Education Outreach Program
Michelle Simmons, Alabama A&M University

Modeling of LH_2/LOX Combustion for Liquid Rocket Propulsion Engines-Enhancement of Generalized Fluid System Simulation Program
Mehmet Sözen, Embry-Riddle Aeronautical University

A Study of the SST in the Cold Tongue of the NSIPP and CCSM2 Coupled Climate Models
Monica Stephens, Spelman College

3-D Photonic Band Gap Crystals
Girija Subramaniam, Pennsylvania State University-Hazelton

The Effect of Advanced Manufacturing Technologies and Techniques on the Cost of Future Earth-To-Orbit Space Transportation Systems
Meenakshi Sundaram, Tennessee Technological University

Justifying Technology Transfer at NASA
Gary Templeton, Mississippi StateUniversity

Structural Health Monitoring of Composite Overwrap Pressure Vessel
Kevin Tseng, Vanderbilt University

Analysis of Acoustic and Vibrational Related Measurements in Propulsion Data
Patrick Vitarius, The University of Alabama in Huntsville

Talking History: Oral Histories of Marshall Space Flight Center
Stephen Waring, The University of Alabama in Huntsville

Dual Pulse Laser Spark Ignition for Rocket Engines
Joseph Wehrmeyer, Vanderbilt University

***International Space Station* and Payload Operations**
Talicia Williams, Alabama A&M University

Electrocomposite of Alumina in a Nickel Matrix
Pei Xiong-Skiba, Austin Peay State University

2003

NASA FACULTY FELLOWSHIP PROGRAM

MARSHALL SPACE FLIGHT CENTER
THE UNIVERSITY OF ALABAMA IN HUNTSVILLE

MECHANICAL CHARACTERIZATION OF A NEW MATERIAL DEVELOPED FOR RADIATION SHIELDING

REPORT NOT AVAILABLE

Prepared By:	Felipe J. Acosta Costa
Academic Rank:	Associate Professor
Institution and Department:	University of Puerto Rico Mayagüez Campus Department of Civil Engineering and Surveying
NASA/MSFC Directorate:	Engineering
MFSC Colleague:	Dr. Raj Kaul

2003

NASA FACULTY FELLOWSHIP PROGRAM

MARSHALL SPACE FLIGHT CENTER
THE UNIVERSITY OF ALABAMA IN HUNTSVILLE

SYSTEM IDENTIFICATION OF X33 USING NEURAL NETWORK

Prepared By:	Shiv Aggarwal
Academic Rank:	Professor
Institution and Department:	Embry Riddle Aero. University Department of Physical Sciences
NASA/MSFC Directorate:	Space Transportation
MSFC Colleagues:	Drs. John Hanson, Young Kim and Chong Lee

Introduction

A failure detection system is needed on board to improve spacecraft survivability [5]. Parameter Identification of spacecraft dynamics will prove useful in case the spacecraft is not performing as desired, and a reconfiguration of control variables is needed [5].

Parameter identification of a system is called system identification. We treat the system as a black box, which receives some inputs that lead to some outputs. The question is: what kind of parameters for a particular black box can correlate the observed inputs and outputs? Can these parameters help us to predict the outputs for a new given set of inputs? This is the basic problem of system identification.

Input **Black Box** **Output**

The X33 is comprised of both rocket and aircraft vehicle design characteristics and was supposed to have the onboard capability of evaluating the current performance and if needed to take the corrective measures to adapt to desired performance [5]. It requires, analytical methods for evaluating its flight performance [7].

Its flight consists of four phases: ascent, transition, entry and TAEM (Terminal Area Energy Management) [4]. It spends about 200 seconds in ascent phase, reaching an altitude of about 180,000 feet and a speed of about 10 to 15 Mach. During the transition phase, which lasts only about 30 seconds, its altitude may increase to about 190,000 feet but its speed is reduced to about 9 Mach. At the beginning of this phase, the Main Engine is Cut Off (MECO) and the control is reconfigured with the help of aero surfaces (four elevons, two flaps and two rudders) and reaction control system (RCS). The entry phase brings down the altitude of X33 to about 90,000 feet and its speed to about Mach 3. It spends about 250 seconds in this phase. Main engine is still cut off and the vehicle is controlled by complex maneuvers of aero surfaces. The last phase TAEM lasts for about 450 seconds and the altitude and speed, both are reduced to zero.

The present project focuses only on the entry phase. Since the main engine remains cut off in this phase, there is no thrust acting on the system. This considerably simplifies the equations of motion by removing linear acceleration and drag from our consideration for system identification purposes. Some non-linearities are computed analytically and are eliminated from equations of motion. Though the modified equations still possess some nonlinearities, we, initially, assume a linear relationship between input and output variables. Under this assumption, Classical Statistics could solve the problem by employing the least sum of squares approach. We do that to have a guidepost. Our method of choice, however, is Neural Network techniques. This choice has many advantages. It is modern, more efficient, works even when the system is nonlinear. Neural Networks try to model the human brain and are capable of pattern recognition.

Variables of the Project

In this section we will mention all the variables used in this project.

Input Variables

α, β, = Vehicle angle of attack, vehicle angle of side slip
p, q, r = body axis roll rate, pitch rate and yaw rate
M, A = Mach Number and Altitude
δts, δ_{ta}, δ_{fa} , δ_{rud} = symmetric trail deflection, asymmetric trail deflection, asymmetric flap deflection, rudder deflection

Output Variables

$\dot{\alpha}$, $\dot{\beta}$, $\dot{p}$, $\dot{q}$, $\dot{r}$ = time rate of change of variables

Other Variables

γ, μ = flight path angle, bank angle (about the velocity vector) (both in radians)
g_0, g_Y, g_L = gravitational acceleration in earth z-axis, Components of g_0 along the wind Y, and Z axis (all in ft/s^2). Also $g_Y = g_0 \cos\gamma \sin\mu$ and $g_L = g_0 \cos\gamma \cos\mu$
I_{ii}, I_{ij} = Vehicle body axes (moment, product) of inertia $\Gamma = I_{xx}.I_{zz} - I_{xz}^2$
V, m = Vehicle velocity, Vehicle mass
Y, L = lateral force along the wind Y-axis, aerodynamic lift along negative wind Z-axis
$\overline{L}$, $\overline{M}$, $\overline{N}$ = rolling, pitching and yawning moments

Equations of Motion

ANSI/AIAA recommended practice of using wind-axis force balances has been adopted. The angular equations of motion are resolved in body (not wind) axes system. The five equations of motion can be written in the matrix form OP = LP + NP where the actual output OP, linear part LP and nonlinear part NP are all 5 x 1 column matrices. Five elements of OP are the output variables $\dot{\alpha}$, $\dot{\beta}$, $\dot{p}$, $\dot{q}$ and $\dot{r}$. Five elements of LP are $-L/(mV \cos\beta) + g_L/(V \cos\beta)$, $Y/(mV) + g_Y/V$, $(I_{zz}.\overline{L} + I_{xz}.\overline{N})/\Gamma$, $\overline{M}/I_{yy}$, and $(I_{xz}.\overline{L} + I_{xx}.\overline{N})/\Gamma$. Notice the nonlinearity in the input variable β for the first element. Five elements of NP are $q - \tan\beta.(p \cos\alpha + r \sin\alpha)$, $p \sin\alpha - r \cos\alpha$, $I_{xz}.(I_{xx} - I_{yy} + I_{zz}).p.q/\Gamma + (Izz.(I_{yy} - I_{zz}) - I_{xz}^2).q.r/\Gamma$, $(I_{zz} - I_{xx}).p.r/I_{yy} + I_{xz}.(r^2 - p^2)/I_{yy}$, and $(I_{xx}.(I_{xx} - I_{yy}) + I_{zz}^2).p.q/\Gamma - I_{xz}.(I_{xx} - I_{yy} + I_{zz}).q.r/\Gamma$. Each of these elements is having nonlinearity in some of the input variables.

Methodology

Matrix NP basically arises because of the inertial cross couplings. Data (about 250 observations) was obtained from 6DOF (six degrees of freedom) MAVERIC (Marshall Aerospace Vehicle

Representation In C) simulation from lift off to TAEM. NP was computed for each observation and then was subtracted from the corresponding output observations. Modified output OPM was given by OPM = OP – NP. This reduced the equations of motion to the matrix form OPM = LP.

Initially another assumption was made. We assumed LP = W*IP where W was the 12 x 5 weight (system identification) matrix and the input IP was the 12 x 1 input column matrix. This assumption is equivalent to saying that elements of OPM are the linear combinations of the elements of IP. The elements of matrix W were identified by neural network design (**newlind**). Five artificial neurons were used in the network, one for each output. For comparison, the Weight matrix was also obtained using classical statistics.

Later on, to account for the nonlinearities in LP, the back propagation was exercised through Levenburg-Marquardt algorithm (**trainlm)**. Finally the same algorithm was applied to the virgin original sets of equations without eliminating any nonlinearities analytically.

Results

In the initial attempt all the 60 parameters of the problem (60 elements of W matrix) were successfully identified. The results were satisfactory. They agreed perfectly with the results obtained from classical statistics. The MSE was 0.01299. The results are not perfect. The imperfections are due to the remaining nonlinearities in LP=OPM because of the nonlinear dependence on β. Another source of imperfection is the time series nature of data, which results in the multicollinearity problems.

Levenberg-Marquardt algorithm is a variation of Newton's method (as modified by Gauss). It is a fast algorithm, which takes care of nonlinearities also. Application of this algorithm to the pair (IP,LP) resulted in an MSE of 0.006335, an improvement by more than a factor of 2 over classical statistics approach. This encouraged us to apply the algorithm to the original pair (IP, OP), which resulted in an MSE of 0.004645, an improvement by a factor of 2.8 over Classical Statistics Approach.

Future Scope of the Project

On the mathematics side one may like to incorporate radial or Volterra orthogonal polynomials. The problem of multicollinearity introduced by the time series nature of the data may be handled by giving some weight to the past observations. The second step would be system identification in the ascent and transition phase of the flight. A last step might be to combine everything we have learnt in an attempt to automate the system.

Resources

This project required the use of many software tools. The main software chosen for the project were MATLAB [2], [8], [9] and NEURAL NETWORK TOOLBOX. MATLAB [6] is software dealing with the manipulation of matrices and NEURAL NETWORK TOOLBOX deals with the methodologies of neural networks. A number of books from Redstone Scientific Information Center (RSIC) provide wealth of information related to the project [1], [3].

Conclusion

The problem of System Identification can be adequately handled by using the presently available resources provided by MATHLAB and NEURAL NETWORK TOOLBOX.

Acknowledgements

The author would like to thank the entire team of engineers and scientists in the vehicle flight mechanics group of the Marshall Space Flight Center's Space Transportation Directorate.

Warren Adams provided the most needed computer hardware support. Bradley Burchett, Mehmet Sozen, and Ashok Batra were generous with their time in clarifying some of the subtleties of Computer Software. My MSFC colleagues Drs. John Hanson, Young Kim and Chong Lee were kind and amiable. They provided guidance without any reservations, whenever I needed.

References

[1] Cooper (1998). *Introduction to Partial Differential Equations with MATLAB*, Birkhauser

[2] Etter (1993), *Engineering Problem Solving with MATLAB*, Prentice Hall

[3] Hagan, Demuth & Beale (1996), *Neural Network Design*, PWS Publishing Company

[4] Hall C.E., Gallaher M.W., and Hendrix N.D. (1998). X33 Attitude Control System Design for Ascent, Transition, and Entry Flight Regimes, AIAA-98-4411 American Institute of Aeronautics and Astonautics, pp 1-10

[5] Hanson J.M. (2002). A plan for Advanced Guidance and Control Technology for 2nd generation Reusable Launch Vehicles AIAA Guidance, Navigation & Control Conference Proceedings pp 1-10

[6] Demuth & Beale (2001), *Neural Network Toolbox (User's Guide version 4)*, The MathWorks

[7] Ward D.G., Monaco J.F., and Bodson, M. (1998). Development and Flight Testing of a Parameter Identification Algorithm for Reconfigurable Control, Journal of Guidance, Control and Dynamics Vol. 21, No. 6, pp 948-956

[8] William Palm III (2001), *Introduction to MATLAB 6 for Engineers*, McGraw Hill

[9] Wilson & Turcotte (1997), *Advanced Mathematics and Mechanics Applications using MATLAB*, CRC Press

2003

NASA FACULTY FELLOWSHIP PROGRAM

MARSHALL SPACE FLIGHT CENTER
THE UNIVERSITY OF ALABAMA IN HUNTSVILLE

REALIZING THE NEW MYTHOLOGY THROUGH THE OLD

Prepared By:	Mary C Bangs
Academic Rank:	Instructor
Institution and Department:	Empire State College Art Department
NASA/MSFC Directorate:	Space Transportation and Center Operations
MSFC Colleague:	Les Johnson Jack B. Hood

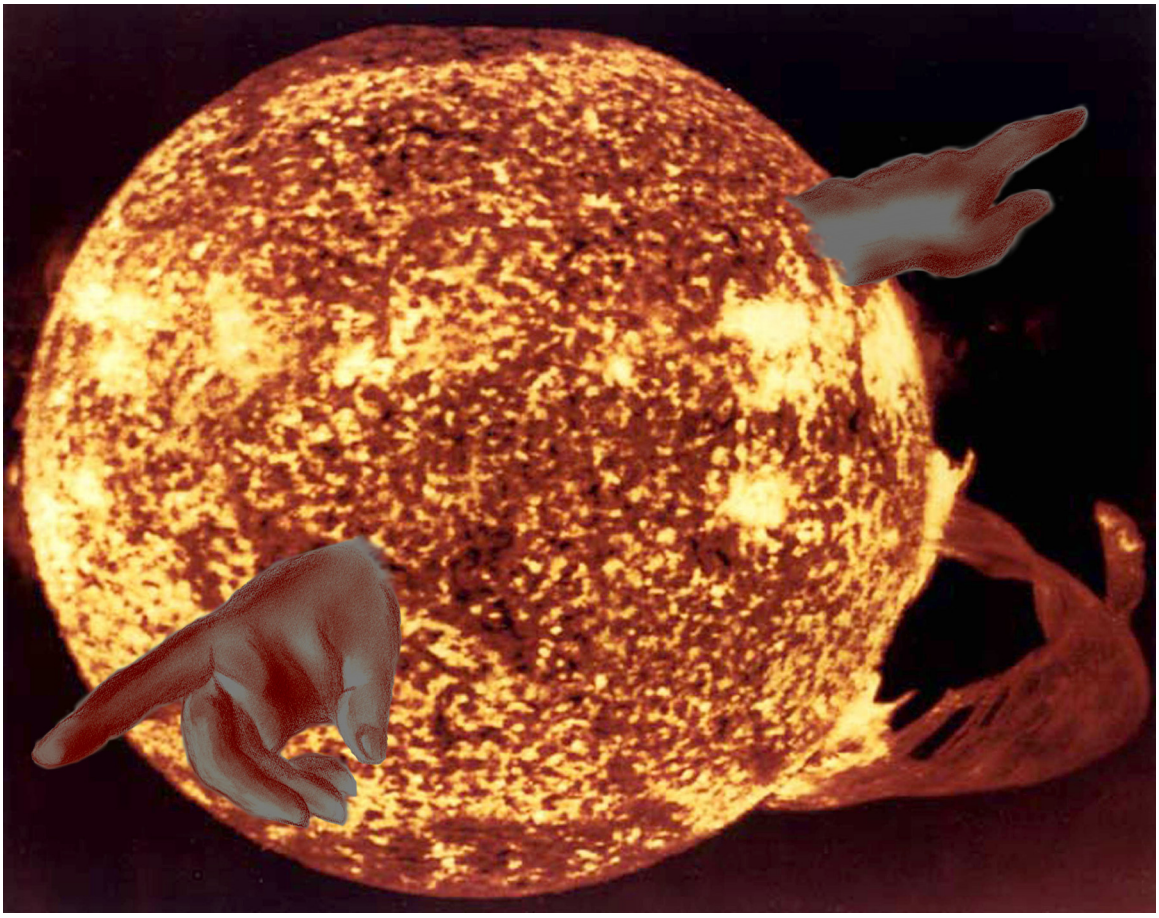

Sun after Michelangelo's panel in the Sistine Chapel, "Creation of the Plants, Sun and Moon"

Introduction

This paper describes the design of a poster of the solar system incorporating space-transportation graphics of Tim McElyea [1], for the In-Space Propulsion Research Group of the Advanced Space Transportation Directorate at MSFC. These design concepts represent spacecraft engineered to optimally function under the widely diverse conditions within our solar system.

The poster is designed to combine elements of ancient and modern mythology. Solar-system planets are named after Roman Gods and Goddesses and so refer to the old mythology. NASA has named rockets, spacecraft and missions after figures of the old mythology, in accordance with this tradition.

During research on this project, it became evident that we are updating the old mythology in humankind's effort to visit and explore the planets in our solar system.

The Old Solar System Mythology

The planets Mercury, Venus, Mars, Jupiter and Saturn were named during Roman times. "Earth" is closely related to the Old Saxon word 'ertha', the Dutch word 'aerde' and the German word 'erda' meaning land. Uranus, Neptune and Pluto were discovered much later; it was decided to name them relating to the pre-existing mythology of the other planets.

In order to arrive at the images for the different planets and moons we might visit, I conducted web searches on Renaissance and European Academy art. The purpose of working off the paintings or sculptures of the mythological figures as they were depicted and widely characterized during the time of the Renaissance and Enlightenment was that they represented an evolution from the Old Mythology.

Mercury

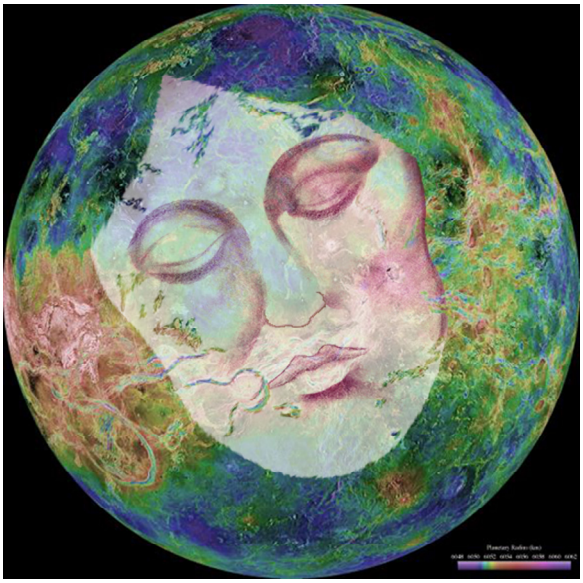

Venus after Giorgione "Sleeping Venus"

Joseph Campbell observed that the myths created by our ancestors no longer make sense within the context of our modern society. Campbell went even farther to warn us that a society with no contemporary myths in which it can believe is in danger of losing an essential part of humanity…We need new myths to help reflect on the values of our culture, our philosophies, our sciences. For example, new myths can have the ability to incorporate both an understanding and a deep sense of respect for the power of modern science and the accompanying technologies offered us without losing sight of our need to touch one another [2,3].

THE NEW MYTHOLOGY

The modern mythology we have been developing through science fiction, science and technology, continues to grow within our culture. One example is our conflicted reaction to the deciphering of the human genome. Another is the widespread interest in the theories of quantum physics, in particular as they refer to the phenomenon of consciousness.

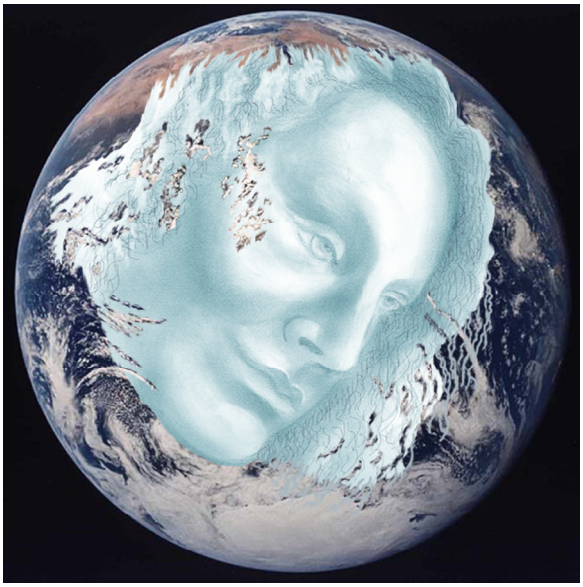

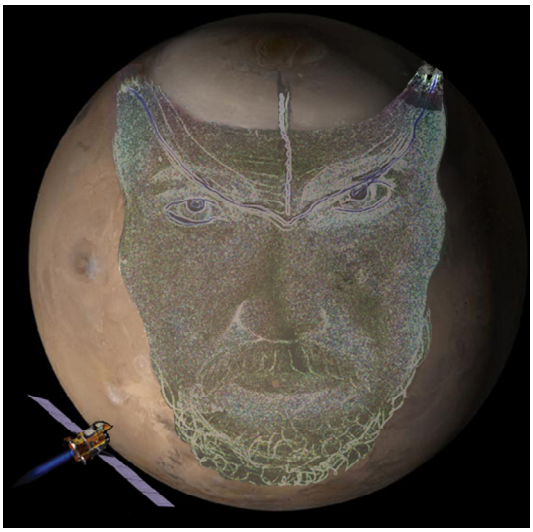

Earth after Leonardo's Madonna **Mars**

As stated by Orson Scott Card [4], "speculative fiction—science fiction in particular—is the last American refuge of religious literature…Real religious literature…explores the nature of the universe and discovers the purpose behind it."

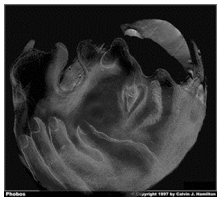

Our Moon after Corregio's Diana **Phobos**

Since its beginnings, space exploration has had significant mythological overtones. Astronauts and cosmonauts are regularly seen as larger-than-life figures. They embody our dreams of transcendence despite the sometimes-mundane duties they perform. Tom Wolf describes the Apollo 11 astronauts as being surprised at the reception they received during their post-flight visit to New York. Expecting a lukewarm or even hostile reception in a big, seemingly indifferent city driven by commerce and greed, they were amazed to witness the diverse population cheering itself hoarse and tough New York policemen openly crying as they passed by [5].

Mythology may be defined as a body of archetypal stories dealing with gods, demigods, and legendary heroes of a particular people. Many would discount mythology, and therefore science fiction as "an ill-founded belief held uncritically, especially by an interested group" (as *Webster's 3rd* definition).

Jupiter after van Dyck's King Charles I, King of England at the hunt

To the contrary, I believe that an educated, informed and critical populace, raised with the values and imagery of a society immersed in the computer age, can see the analogies between the archetypes of the primitive mind and the new mythology that we are creating. Mythology projects the dreams of society, or as Joseph Campbell has said [2], "A myth is a public dream, a dream is a private myth."

Ganymede after Michelangelo's Creation of Adam

Europa after Veronese's Europa

Io after Corregio's Io

Callisto and bear

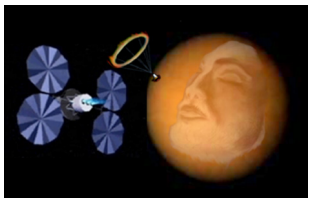

Titan after Michelangelo's captive slave with spacecraft

The astronauts aboard Apollo 8 gave humankind its first encompassing view of our exquisitely beautiful home planet. Perhaps their photographs sparked the environmental movement; they certainly heightened our understanding of our home. NASA officials were surprised by the volume of people logging onto their website during the Mars Pathfinder mission. Scientifically grounded SETI organizations, as well as a wide variety motivated by other beliefs, abound and regularly debate the existence of ETI (Extraterrestrial Intelligence). Millions of home computers currently act as processors for Arecibo's data flow, combing the Milky Way galaxy for radio messages from ETI [6]. In light of these examples, it can only be concluded that millions of Americans are in tune with the New Mythology.

Saturn after Michelangelo's Creation of Adam & spacecraft

The new mythology continues to grow despite the anxiety of many human concerns and slow-moving technical progress; it can be contrasted with popular culture's ability to warp across the

universe during TV commercials. And yet we carry our old myths with us, naming missions after Roman and Greek gods and heroes. But of course our mythology is evolving (as all mythology does) reflecting the culture that it is derived from. According to Joseph Campbell [2], "…myths-that is to say, religious recitations (are) conceived as symbolic of the play of eternity in time. These are rehearsed not for diversion, but for the spiritual welfare of the individual or community."

This sentiment has also been echoed by Carl Jung, who states [7],
"Not for a moment dare we succumb to the illusion that an archetype can be finally explained and disposed of…The most we can do is to dream the myth onwards and give it a modern dress."

Neptune after statue of Apollo at Versailles

CONCLUSION

Jonathan Young, who assisted Joseph Campbell and is the Founding Curator of the Joseph Campbell Archives and Library, has written [8] "The soul of the planet speaks to us through the mythic imagination." In assigning an updated mythology to our solar system, we may be expanding our concept of "the planet" to incorporate the entire solar system?

This preconditions our response to the exploration of the solar system. According to McElyea [1], "Exploring the unknown is one of the most compelling human instincts. It is in this spirit that our space pioneers landed on the moon, peered at the farthest reaches of the universe, and introduced technologies that have transformed our lives."

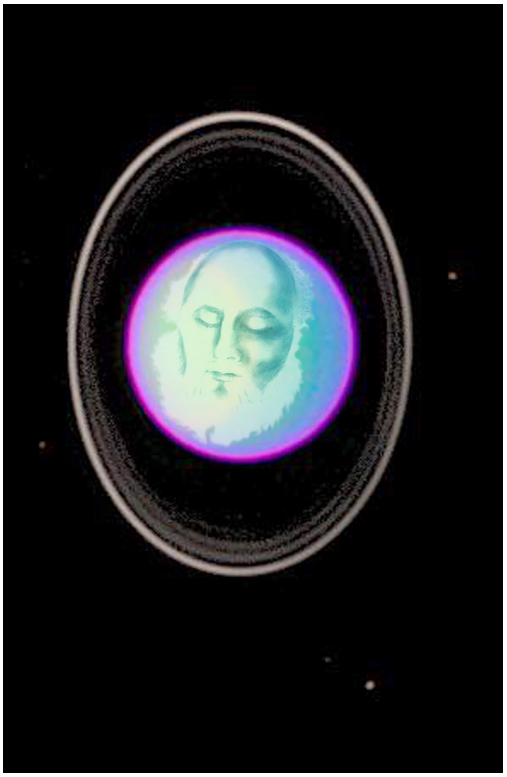

Uranus after Caravaggio's Joseph

Does mathematics function like mythology to provide a way of arriving at the truth or does it in some way apply a human-made (albeit functional) grid over the universe and arrive at conclusions based upon our way of ordering the multidimensional chaos of everything? It seems to be fundamental to humankind to order our world based upon the framework of who we are.

Pluto after Ingres's Jupiter

References:

1. T. McElyea, A Vision of Future Space Transportation, Apogee, Ontario, Canada (2003).

2. J. Campbell, The Masks of God: Primitive Mythology (New York: Penguin, 1976; first published 1959)

3. S. V. Johnson, "Wisconsin Academy Review", A Journal of Wisconsin Culture Vol. 38, number 4 (Fall, 1992).

4. O. S. Card, Cruel Miracles, TOR, New York (1992)

5. T. Wolfe, The Right Stuff, Farrar, Straus and Giroux, New York (1979)

6. http://setiathome.ssl.berkeley.edu

7. C. G. Jung, Collected Works, C. L. Rothgeb and S. M. Clemens, Eds. "Abstracts of the Collected Works of C. G. Jung", vol. 9, part 1, Karnac, London, UK (1992)

8. J. Young, www.folkstory.com/contents.html

2003

NASA FACULTY FELLOWSHIP PROGRAM

MARSHALL SPACE FLIGHT CENTER
THE UNIVERSITY OF ALABAMA IN HUNTSVILLE

EXTRACTION OF IRON FROM MARTIAN SOIL BY MICROWAVE PROCESSING—A FEASIBILITY STUDY

Prepared By:	Walter Boles
Academic Rank:	Professor
Institution and Department:	Middle Tennessee State University Department of Engineering Technology
NASA/MSFC Directorate:	Science Directorate SD 46
MSFC Colleague:	Dr. Laurent Sibille

Introduction:

There are two fundamental reasons to exploit space resources—economics and crew safety. The economic argument is simple. If it costs less to develop and use a space resource than it does to transport that resource to a space location from the Earth, then it makes economic sense to do so. An example is the development of rocket propellants from the soil and atmosphere of Mars. If large quantities of propellants are needed on Mars, it will very likely make economic sense to make them on Mars.

The crew safety argument is a matter of urgency. Again, a Martian example: if one cannot wait a year for critical items for life support to arrive from Earth, then it makes sense to develop the capability to extract and process the materials and fabricate the items needed on Mars.

In addition to propellants and life support items such as water and oxygen, another very important resource is metal for maintenance, repair, and eventually fabrication/construction of new facilities and equipment. Exploitation of space resources where they exist is called in situ resource utilization. This work focuses on how to extract iron, a fundamental metal for subsequent refining process and in space fabrication, from the Martian soil.

This research effort continues work started during the 2002 NASA Faculty Fellowship Program at Marshall Space Flight Center. The 2002 work provided the inspiration and the preliminary evidence that microwave energy can provide the heat necessary to reduce iron oxide in a sample of a Mars soil analog, JSC Mars-1. While quantification of the degree of reduction was not within the scope of the 2002 effort, it is a major emphasis of the 2003 effort. Microprobe and iron Mössbauer spectroscopy were used to analyze the processed samples of Mars-1.

Once procedures are established to reliably determine the yield of iron (a measure of merit), parametric studies pertaining to beneficiation of source material and processing variables can be accomplished. This further research will demonstrate the effectiveness of iron extraction using microwaves. The balance of this paper presents a literature review, a discussion of processing methods, results, and conclusions.

Literature Review

The purpose of this literature review is provide an understanding of how microwaves affect materials and what progress has been made in the specific topic area of this effort—using microwave technology to aid in extracting iron from an iron oxide rich source to facilitate space fabrication. Information on the technology of producing microwaves is beyond the scope of this effort.

The use of microwave energy to generate heat in materials was discovered in 1950 by Raytheon Corporation (Chabinsky 1988). One reference quotes from a 1943 *Scientific America* that engineers working on short wave radio transmitters developed fever due to the irradiation (Committee on Microwave Processing of Materials 1994). In any case, Raytheon marketed the first microwave oven to the public in 1952 (Committee on Microwave Processing of Materials 1994). Even though the microwave oven is nowadays commonplace, it is still considered a

relatively new and emerging industrial technology (Stein et al. 1994). According to Stein et al. (1994)

> Microwave processing of materials is a technology that can provide the material processor a new, powerful, and significantly different tool with which to process materials that may not be amenable to conventional means of processing or to improve the performance characteristics of existing materials. However, because it is fundamentally a new and different technology, it requires the material processor to learn and understand the technology before attempting to use it.
> …. microwave processing is often a difficult method to use and is simply not an appropriate method for many applications. As a consequence, it is important for the processor to become knowledgeable about microwaves and their interaction with materials and seek consultation with appropriate experts if successful processing methods are to be developed.

Microwaves occupy the electromagnetic spectrum between 300MHz and 300GHz and most material processing occurs at frequencies of 915 MHz, 2.45 GHz, 5.8 GHz, and 24.124 GHz (Committee on Microwave Processing of Materials 1994). The typical domestic microwave oven operates at 2.45 GHz. Microwaves heat material through a process called coupling where energy is absorbed by the material from microwaves. Some materials provide good coupling between the microwaves and the material while others do not. Materials that couple very well are called susceptors. Other materials, such as glass, do not couple well and do not exhibit heat transfer under microwave irradiation. Some materials do not couple well at low temperatures but couple very well at elevated temperatures.

Solid metals reflect microwaves. The interior of a domestic microwave oven is lined with metal. A wire mesh protects the door opening. Therefore, the oven cavity reflects microwaves until they are absorbed by material in the oven. If there is no material in the oven, the magnetron may overheat. The magnetron is the microwave-generating device. The magnetron emits a beam of energy that reflects off the metal sides of the cavity. This causes the microwave oven to have hot spots where microwaves interfere in phase, thus increasing the energy density. Magnetrons create coherent, monochromatic electromagnetic radiation. Therefore, in some places the reflected waves effectively cancel out. In other places the intersecting waves are additive and create the hot spot.

The process of coupling or energy transfer is said to occur in three ways: electronic conduction, ionic polarization, and rotation of electric dipoles (Newnham et al. 1991). According to Newnham et al. (1991)

> Electronic conduction can play a key role in microwave heating of metal-like materials or semiconductors. … materials with moderate conductivity heat more effectively than either insulating or highly conductive materials. … many oxide ceramics have resistivities that decrease rapidly with increasing temperature affording more efficient coupling.

> … atomic and ionic polarizations do not generally contribute to microwave absorption.
>
> Without an electric field, the dipoles are randomly oriented and the net polarization is zero. In a static field, the dipoles align with the field and the polarization is maximized. These dipoles can rotate, but they rotate against a friction force.

Therefore, heat is generated in a material subjected to microwave irradiation by the flow of electrons through a resistive circuit and through dipole rotation against a friction force. The continuously reversing voltage drop induced by microwaves causes both phenomena. Water is an example of a material where the rotating dipole effect induces heat and silicon carbide is an example of a material where heating by resistive electron flow occurs.

As a result of these methods of generating heat, microwaves exhibit the following attributes that conventional heating does not (Stein et al. 1994):

- Penetrating radiation and internal heating
- Controllable electric field distributions
- Rapid heating
- Selective heating of material through differential absorption
- Self-limiting reactions

According to Stein et al. (1994) these differences can provide benefits as well as disadvantages depending on the material in consideration and the objectives of the heating process.

The Committee on Microwave Processing of Materials (1994) provides some information on how certain materials heat due to microwave irradiation. Metal powders exhibit moderate heating (iron powder reached 768° C in 7.0 minutes). Sulfide semiconductors, mixed valent oxides, carbon, and graphite are easily heated (FeS_2 reached 1019° C in 6.75 minutes). Alkali halides (e.g. KCL) and oxides (e.g. SiO_2) exhibit very little heating (NaCl reached 87° C in 7.0 minutes). All of the examples were irradiated with 1 kW at 2.45 GHz, which is within the parameters of a domestic microwave oven. It is interesting to note here that solid metals do not couple well with microwaves, as they tend to reflect the energy. Powered metals, however, couple very well as indicated above. Obviously, different materials with different physical conditions behave very differently when irradiated with microwaves.

Since energy transfer is accomplished in two ways. By using materials inventively, different heating schemes can be devised. Here are some examples:

- Direct heating of material
    - This method can be used for materials that couple well with microwave energy.
- Adding a powder susceptor material to a powder material
    - This method can be used for powder materials that do not couple well. The susceptor material, however, may also react chemically as a reducing agent. This may be desirable in some instances.
- Heating a crucible that couples well, which in turn heats the sample material.

    - An example is a silicon carbide crucible that couples well with microwaves.
- Using a susceptor material to heat a temperature sensitive susceptor material to an efficient coupling temperature.
    - An example is the use of silicon carbide in contact with a zirconia crucible. Zirconia only becomes a good susceptor at temperatures at and above 500° C. The silicon carbide provides the initial coupling to raise the zirconia to the coupling temperature.
- Hybrid heating is a general term that describes the use more than one heating method on a single sample.

Some other, unknown, reactions may also take place under microwave irradiation. Fanslow (1991) reports increased speeds of reactions that cannot be explained by the heat effect alone. "These examples present evidence that microwave processing produces chemical and physical reactions that are different from the reactions that would have occurred if the only effect produced by the microwaves had been an increase in temperature" (Fanslow 1991).

The breakdown of gas in the sample may impose a maximum temperature obtainable. Tian et al. (1988) report success in irradiating silicon carbide material under pressure to mitigate the gas breakdown. Temperatures several hundred degrees C higher were obtained under high-pressure argon and nitrogen.

McGill et al. (1988) reports the effect of increased power on some materials. While frequency was held constant at 2.45 GHz, power level was changed incrementally from 500 W to 2,000 W. McGill et al. (1988) reports the two following results among many others:

> The CuO reached a maximum temperature 1 min 25 sec sooner (six times faster) with an increase in power from 500 to 1,000 W. The Fe_3O_4 sample heated to its maximum temperature with a negligible rate change regardless of input power, heating to about 900° C at 1 min, and slowly increasing for the duration for the test …

Microwave frequency also affects coupling. Sklyarevich et al. (1992) state "…millimetric radiation is by 3 orders of magnitude more efficient in interaction with nonmetallic materials than centrimetric radiation." The wavelength of 2.45 GHz is about 12 cm and the wavelength of 100 GHz is about 3mm.

The effect of grain size on coupling with carbon powder was also investigated. Lorenson et al. (1992) report that smaller grain sizes produce more rapid heating. They also report their method of measuring temperature using a sapphire probe connected to fiber optic and optical pyrometry that they indicate is appropriate for a microwave environment.

Oak Ridge National Laboratory has developed guidelines for conducting microwave-processing experiments. Janney et al. (1992) state the following:

Guidelines have been developed at ORNL for conducting meaningful side-by-side conventional and microwave thermal processing experiments on ceramics. These guidelines may be summarized as follows:

1. Microwave and conventional furnaces are inherently different in terms of material processing.
2. Dielectric properties must be explicitly considered in planning microwave experiments, including both temperature and frequency effects.
3. Temperature measurement in a microwave furnace is always an issue. In particular, each new material or experimental setup brings with it new problems in temperature measurement.
4. Thermal gradients may be inherently different for conventional and microwave processing. Conventional samples tend to be cooler in the middle than on the surface; microwave samples tend to be warmer in the middle.
5. Sample size may have to be adapted to microwave processing conditions; in general, a minimum sample size of 50 to 100g is required in the microwave furnace unless indirect heating or ballast/crucible is used.
6. Field effects must be managed in a microwave furnace including arcing of thermocouples to samples and field concentrations around thermocouples. Also, the field uniformity in the microwave cavity (or lack thereof) can have a decided effect on how materials can be processed.
7. It must be recognized that the processing atmosphere interacts with the microwave field. Plasma formation and arcing can be a problem, especially when operating in argon or other gasses with low breakdown potential.

The U. S. Bureau of Mines experimented with microwaves in improving the grindability of iron ores. This is due to the selective coupling of microwave energy and iron-rich areas within the ore. Selective heating then causes differential expansion and cracking in the ore. Walkiewicz et al. (1988) report that microwave irradiation does induce localized heating and breakup of iron ores. They also report, however, that the energy savings in the grinding process is less than the energy consumed in the microwave process. The effort is, therefore, uneconomical.

Some researchers have investigated using microwave energy to drive the carbothermic reduction of iron ore. Standish and Worner (1991) point out that the reduction of metal oxides with carbon is widely used to produce many metals, including iron. They also point out that a phase change from Fe_2O_3 to Fe_3O_4 may increase heating efficiency. This is due to the process by which Fe_2O_3 is converted into Fe with Fe_3O_4 as an intermediate step. Fe_2O_3 is not a good susceptor. Fe_3O_4 is a good susceptor. Therefore, as the reaction progresses, the material becomes better able to absorb the microwaves. The three equations that represent the reaction are indicated in Equations 1, 2, and 3 (Standish and Worner 1991).

$$3Fe_2O_3 + CO = 2Fe_3O_4 + CO_2 \quad (1)$$

$$Fe_3O_4 + CO = 3FeO + CO_2 \quad (2)$$

$FeO + CO = Fe + CO_2$ .....(3)

Standish and Worner (1991) also note that a tremendous amount of heat is lost in the process of "gasification of carbon by the Boudouard reaction." The Boudouard reaction is represented by Equation 4 and provides a mixture of CO and CO_2. At temperatures above 1,000° C an atmosphere of near 100% CO is obtainable (Aguilar and Gomez 1997).

$C + CO_2 = 2CO$ .....(4)

Aguilar and Gomez (1997) report on the results of experiments to demonstrate the feasibility of using microwaves as the heat source in the carbothermic reduction of iron ore. They compared conventional heating with microwave heating with iron ore pellets and powder. The experiments show a maximum of 40% reduction with the microwave heating method and 70% to over 90% for conventional heating. This was true for either pellets or powder. They suggest that one possible reason for this discrepancy is a layer of iron that forms on the exterior of the pellets that prevents microwave energy from penetrating into the center of the pellet. They observed a similar effect in powder where the exterior of the sample exhibited a very high degree of reduction while the interior of the sample exhibited little reduction. Standish and Pramusanto (1991) observed a similar phenomenon and attributed it to a sealing effect where the reducing gas (CO) could not reach through the iron coating of some particles. The existence of unreduced product at the core of iron-coated particles or pellets may be due to the reflection of microwave energy or the exclusion of the reducing agent by the iron surface or both. However, since Aguilar and Gomez (1997) used carbon powder, the argument for the reflection of microwave energy may be more plausible.

Standish and Huang (1991) observed much higher reduction rates for microwave than for conventional heating (up to about 80% and 35% respectively). This is opposite from the result of Aguilar and Gomez and deserves some further study.

Standish and Huang (1991) report that "Most of the liquid metal sank to the bottom of the crucible and some metal granules dispersed in the slag." They also make the following observations:

> Additional benefits of microwave heating that may be expected include
>
> i. Heating of hyperactive Fe_3O_4 at practically the same rate regardless of input power,
> ii. Phase change Fe_2O_3 to Fe_3O_4 enhancing the heating,
> iii. Larger masses being heated faster than smaller masses for same power level, and
> iv. Arcing due to presence of freshly reduced iron supplying additional heat.

Standish and Huang (1991) conclude the following:

> The results of the present experiments have shown that:

1) Carbothermic reduction of both magnetite concentrates and hematite fines can be satisfactorily and rapidly carried out with microwave heating. For the conditions used complete reduction was achieved after about 15 min.
2) Both charcoal and coke are effective reductants but the former is stronger.
3) Lime and limestone are both effective fluxes in the reduction process.
4) Carbon containing products are obtained both with ore without melting the charge.
5) The microwave reduction process at up to 1000° C, and probably generally also, is superior to conventional reduction for otherwise identical conditions.

Standish and Huang (1991) used mixtures of hematite ore fines, magnetite concentrates, coke, charcoal, lime, and or limestone. They used 50g hematite ore fines or 50g magnetite concentrates with 18g or coke and/or charcoal. They also added small amounts of lime or limestone. Total iron content of either iron source was about 63% by weight. Carbon content of coke was about 90% and carbon content of charcoal was about 94%. Therefore, the C/Fe ratios were about 18*0.9/50*0.63 = 51%.

Aguilar and Gomez (1997) used iron ore pellets and iron ore dust with powdered carbon from electric arc furnace electrodes. Their carbon content was 3.5 times the stoichiometric calculation based on preliminary experiments to select the optimum amount for use with pellets. For the left hand side of Equation 3 one mole of FeO plus one mole of CO is 99.8541 g.

(55.845)+(15.9994) + (12.0107) +(15.9994) = 99.8541

The ratio of C to Fe is 12.0107/55.845 = 0.215. Therefore. 3.5 times the stoichiometric quantity is a C/Fe ratio of 0.75 by weight.

Zhong et al. (1997) experimented with 5 and 50-gram samples of iron ore powder mixed with coal dust. They found the best results with 20% more carbon than the stoichiometric calculations would indicate or a C/Fe ratio of 1.2*21.5 = 0.258 by weight. They conclude "A 90% reduction of iron ore by coal can easily be achieved in 10 min with a temperature greater than 1,000° C and with 20% excess stoichiometric carbon."

Kemp Corporation is experimenting using microwave energy in a direct reduction process of iron ore powder to obtain iron. The company's website, http://www.kempdev.com/microwav.htm, shows schematics of a machine that is supposed to provide a mechanical fluidized bed which is subjected to microwave energy.

Boles (2002) reports the results from experiments using microwaves and carbon powder to reduce a Mars soil simulant (JSC Mars-1). With fine carbon powder (graphite) mixed into the simulant at about 10% by weight, visually dramatic reactions began within one minute and totally melted the sample in three to five minutes. Electron Microprobe analysis revealed the

formation of tiny iron spheres along with other interesting formations, some of which occur naturally only in fulgurites (where lightning melts soil). Fulgurites provide evidence of extreme reduction and volatilization (Essene 1986). Interestingly, Boles' samples with coarsely ground carbon added to the simulant produced heating no greater than samples with zero carbon added (about 100° C). In this case the fine carbon powder apparently is the susceptor as well as the reducing agent.

It is interesting to compare the quantity of carbon added for the references cited above. Boles (2002) worked with the JSC Mars-1 Martian soil simulant which contains 2.8% FeO and 9.3% Fe_2O_3. This works out to be

2.8*55.845/(55.845+15.9994) or 2.17% Fe from FeO and

9.3*111.69/(111.69 + 47.9982) = 6.5% Fe from Fe_2O_3.

The total Fe in the JSC Mars-1 is 6.5 + 2.17 = 8.67% by weight. Boles (2002) experimented with carbon quantities between 4% and 12% weight of the sample, which represents ratios of carbon to iron of 46% to 138% by weight. Boles (2002) found that about 8% to 10% carbon (approximately one-to-one ratio of C/Fe) was required to achieve robust reactions.

It is also interesting to note the purity of the reactants. As previously stated, JSC Mars-1 contains 8.67% iron, Aguilar and Gomez (1997) experimented with an ore that was 66.5% iron, Standish and Huang (1991) experimented with ore that was about 67% iron, and Zhong et al. (1996) experimented with ores that were 63% and 70% iron. It is possible that the higher carbon content required for JSC Mars-1 is due to the lower concentration of iron. The JSC Mars-1 does not heat appreciably without a significant amount of carbon present. This would seem to indicate that the carbon is providing the main source of susceptor material for the Martian soil simulant as well as the reducing agent. Table 1 summarizes the iron and carbon content for some authors.

Table 1. Iron – Carbon Content

Reference	Sample Iron content %	C/Fe ratio used %
Boles (2002)	8.67	100
Zhong et al. (1997)	63 or 70	25.8
Standish and Huang (1991)	63	51
Aguilar and Gomez (1997)	66.5	75

Procedures

We used a XXX microwave oven; model YYY (800W, 2.45 GHz). Location of the hot spots in a microwave oven is crucial to consistency. The method used in this work is illustrated in Figures 1 and 2. Figure 1 shows the heat sensitive paper tube structure in the microwave oven. Figure 2 shows the structure after microwaving for five minutes at full power. The hot spots are easily identifiable. The left, bottom, midway back location was selected.

Figure 1. Locating Hot Spot: Heat Sensitive Paper in Oven

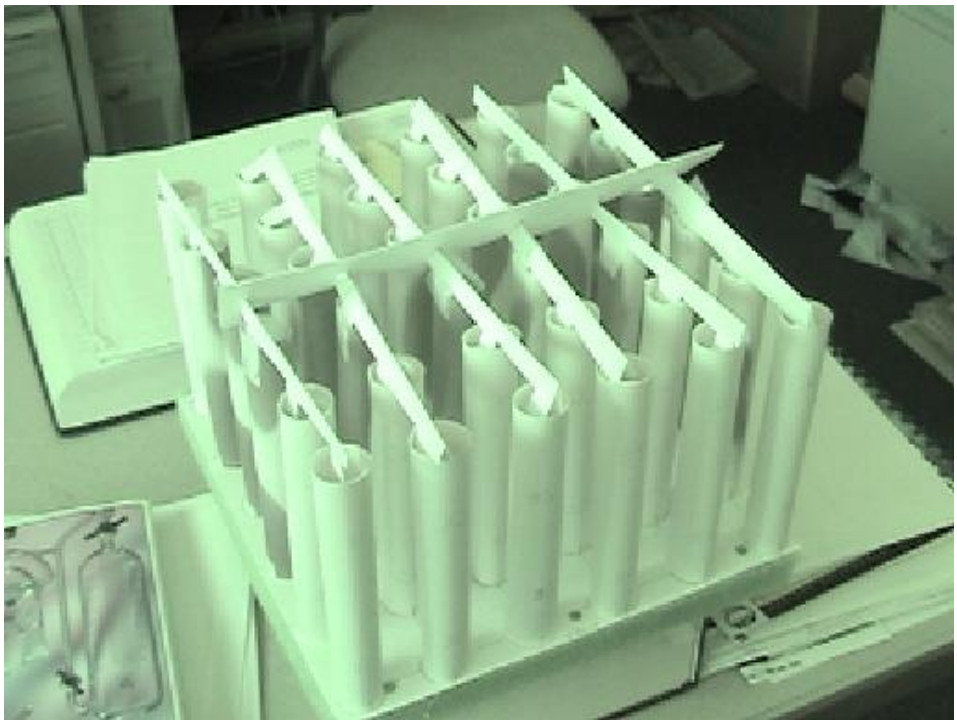

Figure 2. Locating Hot Spot: Heat Sensitive Paper After Microwaving

Samples of one and three grams were prepared with varying amounts of carbon. The carbon and JSC Mars-1 were mixed by hand before placing in an alumina crucible. Alumina fiber gauze (looks like cotton) was used to plug the top of the crucible. This was done to contain the ejection of material during the first few seconds of heating.

Figures 3 and 4 show typical samples after and during microwave processing. In figure 3, the smaller sample was almost fully melted after processing for 8 minutes with 10% carbon and the larger sample was sintered after processing with 6% carbon for 8 minutes. Interestingly, the 2002 work indicated that the Mars-1 did not heat appreciably without carbon. However, the 2003 work indicates that the soil will melt with no carbon added if the sample is correctly placed within a hot spot instead of at its edge. Figure 4 does not represent the most energetic phase. The most energetic phases are too bright to capture with normal digital video equipment. A small alumina thimble crucible was used.

Figure 3: Processed Samples

Figure 4: Irradiated Sample

A significant amount of material is ejected from the crucible during the first few seconds of microwave irradiation. One possible reason is the rapid heating of adsorbed water in the soil. To test this hypothesis, the sample in Figure 5 was heated for two hours in air at 500+ C before mixing and irradiating. The carbon powder was heated in a separate oven at 200 C before mixing with the soil. Cooling of both soil and powder in air occurred before mixing and processing. Since we observed the same ejection of material, it is possible that enough water condensed within the sample before processing. In a separate test, we observed that soil material was ejected during heating in air from room temperature to 300C in a resistive furnace. Heating the soil as a layer to 250C in an aluminum dish before pouring it while hot in a crucible could eliminate the problem. Further heating the soil to 1250C at 10C/minute produced no ejection of material. In conclusion, we can eliminate the ejection of material by removing condensed water but the extreme heating rates generated by microwave energy also produce additional gases. Carbon dioxide and monoxide are certainly produced but also the elimination of nitrates or sulfides not well quantified in the soils may be a contributing factor.

Results

One key objective of summer 2003 work was finding a method to quantify the yield of iron oxide reduction in the soil samples. Many examples found in the literature show that most

studies involving measurement of iron contents assume all iron to be in the form of ferric or ferrous oxides. Communications with laboratories that specialize in performing chemical analyses provide additional evidence of the difficulty of using chemical analysis to differentiate between iron oxide and iron. It was determined that iron Mössbauer spectroscopy was the best method available to reliably make this distinction in a quantitative manner at this time.

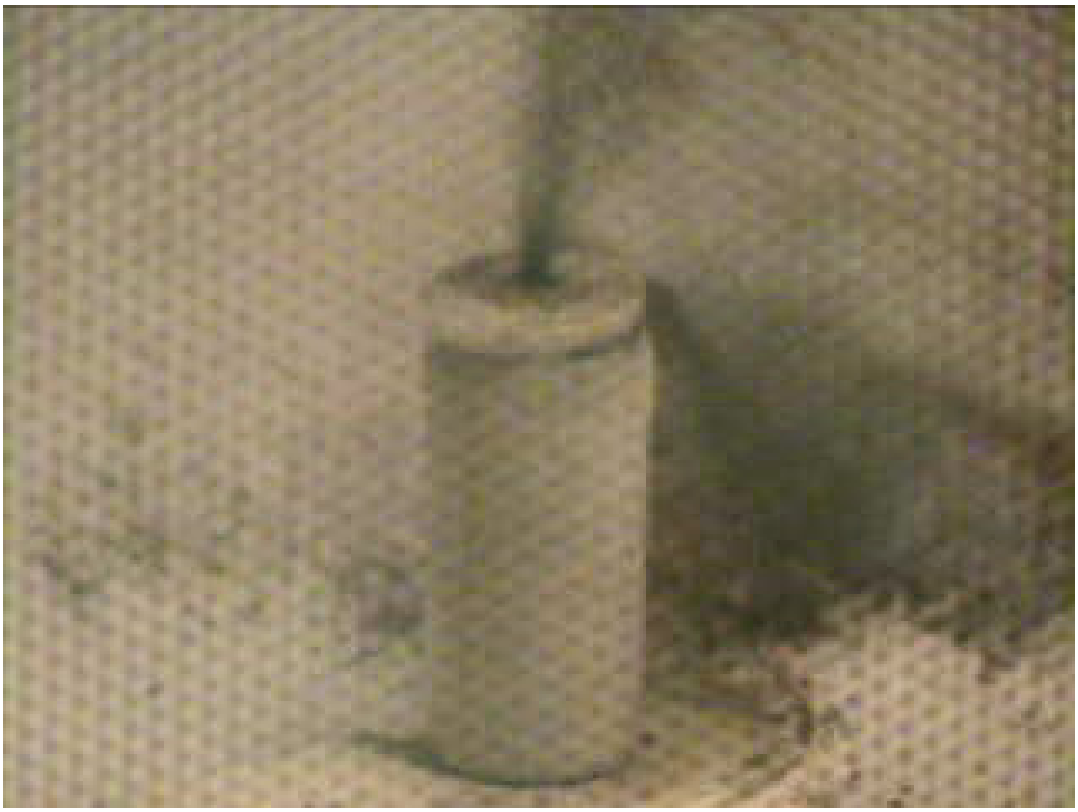

Figure 5: Material Ejection Shortly After Irradiation Begins

Mössbauer spectroscopy, sometimes called iron Mössbauer spectroscopy, is especially suited for identifying iron. A gamma radiation source is repeatedly moved forward and away from the sample and a receptor measures the energy transmitted through a sample. In backscatter iron Mössbauer spectroscopy the detector measures reflected gamma radiation and is on the same side of the sample as the emitter. Iron is particular well suited to absorbing the energy (counts) and has a definite graphical signature as indicated in Figure 6. The two peaks in the figure indicate high absorption for iron. Further explanation of iron Mössbauer spectroscopy is beyond the scope of this work.

Figure 6 shows an iron Mössbauer spectrum of processed JSC Mars1 (10% C, 8 minutes) courtesy of Dr. David Agresti, at the University of Alabama in Birmingham. The spectral model fitted to the raw data includes a broadened sextet (the 1, 2, and 6 peaks are visible in the data), with parameters very close to those of metallic α-iron, at 8.9% (±0.4%) of the total spectral area. According to Dr. Agresti (personal communication)

In short, the interpretation (fitted model) of ~9% metallic iron, plus ~91% ferrous glassy non-magnetically ordered, would be consistent with the Mössbauer data - with one huge caveat: the percentages are spectral areas and converting into real abundances requires information about the so-called "recoil-free fraction," which is known for iron, but we don't have a value for the glass - we would either look it up after characterizing the material or measure it in a dedicated study. However, to assess the progress of a reaction, absolute abundances are probably not needed since spectral areas are proportional to the amount of material (assuming the Mössbauer resonance is far from saturation).

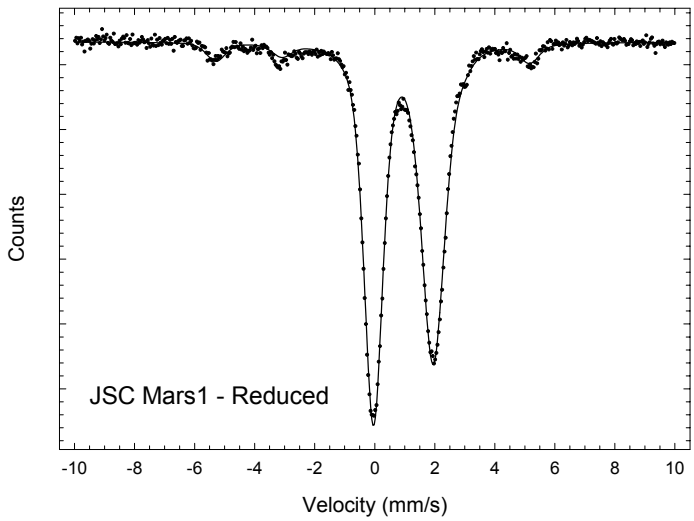

Figure 6: Mössbauer Spectrograph

Thus, if one knows the total abundance of iron oxide, one can use iron Mössbauer spectroscopy to make accurate determinations of iron oxide and iron in a sample. The Mössbauer work was supplemented with electron microprobe analysis.

Figures 7 through 9 are microprobe frames showing the results of processing. Figures 7 and 8 are of a JSC Mars-1 sample subjected to magnetic separation with xx Gauss field prior to processing. Figure 7 is of the non-magnetic portion processed with 12% carbon added by weight. Figure 8 is the magnetic portion processed with 6% carbon added by weight. The sample orientation in the figures is the same as the processing orientation, i.e. the bottom of the figure was also the downward orientation during processing. The carbon content was selected in order to produce similarly energetic reactions (subjectively by visual inspection). The phenomenon of blowout occurred as usual with the non-magnetic portion while it was greatly reduced for the magnetically sensitive portion.

Although not conclusive since the frames represent only a two-dimensional slice of the resultant melted sample, it is interesting to note that the non-magnetic sample shows significant presence of iron micro-spheres (imaged in white) while the magnetic portion does not. Although elemental characterization of the soil performed by other authors tabulates all iron oxides in

either FeO or Fe_2O_3 forms, the effectiveness of the magnetic separation suggest the presence of magnetite Fe_3O_4. Figure 9 is a microprobe frame of a micro-sphere.

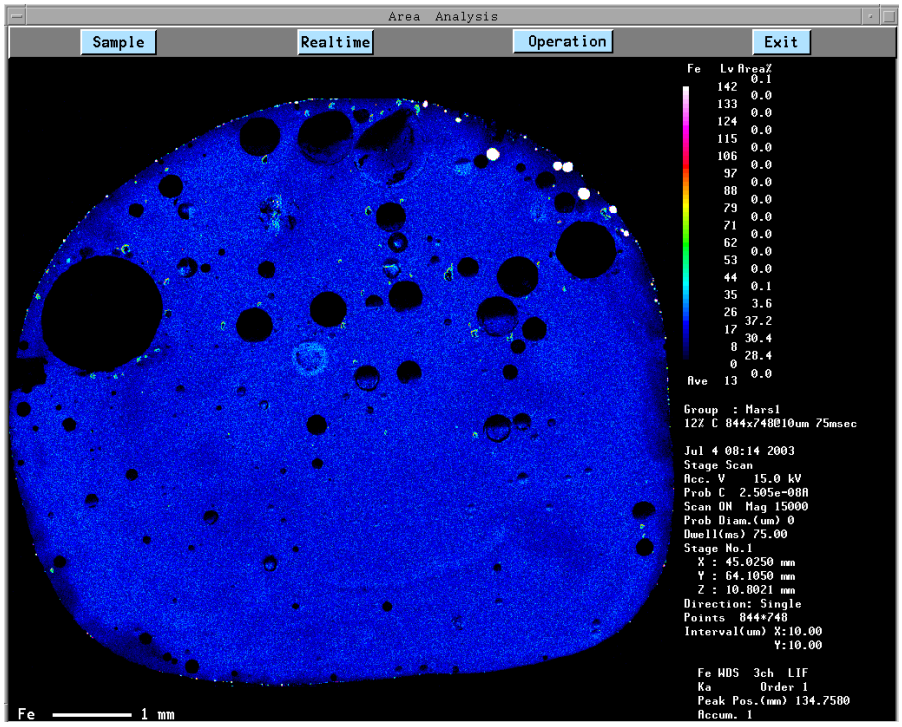

Figure 7: Microprobe Frame of 12% C, Non-Magnetic Portion

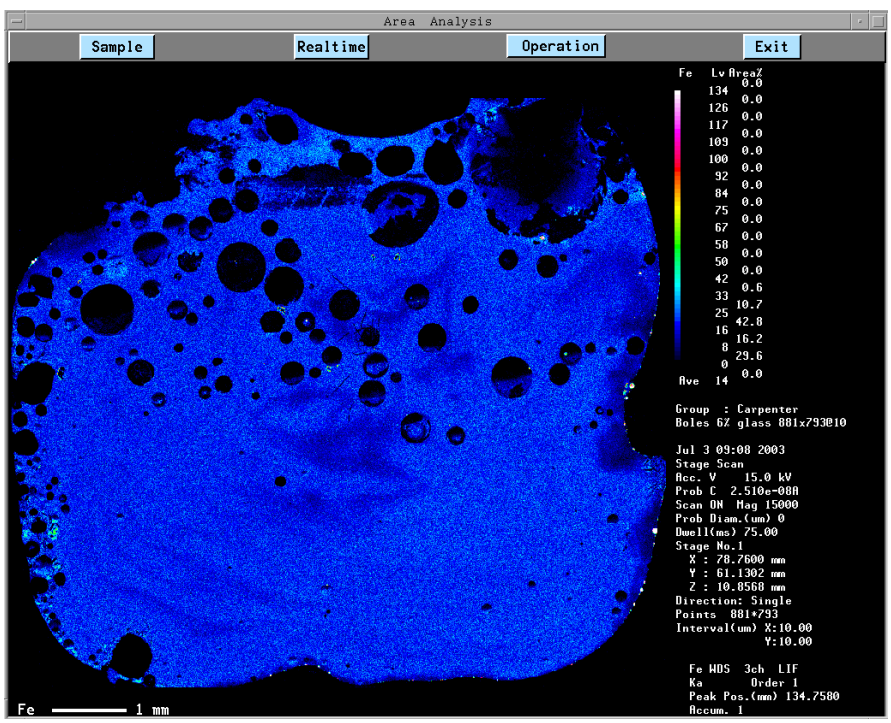

Figure 8: Microprobe Frame of 6% C, Magnetic Portion

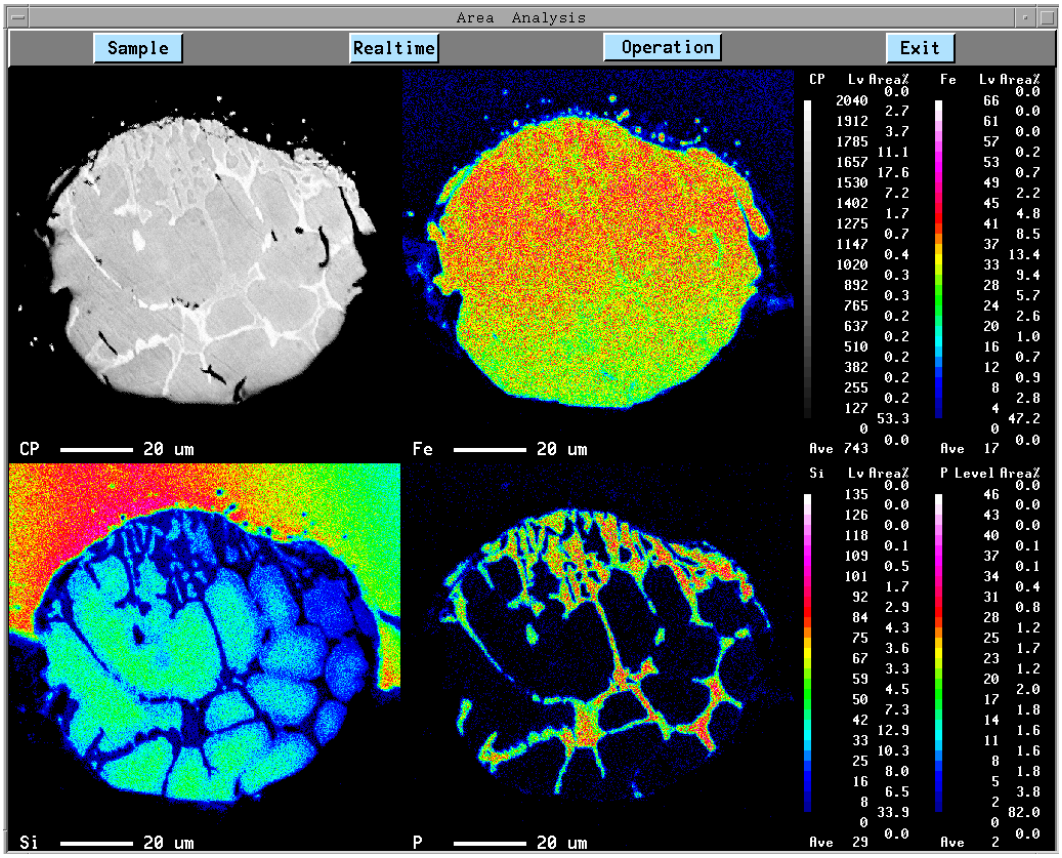

Figure 9: Microprobe Close-up of a Iron Micro Sphere

Color frames in Figure 9 display the concentration of specific elements with brighter shades indicating higher concentrations. The black and white rendering lacks some detail provided by color. It can be seen, however, that this is an iron rich sphere (upper right frame) with phosphorus in the grain boundary areas (lower fight frame). A fraction of the grains indicate the presence of iron silicide while others seem to have a low concentration of Si. The contrast between the Si and Fe maps shows high iron content in the sphere while the surrounding glassy area of silicon rich material is depleted of iron.

Recommendations

Further work is required to reveal the full potential of using microwave energy to produce iron from the soil of Mars. Similar methods may well work for the soils on Earth's moon as well as asteroids. Since this effort has demonstrated feasibility, one can now envision the next phase of research. A follow-on project fully exercising a parameter matrix aimed at optimization of processing parameters and beneficiation methods is called for. Mössbauer spectroscopy supplemented with microprobe analysis should be used to provide comparative results. A preliminary set of variables is listed below:

Pre-Microwave Variables

- Iron content and condition of sample (beneficiation)

- Carbon content of sample
- Grain size of sample
- Grain size of carbon
- Additives other than carbon (CO_2 gas instead of carbon powder, e.g.)

Microwave Variables

- Atmosphere
- Power
- Frequency
- Location within microwave chamber/cavity modes
- Time
- Crucible material and configuration

Conclusion

This work provides strong evidence that iron oxide reduction using microwave energy for Martian soil is feasible. Microwave heating can be very efficient and requires low mass equipment. Low mass, low energy, and simplicity are desirable characteristics for equipment in remote locations such as space.

Exploitation of indigenous resources is crucial for in-space manufacturing and repair, both from an economic and crew safety perspective. Development of technologies such as microwave iron oxide reduction of in-space soils requires robust science to support the engineering and development of such systems. The ability to obtain important gasses and solid materials for in-space fabrication is a crucial and enabling technology for in-space manufacturing and repair.

Acknowledgements

This work represents a team effort with contributions from many people. I would like to thank Dr. Laurent Sibille, my NASA Colleague, for all his assistance in guiding my efforts. Dr. Subhayu Sen and Dr. Paul Carpenter have helped immensely. Dr. David Agresti from the University of Alabama at Birmingham was very helpful and is providing the iron Mössbauer spectroscopy capability.

References

Aguilar, J. A. and Gomez, I. (1997). "Microwaves Applied to Carbothermic Reduction of Iron Ore Pellets." *Journal of Microwave Power & Electromagnetic Energy*, Vol. 32 No. 2, 67-73, International Power Institute, Blacksburg, VA.

Boles, Walter (2002). "The Potential of Microwave Radiation for Processing the Martian Soil." Report, NASA Faculty Fellowship Program, Marshall Space Flight Center, AL.

Chabinsky, Irving J. (1988). "Applications of Microwave Energy Past; Present and Future—Brave New Worlds." *Proc., Materials Research Society Symposium, Vol. 124*, Materials Research Society, Pittsburgh, PA, 17-29.

Committee on Microwave Processing of Materials: An Emerging Industrial Technology, (1994). *Microwave Processing of Materials*, Commission on Engineering and Technical Systems, National Academes Press, Washington, DC.

Essene, E. J. and Fisher, D. C. (1986). "Lightning Strike Fusion: Extreme Reduction and Metal-Silicate Liquid Immiscibility." *Science*, Vol. 234, 189-193.

Fanslow, Glenn, E. (1991). "Microwave Enhancement of Chemical and Physical Reactions." *Proc., Materials Research Society Symposium, Vol. 189*, Materials Research Society, Pittsburgh, PA, 43-48.

Janney, Mark A., Kimrey, Hal D., and Kiggans, James O., (1992). "Microwave Processing of Ceramics: Guidelines Used at the Oak Ridge National Laboratory." *Proc., Materials Research Society Symposium, Vol. 269*, Materials Research Society, Pittsburgh, PA, 173-185.

Lorenson, Claude P., Patterson, Mark C. L., Risto, Gail, and Kimber, Robert (1992). "The Effect of Particle Size on Microwave Heated Carbon and the Subsequent Crystallite Growth." *Proc., Materials Research Society Symposium, Vol. 269*, Materials Research Society, Pittsburgh, PA, 129-135.

McGill, S. L., Walkiewicz, J. W., and Smyres, G. A. (1988). "The Effects of Power Lwvel on the Microwave Heating of Selected Chemicals and Minerals." *Proc., Materials Research Society Symposium, Vol. 124*, Materials Research Society, Pittsburgh, PA, 247-252.

Standish, H. and Huang, W. (1991). "Microwave Application in Carbothermic Reduction of Iron Ores." *ISIJ International*, Vol. 31, No. 1, 241-245.

Standish, N. and Pramusanto (1997). "Reduction of Microwave Irradiated Iron Ore Particles in CO." *ISIJ International*, Vol. 31, No. 1, 11-16.

Standish, N. and Worner, H. (1991). "Microwave Application in the Reduction of Metal Oxides with Carbon." *Iron & Steelmaker*, Vol. 18 Number 5, May

Stein, Dale F., Edgar, Richard, H., Iskander, Magdy F., Johnson, Sylvia M., Lob, Chester G., Shaw, Jane M., Sutton, Willard H., Tien, Ping K., and Munns, Thomas E. (1994). "Microwave Processing—An Emerging Industrial Technology." ." *Proc., Materials Research Society Symposium, Vol. 347*, Materials Research Society, Pittsburgh, PA, 3-7.

Tian, Yong-Lai, Brodwin, Morris E., Dewan, Hardial S., and Johnson, D. Lynn (1988). "Microwave Sintering of Ceramics Under High Gas Pressure." *Proc., Materials Research Society Symposium, Vol. 124*, Materials Research Society, Pittsburgh, PA, 213-218.

Walkiewicz, J. W., McGill, S. L., and Moyer, L. A. (1988). "Improved Grindability of Iron Ores Using Microwave Energy." ." *Proc., Materials Research Society Symposium, Vol. 124*, Materials Research Society, Pittsburgh, PA, 297-302.

Yarevich, V. Skl, Detkov, A, Shevelev, M., and Decker, R. (1992). "Interaction Between Gyrotron Radiation and Powder Materials." *Proc., Materials Research Society Symposium, Vol. 269*, Materials Research Society, Pittsburgh, PA, 163-169.

Zhong, S., Geotzman, H. E., and Bleifuss, R. L., (1997). "Reduction of Iron Ore with Coal by Microwave Heating." *Minerals and Metallurgical Processing*, November 1996, 174-178

2003

NASA FACULTY FELLOWSHIP PROGRAM

MARSHALL SPACE FLIGHT CENTER
THE UNIVERSITY OF ALABAMA IN HUNTSVILLE

GENETIC ALGORITHM TUNED FUZZY LOGIC FOR GLIDING RETURN TRAJECTORIES

Prepared By:	Bradley Burchett
Academic Rank:	Assistant Professor
Institution and Department:	Rose-Hulman Institute of Technology Department of Mechanical Engineering
NASA/MSFC Directorate:	Space Transportation
MSFC Colleague:	Dr. John Hanson

Introduction

The second generation reusable launch vehicle will leverage many new technologies to make flight to low earth orbit safer and more cost effective. One important capability will be completely autonomous flight during reentry and landing, thus making it unnecessary to man the vehicle for cargo missions with stringent weight constraints. Implementation of sophisticated new guidance and control methods will enable the vehicle to return to earth under less than favorable conditions.

The return to earth consists of three phases--Entry, Terminal Area Energy Management (TAEM), and Approach and Landing. The Space Shuttle is programmed to fly all three phases of flight automatically, and under normal circumstances the astronaut-pilot takes manual control only during the Approach and Landing phase. The automatic control algorithms used in the Shuttle for TAEM and Approach and Landing have been developed over the past 30 years. They are computationally efficient, and based on careful study of the spacecraft's flight dynamics, and heuristic reasoning. The gliding return trajectory is planned prior to the mission, and only minor adjustments are made during flight for perturbations in the vehicle energy state.

With the advent of the X-33 and X-34 technology demonstration vehicles, several authors investigated implementing advanced control methods to provide autonomous real-time design of gliding return trajectories thus enhancing the ability of the vehicle to adjust to unusual energy states. [1-3,5] The bulk of work published to date deals primarily with the approach and landing phase of flight where changes in heading angle are small, and range to the runway is monotonically decreasing. These benign flight conditions allow for model simplification and fairly straightforward optimization. This project focuses on the TAEM phase of flight where traditional methods have produced limited results. The simple genetic algorithm is used to tune several human knowledge based fuzzy logic controllers.

Genetic Algorithm Tuned Fuzzy Logic

Human beings perform a wide variety of complex tasks in every day life without precise mathematical calculations. One apt example is driving an automobile. The human operator readily adapts to different vehicles, and moves the controls to precisely navigate the vehicle without calculating steering angles, pedal pressures, etc. Fuzzy Logic methods provide a method to formalize proven human knowledge into an autonomous algorithm making it unnecessary for precise math models or dynamic inversion of a plant. [8] Fuzzy Logic control has been used in a wide array of applications including approach and landing control of a light aircraft [7]

The genetic algorithm (GA) is a reinforcement learning method that can optimize a system without any analytic or numerical gradient information. [4] It is based on the idea of 'survival of the fittest'. GAs operate on a set of possible solutions known as the population. Typically a successful GA optimization requires three elements, 1) a coding scheme, 2) a fitness function, and 3) a reproduction scheme. The free parameters are typically coded to facilitate propagation of the population through the reproduction operator. In this work, we have used concatenated binary linear mapping, meaning that each free parameter is coded as an integer proportion of the appropriate search space and converted to a binary string. All coded free parameters are then

concatenated in to a single binary string representing one possible solution. This string is referred to as a 'chromosome'. When using the GA to tune fuzzy logic controllers, the fitness function must be chosen carefully. In this work, each fitness function is chosen as the average squared tracking error for a particular coordinate of the trajectory during a particular phase of flight. Reproduction is accomplished in four steps. First, the 'mating pool' must be selected. Here this is done by forming a biased roulette wheel, then 'spinning the wheel' a number of times equal to the population size. The probability of selection assigned to a particular string is equal to the string's proportion of total population fitness. Once the mating pool is determined, parent chromosomes are paired randomly. In order to keep the population size constant, each pair of parent chromosomes then produces two offspring through crossover. Crossover is accomplished by randomly choosing a crossover site for each set of parent strings. Each parent is then clipped at the crossover site, and children are formed by trading bits to the right of the crossover site. This reproduction method provides a way to share the good characteristics within a population, and guarantees that average population fitness will increase as the training progresses. This final step of reproduction is mutation. Mutation is the random changing of a small portion of bits within the population. Mutation allows the population to explore novel, random search directions. Typical mutation rates are between one and 0.1 percent. GAs are competitive with other search methods, especially for problems with a large number of free parameters. Since the user defines the population size, he essentially defines the number of search 'directions'. Gradient based methods don't enjoy this luxury.

Last year we developed several fuzzy controllers based on human knowledge. These controllers were able to successfully plan and fly trajectories for TAEM. In order to optimize performance, the existing controllers have now been tuned using a genetic algorithm. When tuning fuzzy logic controllers with GAs, the researcher may choose various parts of the fuzzy system as free parameters. That is, the GA could be used to select either input membership functions, output membership functions, rule antecedents, rule consequents, or some combination of these. After some preliminary limited success tuning membership functions, we chose to tune only the rule consequents. This choice follows from previous work by Karr and Freeman. [6] If the input membership functions are chosen to cover all possible values of the input variables, the output membership functions are chosed to span an appropriate actuator range with the right number of divisions, and the rule antecedents are chosen to cover all possible combinations of input membership functions, then there is no reason to modify these parts of the system.

The tuning was accomplished through a clever integration of a Matlab based implementation of the GA with the MAVERiC high fidelity simulation available at Marshall. Our top level Matlab program generates the initial population, writes candidate controller parameters to a text file, reads actual trajectory information from a text file, then propagates the population. The initial population is typically generated by encoding the controller parameters from a human knowledge based solution, then filling the population with strings that are a gross mutation of the first string. Each string is then decoded into controller parameters, and the parameters are written to a text file. At this point, the program sends a system level command to run the MAVERiC C/FORTRAN based simulation. MAVERiC writes any number of user determined varibles describing the actual path flown to a text file at a user determined sample rate. The top level program then calls a Matlab subroutine that reads in the actual path and computes the appropriate

fitness level. Finally, we have implemented the reproduction scheme described above in Matlab to propagate the population.

Results

After some attempts to tune all channels for all flight phases simultaneously, we realized that the controllers must be tuned in a specific order to guarantee good performance. First, the pre-final portion of the bank controller must be tuned to insure the smallest possible dispersion from runway centerline at autoland interface. The left half of Figure 1 shows two cases of the pre-final portion. Performance of a human knowledge based guidance system is shown as dash-dot lines. Performance of the genetic algorithm selected rules is shown as solid lines. The GA case demonstrates quicker intercept of extended runway centerline with less oscillation for a smaller average squared tracking error.

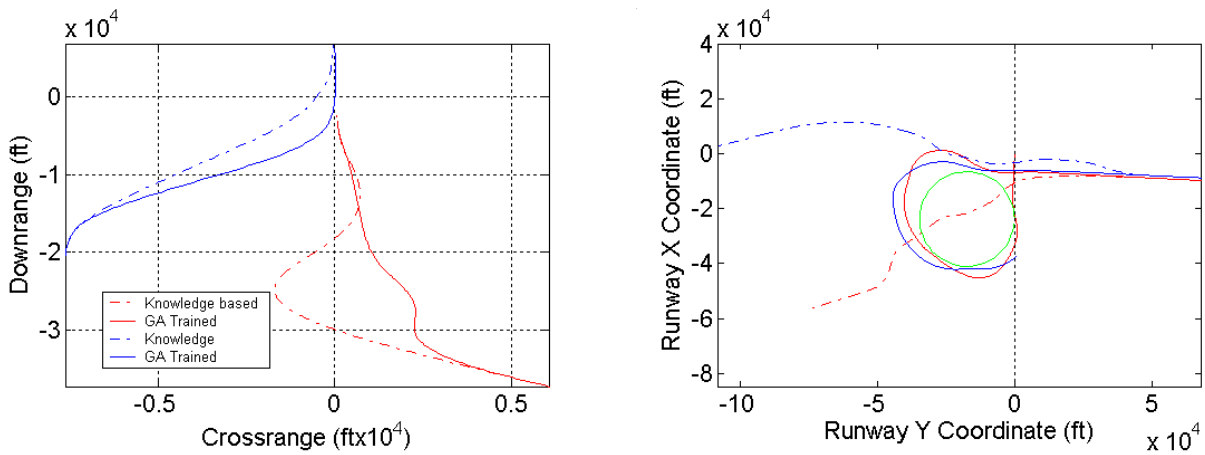

Figure 1: Results of Genetic Algorithm Tuning of TAEM Fuzzy Guidance System

Table 1 shows a comparison between the rule consequents for pre-final chosen by a human expert with those generated by GA tuning. The human expert picked rules that cause the system to behave as a proportional-derivative controller. The GA chooses zero control in many instances where the error is already decreasing.

Table 1: Rules comparison between Human Expert Knowledge, and Genetic Algorithm Selected

	Crossrange y									
$\dot{y}$	Human Knowledge Based					Genetic Algorithm Based				
	LN	N	Z	P	LP	LN	N	Z	P	LP
LN	LP	LP	LP	Z	N	LP	LP	LP	Z	Z
N	LP	LP	P	SN	LN	SP	SN	P	SN	LN
Z	LP	P	Z	N	LN	P	P	Z	N	Z
P	LP	SP	N	LN	LN	SN	LP	Z	LN	LN
LP	P	Z	LN	LN	LN	LP	P	LN	Z	Z

The right half of Figure 1 shows the results for the heading alignment cone (HAC) turn. The desired HAC circle is shown in green, and runway centerline is shown as a dotted vertical line.

In this case, the initial rule base was randomly chosen. For the cases shown, with a random rule base, the guidance causes the craft to wander off, largely ignoring the desired circular ground path. After thirteen generations of GA tuning, the guidance produces a 270 degree turn, and in the high energy case, successfully reaches auto-land interface. GA tuning of the rules for vertical axis control have resulted in comparable performance improvements.

Conclusions

The simple genetic algorithm is a powerful optimization tool, especially suited to problems where cost function gradients are undefined or difficult to calculate. When applied to systems with a large number of adjustable parameters, the GA is competitive if not superior to gradient-based methods. Fuzzy Logic based controllers can be tuned for optimal tracking performance using the GA. This method requires that the performance criterion be carefully defined so that the GA is constrained from finding rules that result in competitive scores without following the expected path. Future development will result in a fuzzy system that will be able to plan and fly near optimal trajectories without the need of path prediction through on-line integration of the equations of motion.

References

[1] Barton, G. H., (1999), "Autolanding Trajectory Design for the X-34," AIAA Atmospheric Flight Mechanics Conference and Exhibit, Portland, OR, AIAA Paper No. 99-4161, 1999.

[2] Barton, G. H., (2001), "New Methodologies for Assessing the Robustness of the X-34 Autolanding Trajectories," *Advances in the Astronautical Sciences,* Volume 107 Guidance and Control 2001, pp. 193-214.

[3] Girerd, A., Barton, G., (2000) "Next Generation Entry Guidance--Onboard Trajectory Generation for Unpowered Drop Tests," AIAA Guidance, Navigation, and Control Conference, Denver, CO, Paper No. 2000-3960, 2000.

[4] Goldberg, D. E., *Genetic Algorithms in Search, Optimization, and Machine Learning,* Addison-Wesley, Reading, MA, 1989.

[5] Grantham, K. "Adaptive Critic Neural Network Based Terminal Area Energy Management / Entry Guidance," 41st AIAA Aerospace Sciences Meeting and Exhibit, Reno, NV, 2003.

[6] Karr, C. L., *Practical Applications of Computational Intelligence for Adaptive Control,* CRC Press, Boca Raton, FL, 1999.

[7] Larkin, L. I., "A Fuzzy Logic Controller for Aircraft Flight Control," *Industrial Applications of Fuzzy Control*, M. Sugeno, Ed., Elsevier Science Publishers, North-Holland, 1985, pp. 87-103.

[8] Lee, C. C., "Fuzzy Logic in Control Systems: Fuzzy Logic Controller--Part I," *IEEE Transactions on Systems, Man, and Cybernetics,* Vol. 20, No. 2, pp. 404-417.

2003

NASA FACULTY FELLOWSHIP PROGRAM

MARSHALL SPACE FLIGHT CENTER
THE UNIVERSITY OF ALABAMA IN HUNTSVILLE

DEVELOPING A SET OF SIMILARITY RULES FOR SCALING SOLAR SAIL SYSTEMS

REPORT NOT AVAILABLE

Prepared By:	Stephen Canfield
Academic Rank:	Associate Professor
Institution and Department:	Tennessee Technological University Mechanical Engineering
NASA/MSFC Directorate:	Transportation
MFSC Colleague:	Dr. Greg Garbe

2003

NASA FACULTY FELLOWSHIP PROGRAM

THE UNIVERSITY OF ALABAMA IN HUNTSVILLE
MARSHALL SPACE FLIGHT CENTER

DEVELOPMENT AND VERIFICATION OF DIGITAL IMAGE CORRELATION FOR NDE

Prepared By:	Tsuchin Philip Chu
Academic Rank:	Associate Professor
Institution and Department:	Southern Illinois University Carbondale Department of Mechanical Engineering and Energy Processes
NASA/MSFC Directorate:	Engineering
MSFC Colleague:	Dr. Sam Russell

Introduction

Image correlation of speckle patterns has been used extensively to measure surface displacements and deformations. The use of laser speckle can be found in many types of coherent imagery. Fraley, et al. [1] in the early 1980's proposed the use of the two-dimensional correlation method to measure the local displacement with laser speckle patterns. This approach has been applied in several special cases as a calculation procedure to determine the local displacement components due to uniform translation in pixel resolution [2]. A novel approach using coarse-fine search that determined the local displacement and deformation gradients with sub-pixel accuracy was later developed by Chu et al. [3]. This method requires a pair of digital images of the surfaces with random speckle patterns before and after deformation to be correlated. A much faster approach for image correlation was developed by Sutton, et al [4] by employing a second order Newton Raphson method. This method improved the computation speed of the correlation. However, it presented some convergence difficulties. This report describes the development of a new sub-pixel digital image correlation (SPDIC) software using a bisection search method. This search routine will always converge and is much faster than the traditional coarse-fine search method with 10 divisions on each level of search.

Theoretical Background of SPDIC

Two images are analyzed to estimate displacements and strains. The aim of the method is to find the displacements and deformations of small subsets from the second image relative to the first one. This is accomplished by comparing the intensity levels (0-255) of the subsets in the images. Usually the method for comparing two subsets is commonly given by the use of the cross-correlation coefficient, C:

$$C\left(\xi(u,\frac{\partial u}{\partial x},\frac{\partial u}{\partial y}),\eta(v,\frac{\partial v}{\partial x},\frac{\partial v}{\partial y})\right)=\frac{\int_{\Delta M^*} f(x,y)f*(x+\xi,y+\eta)dA}{\left[\sqrt{\int_{\Delta M}\left[f(x,y)\right]^2 dA\int_{\Delta M^*}\left[f*(x+\xi,y+\eta)\right]^2 dA}\right]}$$

where ΔM is the subset in the undeformed image, ΔM* is the subset in the deformed image, u and v are the displacement in X and Y directions. The values of u, v, $\frac{\partial u}{\partial x}$, $\frac{\partial u}{\partial y}$, $\frac{\partial v}{\partial x}$ and $\frac{\partial v}{\partial y}$ which maximize C are the local deformation gradients for the selected subset, the best correlation value is defined as 1. To increase the computational speed, the least-squared correlation coefficient is used in the current program.

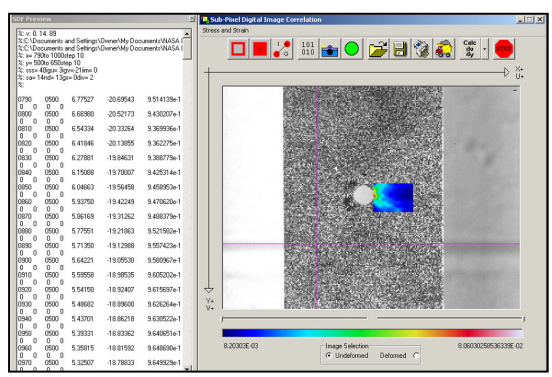

Fig. 1. GUI of SPDIC

Software Development and Features

Figure 1 shows the graphic user interface (GUI) of the Sub-Pixel Digital Image Correlation (SPDIC) software program. Two very important features were implemented in this program. ***First, the bisection method is employed in the fine search routine to replace the traditional coarse-fine search approach which uses 10 divisions in each level of search.*** The

computational time is dramatically reduced while the same level of accuracy is maintained. This method may be slower than the Newton-Raphson method, but it will always converge and it does not require the calculation of the derivatives of the correlation function. The latest version of the program allows the user to select the number of divisions from 2 (bisection) to 10 (traditional coarse-fine search). ***Second, four gradient terms are added to the fine search routine.*** This approach increases the accuracy of the correlation for large deformation. It also allows the deformation gradients to be obtained directly from correlation. However, if the deformation is small, the gradient terms will not increase the accuracy much. Therefore it is recommended that only the displacement terms to be used in correlation in order to reduce the computational time. In addition to the two main features mentioned above, bi-cubic interpolation of images is added later as an option. However, preliminary tests do not show any improvement of the correlation accuracy. A mechanism to speed up the correlation process is also implemented into the nested loops of calculating the correlation values. The program keeps track of the extreme correlation value. A loop will be terminated prematurely when the sum reaches this value so that some computational time could be saved. The database is saved automatically once the correlation is done. The user can open the database file in the SPDIC program to show the results without going through the lengthy correlation process again.

The preprocessor allows the user to enter data for correlation. The undeformed and deformed bitmap speckle image files need to be opened first. The user can then select an area of interest (AOI) for scanning. Default values are given for the scan area, the sub-image window size, the step sizes, the gradient ranges, and the initial guess of the displacements. All these default values can be changed easily. The search distance, the number of decimal places of the results, and the number of divisions can be chosen from slide bars. The user has the option of choosing either bilinear or bicubic interpolation method for subpixel image correlation. The user can also choose to use gradients when the deformation is large. It is very important to select a large enough search distance so that all possible displacements within the AOI can be accounted for. Otherwise it may result in finding the wrong displacements. A more intelligent coarse search routine which will automatically adjust the search distance for new location is under development at this stage. Much work has been devoted to provide a user-friendly postprocessor. The user has the option of many features to display and save the results.

- Pseudo-color contour plots of displacements and gradients can be displayed. They can also be saved individually or as a whole to bitmap files for future reference. The user can choose to save the bitmap images with the undeformed or deformed speckle images or both.
- The tabulated results of displacements as well as the deformation gradients, both calculated and correlated, can be saved to a comma separated value file (*.csv* file) for further analysis. The normalized correlation values (0 to 1, 1 being the best fit) are also saved.
- The normal, shear, and principle strain components can be calculated and displayed by selecting the "Stress and Strain" pull-down menu and then selecting the desired strain to be shown. The strains are calculated using both the first and second-order deformation gradient terms. The user will have to enter the values of Young's modulus and the Poisson ratio in order to use this option. The stress components including normal, shear, principal, von-Mises, and maximum shear can also be displayed. The normal stresses are calculated using linear plane stress formula for isotropic materials. All results can be saved as a *.csv* file.

Verification of the Software

Several tests and experiments have been performed in order to verify and determine the accuracy and performance of the SPDIC software as well as the digital imaging system in the NDE lab. The accuracy of the digital image correlation method depends on many factors which include the imaging system, types of speckle patterns, speckle sizes, loading conditions, and the magnitude of strains. As a rule of thumb, it is recommended that two successive sets of images without any deformation shall be correlated first to determine the resolution and accuracy of the specific setup. Figure 2 shows the average and the extreme values of the u-displacement when two sets of speckle images without motion or deformation were correlated over 35 locations. Various sub-image window sizes were used and the results show the convergence of the extreme values. The u-displacement only deviates about 0.0008 mm (0.02 pixels) with a standard deviation of 0.00041 mm (0.01 pixels) when the sub-image size reaches 1.61 mm (40 pixels). Other tests show that the standard deviation and the deviations are in the same order of magnitude.

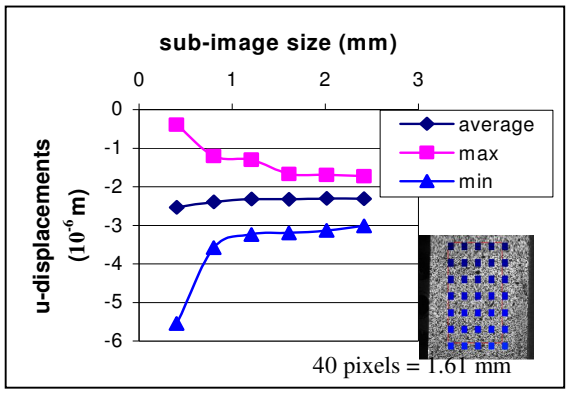

Fig. 2. u-displacement deviation

Tests were conducted on digitally deformed images to eliminate the bias due to signal noises and environmental effects. A speckle image was digitally stretched to simulate the deformation of a specimen under uni-axial tensile loads. A Poisson ratio of 0.3 is use for the calculation. Rigid body rotation through angles of 2 and 10 radians were also done digitally. MATLAB image processing toolbox was used to digitally transform the speckle image. Bicubic interpolation was used in all transformations to smooth the images. This may cause the undesired results during the correlation process since the bicubic interpolation option was not available at the time of tests. The overall results confirm that the SPDIC program is performing correctly.

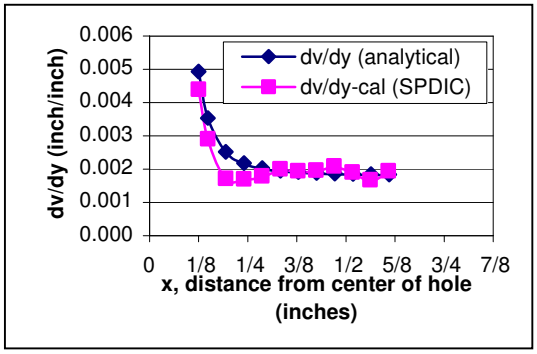

Fig. 3. Plot of dv/dy from the edge of the hole with 4,000-lb load

An experiment was performed on an aluminum alloy plate with a 6.35-mm (1/4-inch) center hole as shown in Figure 1. The width of the specimen is 50.8 mm (2 inches) and the thickness is 3.175 mm (1/8

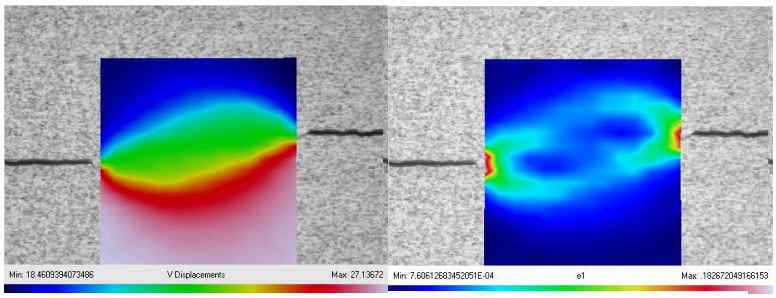

Fig. 4. Displacement and strain at crack tips

inch). A SATEC Testing Machine was used to apply tensile load to the specimen. Images of the speckle patterns before loading and with loads of 2000, 4000, and 6000 lbs applied were recorded. The normal strain (ε_{yy}) in the vertical direction due to a load of 4,000 lbs is shown in Figure 1. Since the gradient in the horizontal direction (du/dx) is very small, ε_{yy} has almost the same value as dv/dy. Figure 3 shows that the calculate dv/dy values from correlation are in close agreement with the analytical values based on linear elastic deformation theory. To demonstrate the performance of the SPDIC software, correlation was conducted on a pair of speckle images which were taken before and after two cracks propagated to the center region of interest. As can be seen in Figure 4, both pseudocolor images of v-displacement and major strain show high stress concentration regions at the crack tips very clearly. This shows the potential of using SPDIC as an NDE tools to detect embedded cracks or flaws.

Conclusions and Recommendations

A sub-pixel digital image correlation (SPDIC) software is developed. The accuracy of the system has been verified. Experiments have been performed to show the capabilities of the software. More needs to be done to improve the program. A new and improved GUI with multiple windows, pull-down menu, and toolbars is under development. It is recommended that schemes for correlation around contours, such as curved boundaries or cracks will need to be developed. Correlation using custom-designed patterns and grid patterns will also need to be studied. To scan a large area, a device with tracks which will allow precise and quick movement of cameras has to be developed. Finally, 3-D image correlation routine using two cameras will need to be implemented into SPDIC for measuring out-of-plane displacements.

Acknowledgment

The author would like to thank Dr. Sam Russell of NASA/MSFC for providing the opportunity to develop the SPDIC software for future NDE applications. The author would also like to acknowledge Mr. Matt McDougal, an undergraduate student at UAH, for his contribution in coding SPDIC in Visual Basic.

References

1. Fraley, J.E., Hamed, M.A., Peters, W.H., and Ranson, W.F., "Experimental Boundary Integral Equation Application in Speckle Interferometry," *Proc.* 1981 *SESA Spring Conference,* 1981, pp. 68-71
2. Peters, W.H., and Ranson, W.F., "Digital Imaging Techniques in Experimental Stress Analysis," *Optical Engineering,* Vol. 21, 1982, pp. 427-431
3. Chu, T.C., Ranson, W.F., Sutton, M.A. and Peters, W.H., “Applications of Digital-image-Correlation Techniques to experimental Mechanics,” *Experimental Mechanics*, Vol.26, 1986, pp. 230-237.
4. Sutton, M.A., Cheng, M., Peters, W.H., Chao, Y.J., and McNeil, S.R., "Application of an Optimized Digital Correlation Method to Planar Deformation Analysis," *Image and Vision Computing,* Vol. 4,1986, pp. 143-150.

2003

NASA FACULTY FELLOWSHIP PROGRAM

MARSHALL SPACE FLIGHT CENTER
THE UNIVERSITY OF ALABAMA IN HUNTSVILLE

SEMI-AUTOMATED ACQUISITION OF FLIGHT SOFTWARE REQUIREMENTS

Prepared By:	Harry S. Delugach
Academic Rank:	Associate Professor
Institution and Department:	Univ. Alabama in Huntsville Computer Science Department
NASA/MSFC Directorate:	Engineering
MSFC Colleague:	Dr. Luis Treviño

Overview and Scope

There has been a need in the Flight Software Division for tools to assist in the re-use of "generic" software requirements from project to project. During this project, I developed a prototype requirements acquisition tool for flight software developers, based on the technologies of repertory grids, formal concept analysis and conceptual graphs, that permits the re-use of existing requirements "patterns" and underlying domain knowledge across multiple projects and applications. The techniques developed can also be used to model the software development process itself, thereby offering the potential for process analysis and improvement.

The initial prototype is focused on the requirements acquisition and specification phase of software development. It is an interactive tool that is intended for experienced software developers who want to develop initial requirements in a particular sub-domain (as yet undetermined) of flight software requirements. The goal is to efficiently and effectively identify and specify requirements for a particular project, based on pre-existing requirements patterns of previous projects and applications.

The use of a knowledge representation and reasoning technique (conceptual graphs) will allow some automated completeness and consistency checking within the requirements. To show the generality of the approach, the initial effort not only involves requirements but also some preliminary results in modeling the software development process itself. The approach should also support some automated design and testing activities, once a sufficient library of conceptual graph patterns is acquired over several projects.

Rationale

Software requirements development includes the process of eliciting, identifying, and analyzing user requirements. As a human-centered activity, it involves many underlying assumptions and deep knowledge about the domain in which the software will operate. During requirements analysis, it is important to learn as much as possible about assumptions and domain, because mistakes in requirements are costly over the course of software's lifetime, especially if they are not detected until later in development.

One important aspect of developing requirements is to develop an ontology of the software domain, including terms, relationships and constraints. This project is based on the belief that requirements development is a knowledge-based activity, requiring capabilities for modeling and reasoning. The approach is therefore centered on a knowledge representation and reasoning technique (conceptual graphs) that will allow automated reasoning and analysis. Conceptual graphs support various kinds of reasoning and transformations, form a general representation capable of representing natural language and also allow interchange of captured knowledge among other knowledge-based systems as well as conventional development systems.

Approach

The prototype is based on the Troika approach, which Brian Lampkin developed under my supervision. An early summary of the approach can be found in (Lampkin 1999). It involves three technologies for knowledge management: repertory grids, formal concept analysis and conceptual graphs, hence its name of Troika, after a three-horse sled.

Repertory grids

Repertory grids have been used for decades in acquiring concepts from human users. They are based around the idea of a grid showing which attributes that person assigns to each concept. A single repertory grid is represented as a matrix whose columns have element labels and whose rows have "construct" (attribute) labels. In a sense, a grid is a representation for a class of objects, or individuals. For example, the grid shown in Figure 1 represents the relationship "sensor has characteristic",

sensor has characteristic						
characteristic	T1	P16	S1	S2	MCC_I1	MCC_I2
has scaling function	YES	YES	YES	YES	YES	YES
senses temperature	YES	no	no	no	no	no
senses pressure	no	YES	no	no	no	no
senses speed of motor 1	no	no	YES	no	no	no
senses speed	no	no	YES	YES	no	no
senses current	no	no	no	no	YES	YES
current from motor 1	no	no	no	no	YES	no
senses still drive	no	no	YES	no	YES	no
senses pump drive	no	no	no	YES	no	YES

Figure 1: Repertory grid for the relationship "Sensor has characteristic".

Automated techniques exist for building up such a matrix through simple questioning of an analyst whose answers determine the concepts and attributes that are considered relevant. Further techniques allow concepts and sub-concepts to be distinguished based on their shared attributes.

Formal concept analysis

Formal concept analysis is a conceptual clustering technique whereby concepts can be identified as those individuals possessing a common set of attributes. It has been developed by Wille and others (Ganter and Wille 1999). Concepts are organized in a lattice, which loosely corresponds to a type hierarchy in an ontology. Figure 2 shows the type lattice that would correspond to the repertory grid acquired in Figure 1. Note that each node shows both an attribute and a (possibly empty) set of instances or individuals. The meaning is that the individuals possess that attribute and all other attributes in the higher nodes of the lattice. For example, the node with individual "MCC_I2" means that MCC_I2 has a scaling function, senses the pump drive and senses current.

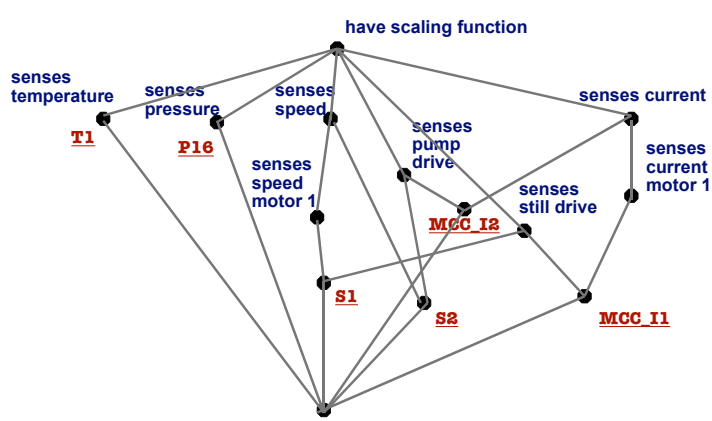

Figure 2: Concept lattice of sensor characteristics.

Conceptual graphs

The representation will be conceptual graphs, which combines semantic networks and logic-based representations. Conceptual graphs are a knowledge modeling and reasoning technique begun by Sowa (Sowa 1984; Sowa 2000). A conceptual graph consists of concepts (rectangles), relations (ovals), and actors (diamonds) as shown in Figure 3.

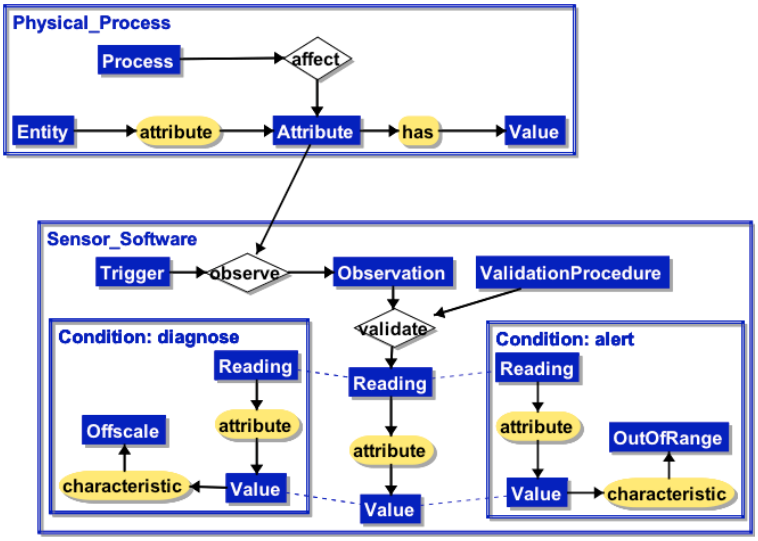

Figure 3: Conceptual graph of a sensor and its environment.

The Troika approach

The approach is described in more detail in (Delugach and Lampkin 2000) and (Lampkin 1999). In brief, the approach involves using a requirements pattern in conceptual graphs to guide an interactive dialog with a human user who will answer guided questions in order to construct a repertory grid. Using this repertory grid, formal concept analysis will be used to identify additional concepts that were not in the original pattern, as well as subtypes of the pattern's concepts. These additional concepts make an augmented conceptual graph, which can in turn be used to guide the human user in acquiring even more requirements (or refining existing ones).

The basic steps of the acquisition process are:

- Develop pre-existing "generic" requirements patterns in the form of conceptual graphs, adding definitions from Wordnet (Miller 1995) chosen by the user.
- Use automated techniques to create repertory grids via an interactive dialog to acquire more specific requirements knowledge graphs.
- Organize the knowledge into concepts using formal concept analysis, thereby forming entity clusters of concepts based on the set of attributes they share.
- Augment the existing type hierarchy.

After the process is performed, the following workflow products resulted:

- Augmented pattern graphs
- Filled-in repertory grids
- Terms and definitions
- Type hierarchies, including new definitions
- English summary of results

These products can be used for a number of purposes in modeling both the software requirements themselves, among them:

- Formal specification of the conceptual model
- A graphical representation can be used for validating the conceptual model, either by inspection or group meetings
- Conceptual model can be analyzed for taking metrics and for tracking quality
- Reasoning can be performed on the knowledge acquired, answering queries and forming reports for the user.
- Patterns can be compared formally to the actual knowledge acquired so that the efficiency and effectiveness of the acquisition process can be traced.
- Natural language (English) versions can be produced for use in further reports.
- A rationale for requirements can be formally stated and recorded.

I have produced a fully documented prototype called CharGer (Delugach 2003), written in Java, with several requirements patterns and some underlying knowledge, that will help in identification of requirements in some sub-domain of flight software.

Future work

I intend to continue work on the prototype to improve and enhance it in several areas. The natural language phrasing needs to be streamlined for understandability. Multiple-word phrases can be parsed which will usually result in additional sub-types for the models. Repertory grids can be organized into related sets, as first introduced by Wolf (Wolf and Delugach 1996). Of course, much work remains in populating the models with many more patterns, based on interviews with software developers.

References

Delugach, H. and B. Lampkin (2000). Troika: Using Grids, Lattices and Graphs in Knowledge Acquisition. *Working with Conceptual Structures: Contributions to ICCS 2000*. G. Stumme. Aachen, Germany, Shaker Verlag**:** 201-214.

Delugach, H. S. (2003). CharGer - A Conceptual Graph Editor, Univ. of Alabama in Huntsville, http://www.cs.uah.edu/~delugach/CharGer.

Ganter, B. and R. Wille (1999). *Formal Concept Analysis: Mathematical Foundations*. Heidelberg, Springer-Verlag.

Lampkin, B. E. (1999). Troika: A Hybrid Approach To Knowledge Acquisition And Representation Using Graphs, Grids And Lattices. *Computer Science*. Huntsville, AL, USA, Univ. of Alabama in Huntsville

Miller, G. A. (1995). "WordNet: A Lexical Database for English." *Communications of the ACM* **38**(11): 39-41.

Sowa, J. F. (1984). *Conceptual Structures: Information Processing in Mind and Machine*. Reading, Mass., Addison-Wesley.

Sowa, J. F. (2000). *Knowledge Representation: Logical, Philosophical, and Computational Foundations*, Brooks/Cole.

Wolf, R. P. and H. S. Delugach (1996). Knowledge Acquisition via Tracked Repertory Grids, Computer Science Dept., Univ. Alabama in Huntsville**:** report no**.** TR-UAH-CS-1996-02 ftp://www.cs.uah.edu/techreports/TR-UAH-CS-1996-02.pdf.

2003

NASA FACULTY FELLOWSHIP PROGRAM

MARSHALL SPACE FLIGHT CENTER
THE UNIVERSITY OF ALABAMA IN HUNTSVILLE

THETA-D CONTROL TECHNIQUE FOR ASCENT CONTROL OF REUSABLE LAUNCH VEHICLES

Prepared By:	David Drake
Academic Rank:	Graduate Student
Institution and Department:	University of Missouri-Rolla Department of Mechanical and Aerospace Engineering and Engineering Mechanics
NASA/MSFC Directorate:	Transportation 54
MSFC Colleague:	Charles Hall

Introduction

The current flight control of reusable launch vehicles is based on table look-up values for specific flight conditions. This approach to control allocation is not very robust in the face of system changes or plant uncertainties. In order to handle changing flight conditions, disturbances, or vehicle uncertainties; separate off-line calculations of gain values need to be made and stored for look-up during the on-line run. An optimal or sub-optimal control formulation reduces the need for multiple off-line runs and gives the added advantage of robustness of the controller in the face of external disturbances and plant uncertainties.

The θ-D control design is done by making modifications to the optimal control approach. These modifications cause the θ-D control law to produce a set of algebraic calculations that are easy to implement in any computer application. The control law developed here yields sub-optimal results to the ascent phase of the RLV which track as well or better than the PID baseline control law. In this paper, the θ-D technique is explained, vehicle dynamics put forth, controller design explained, simulation results presented, and conclusions made.

θ-D Control Technique

The θ-D control synthesis[1] was formulated for the state feedback control problem of a class of nonlinear regulator problems. The time-invariant system is described by

$$\dot{x} = f(x) + B(x)u \tag{1}$$

with the cost function of:

$$J = \frac{1}{2}\int_0^\infty (x^T Qx + u^T Ru)dt \tag{2}$$

The solution to the optimal control problem presented in (1) and (2) is assumed to exist and to be unique. The optimal solution to the nonlinear regulator problem can be obtained by solving the Hamilton-Jacobi-Bellman[2] (HJB) partial differential equation, which is given by

$$\frac{\partial V^T}{\partial x} f(x) - \frac{1}{2}\frac{\partial V^T}{\partial x} B(x)R^{-1}B^T(x)\frac{\partial V}{\partial x} + \frac{1}{2}x^T Qx = 0 \tag{3}$$

The HJB is very difficult to solve generally, which makes minimizing the optimal cost via optimal control techniques difficult and sometimes unrealizable for nonlinear systems. An original optimal control is given by

$$u = -R^{-1}B^T(x)\frac{\partial V}{\partial x} \tag{4}$$

To enable the use of the optimal control technique in a nonlinear system, perturbations are added to the cost function, which transforms (2) into

$$J = \frac{1}{2}\int_0^\infty [x^T(Q + \sum_{i=1}^{\infty} D_i\theta^i)x + u^T Ru]dt \tag{5}$$

The introduction of these perturbations causes the state equation to become

$$\dot{x} = f(x) + B(x)u = \left[A_0 + \theta\left(\frac{A(x)}{\theta}\right)\right]x + \left[B_0 + \theta\left(\frac{B(x)}{\theta}\right)\right]u \tag{6}$$

By defining $\lambda = \frac{\partial V}{\partial x}$ and substituting λ and equation (5) into the HJB equation, the perturbed HJB equation is

$$\lambda^T f(x) - \frac{1}{2}\lambda^T B(x)R^{-1}B^T(x)\lambda + \frac{1}{2}x^T(Q + \sum_{i=1}^{\infty} D_i\theta^i)x = 0 \tag{7}$$

A power series expansion for λ in terms of θ is assumed: $\lambda = \frac{\partial V}{\partial x} = \sum_{i=0}^{\infty} T_i\theta^i x$ (8)

with the T_i being symmetric matrices. By substituting equation (8) into equation (7) and equating the coefficients of the powers of θ to zero, the following equations arise

$$T_0 A_0 + A_0^T T_0 - T_0 B_0 R^{-1} B_0^T T_0 + Q = 0 \tag{9}$$

$$T_n\left(A_0 - B_0 R^{-1} B_0^T T_0\right) + \left(A_0^T - T_0 B_0 R^{-1} B_0^T\right) T_n = -\frac{T_{n-1} A(x)}{\theta} - \frac{A^T(x) T_{n-1}}{\theta} + \sum_{i=0}^{n-1} T_i \left(B_0 R^{-1} \frac{B^T(x)}{\theta} + \frac{B(x)}{\theta} R^{-1} B_0^T \right) T_{n-1-i} + \sum_{i=0}^{n-2} T_i B(x) R^{-1} B^T(x) T_{n-2-i} + \sum_{i=1}^{n-1} T_i B_0 R^{-1} B_0^T T_{n-i} \tag{10}$$

Looking at equations (9) and (10) it can be seen that equation (9) is an Algebraic Ricatti Equation (ARE) and equation (10) is a Lyapunov equation that is linear in terms of T_i and θ. The control is obtained in terms of the power series for λ as $u = -R^{-1} B^T(x) \lambda = -R^{-1} B^T(x) \sum_{i=0}^{\infty} T_i(x) \theta^i x$ (11)

Expressions for the perturbation matrices are setup using the following pattern

$$D_n = k_n e^{-l_n t} [-\frac{T_{n-1} A(x)}{\theta} - \frac{A^T(x) T_{n-1}}{\theta}] \tag{12}$$

with $k_i > 0$ and $l_i > 0$ for i=1,…,n are constants. It is possible that the state-dependant term on the right hand side of the Lyapunov equations, A(x), can result in a large control for large initial conditions or as the magnitude grows large when x increases. The D_i terms are used to cancel this large control problem, dying off as time increases due to the negative exponential. θ used in this technique is introduced for the purpose of the power series expansion only. It is an intermediate variable throughout the process and its value does not matter as it gets canceled in the control.

RLV Dynamics Equations

The dynamics equation[3] that governs the rotational motion of the rigid body RLV is given by:

$$J\dot{\omega} = -\Omega J \omega + T \tag{13}$$

where $J \in R^{3x3}$ is the moment of inertia matrix, the angular rate vector is $\omega = \begin{bmatrix} \omega_x & \omega_y & \omega_z \end{bmatrix}^T$, the control vector is $T = \begin{bmatrix} drc & dpc & dyc \end{bmatrix}^T$, and Ω is in terms of the body rates. The transformation from angular rates to the p-q-r formulation is given by

$$\dot{\gamma} = R(\gamma)\omega \tag{14}$$

where $\gamma = \begin{bmatrix} \varphi & \theta & \psi \end{bmatrix}^T$ with φ being the roll angle, θ being the pitch angle, and ψ being the yaw angle. $R(\gamma)$ is a nonlinear transformation matrix and is a function of the Euler angles. The directional motion of the RLV was not considered in the dynamics formulation for the problem. However, the directional motions were handled by the X33 simulator, which will be covered later in the results portion of this paper.

θ-D Controller Design

Previous applications of the θ-D technique to other problems have shown that taking up to two perturbation terms is sufficient for approximating the infinite series and attaining good results. For this reason, two perturbation terms were used for the given RLV problem. To apply the θ-D technique, a problem of the form of equation (1) is required. Upon examination of equation (13), the given dynamics are properly suited for the θ-D method.

The dynamics shown above were used in the θ-D approximation method to come up with a control law. Angular rates, Euler angle errors, and Euler angle error integrals were decided as the states to be used. A set of nine states was used, the states being:

$$x = \left[(\varphi_s - \varphi_c)_I \quad (\theta_s - \theta_c)_I \quad (\psi_s - \psi_c)_I \quad \omega_x \quad \omega_y \quad \omega_z \quad (\varphi_s - \varphi_c) \quad (\theta_s - \theta_c) \quad (\psi_s - \psi_c) \right]^T \tag{15}$$

with a subscript c denoting a commanded value and a subscript s denoting a sensed, or actual value. The nonlinear equation (6) was partitioned the following way

$$\dot{x} = \left[A_0 + \theta \left(\frac{A(x)}{\theta} \right) \right] x + Bu \tag{16}$$

where $B \in R^{9x3}$ is a matrix, $A(x) \in R^{9x9}$ is a state dependent matrix, and $u \in R^{3x1}$ is the control vector of torques. A, b, and u are:

$$A(x) = \begin{bmatrix} 0 & 0 & I \\ 0 & -J^{-1}\Omega J & 0 \\ 0 & R(\gamma) & 0 \end{bmatrix} \tag{17}$$

$$B = \begin{bmatrix} 0 & J^{-1} & 0 \end{bmatrix}^T \tag{18}$$

$$u = \begin{bmatrix} drc & dpc & dyc \end{bmatrix}^T \tag{19}$$

where drc is the commanded torque in the roll plane, dpc is the commanded torque in the pitch plane, and dyc is the commanded torque in the yaw plane. An optimal control cost function of

$$J = \frac{1}{2} \int_0^\infty \left[x^T \left(Q + D_1\theta + D_2\theta^2 \right) x + u^T R u \right] dt \tag{20}$$

was used where $Q \in R^{9x9}$ is diagonal matrix, $R \in R^{3x3}$ is a diagonal matrix, $D_1 \in R^{9x9}$ and $D_2 \in R^{9x9}$ are diagonal matrices, and θ is a scalar value. The control is taken to be of the form

$$u = -R^{-1} b^T \left(T_0 + T_1\theta + T_2\theta^2 \right) x \tag{21}$$

The terms to be defined at the beginning of this controller design are: Q, R, A_0, D_1, D_2, and θ. These values remain the same in training and in the 6DOF runs. With Q, R, and A_0 selected, the Algebraic Ricatti Equation can be solved to determine the T_0 matrix which remains constant throughout the solution process. These values now defined, the θ-D sub-optimal solution procedure is a simple iterative process that can be solved online with little computational power required.

Simulation Results

The designed θ-D controller was first implemented in a Matlab model. This was done so that multiple tuning runs could be done before implementing the controller in the 6DOF simulator. Only the rotational dynamics shown in equation (13) were used in the Matlab model, to examine the effect of variations on Q, R, A_0, D_1, and D_2. No high fidelity vehicle models were applied in the Matlab model due to their complicated nature. When this model tracked well, the controller with the tuned values were imported into the 6DOF simulator and then run.

The 6DOF high fidelity simulator (Maveric)[4] run by the NASA Marshall Space Flight Center (MSFC) was used to test the θ-D control allocation presented in this paper. The simulator models the dynamics of the X-33 RLV that NASA was using as a RLV demonstration vehicle. The X-33 model has eleven control deflections that it uses to achieve the commanded torques. Mechanical actuators move these deflections as required by the commanded torques.

The simulator issues a set of commanded Euler angles which are scheduled in reference to the magnitude of relative velocity of the vehicle and the body rates are commanded to be zero at all times. A nominal run in the simulator uses a smoothed reference wind and assumes all control surfaces are functioning properly throughout the entire flight profile. The X33 is capable of

reconfiguring its engines in the event that one of them fails. Such an occurrence, is referred to as a Power Pack Out (PPO), and allows both engines to provide thrust vector control at half the nominal values. These are but two cases out of a suite of forty-six test cases. A nominal case, a PPO case, and 10 other cases were simulated in Maveric. In the 12 cases tested, Euler angle tracking and torque levels were on the same level with the Proportional Integral Derivative (PID) control law used by the X33. The θ-D method did have better results throughout some of the cases. Although it was only trained with 3DOF it tracked well when run in the 6DOF simulator.

Conclusion

A new controller has been designed for the ascent phase of a reusable launch vehicle. The θ-D controller has been implemented in a 6DOF high fidelity simulator and the results show that it achieves accurate tracking of the RLV Euler angles. This new controller is an improvement over current methods in that it does not require a set of scheduled gains and is able to handle all cases with one set. A significant amount of time is saved by not having to schedule gains and run stability tests over each set of these gains. This reduction in time and tuning can reduce the cost associated with payload changes, vehicle failures, and poorly modeled system dynamics. θ-D approximation technique shows promise in the control of RLVs and can be extended to other nonlinear control problems. The results for the ascent phase are promising and this method has been submitted to MSFC for further testing. Also, the extension of this control technique to the entry portion of flight is planned. For a more detailed explanation of the θ-D technique and its application to RLV, see references [1] and [5].

Acknowledgements

The author would like to thank the personnel of the Guidance and Control group, TD54, in the Transportation Directorate at Marshall Space Flight Center. In particular, Charlie Hall has been extremely helpful and this work would not be possible without him.

References

[1] Xin, Ming and Balakrishnan, S. N.
" A New Method for Suboptimal Control of a Class of Nonlinear Systems"
Proceedings of IEEE Conference on Decision and Control; Las Vegas, NV,
Dec. 10-13, 2002

[2] Bryson , A. E. and Ho, Y.
Applied Optimal Control; Taylor & Francis, Bristol, PA, 1975

[3] Shtessel, Y. B., Hall C. E., Jackson M. E.
"Reusable Launch Vehicle Control in Multiple Time Scale Sliding Modes"
AIAA Guidance, Navigation, and Control Conference; Denver, CO, Aug. 14-17, 2000

[4] McCarter, J.
"Maveric User's Guide"; NASA / MSFC / TD54, June 25, 1999

[5] Drake, David
"θ-D Control for Ascent Phase of Reusable Launch Vehicles"
AIAA Region V Student Paper Conference; Boulder, Colorado, March 9-11, 2003

2003

NASA FACULTY FELLOWSHIP PROGRAM

MARSHALL SPACE FLIGHT CENTER
THE UNIVERSITY OF ALABAMA IN HUNTSVILLE

CONTROLS FOR REUSABLE LAUNCH VEHICLES DURING TERMINAL AREA ENERGY MANAGEMENT

Prepared By:	Brian J. Driessen
Academic Rank:	Assistant Professor
Institution and Department:	University of Alabama in Huntsville Department of Mechanical and Aerospace Engineering
NASA/MSFC Directorate:	Transportation
MSFC Colleague:	Charles E. Hall

Notation

R ..... rotation matrix from a frame fixed to the vehicle and a global inertial reference frame. Or, if w is a vector expressed in the vehicle's coordinate frame, then Rw is the same vector expressed in the global frame.

$\vec{i}_G, \vec{j}_G, \vec{k}_G$ ..... global x-axis (North), global y-axis (East), global z-axis (Down)

$\vec{i}_A, \vec{j}_A, \vec{k}_A$ ..... vehicle x-axis (forward), vehicle y-axis (right), vehicle z-axis (down)

J ..... inertia matrix of RLV vehicle, $J \in R^{3\times3}$, $J = J^T > 0$

m ..... vehicle mass

g ..... acceleration due to gravity

q ..... Euler angles of RLV orientation, $q \in R^3$ (roll, pitch, and yaw), representing the orientation of the vehicle relative to a global inertial reference frame. $q \equiv (q_{roll}, q_{pitch}, q_{yaw})^T$.

ω ..... angular velocity of RLV expressed in vehicle coordinates, $\omega \in R^3$

a ..... acceleration of the center of mass of the vehicle, expressed in the vehicle-fixed reference frame

a_n ..... projection of a onto the global negative z unit axis $-\vec{k}_G$, i.e., the "upward" component of a, also called the "normal acceleration" of the vehicle

υ_m ..... vehicle Mach number (at center of mass)

δ ..... $\delta \in R^8$ is the vector of control surface positions, for left and right rudders, left and right flaps, two inboard elevons, and two outboard elevons.

$\delta_{\min}$, $\delta_{\max}$ ..... $\delta_{\min} \in R^8$, $\delta_{\min} < 0$, $\delta_{\max} \in R^8$, $\delta_{\max} > 0$, denote the lower and upper limits of the control surface positions δ.

$\dot{\delta}_{\max}$ ..... $\dot{\delta}_{\max} \in R^n$ denotes an upper limit on $|\dot{\delta}|$, about 30 degrees per second for each control surface.

τ_a ..... $\tau_a \in R^3$, net aerodynamic torque exerted on the vehicle, expressed in the vehicle frame. τ_a is a function primarily of vehicle's mach number υ_M, "angle of attack" α, "sideslip angle" β, and control surface positions δ. That is, $\tau_a = \tau_a(\upsilon_M, \alpha, \beta, \delta)$.

S_τ ..... $\partial\tau_a/\partial\delta$, called the "torque sensitivity matrix."

F_a ..... net aerodynamic linear (Newtons) force exerted on the vehicle, expressed in the vehicle frame. F_a is a function primarily of vehicle's mach number υ_m, "angle of attack" α, "sideslip angle" β, and weakly a function of control surface positions δ. That is, $F_a = F_a(\upsilon_M, \alpha, \beta)$.

T_g ..... delay, in seconds, before a new guidance command is sent to the controller

T ..... sampling time of the controller, seconds, i.e., rate at which the controller outputs new δ commands to the motors.

$A(q)$ ..... $A \in R^{3\times3}$. known partial derivative of ω with respect $\dot{q}$. A is nonsingular along any guidance commanded trajectory. A is a function of q. $\omega = A(q)\dot{q}$.

M ..... JA

subscript d..... denotes a guidance-commanded quantity. For example, $q_{roll)d}$ is the guidance-commanded value of q_{roll}.

$sk(v)$ .....……. the 3 by 3 matrix that when post-multiplied by a vector w gives the cross product of v and w. Or, $sk(v)w = v \times w$.

The Problem

During the terminal energy management phase of flight (last of three phases) for a reusable launch vehicle, it is common for the controller to receive guidance commands specifying desired values for (i) the roll angle q_{roll}, (ii) the acceleration a_n in the global negative z direction (upward and called "normal acceleration"), and (iii) ω_3, the projection of ω onto the body-fixed axis $\bar{k}_A$, is always indicated by guidance to be zero. These guidance commands are received every T_g seconds, $T_g \approx 1\sec$. The objective of the controller is to regulate the actual values of these three quantities, i.e make them close to the commanded values, while maintaining system stability.

The equations of motion are given by:

$$\begin{aligned} JA\ddot{q} &= -J\dot{A}\dot{q} - sk(A\dot{q})JA\dot{q} + \tau_a \\ M\ddot{q} &= f + \tau_a \\ \ddot{q} &= F + M^{-1}\tau_a \\ ma &= F_a + mgR^T e_3 \end{aligned} \quad , \quad \text{where} \quad \begin{aligned} f &\equiv -sk(A\dot{q})JA\dot{q} - J\dot{A}\dot{q} \\ M &\equiv JA \\ F &\equiv M^{-1} f \\ e_3 &\equiv (0,0,1)^T \end{aligned} \tag{1}$$

The following quantities are measured and available to the controller very T seconds: δ, q, ω, a, α, β, and υ_M.

In the next section, we present a potentially-low-maintenance decentralized controller that "automatically" avoids torque-saturation issues, effector-location-saturation issues, and effector-rate-saturation issues.

Proposed Controllers

Define the four generalized errors:

$$s_{roll} \equiv \ddot{q}_{roll} + 2\gamma\dot{q}_{roll} + \gamma^2(q_{roll} - q_{roll)d}), \qquad \gamma > 0 \tag{2}$$

$$s_{pitch} \equiv \ddot{q}_{pitch} + \gamma(\dot{q}_{pitch} - \dot{q}_{pitch)c}), \qquad \gamma > 0 \tag{3}$$

$$s_{yaw} \equiv \ddot{q}_{yaw} + \gamma(\dot{q}_{yaw} - \dot{q}_{yaw)c}), \qquad \gamma > 0 \tag{4}$$

$$s_{\omega_3} \equiv \dot{\omega}_3 + \gamma\omega_3, \quad \gamma > 0 \tag{5}$$

where $\dot{q}_{pitch)c}$ and $\dot{q}_{yaw)c}$ will be defined shortly. In (2), s_{roll} is designed to cause q_{roll} to remain close to $q_{roll)d}$. In (5), the same applies to cause ω_3 to remain close to zero. In (3), if $\dot{q}_{pitch)c}$ is chosen to be proportional to the acceleration error $-(a_n - a_{n)d})$, then the vehicle should pitch upward if the normal acceleration is too low and thereby increase the normal acceleration. We can choose:

$$\dot{q}_{pitch)c} = \begin{Bmatrix} \left(\frac{2\pi}{180}\right)\tanh\left(-2\left(\alpha - \frac{2.5\pi}{180}\right)/\left(\frac{2\pi}{180}\right)\right), & \alpha < \frac{2.5\pi}{180} \\ \left(\frac{2\pi}{180}\right)\tanh\left(-2\left(\alpha - \frac{15\pi}{180}\right)/\left(\frac{2\pi}{180}\right)\right), & \alpha > \frac{15\pi}{180} \\ -k(a_n - a_{n)d}), \quad k > 0, \quad otherwise \end{Bmatrix} \quad rad/s \tag{6}$$

where the first two cases in (6) are chosen to help keep the angle of attack α within a reasonable range of $[2.5^\circ, 15^\circ]$. The generalized error s_{yaw} in (4) comes from a desire to keep the sideslip angle β small. The value of β decreases if the yaw angle increases. Therefore, we can choose:

$$\dot{q}_{yaw)c} = sat(\tfrac{1}{2}\beta, \tfrac{60\pi}{180}) \qquad \text{rad/s} \tag{7}$$

where

$$sat(*,\#) \equiv \begin{Bmatrix} *, & if \quad |*| \le \# \\ \#, & if \quad * > \# \\ -\#, & if \quad * < -\# \end{Bmatrix}, \qquad \# > 0 \tag{8}$$

It remains to choose a commanded effector location δ that will tend to make the generalized errors small. Let

$$s \equiv (s_{roll}, s_{pitch}, s_{yaw}, s_{\omega_3})^T \tag{9}$$

Define the following Lyapunov function:

$$V \equiv \tfrac{1}{2} s^T s \tag{10}$$

If V is made small, we have $\|s\|$ small. We have:

$$\dot{V} = s^T \dot{s} \tag{11}$$

Since the partial derivative of $\dot{V}$ with respect to $\dot{\delta}$ is

$$\frac{\partial \dot{V}}{\partial \dot{\delta}} = \begin{bmatrix} M^{-1} S_\tau \\ (J^{-1} S_\tau)_{3,:} \end{bmatrix} \equiv c \tag{12}$$

(where $(J^{-1}S_\tau)_{3,:}$ denotes the third row of $(J^{-1}S_\tau)$), $\dot{V}$ can be made most negative by choosing:

$$\dot{\delta}_i = -\dot{\delta}_{\max)i} sign(c_i), \qquad \text{(i=1,…,8)} \tag{13}$$

In the discrete-time implementation, the commanded δ_c comes from the more stringent of the below bounds on $\delta_c(t+T)$:

$$\delta_i(t) - \dot{\delta}_{\max)i} T \le \delta_{c)i}(t+T) \le \delta_i(t) + \dot{\delta}_{\max)i} T, \qquad \text{(i=1,…,8)} \tag{14}$$

$$\delta_{\min)i} \le \delta_{c)i}(t+T) \le \delta_{\max)i}, \qquad \text{(i=1,…,8)} \tag{15}$$

With s a function of $\ddot{q}$, we note that implementation of the controller (13) requires an estimate of τ_a, and the calculation of c in (12)-(13) requires an estimate of $S_\tau \equiv \partial\tau_a / \partial\delta$. A model based

estimate of τ_a can be obtained since α, β, υ_M, and δ are all measured. And, an estimate of $S_\tau \equiv \partial\tau_a/\partial\delta$ can be obtained by differencing the aerodynamic look up tables using large changes in δ to avoid numerical noise. Such large changes for the differencing are reasonable since τ_a is fairly linear in δ, i.e., the partial derivatives $\partial^2\tau_a/\partial\delta_i\partial\delta_j$ are small.

In the next section, we present numerical simulation results for a set of typical guidance commands.

Results

A set of typical guidance commands $(a_{n)d}, q_{roll)d})$ were used to test the proposed controller. As the motors controlling the deflection surfaces δ have a time constant of about 0.05 seconds, we chose a controller sample period of $T = 0.05s$. All measured signals were re-read at the controller update rate *T*. The guidance commands $(a_{n)d}, q_{roll)d})$ were read every $T_g = 1s$ seconds and linearly interpolated at the controller's sampling rate *T*. Additionally, a discrete time delay of 0.01 seconds in the controller was intentionally imposed in the simulation. The gains were chosen to give 2% time constants of 1 second, or $\gamma = 4$ (see (2)-(5)). S_τ was estimated by numerical differencing of the aerodynamic look up tables for τ_a, using $[\delta_i, \delta_i + 15]$ degrees if $\delta_i < 0$ and $[\delta_i - 15, \delta_i]$ degrees if $\delta_i \geq 0$. Finally, k in (6) was chosen to be 10^{-4}.

Figures 1 through 3 below show plots of $(q_{roll}, q_{roll)d})$), $(a_n, a_{n)des})$, and $(\omega_3, 0)$, respectively versus time on the horizontal axis. The maximum error in q_{roll} was 7.5°. The maximum error in a_n was $0.98\,g's$. The maximum error in ω_3 was $2.1^\circ/s$. These compare well with a prior controller. And, again the control allocation of the redundant actuators was "automatically" determined.

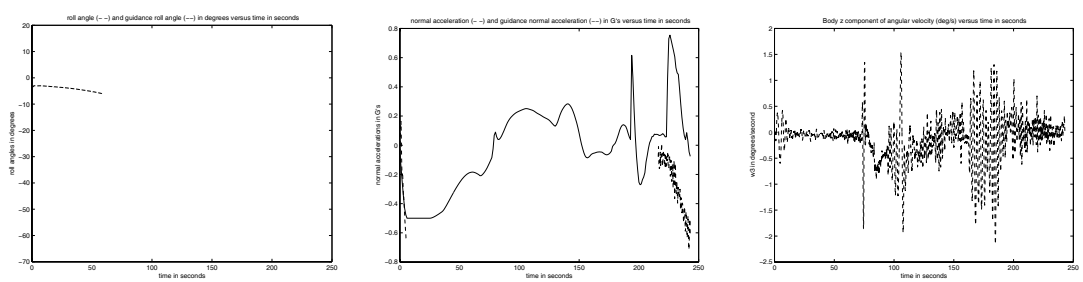

Figures 1-3. roll (deg), a_n (g's), ω_3 (deg/s). dashed = actual, solid = guidance

Acknowledgements

The author would like to thank the entire team of engineers and scientists in the guidance and control research area of the Marshall Space Flight Center's Transportation Directorate. Special thanks goes to my NASA colleague Charley Hall and the NFFP program managers Gerry Karr and Jeanelle Bland.

2003

NASA FACULTY FELLOWSHIP PROGRAM

MARSHALL SPACE FLIGHT CENTER
THE UNIVERSITY OF ALABAMA IN HUNTSVILLE

THE MATRIX RELOADED: CHARACTERISTIC MATRICES FOR SPHERICAL SHELL PHOTONIC SYSTEMS

Prepared by:	Kirk A. Fuller
Academic Rank:	Research Scientist
Institution and Department:	University of Alabama in Huntsville
	Earth System Science Center
NASA/MSFC Directorate:	Biological and Physical Sciences
MSFC Colleague:	Dr. David D. Smith

Introduction

The very high quality factors sustained by microcavity optical resonators are relevant to applications in wavelength filtering, routing, switching, modulation, and multiplexing/demultiplexing. Increases in the density of photonic elements require that attention be paid to how electromagnetic (EM) coupling modifies their optical properties. This is especially true when cavity resonances are involved, in which case, their characteristics may be fundamentally altered. Understanding the optical properties of microcavities that are near or in contact with photonic elements—such as other microcavities, nanostructures, couplers, and substrates—can be expected to advance our understanding of the roles that these structures may play in VLSI photonics, biosensors and similar device technologies.

In earlier work, a parallel was established between multiple reflection of partial waves in concentrically stratified spheres and multiple reflection of plane waves in 1-dimensional multilayered structures (Smith and Fuller, 2002). Establishing a parallel between the transfer matrix used in the study of plane-parallel photonic structures and the matrix characterizing transfer of partial waves in concentric spheres is the focus of this paper. We derive explicit expressions for the elements of the transfer matrix for concentric spherical layers, and from those expressions derive the scattering coefficients of a multilayered sphere.

Interrelation of Fields

The geometry of the problem is illustrated in Figure 1 for the case of a sphere with a concentric spherical inclusion (which may, itself, be a multilayered structure). The inner (outer) radius of the shell is R_C (R_S) and its refractive index is m_1. The wavelength of light (plane wave radiation is assumed) incident on the particle is λ_0.

The electric fields at all points are expressed as expansions in vector spherical harmonics, of the form

$$\mathbf{E} = \sum_{np} \mathcal{E}_{np} \mathbf{N}_{np}, \qquad p = 1\ (2) \Rightarrow TM\ (TE) \quad \text{polarization}, \tag{1}$$

the expansion coefficient $\mathcal{E}_{np}$ is an amplitude that may be determined from boundary conditions, and the vector spherical harmonics are of the form

$$\mathbf{N}_{np} = (R_{np}\hat{\mathbf{e}}_r + \Theta_{np}\hat{\mathbf{e}}_\theta + \Phi_{np}\hat{\mathbf{e}}_\phi) \times \begin{array}{lll} \cos\phi, & \mathbf{N}_{np} & \text{even} \\ \sin\phi, & \mathbf{N}_{np} & \text{odd} \end{array}. \tag{2}$$

Because we will be interested in matching boundary conditions at concentric spherical surfaces, the radial component of $\mathbf{N}_{np}$ will not be needed. Explicit expressions for the other components are

$$\Theta_{np} = i^{p-1}\,\frac{\xi_n^{[2-p]}(\eta)}{\eta}\tau_{np} \quad \text{and} \quad \Phi_{np} = i^{p}\,\frac{\xi_n^{[2-p]}(\eta)}{\eta}\tau_{n(3-p)}, \qquad \eta = 2\pi\mathsf{m}r/\lambda_0 \tag{3}$$

where the τ functions are expressed in terms of associated Legendre functions $P_n^m(\cos\theta)$ as

$$\tau_{n1} = \frac{d}{d\theta}P_n^1(\cos\theta) \quad \text{and} \quad \tau_{n2} = \frac{1}{\sin\theta}P_n^1(\cos\theta) \tag{4}$$

and $\xi_n(\eta)$ are Riccatti Hankel functions of the first kind. In terms of Riccatti Bessel and Neuman functions, we have

$$\xi_n(kr) = \psi_n(kr) + i\chi_n(kr), \tag{5}$$

such that $\mathbf{N}_{np} = Rg\mathbf{N}_{np} + i\,Ig\mathbf{N}_{np}$, where Rg and Ig stand for 'regular' (finite at the origin) and irregular.

Consider now the fields defined by the propagation vectors $\mathbf{k}$ in Figure 1. The expansions for the inward and outward propagating fields at surface I are taken to be

$$\mathbf{E}^{I-} = \sum_{np} \mathcal{E}^{I-}_{np}\, Rg\mathbf{N}_{np} \quad \text{and} \quad \mathbf{E}^{I+} = \sum_{np} \mathcal{E}^{I+}_{np}\, \mathbf{N}_{np}, \tag{6}$$

and likewise at surface II. The fields scattered a the outer surface and transmitted to the core are, respectively,

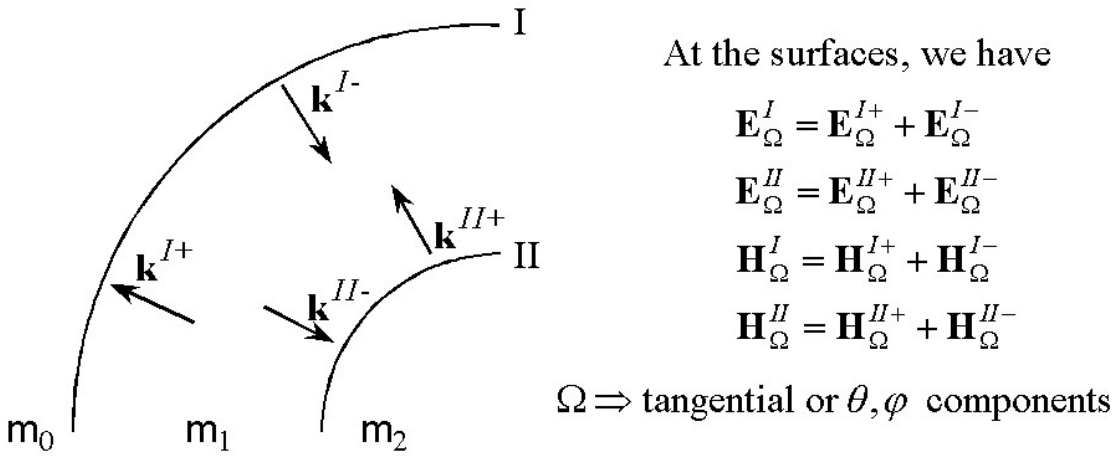

Figure 1: Geometry of the problem

taken to be

$$\mathbf{E}^{sca} = \sum_{np} \mathcal{E}^{r}_{np}\mathbf{N}_{np} \quad \text{and} \quad \mathbf{E}^{tra} = \sum_{np} \mathcal{E}^{t}_{np} Rg\mathbf{N}_{np}. \tag{7}$$

Because the layers are concentric, the vector spherical harmonics associated with each of them are orthogonal and the nth partial wave appearing in the expansions may be treated independently from all other $n' \neq n$.

The magnetic fields may be found from the electric fields from

$$\mathbf{H} = -i\nabla \times \mathbf{E}/\omega\mu \quad \text{and} \quad \nabla \times \mathbf{N}_{np} = k\mathbf{N}_{n(3-p)} \tag{8}$$

The θ, ϕ components of $\mathbf{E}$ and $\mathbf{H}$ are

$$\begin{aligned}
E_{\theta n1} &= \frac{z_n'(\eta)}{\eta}\,\tau_{n1}\,\mathcal{E}_{n1} & E_{\phi n1} &= i\frac{z_n'(\eta)}{\eta}\,\tau_{n2}\,\mathcal{E}_{n1} \\
H_{\phi n1} &= -u\frac{z_n(\eta)}{\eta}\,\tau_{n1}\,\mathcal{E}_{n1} & E_{\theta n1} &= iu\frac{z_n(\eta)}{\eta}\,\tau_{n2}\,\mathcal{E}_{n1} \\
E_{\theta n2} &= i\frac{z_n(\eta)}{\eta}\,\tau_{n2}\,\mathcal{E}_{n2} & E_{\phi n2} &= -\frac{z_n(\eta)}{\eta}\,\tau_{n1}\,\mathcal{E}_{n2} \\
H_{\phi n2} &= iu\frac{z_n'(\eta)}{\eta}\,\tau_{n2}\,\mathcal{E}_{n2} & H_{\theta n2} &= u\frac{z_n'(\eta)}{\eta}\,\tau_{n1}\,\mathcal{E}_{n2},
\end{aligned} \tag{9}$$

where z_n represents the choice of ψ_n or ξ_n appropriate to the direction of propagation, and $u = -ik/\omega\mu$. Denoting the logarithmic derivative $z_n'(\eta)/z_n(\eta)$ as D_n, H is expressed in terms of E:

$$\begin{aligned}
H_{\phi n1} &= -\frac{u}{D_n}E_{\theta n1} & H_{\theta n1} &= \frac{u}{D_n}E_{\phi n1} \\
H_{\phi n2} &= uD_nE_{\theta n2} & H_{\phi n2} &= -uD_nE_{\theta n2}
\end{aligned} \tag{10}$$

The next step is to assign the $I-$ and $II+$ partial fields the amplitudes $\mathcal{E}_{np}^{I-}$ and $\mathcal{E}_{np}^{II+}$, evaluate them at their respective opposing surfaces (II and I), and thereby obtain expressions that relate the fields at one surface those at the other. From Eqs. 9, for example, we see that $E_{\theta n1}^{II-}/E_{\theta n1}^{I-} = (R_S\psi_n'(\eta_C))/(R_C\psi_n'(\eta_S))$. With the definitions

$$\mathcal{J}_n = \frac{R_S\,\psi_n(\eta_C)}{R_C\,\psi_n(\eta_S)}, \quad \widetilde{\mathcal{J}}_n = \frac{R_S\,\psi_n'(\eta_C)}{R_C\,\psi_n'(\eta_S)}, \quad \mathcal{H}_n = \frac{R_S\,\xi_n(\eta_C)}{R_C\,\xi_n(\eta_S)}, \quad \widetilde{\mathcal{H}}_n = \frac{R_S\,\xi_n'(\eta_C)}{R_C\,\xi_n'(\eta_S)} \tag{11}$$

we may write

$$\begin{array}{llll}
E_{\theta n1}^{II-} = \widetilde{\mathcal{J}}_n E_{\theta n1}^{I-} & E_{\phi n1}^{II-} = \widetilde{\mathcal{J}}_n E_{\phi n1}^{I-} & H_{\theta n1}^{II-} = \mathcal{J}_n H_{\theta n1}^{I-} & H_{\phi n1}^{II-} = \mathcal{J}_n H_{\phi n1}^{I-} \\
E_{\theta n2}^{II-} = \mathcal{J}_n E_{\theta n2}^{I-} & E_{\phi n2}^{II-} = \mathcal{J}_n E_{\phi n2}^{I-} & H_{\theta n2}^{II-} = \widetilde{\mathcal{J}}_n H_{\theta n2}^{I-} & H_{\phi n2}^{II-} = \widetilde{\mathcal{J}}_n H_{\phi n2}^{I-} \\
E_{\theta n1}^{II+} = \widetilde{\mathcal{H}}_n E_{\theta n1}^{I+} & E_{\phi n1}^{II+} = \widetilde{\mathcal{H}}_n E_{\phi n1}^{I+} & H_{\theta n1}^{II+} = \mathcal{H}_n H_{\theta n1}^{I+} & H_{\phi n1}^{II+} = \mathcal{H}_n H_{\phi n1}^{I+} \\
E_{\theta n2}^{II+} = \mathcal{H}_n E_{\theta n2}^{I+} & E_{\phi n2}^{II+} = \mathcal{H}_n E_{\phi n2}^{I+} & H_{\theta n2}^{II+} = \widetilde{\mathcal{H}}_n H_{\theta n2}^{I+} & H_{\phi n2}^{II+} = \widetilde{\mathcal{H}}_n H_{\phi n2}^{I+}
\end{array} \tag{12}$$

<u>The Matrix Elements</u>

We now have the ingredients we need to express the fields at surface I in terms of those at surface II. We first rewrite $E_{\theta n1}^{II} = E_{\theta n1}^{II+} + E_{\theta n1}^{II-}$ as

$$E_{\theta n1}^{II} = \widetilde{\mathcal{H}}_n E_{\theta n1}^{I+} + \widetilde{\mathcal{J}}_n E_{\theta n1}^{I-} \tag{13}$$

and $H_{\phi n1}^{II} = H_{\phi n1}^{II+} + H_{\phi n1}^{II-}$ as

$$H_{\phi n1}^{II} = -\frac{u}{D_n^+}\widetilde{\mathcal{H}}_n E_{\theta n1}^{I+} - \frac{u}{D_n^-}\widetilde{\mathcal{J}}_n E_{\theta n1}^{I-}. \tag{14}$$

Denoting $\Delta_n = (1/D_n^- - 1/D_n^+)^{-1}$, solving Eqs. 13 and 14 for $E_{\theta n1}^{I+}$ gives

$$E_{\theta n1}^{I+} = \frac{\Delta_n}{\widetilde{\mathcal{H}}_n}\left(\frac{1}{D_n^-}E_{\theta n1}^{II} + \frac{1}{u}H_{\phi n1}^{II}\right), \tag{15}$$

and solving for $E_{\theta n1}^{I-}$

$$E_{\theta n1}^{I-} = -\frac{\Delta_n}{\widetilde{\mathcal{J}}_n}\left(\frac{1}{D_n^+}E_{\theta n1}^{II} + \frac{1}{u}H_{\phi n1}^{II}\right), \tag{16}$$

which now allows $E_{\theta n1}^{I} = E_{\theta n1}^{I+} + E_{\theta n1}^{I-}$ to be written as

$$E_{\theta n1}^{I} = \Delta_n\left(\frac{1}{D_n^-\widetilde{\mathcal{H}}_n} - \frac{1}{D_n^+\widetilde{\mathcal{J}}_n}\right)E_{\theta n1}^{II} + \frac{\Delta_n}{u}\left(\frac{1}{\widetilde{\mathcal{H}}_n} - \frac{1}{\widetilde{\mathcal{J}}_n}\right)H_{\phi n1}^{II}, \tag{17}$$

$$E_{\theta n1}^{I} \equiv \mathcal{F}_{11}E_{\theta n1}^{II} + \mathcal{F}_{12}H_{\phi n1}^{II}. \tag{18}$$

Thus we begin to construct the matrix $\mathcal{F}$ that transforms the fields at surface II into those at I:

$$\begin{pmatrix} E_{\theta n1}^{I} \\ H_{\phi n1}^{I} \\ E_{\phi n1}^{I} \\ H_{\theta n1}^{I} \end{pmatrix} = \begin{pmatrix} \mathcal{F}_{11} & \mathcal{F}_{12} & 0 & 0 \\ \mathcal{F}_{21} & \mathcal{F}_{22} & 0 & 0 \\ 0 & 0 & \mathcal{F}_{33} & \mathcal{F}_{34} \\ 0 & 0 & \mathcal{F}_{43} & \mathcal{F}_{44} \end{pmatrix} \begin{pmatrix} E_{\theta n1}^{II} \\ H_{\phi n1}^{II} \\ E_{\phi n1}^{II} \\ H_{\theta n1}^{II} \end{pmatrix} \tag{19}$$

Working out the other matrix elements, it is found that there are only two more which are independent:

$$\mathcal{F}_{21} = u\Delta_n^H\left(\frac{1}{\mathcal{J}_n} - \frac{1}{\mathcal{H}_n}\right) \quad \text{and} \quad \mathcal{F}_{22} = \Delta_n^H\left(\frac{D_n^+}{\mathcal{J}_n} - \frac{D_n^-}{\mathcal{H}_n}\right), \qquad \Delta_n^H = \Delta_n/D_n^-D_n^+ \tag{20}$$

The Scattering Coefficients

With a means to connect the fields at the internal surfaces of the shell, boundary conditions for the fields at those surfaces may be used to relate them to the fields external to the shell, i. e. at $r = R_S + \epsilon$ and $r = R_C - \epsilon$. This then allows one to obtain expressions for the amplitudes of the partial waves reflected from the shell, as well as for those transmitted through it.

The total field outside the shell is

$$\begin{pmatrix} E^{inc}_{\theta n1} + E^{r}_{\theta n1} \\ H^{inc}_{\phi n1} + H^{r}_{\phi n1} \\ E^{inc}_{\phi n1} + E^{r}_{\phi n1} \\ H^{inc}_{\theta n1} + H^{r}_{\theta n1} \end{pmatrix} = \begin{pmatrix} E^{I}_{\theta n1} \\ H^{I}_{\phi n1} \\ E^{I}_{\phi n1} \\ H^{I}_{\theta n1} \end{pmatrix} = \mathcal{F} \begin{pmatrix} E^{II}_{\theta n1} \\ H^{II}_{\phi n1} \\ E^{II}_{\phi n1} \\ H^{II}_{\theta n1} \end{pmatrix} = \begin{pmatrix} \mathcal{F}_{11} & \mathcal{F}_{12} & 0 & 0 \\ \mathcal{F}_{21} & \mathcal{F}_{22} & 0 & 0 \\ 0 & 0 & \mathcal{F}_{11} & -\mathcal{F}_{12} \\ 0 & 0 & -\mathcal{F}_{21} & \mathcal{F}_{22} \end{pmatrix} \begin{pmatrix} E^{t}_{\theta n1} \\ H^{t}_{\phi n1} \\ E^{t}_{\phi n1} \\ H^{t}_{\theta n1} \end{pmatrix} \tag{21}$$

Expanding the 'reflected' and 'transmitted' fields as prescribed in Eq. 7 the first block in the $\mathcal{F}$ matrix yields

$$\frac{\psi'_n(\eta_0)}{\eta_0} + \frac{\xi'_n(\eta_0)}{\eta_0}\mathcal{E}^r_{n1} = \left(\frac{\psi'_n(\eta_C)}{\eta_C}\mathcal{F}_{11} - u_2\frac{\psi_n(\eta_C)}{\eta_C}\mathcal{F}_{12}\right)\mathcal{E}^t_{n1}, \tag{22}$$

$$-u_0\frac{\psi_n(\eta_0)}{\eta_0} - u_0\frac{\xi_n(\eta_0)}{\eta_0}\mathcal{E}^r_{n1} = \left(\frac{\psi'_n(\eta_C)}{\eta_C}\mathcal{F}_{21} - u_2\frac{\psi_n(\eta_C)}{\eta_C}\mathcal{F}_{22}\right)\mathcal{E}^t_{n1}. \tag{23}$$

Dividing one by the other and solving for $\mathcal{E}^r_{n1}$ gives

$$\mathcal{E}^r_{n1} = \frac{\xi'_n(\eta_0)}{\psi'_n(\eta_0)}\,\frac{u_0\left(D^{t-}_n\mathcal{F}_{11} - u_2\mathcal{F}_{12}\right)/D^{0-}_n - \left(u_2\mathcal{F}_{22} - D^{t-}_n\mathcal{F}_{21}\right)}{\left(u_2\mathcal{F}_{22} - D^{t-}_n\mathcal{F}_{21}\right) - u_0\left(D^{t-}_n\mathcal{F}_{11} - u_2\mathcal{F}_{12}\right)/D^{0+}_n} \tag{24}$$

We have likewise shown that

$$\mathcal{E}^r_{n2} = \frac{\xi'_n(\eta_0)}{\psi'_n(\eta_0)}\,\frac{u_0\left(D^{t-}_n\mathcal{F}_{22} + u_2\mathcal{F}_{21}/u_1^2\right)/D^{0-}_n - \left(u_2\mathcal{F}_{11} + D^{t-}_n\mathcal{F}_{12}/u_1^2\right)}{\left(u_2\mathcal{F}_{11} + D^{t-}_n\mathcal{F}_{12}/u_1^2\right) - u_0\left(D^{t-}_n\mathcal{F}_{22} + u_2\mathcal{F}_{21}/u_1^2\right)/D^{0+}_n} \tag{25}$$

By providing a simple linear relation of the fields at surface I to those at II within the medium they bound, we have ensured that one may calculate the scattering coefficients from Eqs. 24 and 25 for a multilayered system: The $\mathcal{F}$ matrices for such a system will simply be the product of the $\mathcal{F}$ matrices of the individual layers.

Acknowledgments

The author wishes to express his great appreciation for the many valuable discussions with Dr. David D. Smith. It was Dr. Smith who first thought of taking the transfer matrix approach, and called my attention to its use in treating plane parallel layered systems. The productive environment for the conduct of this research provided by MSFC and the NFFP is also gratefully acknowledged.

References

Fuller, K. A. and D. W. Mackowski, "Electromagnetic Scattering by Compounded Spherical Particles," in *Light Scattering by Nonspherical Particles*, M. I. Mishchenko, J. W. Hovenier, and L. D. Travis, Eds., Academic Press, NY 2000.

Smith, D. D. and K. A. Fuller, Photonic bandgaps in Mie scattering by concentrically stratified spheres, accepted for publication, J. Opt. Soc. Am. B, **19** No. 10. (2002).

2003

NASA FACULTY FELLOWSHIP PROGRAM

MARSHALL SPACE FLIGHT CENTER
UNIVERSITY OF ALABAMA IN HUNTSVILLE

PROBABILISTIC RISK ASSESSMENT FOR HUBBLE SPACE TELESCOPE END OF MISSION CONCEPTUAL STUDY

Prepared By:	Kye Gilder
Academic Rank:	Instructor
Institution and Department:	U.S. Coast Guard Academy Department of Mathematics
NASA/MSFC Directorate:	Safety and Mission Assurance Office QS10
MSFC Colleague:	Vyga Kulpa

The Hubble Space Telescope

The Hubble Space Telescope (HST) was NASA's first orbiting optical space observatory. The Hubble was designed in the 1970s and was launched on April 24, 1990, by the space shuttle Discovery. From its low orbit approximately 600 kilometers (375 miles) above the surface of the Earth, Hubble peers out into space with a 2.4-meter primary mirror. The near vacuum of space affords the Hubble Space Telescope with a definite and unfair advantage over ground-based observatories. The Earth's atmosphere absorbs significant amounts of ultraviolet and infrared radiation and also distorts visible light images as well. In the upper reaches of the atmosphere, the Hubble Space Telescope is able to capture images and spectra from distant stars, which would be difficult or impossible to obtain from ground-based observatories or other satellites. Just recently the Hubble Space Telescope "precisely measured the mass of the oldest known planet in our Milky Way galaxy. At an estimated age of 13 billion years, the planet is more than twice as old as Earth's 4.5 billion years"[1].

The Hubble Space Telescope has been remarkably successful for numerous reasons. One of the key reasons is that the HST is the first spacecraft specifically designed to benefit from on-orbit astronaut servicing. This fundamentally different approach enables the periodic maintenance and upgrade missions to HST that have significantly improved its scientific performance since it was launched. The HST has a modular design that allows the astronauts to easily take it apart, replace equipment, and upgrade instruments. During the past thirteen years there have been four servicing missions. "These service missions ensure that Hubble produces first-class science using cutting-edge technology. In fact, each time a science instrument in Hubble is replaced, it increases Hubble scientific power and overall performance."[2] As the only space observatory of its kind, the HST's management, maintenance, and operations all require unique and innovative approaches. NASA's Goddard Space Flight Center (GSFC) manages the Hubble Space Telescope Program for the Office of Space Science (OSS) at NASA Headquarters.

Intoduction to Probabilistic Risk Assessment

"Probabilistic Risk Assessment (PRA) is a comprehensive, structured, and logical analysis method aimed at identifying and assessing risks in complex technological systems for the purpose of cost-effectively improving their safety performance" [2].

During the past fifty years, NASA has been a leader in much of the technologies it has employed in its projects and programs. Presently, NASA's objective is to rapidly become a leader in PRA and to use this methodology effectively to ensure mission and programmatic success, and to achieve and maintain high safety standards.

"Fault Tree Analysis (FTA) is one of the most important logical and probabilistic techniques used in Probabilistic Risk Assessment and system reliability today. FTA can be simply described as an analytical technique, where by an undesired state of the system is specified, and the system is analyzed in the context of its environment and operation to find all realistic ways in

[1] www.hubblesite.org
[2] www.hubble.nasa.gov

which the undesired event can occur. A fault tree thus depicts the logical interrelationships of basic events that lead to the undesired event, the top event of the fault tree" [1]. It is important to understand that both qualitative and quantitative evaluations can be performed on a fault tree.

In the risk management process, FTA is used to qualitatively **identify** and assess risk issues and concerns. PRA then follows during the **analysis** phase where risks impact and severity are evaluated [3]. The essence of risk and PRA is: 1.) What can go wrong? 2.) How likely or how frequently does it happen? 3.) What are the consequences?

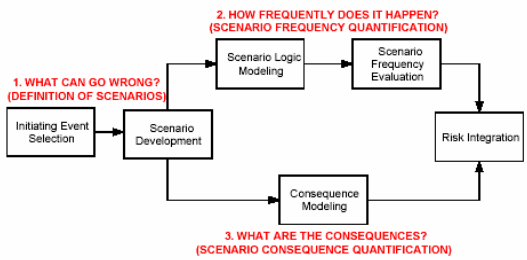

Figure 1: Implementation of the Triple Definition of Risk in PRA

Hubble Space Telescope End of Mission Study Scenario

Although the Hubble Space Telescope has had an impressive and successful thirteen-year career, the Hubble's life as a space observatory, like all good things, must come to an end. In May 2003, a Hubble Space Telescope End of Mission (EOM) study team was formed at Marshall Space Flight Center (MSFC) to investigate various alternatives to successfully deorbit the HST by attaching a deorbiting stage to the Hubble's aft end. In addition to successfully and safely derorbitting the HST, the deorbiting stage would be designed to extend Hubble's functionality for up to five additional years. Sixteen different options were to be developed and analyzed with regards to the status of the HST (operational or non-operational), deorbiter fuel type (bi-propellant, mono-propellant, or gel propellant), and the method of launch (expendable launch vehicle or space shuttle). Eight alternatives are shown in Table 1.

Boeing Delta II Expendable Launch Vehicle (ELV)	**Space Shuttle Launch**
Bi-Propellant NTO / MMH * Baseline Scenario	Bi-Propellant NTO / MMH
Bi-Propellant NTO / Hydrazine Hydrazine RCS	Bi-Propellant NTO / Hydrazine Hydrazine RCS
Mono-Propellant Hydrazine	Mono-Propellant Hydrazine
Gel Propellant	Gel Propellant

Table 1: Proposed Study Options (HST Operational)

Application of PRA to HST EOM Study

The objective of the research project was to incorporate the Probabilistic Risk Assessment process to a NASA "concept" study -- a feat that has never been completed or documented to date. NASA NPG.807.XX was drafted to guide the implementation of the PRA application to NASA programs and projects, and clearly spells out when a "full scope", "limited-scope", and "simplified" scenario-based PRA are to be used [2, 5]. However, research and documentation is lacking concerning the PRA application to a "concept" study. Therefore, the project focus was to develop the qualitative first phase of the PRA process -- "What can go wrong?"

In the initial phase of a PRA, the *initiating events*, events that perturb the system or cause it to change its operating state or configuration, and *scenario development* take place (Figure 1). Scenario development consists of modeling sequences of events that need to occur in order for the undesired *end state* to transpire [1]. For the HST EMO study, the end state was defined to be "Loss of Mission" (LOM) where the "mission" is defined in the study's problem scenario.

The HST EOM study team selected the HST operational, ELV, and bi-propellant fuel as the baseline scenario (Table 1). Working with the HST EOM study project experts, the first task undertaken was to thoroughly develop an event logic diagram that identified critical initiating events leading to LOM for the baseline scenario. The critical events were developed in levels where increasing levels indicated greater event details. Figure 2 illustrates the first three levels of the event logic diagram.

Level 0	Level 1	Level 2
LOSS OF MISSION (LOM)		
	Loss of Deorbiter	
		Delta II Launch Failure
		Delta II Payload Separation Failure
		Deorbiter Destroyed/Disabled
	No Docking with HST	
		No Rendezvous
		AR&D Failure
	HST - No Life Continuation	
		Main Propulsion Failure
		RCS Failure
		Electrical Power Failure
		Communication Failure
		Thermal Control System Failure
	HST - Impaired	
		Physical Damage
		Functionality Degraded
	No Deorbit Burn	
		Electrical Power Failure
		Communication Failure
		Thermal Control System Failure
		Main Engine(s) Do Not Ignite
		RCS Thruster(s) Do Not Ignite
		Main Engine(s) Do Not Turn Off
		RCS Thruster(s) Do Not Turn Off

Figure 2: Structure of Abbreviated Event Logic Diagram

At the present time, the event logic diagram consists of nine levels of complexity for the baseline scenario. Since the HST EOM project is a concept study, Level 9 and beyond are specific to actual component and equipment and thus are vaguely defined. However, once specific components and equipment are clearly identified in the design process, the event logic diagram can then be used to transition to event logic model from a qualitative to quantitative model. Specific component and equipment heritage data can be used to conduct Fault Tree Analysis, Failure Mode and Effects Analysis (FMEA) [4], and PRA in order to determine numerical quantities related to safety and reliability such as the probability of component failures, the probability of sub-system failures, and the probability of overall system failure (i.e., LOM).

Future Research and Recommendations

The concept study team has determined through its analysis that all sixteen options discussed in HST EOM Study Scenario section of this paper were deemed to be physically infeasible due to violations of some basic ground rules concerning the deorbiter spacecraft's mass and center of gravity. Therefore, the PRA process cannot be continued or effectively applied until the project team is able to develop at least one feasible solution or scenario. The HST EOM study team is presently analyzing a variation of the original scenario following Goddard Space Flight Center relaxation of various project specifics and constraints. Due to conceptual nature of the study, it is very difficult to quantitatively analyze the event logic diagram or to perform a complete PRA. Simply, components and/or specific designs are not well defined. Therefore, application of the PRA process may prove to be more effective if considered during Phase A studies and in accordance with references [2] and [5] rather than during conceptual study.

Acknowledgements

The author would like to thank Vyga Kulpa, Marshall Space Flight Center's Safety and Mission Assurance Office, and Dr. Madara Ogot, Rutgers University for this research opportunity and their assistance. In addition, the author would like to thank Adam Gowan, Tennessee Tech coop student, for his research and administrative assistance.

References

[1.] Stamatelatos M. (2002), Fault Tree Handbook with Aerospace Applications, Office of Mission and Quality Assurance, NASA Headquarters, Washington, DC.
[2.] Stamatelatos M. (2002), Probabilistic Risk Assessment Procedure Guide for NASA Managers and Practitioners, Office of Mission and Quality Assurance, NASA Headquarters, Washington, DC.
[3.] Stamatelatos M, Larson W. (2003), Space Launch and Transportation Systems (SLaTs): Design and Operations MSFC Course Handout.
[4.] Massachusetts Institute of Technology Center For Space Research (2001), Failure Mode and Effects Analysis (Document No. 36-01406).
[5.] Probabilistic Risk Assessment (PRA) Guidelines for NASA Programs and Projects, NASA Procedure and Guidelines NPG.807.XX (draft).

2003

NASA FACULTY FELLOWSHIP PROGRAM

MARSHALL SPACE FLIGHT CENTER
THE UNIVERSITY OF ALABAMA IN HUNTSVILLE

ANALYSIS OF TRANSFER FUNCTIONS AND SAMPLING RATE IN PROPULSION MEASUREMENTS

Prepared by:	Dr. Don A. Gregory
Academic Rank:	Professor
Institution and Department:	University of Alabama in Huntsville Physics Department
NASA/MSFC Directorate:	Transportation
MSFC Colleague:	John T. Wiley

Introduction

Any device that makes a measurement has certain characteristics of its own that determine just how trustworthy the data from the device is. There are two aspects of data collection and analysis that are of interest here, the transfer function of the detector and the sampling of the data the detector reports. Analyzing data analysis methods currently used is a significant concern to many researchers in the field of experimental propulsion. For example, if a sensor is used to measure pressure and the device cannot respond very fast, then the measurement of a short duration shock will be suspect[1]. The sensor will still produce a measurement because a pressure change will have occurred, but exactly what that pressure means will be debatable. It is not the peak pressure but the time average that will be seen and often the peak can be orders of magnitude larger than the average, and it is the peak pressure that causes damage to equipment. The response time of the sensor must be much faster than the event in order to accurately capture the data. A simple model has been created which shows what can happen if time dependent information is sampled at different rates. The average value of a time dependent parameter is calculated as an example in the analysis presented here. Five different type functions were chosen: sinusoidal, pseudo-sinusoidal, symmetric triangular, asymmetric triangular, and random. The results illustrate just how important sampling is when the data is in the form of a time dependent function, as it often is.

Theory

Transfer Functions

Transfer functions describe what happens to a signal as it is transmitted through a system. If the system is linear then what happens to the signal can be broken up into what happens to pieces of the signal and then the pieces can be summed to recover what happened to the entire signal. This can be expressed in the following brief introduction to linear system theory. Let the input and output signals be given by:

$$g_i(t_1) = \text{input function of time} \tag{1}$$

$$g_o(t_2) = \text{output function of time} \tag{2}$$

and let the system operator be designated as $\mathcal{S}$. The function of the system operator is to produce the output when given the input function (or value). This means:

$$g_o(t_2) = \mathcal{S}\{ g_i(t_1) \}. \tag{3}$$

Now if the system is linear:

$$\mathcal{S}\{ a\, v(t_1) + b\, u(t_1) \} = a\, \mathcal{S}\{ v(t_1) \} + b\, \mathcal{S}\{ u(t_1) \} \quad ^{2}, \tag{4}$$

where both a and b are constants and u and v are arbitrary functions of time. The system transfer function is generally written in terms of the Fourier transform of the input and output functions:

$$H(\omega) = G_o(\omega) / G_i(\omega), \qquad (5)$$

where G_o and G_i are the Fourier transforms of the output and input functions and $H(\omega)$ is actually also a Fourier transform. It is the Fourier transform of the so-called impulse response. This is the response of the system to a delta function input[3]. The concern in this investigation is in developing a technique for calculating the transfer function. If the input could be true white noise, which contains all frequencies, then the transfer function would be completely specified. A truly random function is difficult to create and in practice it was found that the transfer function could be determined using a collection of sinusoidal input functions summed and then Fourier transformed. All of the output functions, one for each input, were then summed and also Fourier transformed. The Fourier transform of a sum is the sum of the Fourier transforms, so that the equation for $H(\omega)$ is still valid. Examples are given below for fabricated inputs just to illustrate the technique.

Consider an input function formed by summing sine functions of many different frequencies. In frequency (Fourier transform) space, the power spectrum (magnitude squared) of this function is a comb function, as shown below. Now consider a transfer function consisting of a tapered filter with an element of added noise. This may be represented mathematically as the sum of a Gaussian function centered at zero and a low-amplitude random signal. The output signal spectrum will be the product of the Fourier transform of the input signal and the transfer function. The output signal itself is obtained by Fourier transforming the output signal spectrum. The subtle but important differences between the definitions of the Fourier transform and the power spectrum are not applicable in this case because of the functions chosen. The magnitude squared of the Fourier transform of the sinusoid is still a delta function.

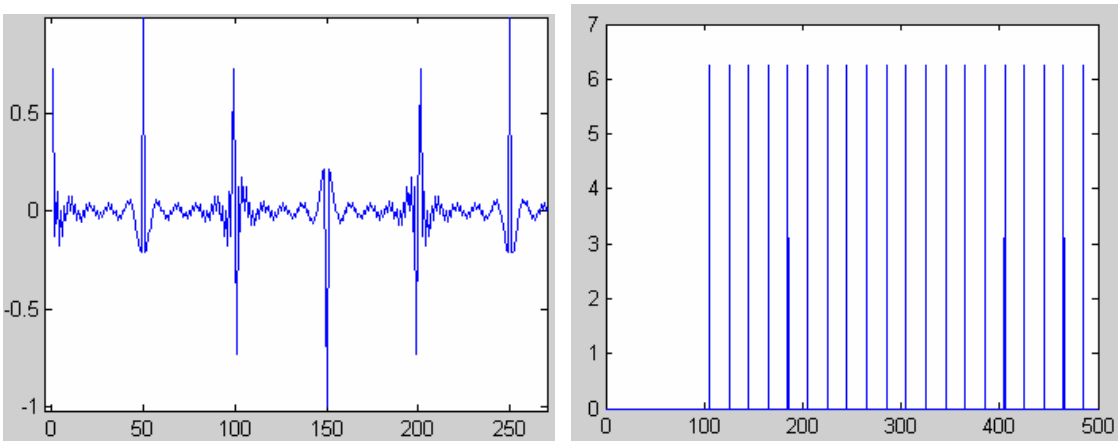

(a) **(b)**

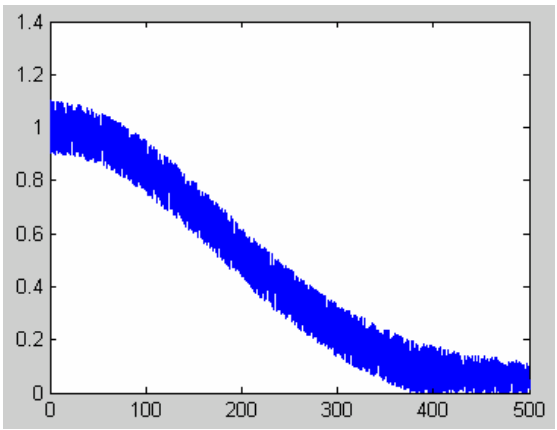

(c)

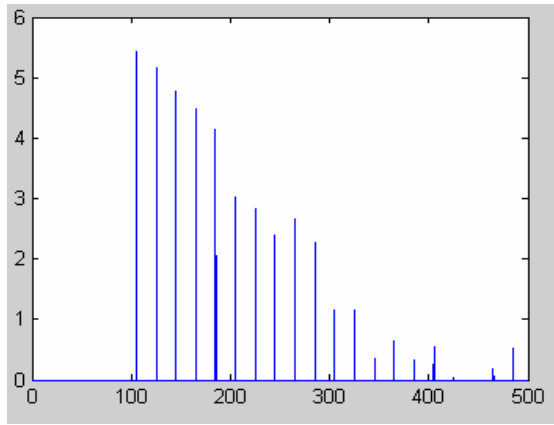

(d)

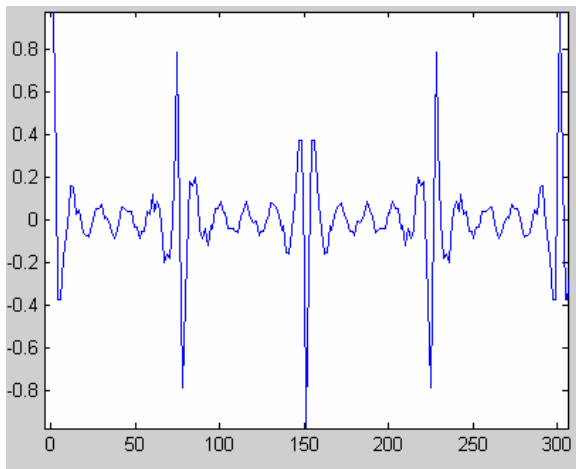

(e)

Figure 1: (a) The input signal versus time. (b) Power spectrum (magnitude squared of the Fourier Transform) of the input signal in frequency space. (c) The transfer function of the system versus frequency. (d) Power spectrum of the output signal in frequency space. (e) The output signal versus time.

Data Analysis

Digitally analyzing any analog signal first requires that signal to be sampled. The classic sampling theorem of Nyquist is routinely quoted and is in fact often sufficient for sinusoidal periodic data streams[4]. If the signal is periodic but not sinusoidal, the rules are still strictly applicable, but the application is not always useful. The Nyquist sampling theorem states that at least two points are necessary to reproduce a sinusoidal function. Fourier analysis is based on the notion that any function can be written in terms of sine and cosine basis functions. It seems reasonable then to Fourier transform the time dependent signal and look for the highest

frequency present and sample at a frequency of at least twice that value. The problem comes from the fact that, at these high frequencies, there is practically no signal, so it is pointless to sample the signal at a high frequency when the amount of information at that frequency is very small. A series of functions, not necessarily representing realistic data, is chosen here to illustrate what can happen when data is not sampled at the correct rate. If a physical parameter, such as pressure, is being monitored using a standard strain gauge type sensor, which is certainly an analog device, and the output voltage is digitized, then it is very important to know at what rate the digitization takes place. The true time dependence is not always displayed but rather an average is often computed and displayed. In fact, all sensors have characteristic time constants that must be accounted for in data interpretation. The averaging is done digitally- or electronically with the use of a low pass filter. This average value is then taken as the value of the pressure, when in reality it probably should not be used, at least not for important decisions making purposes. The functions chosen here for illustrating the analysis are simple and are constructed to have a zero average value. The functions are then sampled at various frequencies and the average of the sampled values computed. The difference in this value from zero is an indication of the error that would be inherent in the average. The errors are displayed more concisely by computing the standard deviation of the entire sampled data set and then calculating the percent of one standard deviation each data point represents. There are some surprises in the results and some things are as expected. The high frequency sampling produces the lowest error as expected, but there are other frequencies that can produce low errors as well. A random signal was also chosen for analysis. The signal was constructed so as to have zero mean, just as the analytic signals used previously.

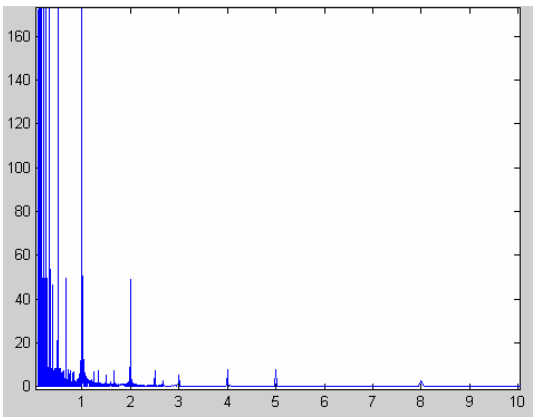

(a)

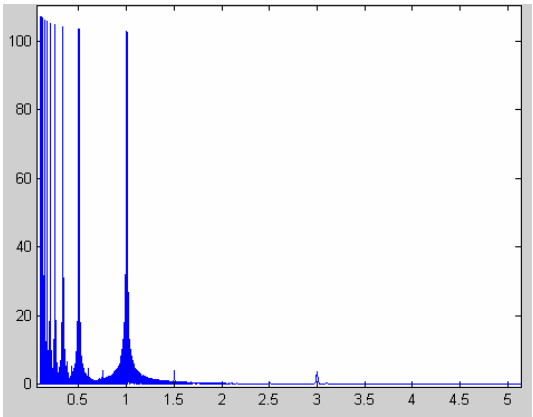

(b)

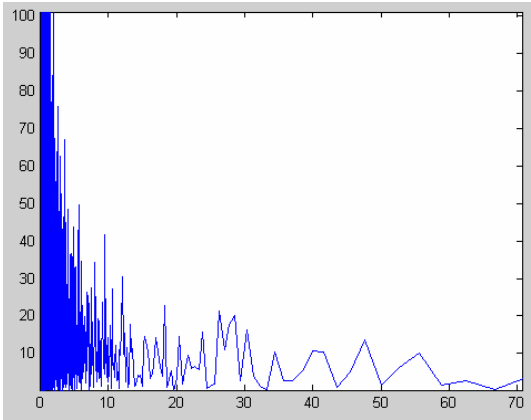

(c)

Figure 2: Error (in percent of one standard deviation) versus number of samples per cycle for (a) a periodic asymmetric triangle function, and (b) a periodic parabolic pseudosine, and (c) a random function. The percent of one standard deviation for the last plot is versus the number of samples taken per 1000 data points since the function is not periodic.

CONCLUSION

The models created in this investigation have drawn attention to the data analysis procedures utilized in rocket motor testing. Transfer functions, even simple linear ones, must be determined carefully if data collected from an experiment is to be believed. A great deal of experimental data was also taken in this area and it is presented in another paper in this report[5].

It is obvious that the sampling rate is not a trivial decision, and that it must be determined based on the requirements of the test being done. For a true sinusoidal function the Nyquist criterion was sufficient to reproduce the function with zero error as expected. It was found however that the condition of periodicity is not sufficient for the Nyquist sampling to reproduce the function exactly. Two periodic but not sinusoidal functions were examined and errors in calculating the average value of the function were found to be as large as 10 percent of one standard deviation even if the sampling was 5 per cycle. The random function showed serious sensitivity to sampling as well. An error of about 20 percent of one standard deviation is seen for sampling rates about 30 per 1000 points. There is no direct comparison of the last graph with the previous two however because the function used to generate the last graph was not periodic.

---

[1] Halliday, D., Resnick, R., and Walker, J., *Fundamentals of Physics*, John Wiley and Sons, 5th Ed., 1997 (687)
[2] Poularikas, A. and Seely, S., *Signals and Systems*, Krieger Publishing, 2nd Ed., 1991 (129)
[3] Hecht, Optics, Addison-Wesley Publishing, 2nd Ed., 1987 (484)
[4] Randall, R. and Tech, B., Application of B & K Equipment to Frequency Analysis, Bruel & Kjaer, Denmark, 2nd Ed., 1977 (19)
[5] Vitarius, P., Analysis of Acoustic and Vibrational Related Measurements in Propulsion Data, NASA Faculty Fellowship Program, 2003, paper LII

2003

NASA FACULTY FELLOWSHIP PROGRAM

MARSHALL SPACE FLIGHT CENTER
THE UNIVERSITY OF ALABAMA IN HUNTSVILLE

A MATHEMATICAL MODEL FOR PREDICTING GAS DISTRIBUTION IN A PACK BED UNDER MICROGRAVITY CONDITIONS

Prepared By:	Dr. Boyun Guo
Academic Rank:	Associate Professor
Institution and Department:	University of Louisiana at Lafayette Department of Petroleum Engineering
NASA/MSFC Directorate:	Flight Projects
MSFC Colleague:	Donald W. Holder

Introduction

NASA has successfully designed, tested and implemented in a space station a Volatile Removal Assembly (VRA) as part of a Closed Environment Life Support System (CELSS). The VRA contains 4 catalyst-packed reactors performing catalyst oxidation of water at elevated pressure and temperature under microgravity conditions. Although the technology has been proven to be successful, the current designing practice relies on an empirical model in engineering calculations. It has been unclear as to how much deviation from the current design is allowed in the future VRA designs. The efficiency of catalyst oxidation is controlled by the total oxygen-water contact area, which depends on oxygen gas distribution in the reactor. The objective of this study was to perform an in-depth investigation of two-phase flow mechanics and develop a mathematical model for predicting oxygen gas distribution in the pack bed under microgravity conditions.

Previous investigations by Backer *et al.* [1], Tour and Lerman [2], Weekman and Myers [3] have shown wall-effect on fluid distribution in pack beds. Wilknison [4] conducted computer simulations on invasion of water into oil by capillary force in lattices. Frette *et al.* [5] conducted experimental studies and computer simulations on slow upward-fluid migration due to buoyancy. All these studies were conducted under 1-G gravity conditions. We have found that Frette *et al.*'s scaling model is not accurate under mircogravity conditions. A study on capillary imbibitions under microgravity conditions was conducted by NASA's Marshall Space Flight Center [6]. Studies in the literature [5] and [6] indicate that interfacial force becomes dominating in low buoyancy environments created by either reducing fluid-fluid density contrast or flying parabolas under low viscous force conditions. Investigations of the effect of viscous force on the fluid transport in porous media under microgravity conditions have not been found.

Mathematical Model

Consider two-phase in a cylindrical pack bed of length L. Darcy's law gives:

$$\left(\rho_l - \rho_g\right) gL\cos(\delta) + \frac{L}{k_a A}\left(\frac{\mu_l Q_l}{k_{rl}} - \frac{\mu_g Q_g}{k_{rg}}\right) - \frac{2\sigma\cos(\theta)}{a} = 0 \tag{1}$$

where ρ_l and ρ_g are density of liquid and gas, respectively, g is gravitational acceleration, δ is the angle of the pack bed axis with respect to g-direction, k_a is the absolute permeability of the pack, A is the cross sectional area of the pack bed, μ_l and μ_g are viscosity of liquid and gas, respectively, Q_l and Q_g are volumetric flow rates of liquid and gas, respectively, k_{rl} and k_{rg} are relative permeability to liquid and gas phase, respectively, σ is gas-liquid interfacial tension, θ is liquid contact angle, and a is the average pore radius. The relative permeabilities in Eq. (1) are functions of phase saturations (volume fractions). A numerical model can be setup to compute gas distribution in the reactor. Equation (1) has been modified to account for the wall-effect as follows:

$$\left(\rho_l - \rho_g\right) gL\cos(\delta) + \frac{L}{k_a}\left(\frac{\mu_l \frac{A_j}{A} Q_l}{A_j k_{rl}} - \frac{\mu_g \Gamma_j \lambda \frac{A_j}{A} Q_g}{A_j k_{rg}}\right) - \frac{2\sigma\cos(\theta)}{a} = 0 \tag{2}$$

where

$$\Gamma = 1 - \exp[-\psi(R - r)] \qquad \text{and} \qquad \lambda = \frac{A}{\sum_{j=1}^{n} \Gamma_j A_j} \tag{3}$$

where R is the inner radius of the reactor, r is the radial distance of the point of interest from the centerline of the reactor, $\psi = 1.68$ based on Tour and Lerman's [2] data, and the subscript j is the radial grid block index in the numerical model.

All the fluid properties are temperature dependent. The mathematical model used for computing the average fluid temperature profile under steady flow conditions is not presented here, but is available from the author upon request.

Determination of Key Parameters

The following relative permeability models are used based on lab measurements:

$$k_{rl} = \left(\frac{S_w - 0.50}{1 - 0.50 - 0.15} \right)^{2.9} \qquad \text{and} \qquad k_{rg} = 0.023 \left(1 - \frac{S_w - 0.50}{1 - 0.50 - 0.15} \right)^{2.5}. \tag{4}$$

where S_w is water saturation (in pore volume).The absolute permeability was determined to be 3066 Darcies on the basis of matching experimental data to the Schechter-Guo gravity drainage equation [7]. All the basic parameter values are summarized in Table 1.

Results

Fluid flow in the reactor was mathematically simulated using a 2-D grid system containing 10x5 grid blocks. Computed steady temperature profile is shown in Figure 1, which indicates lower temperature near the inlet and very slightly higher temperature near the reactor wall. The average-temperature profile is plotted in Figure 2. Predicted gas saturation (fraction of pore volume) under gravity of 1-G is presented in Figure 3. Integration of the gas saturation values over the pack volume gives a gas holdup value of 0.2062. Residence times of gas and water are 104.33 seconds and 50.11 seconds, respectively. Predicted gas saturation under gravity of 0.01-G is illustrated in Figure 4, which yields a gas holdup of 0.3273. Residence times of gas and water are 165.57 seconds and 42.47 seconds, respectively. The residence time of water dropped by 15.25% from 1-G to 0.01-G condition. Both Figures 3 and 4 indicate that the variation in gas distribution in the radial direction is minimal. Figure 5 illustrates the effect of gravity on gas holdup. Figure 6 illustrates the effect of gravity on liquid residence time loss.

Discussion

The following facts should noted regarding the results of this mathematical model:

1. Oxidation in the reactor consumes oxygen and thus reduces gas holdup. This effect is not considered in the present mathematical model.
2. The results were obtained assuming steady flow in the vertical direction. It can be shown that gas channels develop in the reactor during dynamic flying conditions.
3. The difference between the residence times of water and gas indicates that there exists potential to maximize reactor performance using different injection rates.

Conclusions

The following conclusions are drawn on the basis of theoretical analyses:

1. Gas holdup in the reactor is predicted to increase from 0.2062 under 1-*G* to 0.3273 under 0.01-*G* conditions. This reduces water residence time by 15.25%.
2. The effects of temperature variation and wall-effect in the reactor on the gas distribution are negligible.

Acknowledgement

The author is grateful to the NASA Faculty Fellowship Program for financially supporting this research project.

References

[1] Backer, D.W., Chilton, R.F., and Vernon, D.E. (1935), *Trans. Am. Inst. Chem. Eng*., 31, pp 296-302.

[2] Tour, R.S. and Lerman, F. (1939), "The Unconfined Distribution of Liquid in Tower Packing," *Trans. Am. Inst. Chem. Eng.*, 35, pp 719-42.

[3] Weekman, V.W., Jr. and Myers, J.E. (1964), "Fluid-Flow Characteristics of Concurrent Gas-Liquid Flow in Packed Beds," *AIChE Journal*, Vol. 10, No. 6, pp 951-957.

[4] Wilkinson, D. 1984, "Monte Carlo Study of Invasion Percolation Clusters in Two-Dimensions and Three-Dimensions," *Physics Review A*, Vol. 30, pp 520-522.

[5] Frette, V., Feder, J, Jossang, T., and Meakin, P. 1992, "Buoyancy-Driven Fluid Migration in Porous Media," *Physical Review Letters*, Vol. 68, No. 21, pp 3164-3167.

[6] Noever, D.A. and Cronise, R.J. 1994, "Weightless Bobble Lattices : A case of Froth Wicking," *Phys. Fluids*, Vol. 6, No. 7, pp 2493-2500.

[7] Schechter, D.S. and Guo, B. 1996, "Mathematical Modeling of Gravity Drainage after Gas Injection into Fractured Reservoirs," SPE 35170, proceedings of the SPE Improved Oil Recovery Symposium, pp 23-35.

Table 1- Parameters of the Pack Bed Reactor

Pack bed length	11	inches
Reactor inner radius	0.69	inches
Pressure at outlet	65	psia
External temperature	270	F
Fluid temperature at inlet	265	F
Water injection rate	15	lb/hour
Gas injection rate	0.008	lb/hour
Water density	1000	kg/m^3
Gas-water contact angle	45	deg
Average pore radius	0.0003	m
Absolute permeability	3066	Darcy
Pack bed porosity	0.447	
Specific heat of fluid	10.00	kcal/kg-C

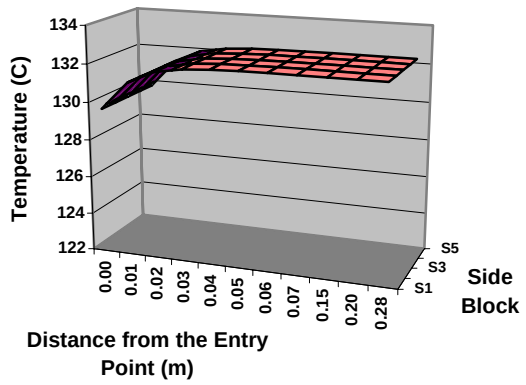

Figure 1- Temperature Distribution

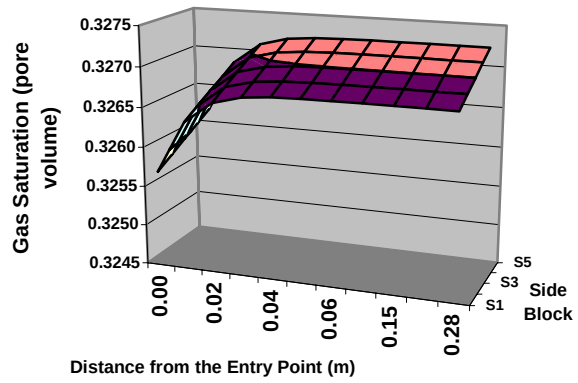

Figure 4- Gas Distribution under 0.01-G

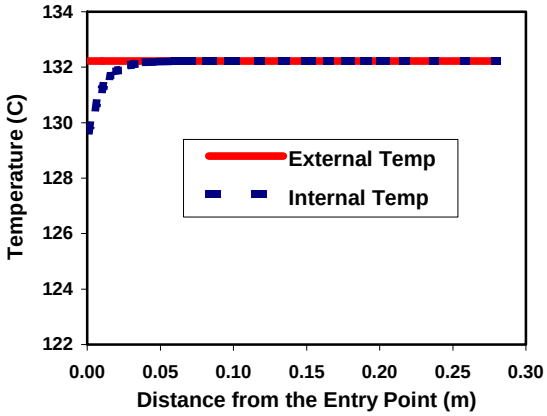

Figure 2- Average-Temperature Profile

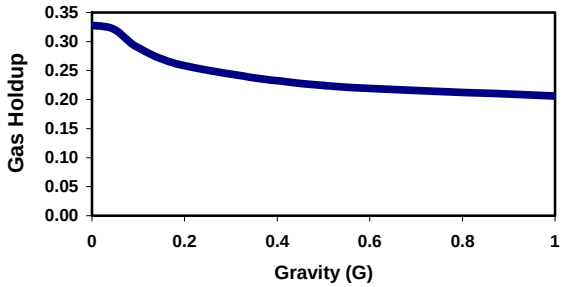

Figure 5- Effect of Gravity on Gas Holdup

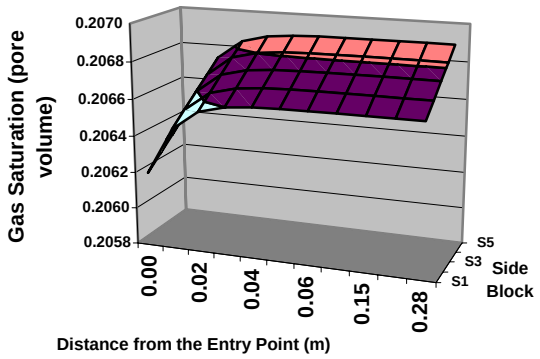

Figure 3- Gas Distribution under 1-G

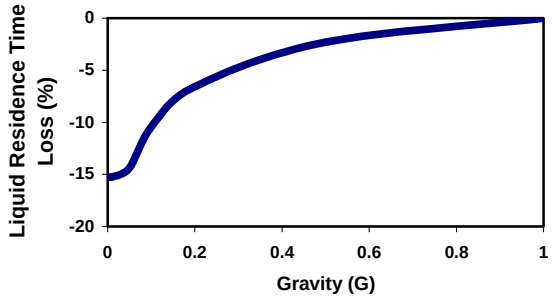

Figure 5- Effect of Gravity on Liquid Residence Time Loss

2003

NASA FACULTY FELLOWSHIP PROGRAM

MARSHALL SPACE FLIGHT CENTER
THE UNIVERSITY OF ALABAMA IN HUNTSVILLE

ROCKET AND PAYLOAD DESIGN, DEVELOPMENT AND LAUNCH INITIATIVE

Prepared By:	Razi (Bobby Blockum) Hassan
Academic Rank:	Assistant Professor
Institution and Department	Alabama A&M University Chemistry Department
NASA/MSFC Directorate:	Customer & Employee Relations
MSFC Colleague:	Dr. Sheila Nash-Stevenson

Program/Project Overview and Objectives

The summer 2003 NFFP/ASGC Accompanying Students Program features six participants, all Alabama A&M University students. They worked with NASA/MSFC Scientists/Engineers for 10 weeks. It was funded by the NASA Space Launch Initiative, the Alabama Space Grant Consortium, The NASA Summer Faculty Fellowship Program, and Alabama A&M University. The Project's four majors Objectives:

I) A Mentored Research paper in Space Science
II) Simulated Design of a Solid Rocket
III) Construction of a Thor and Proteus Rocket
IV) Travel to Boulder, Colorado to build and launch a payload to fly on a Balloon.

A sub-goal will be to review Calculus I and Differential Equations.

Program/Project Goals

Our goals are consistent with the **Mission III** of NASA's Goals and Objectives:
To inspire the next generation of explorers:

- Inspire and motivate students to pursue careers in science, technology, engineering, and mathematics.
- Improve student proficiency in science, technology, engineering, and mathematics by creating a culture of achievement, using educational programs, products, and services based on NASA's unique missions, discoveries, and innovations.
- Motivate K-16+ students from diverse communities to pursue Science and mathematics courses and, ultimately, college degrees in science, technology, engineering, and mathematics.
- Enhance science, technology, engineering, and mathematics instruction with unique teaching tools and experiences that only NASA/MSFC can provide, that are compelling to educators and students.
- Improve higher education capacity to provide for NASA's and the Nation's future science and technology work force requirements.

Major Challenges

Our team plans to successfully launch a reusable rocket with payloads next November. Alabama A&M University (AAMU) and the University of Alabama in Huntsville (UAH) successfully launched a rocket on May 24, 2002. As a result of our previous experience with the Alabama A&M University, we are qualified to achieve this goal. Our major challenge will be to pull together the required skills and material resources in order to accomplish this task.

Proposed Solutions

To solicit these skills, our team will coordinate efforts with the AAMU Science Mathematics Tutorial Center, School of Engineering, and the Departments of Chemistry and Physics. We will solicit assistance from NASA/MSFC in the areas of Design, Propulsion, Avionics, Telemetry, Reusable Rocket Launch, and Payloads.

Education Relevance

By being involved with NASA/MSFC Engineers and Scientists, AAMU students got hands-on experience on rocketry. NASA's MSFC has the expertise on Rocket Design and Propulsion as one of its primary tasks. This Program/Project should, therefore, enhance our students' ability to be involved in future space exploration at NASA and other similar institutions. This experience will also demonstrate the relevance of their academics to the real world.

Payload

The proposed payload projects for the Proteus Rocket are listed below:

1. The quality of the electroplated nickel is affected by hydrogen produced at the cathode. This payload will be a 450 mL electroplating bath containing nickel sulfamate. It will measure the effects of gravity on the hydrogen gas produced in the process.

2. Recently observed phenomena of generation of high electric voltage (up to 100 kV) and emission of electron beam pulses by optical and/or thermal excitation of ferroelectrics is called Ferroelectric Emission (FEE) and is now tested for different applications. We are investigating these new effects starting from PLZT ceramics and specially doped $LiNbO_3$ crystals. This payload will further investigate the effect of a changing radiation field aboard the Proteus Rocket (2 miles).

3. Upon completion of the Boulder payload project, the group decided to use the payload developed there for the Proteus Rocket.

Expected Outcomes

AAMU students will have an opportunity to participate with MSFC/NASA and other local scientists to learn some of the skills of Space Travel. The skills they will gain from this involvement will enable them to design, build, and launch reusable rockets, which will lead to careers in aerospace science and engineering.

Table 1: Student Information

Names	Majors	Class	Mentor /Org. Code	E-Mail	Bldg/ Room #	Phone
Lawson, Angela	Civ Eng	Sr	Ken Cooper ED43	Alawson81@ Yahoo.com	4707/ 142	289-4733 544-8591
Macklin, Lionel	Elec. Eng	Sr	Michael Lee ED40	Lioneljr27@ Yahoo.com	4566/ 153	289-8240 544-4174
Martin, John	Mech Eng	Sr	Nasser Barghouty SD46 (Muhammed Seif)	Jmartin7 @aamu.edu	4481 /221B 224A	652-6695 544-0238 544-5171
Miller, William	Civ Eng	Sr	Kirk Sorenson	William.miller @aamu.edu	4203 /2132	694-2643 544-4109
Penn, Harold Jr.	Physics	Jr	Jonathan Jones TD40	Harold_pennjr@ yahoo.com	4776 / Lab	678-230-8213 544-1043
Simmons.Michelle	Physics	Grad	Mike Tinker ED21		4666 / 117	651-5248 544-4973
Williams, Talicia	Comp. Sci /Math	Sr	Mark McElyea FD33	Twilliams20@ aamu.edu	4610 /2001 B	651-7974 544-2034

Summary

Time did not permit the completion of the smaller Thor Rocket. For a more complete description of the summer program and pictures you may go on the AAMU webpage: http://www.rocket.sas.aamu.edu

2003

NASA FACULTY FELLOWSHIP PROGRAM

MARSHALL SPACE FLIGHT CENTER
THE UNIVERSITY OF ALABAMA IN HUNTSVILLE

CONCEPTS FOR A LESSONS LEARNED SOFTWARE SYSTEM

Prepared By:	J. Scott Hawker
Academic Rank:	Assistant Professor
Institution and Department:	University of Alabama Department of Computer Science
NASA/MSFC Directorate:	Engineering
MSFC Colleague:	Paul Gill

Introduction

NASA, like any learning organization, must capture its experience and learn from it. Lessons learned are crucial to the agency's continued success. However, the GAO-02-195 report called for significant improvements in the way NASA collects and shares lessons learned information.

This report describes a software system to support the capture, approval, and communication of lessons learned at NASA. The report defines the system context, outlines the requirements, and sketches an architecture for the system. Further details are available in a report from the NASA Technical Standards Program Office.

System Context

As Figure 1 illustrates, lessons learned are generated while executing projects and programs. After acquiring and approving the lessons learned, they are available for use in later projects and programs. The lessons also serve as a source for new and updated standards and training materials. The proposed software system facilitates the acquisition of lessons from projects, the performance of the approval process, the management of lessons, and the communication of lessons to projects and programs.

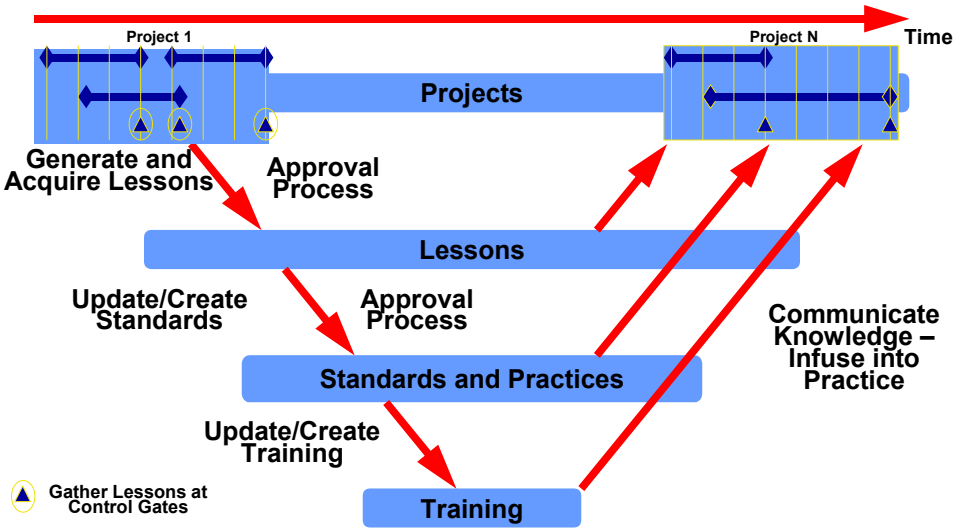

Figure 1: Generation and communication of knowledge begins with lessons.

Figure 2 shows the Lessons Learned Software System as part of a broader software and human system. The broader system has the following tasks:

- submit new lessons
- approve lessons
- manage lessons

- find and apply lessons
- perform tasks to produce aerospace products and capabilities (PAPAC)
    - system engineering process tasks
    - program and project management process tasks

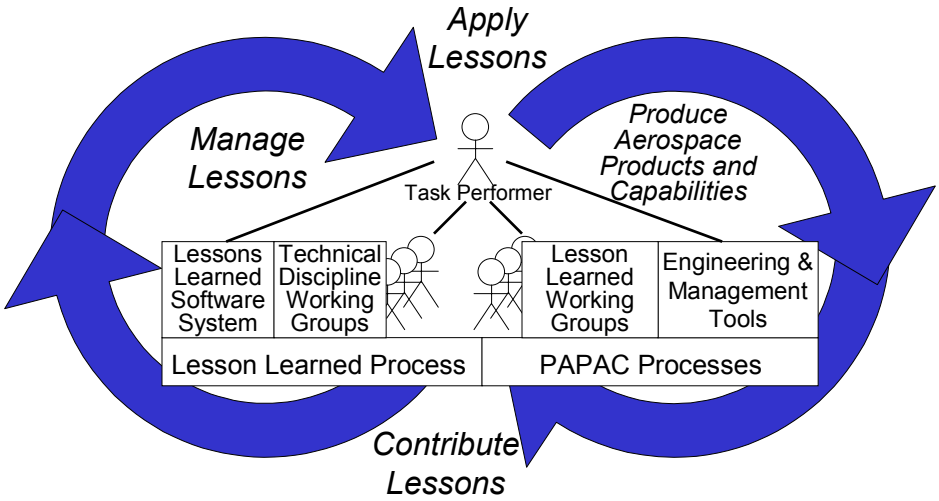

Figure 2: The Lessons Learned Software System as part of a broader system.

<u>Lessons Learned Software System Requirements</u>

The Lessons Learned Software System, as part of the broader system, has the following overall responsibilities:

- Store and display lessons learned
- Integrate existing (legacy) lessons learned systems into what the user perceives as a single, integrated system
- Accept new lessons learned
- Provide search and retrieval of lessons relevant to a given program/project management or engineering task
- Facilitate the following human workflows
    - Document and submit a lesson
    - Review and approve a lesson
        - with modification cycles, as necessary
    - Add approved lesson to system
    - Find and use lessons
    - Perform program/project management and system engineering tasks
        - Facilitate the application and contribution of lessons within the context of these tasks

Detailed requirements for the system are documented in a separate report.

Architecture Concepts

This section presents architecture concepts toward a possible system design that realizes the requirements for the Lessons Learned Software System. The conceived architecture, shown in Figure 3, combines a number of off-the-shelf components:

- lesson repositories
  - a native XML database
  - legacy repositories
  - file system to store files associated with lessons
- a user, task, and lesson metadata repository
- a search engine
- a workflow engine
- a web server
- applications running on an application server
- a web browser

The next section details the architecture to address lesson manipulation. A separate report details the architecture for search, workflow, and other functions.

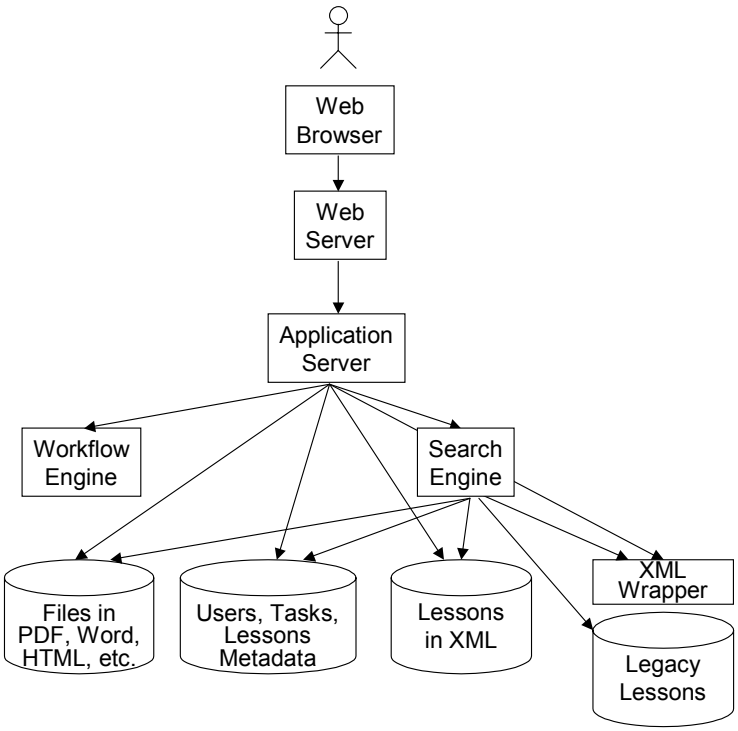

Figure 3: Architecture overview.

Lesson Manipulation

The proposed lesson creation and manipulation architecture, shown in Figure 4, uses XML to represent lessons, and it uses Java applications to create and manipulate lessons. A lesson is an XML document stored in a native XML database (a database that stores XML documents in their

native format, rather than converting them to relational tables or some other storage model). The lesson document conforms to an XML schema that defines the allowed fields and structure of the document. A base schema defines the minimal required elements in a lesson. Extensions to this base schema allow alternate lesson fields to be included in an alternate lesson format. XML stylesheets for a schema define how to display XML documents that conform to the schema. Stylesheets are defined using the eXtensible Stylesheet Language (XSL) or Cascading Stylesheets (CSS). By defining a family of XML schemas and corresponding XML stylesheets, the system can accommodate multiple lesson learned formats presented in a consistent, uniform way. To assure stability, all XML schemas and stylesheets should be defined in XML namespaces under control of the Lessons Learned Software System.

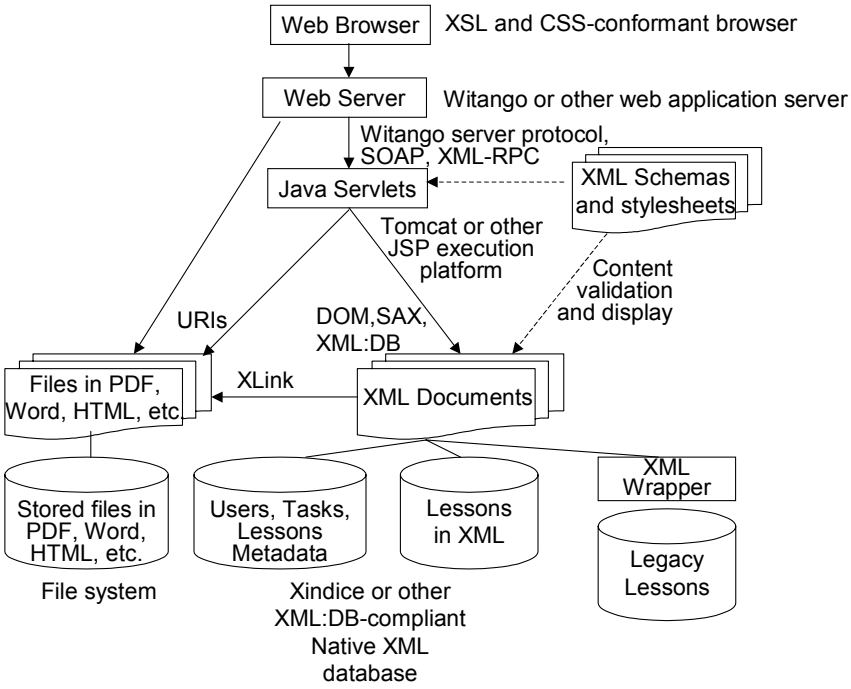

Figure 4: Lesson creation and manipulation architecture.

Java applications, packaged and launched as Java Servlets, use DOM, SAX, and other protocol standards to create, validate, and manipulate XML documents. New lessons (as opposed to existing, legacy lessons) are stored in a native XML database. Access to the database is via the XML:DB protocol. Files associated with lessons are stored in the local file system and referenced as URIs (web links). From within the XML documents, additional semantics of the associated file are defined using the XLink standard.

Note that Witango 5 has built-in support for creating and manipulating XML documents, so some functionality could be implemented directly in Witango rather than in Java applications.

Legacy lessons that are stored in databases can be made part of the system if an XML wrapper can be defined. This involves defining an XML schema and stylesheet for the lesson (hopefully, extending the base lesson schema) and implementing the DOM or SAX protocol for the lesson. For example, there are implementations that present ODBC-compliant data tables as DOM objects.

2003

NASA FACULTY FELLOWSHIP PROGRAM

MARSHALL SPACE FLIGHT CENTER
THE UNIVERSITY OF ALABAMA IN HUNTSVILLE

INVESTIGATION OF NICKEL ELECTROCODEPOSITION WITH THE AID OF REVERSE-PULSE PLATING

Prepared By:	Ryan Hulguin
Academic Rank:	Accompanying Student of Dr. Pei Xiong-Skiba
Institution and Department:	Austin Peay State University Department of Physics and Astronomy
NASA/MSFC Directorate:	Science
MSFC Colleague:	Dr. Brian Ramsey
UAH Colleague:	Darell Engelhaupt

Introduction

It is well known that the introduction of fine inert particles in a metal can lead to an improvement of strength, due to enhanced pinning of moveable dislocations [2]. Placing these fine particles in a plating bath and keeping them in suspension allows some of the particles to be codeposited with the plated metal [6]. This combination is known as an electrocomposite and the process is known as electrocodeposition.

Previous experiments have shown that nickel electrocomposites with as little as 1.0 weight percent alumina particles improve tensile strength, yield strength, and hardness [5]. Alumina (Al_2O_3) is often the particle of choice since it is readily available in monodispersed sizes and different crystallographic phases (e.g., α, γ, and θ) [6]. Chang and Lee [1] concluded that a key factor for controlling alumina content in electrocomposites is the influence of electrochemical potential. This viewpoint predicts that suitable periodic reverse-pulse plating will have a strong effect on increasing alumina content in the electrocomposite. A reverse-pulse plating method was later developed by Podlaha and Landolt [4] for the codeposition of nanosized, γ-alumina particles in a copper matrix. Their results demonstrate that the maximum particle concentration is found when the deposit thickness per cycle approaches the particle diameter size. They were able to increase the particle concentration nearly five to six times the concentration achieved with DC plating. This study will investigate whether periodic reverse-pulse plating can achieve similar increases in a nickel matrix.

Experiment

Connected to a DC motor was a threaded support rod. A stainless steel cone with a surface area of 50 cm^2 was then attached to the support rod to provide a rotating conical electrode. Rubber washers, Teflon gaskets, plastic spacers, and a threaded plastic end cap was used to ensure that only the outer surface of the cone was exposed to the plating path. A PVC pipe of 1” diameter with drilled holes spaced approximately 1 cm apart was used as the other electrode. The pipe was capped on one end, had a coiled titanium wire inserted into it, was filled with nickel chips, and then capped on the other end with part of the wire protruding through a small hole in the cap. A sheet of 100% cotton Webril Wipes was positioned around the PVC pipe to provide one layer of thickness and served as a filter. Three strong rubber rings hold the filter in place. Through the use of a modified cover, the nickel filled pipe and the rotating electrode were suspended into a 4000 mL beaker. The rotating electrode was placed in the center of the beaker and the PVC pipe was placed 2 ¼” away from the rotating electrode. Figure 1 shows a diagram of the electrocodeposition setup.

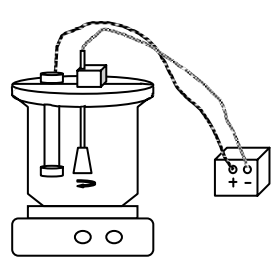

Figure 1. Diagram of electrocodeposition setup for DC plating.

A series of DC plating with current densities ranging from 3.4-50 mA/cm^2 was performed in a plating bath with properties listed in Table 1. Baikalox alumina particles were used in this study. They were of the γ phase and had a diameter of .05 μm. The plating bath was prepared in the beaker and then set on top of a Corning stirrer/hot plate. The stirring knob was always on setting 7, and the temperature knob was manually adjusted around settings 2 and 3 to maintain a bath temperature between 47-52°C. Constant current for DC plating was provided by a Hewlett Packard E3610A power supply. The pH levels were measured with an Orion 420A+ pH meter and maintained below 4.15 through the use of sulfamic acid.

Table 1
Properties of the DC plating bath

Chemical composition	Nickel metal as sulfamate	100 g/L
	Nickel bromide	2.288 g/L
	Boric acid	35 g/L
	Sodium dodecyl sulfate	.2 g/L
	Alumina powder	50 g/L
Temperature	47-52°C	
pH	3.57-4.15	
Rotating cone rpm	500	

After finishing the series of DC plating, the composite cones were removed through the use of a mechanical pusher and sent to a laboratory to obtain the composites' densities. The results could then be used to calculate the weight percent of alumina by assuming

$$m_{Ni} + m_{Al2O3} = m_{comp} \quad (1)$$

$$v_{Ni} + v_{Al2O3} = v_{comp} \quad (2)$$

and then using the definition of density along with simple algebra to obtain

$$Al_2O_3 \text{ wt\%} = 100 * \rho_{Al2O3} ((\rho_{Ni} / \rho_{comp}) - 1) / (\rho_{Ni} - \rho_{Al2O3}) \quad (3)$$

where ρ_{Ni} = 8.89 g/cm^3 and ρ_{Al2O3} = 3.3 g/cm^3. Figure 2 shows how the weight percent of incorporated alumina is affected by current density in DC plating.

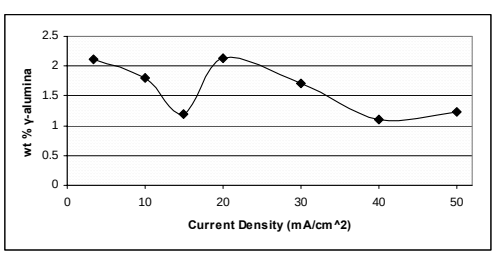

Figure 2. Particle incorporation vs. current density in DC plating.

A National Instruments Labview VI was modified by the author so that a computer could serve as a function generator to allow a Kepco BOP 20-20M power supply to carry out reverse-pulse plating. However, before attempting reverse-pulse plating, one sample was plated with regular pulse plating with no anodic pulse. This sample had unusual bumps around the edges. An extra .1 g/L of sodium dodecyl sulfate was then added to the solution in an attempt to remedy the

undesirable bumps. Two different samples were plated afterwards bump-free. There was no significant increase in alumina weight percent when compared to DC plating so further attempts at regular pulse plating were ceased and the results will not be included in this study.

The first two attempts at reverse-pulse plating were unsuccessful. Layers of the electrocomposite would peel away from the conical electrode and would not reattach themselves. An additional 2.288 g/L of nickel bromide solution was added to the plating bath in hopes of stopping the peeling. This modified solution performed, but with limited success. A detailed summary of the initial reverse-pulse plating attempts is given in Table 2. One of these attempts led to a significant increase in alumina weight percent. However, efforts to plate more and strip down to the same thickness per cycle eventually stripped down to the stainless steel cone. It was believed that tensile stress was the reason for this phenomenon, so 3 g/L of naphthalene-1,3,6-trisulfonic acid (NTSA) was added to minimize the internal stress. A series of reverse-pulse plating was carried out in this final bath utilizing the successful parameters found in Table 2. The cathodic pulse period was varied to plate an integer multiple of .05 μm and the anodic pulse period was adjusted accordingly to allow the deposit thickness per cycle to approach .05 μm.

The average thickness per cycle for a nickel plating bath as defined by [3] is

$$s\ (\mu m) = (\ 109.5\ )\ (\ a\ )\ (\ t\ )\ (\ I\ /\ A\ )\ /\ (\ d\ ) \qquad (4)$$

where a is the current efficiency, which is assumed to be 0.95 in this study, t is the time in hours, I / A is the current density in A/dm^2, d is the density of nickel in g/cm^3 and s is the average thickness in μm. Equation (4) must be modified to accommodate an anodic pulse and to handle time and current density in more convenient units. After modification, equation (4) becomes

$$s\ (\mu m) = (\ 3.421 * 10^{-4}\ )\ (\ 0.95\ ) * (\ (\ T\ )\ (\ j_p\ ) - (\ T'\ )\ (\ j_r\ )\ ) \qquad (5)$$

where T and T' are the cathodic/anodic pulse periods respectively in seconds, and j_p and j_r are the cathodic/anodic current densities respectively in mA/cm^2. j_p and j_r are both considered positive.

Results and Discussion

The results from the initial reverse-pulse plating attempts are shown in Table 2 below.

Table 2. Summary of Reverse-Pulse Plating Before NTSA Additive

Nickel bromide (g/L)	j_p (mA/cm^2)	j_r (mA/cm^2)	T (s)	T' (s)	Al_2O_3 wt%	Approx. Thickness/ Cycle (μm)[a]
4.576	40	40	0.5	0.1	1.3427	0.0052
4.576	40	40	0.1	0.02	0.76208	0.00104
4.576	40	80	0.1	0.02	0.9905	0.00078
4.576	20	40	15	3	14.883	0.0585
4.576	20	40	50	21	------[b]	0.052

[a] Reverse-pulse plating performed after 30 minutes of initial DC plating at 20 mA/cm^2.
[b] This attempt stripped down to the stainless steel cone

It is interesting to note that reverse-pulse plating can either decrease or increase the alumina weight percent when compared to Figure 2. Table 2 shows that if the anodic current density is

twice that of the cathodic current density, there is a slight increase in particle incorporation. When the approximate thickness per cycle approaches the particle diameter size, there is a significant increase in particle incorporation.

Figure 3 shows the reverse-pulse plating results in the final plating bath containing NTSA. Plating with higher integer multiples provides higher alumina incorporation comparable to that achieved without the use of NTSA. DC plating in the NTSA bath seems to have very little particles incorporated and would imply that NTSA mainly allows alumina particles to deposit during the anodic pulse. This observation might be able to explain why doubling the anodic current density yields higher alumina incorporation. Perhaps the alumina particles prefer an anodic electrode by nature, and introducing NTSA intensifies this preference by significantly influencing the particle/electrode interaction forces.

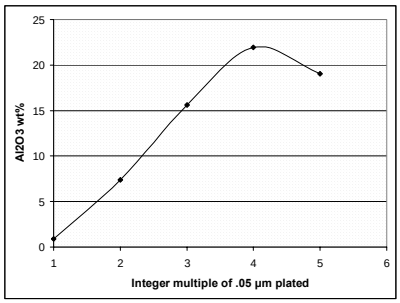

Figure 3. Reverse-pulse plating results from NTSA bath.

Conclusion

Periodic-reverse pulse plating can either increase or decrease the amount of incorporated alumina in a nickel bath. Setting the anodic current density to twice that of the cathodic current density yields a slight increase, while setting the approximate thickness per cycle to approach the particle size provides a significant increase. An increase in particle concentration of nearly seven times that of DC plating was achieved without the use of NTSA. More aggressive plating parameters required the use of NTSA and more time to achieve even higher increases.

References

[1] Chang, Y. S. and Lee, J. Y., *Materials Chemistry and Physics*, 20, 309, (1988).

[2] Ferkel, H., Müller, B., Riehemann, W., *Materials Science and Engineering*, A234-236, 474, (1997).

[3] *Modern Electroplating,* John Wiley & Sons, Inc., pp. 1-28, 142, (2000).

[4] Podlaha, E. J. and Landolt, D., *Journal of the Electrochemical Society*, 144, 7, (1997).

[5] Safranek, W., *The Properties of Electrodeposited Metals and Alloys*, American Elsevier, pp. 327, (1974).

[6] Talbot, J. B. and Stojack, J. L., *Journal of the Electrochemical Society*, 146, 4504, (1999).

2003

NASA FACULTY FELLOWSHIP PROGRAM

MARSHALL SPACE FLIGHT CENTER
THE UNIVERSITY OF ALABAMA IN HUNTSVILLE

INITIAL ASSESSMENT OF CHEM FOR RBCC FLOW FIELD PREDICTION

Prepared By:	Ziaul Huque
Academic Rank:	Associate Professor
Institution and Department:	Prairie View A&M University Department of Mechanical Engineering
NASA/MSFC Directorate:	Transportation
MSFC Colleague:	Roberto Garcia

Introduction

A major goal driving current space propulsion research is to significantly decrease the cost of access to space. There are efforts underway to develop reusable launch vehicles that promise to decrease long-term costs as compared to the traditional expendable staged vehicles. One way to use high-efficiency airbreathing cycles during ascent in a reusable system is through the use of combined-cycle propulsion (CCP) systems.

There are many types and variations of CCP systems; one class of rocket-based CCP system which shows promises for Earth-to-orbit (ETO) missions are typically referred to as rocket-based combined-cycle (RBCC) engines. Although there are several design variations for the RBCC engine, the gamut of concepts includes four flight regimes, viz. rocket-ejector, ramjet, scramjet and all rocket [1]. Of these four flight regimes, the rocket ejector mode that encompasses vehicle flight Mach numbers from zero to roughly two is the least understood. To date, experiments have been conducted for both diffusion and afterburning as well as the simultaneous mixing and combustion rocket-ejector configurations [2-4].

Recent experimental studies of the rocket-ejector mode of a RBCC engine were performed at the Propulsion Engineering Research Center at Pennsylvania State University (PSU) [5, 6]. Both single-rocket and twin-rocket results using gaseous hydrogen/gaseous oxygen propellants are published. Experiments were conducted with both direct-connect and sea-level static configurations. Computational fluid dynamics (CFD) analyses of several cases were conducted at NASA Marshall Space Flight Center to validate/refine the FDNS code [7] as well as to provide further insight into the rocket-ejector mode of operation.

The major objective of the current summer research is to make initial assessment of an alternate CFD code, Chem, under development at Mississippi State University which is intended to be used extensibly at NASA Marshall. Test data from two cases, both sea-level static, but one single-rocket and the other twin-rocket configuration are used for the purpose. The single-rocket case is the Case 6 of the PSU experiments, with chamber pressure of 34.02 atm. and oxygen/fuel ratio of 8. The twin-rocket case has a chamber pressure of 13.6 atm. and oxygen/fuel ratio of 8. A schematic of the RBCC geometry used is shown in Figure 1.

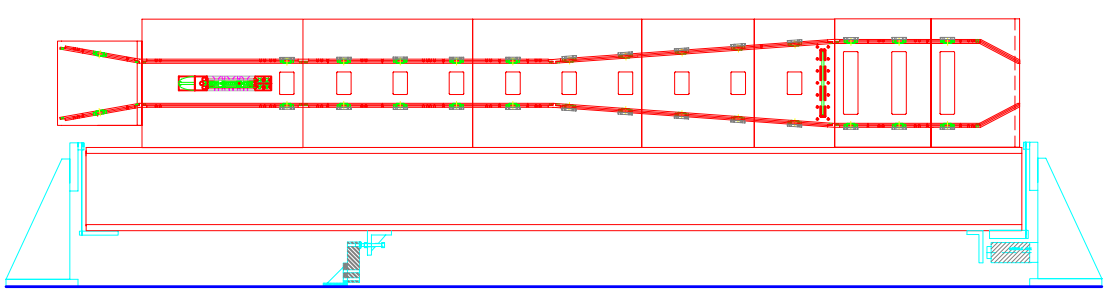

Figure 1: Rocket-ejector setup with sea-level static configuration.

Computational Approach

Solution Algorithm

Chem is a general purpose, multidimensional, multi-species, viscous chemistry solver built upon a rule-based specification system.

Both cases were simulated steady state with the same parameters and models except the thruster conditions. For the single-rocket configuration the thruster is used as an integral part of the RBCC geometry. For the twin-rocket configuration, the thruster exit conditions were used as primary flow inlet boundary conditions. The baseline model or BSL_model_decoup was used for turbulence model. The model is developed by blending the Wilcox $\kappa-\omega$ and the $\kappa-\varepsilon$ models. To achieve this, the $\kappa-\varepsilon$ model is first transformed into $\kappa-\omega$ formulation. The original $\kappa-\omega$ equations are then multiplied by a blending function F_1 and transformed $\kappa-\varepsilon$ equations by $(1-F_1)$, and then both are added together. The blending function F_1 is designed so that it is the unity at the wall, and gradually approaches zero away from the wall. For both cases hydrogen/air, 7 species-32 reactions system were solved.

Grid and Boundary Conditions

The computational domain consisted of one quarter of the experimental internal flow path. Symmetry planes were used on the vertical and horizontal centerlines. Structured grids were implemented. The single-rocket configuration contained 520730 nodes. The twin-rocket configuration contained 738525 nodes.

The single-rocket setup for CFD simulation differed from the twin-rocket in that the primary thruster was included as an integral part of the computational domain. In order to reduce the size of the grid the thruster chamber length used was 6.35 cm instead of 20.32 cm. For the twin-rocket system the thruster was not included as a part of the computational domain. For this case the thruster exit was set as a fixed inlet boundary condition. The zones upstream of the inlet and downstream of the RBCC duct exit nozzle had free stream boundary conditions specified on their perimeter. In both cases the afterburner injection ports were modeled as equivalent area squares with a fixed inlet mass flow.

Results and Discussion

Flow Field Overview

Mach number, temperature and static pressure distribution from the initial simulation with Chem are shown as color contours in Figure 2 for the single-rocket configuration. Figure 3 shows the color contours of the same parameters for the primary thruster. Figure 4 shows the color contour of the Mach number of the RBCC duct for twin-rocket configuration.

The rocket engine plumes are clearly visible in the middle of the RBCC ducts. For both cases the flow was generally two-dimensional between the rocket engine exit and the afterburner hydrogen injection. The plume is much shorter for the twin-rocket configuration because of the lower

primary thruster chamber pressure (13.6 atm.). Figure 3 clearly shows the flow becomes supersonic at the primary thruster throat. In both cases the Mach number contours indicate the flow was entirely subsonic as it entered the diffuser section of the duct. In neither case did the flow choke at the RBCC throat. The average RBCC duct nozzle exit Mach number were approximately 0.76 and 0.39 respectively for the single-rocket and twin-rocket configurations.

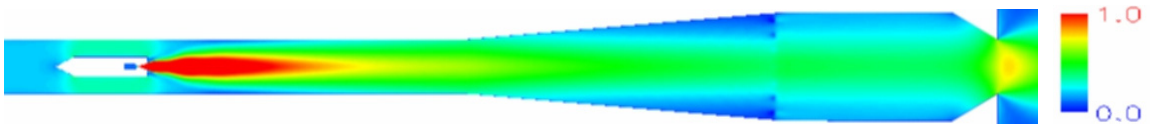

(a) Mach Number

(b) Temperature

(c) Pressure

Figure 2: Calculated Mach number, temperature and static pressure contour lines of RBCC duct for single-rocket configuration.

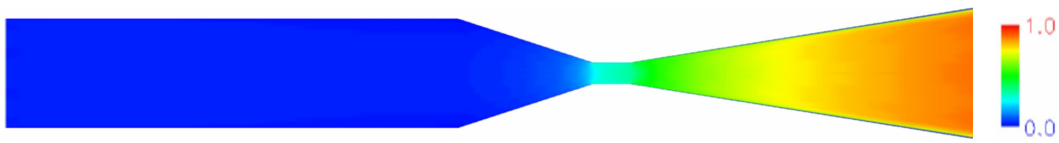

(a) Mach Number.

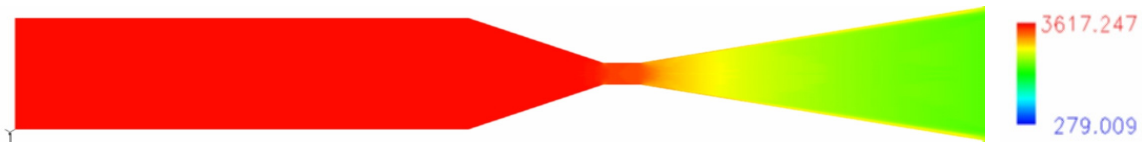

(b) Temperature

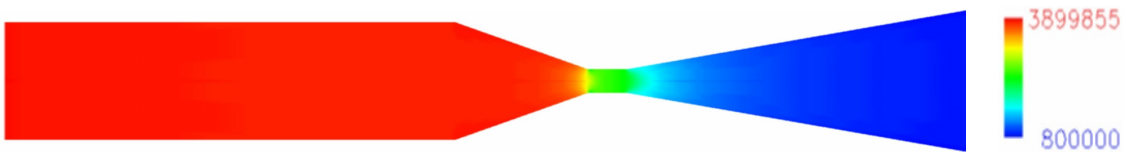

(c) Pressure

Figure 3. Calculated Mach number, temperature and static pressure contour lines of the thruster for single-rocket configuration.

Figure 4. Calculated Mach number contour lines of the of RBCC duct for twin-rocket configuration.

Entrained Air

The experimental data for single-rocket case indicated a by-pass ratio (mass flow of air/mass flow of rocket) of 1.84. The computed by-pass ratio was 1.1. On the other hand the computed by-

pass ratio for twin-rocket case was 2.04 compared to the experimental data of 2.17. The reason for such a low computed by-pass ratio for single rocket case is believed to be the primary thruster solution. The computed values at the exit of the thruster were compared to those used as inlet conditions in the previous simulation with FDNS by Ruf, et. al. [7] and found to be significantly different (pressure and temperature much lower and Mach number slightly higher). One of the reasons could be the coarser grids and the shorter thruster length used compared to the previous independent thruster simulation performed by Tucker [8].

Static Pressure

The static pressure results for the single-rocket and twin-rocket configurations are shown in Figures 5 and 6 respectively. For both cases top wall measurement and simulation values were used. The computed pressures show good qualitative agreement with the trend of the experimental data. For the single-rocket case the CFD results over predicted the values. The reasons again are believed to be connected with the low entrainment of the secondary flow. In case of twin-rocket the CFD results under predicted the experimental values. The results for twin-rocket case shown are intermediate results. A completely converged case is expected to provide improved comparison.

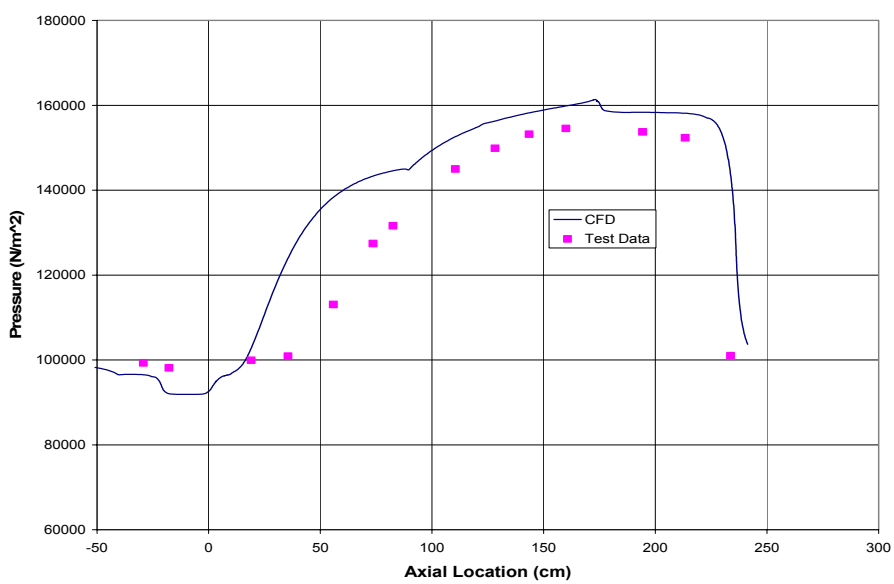

Figure 5: Static pressure comparison for single-rocket configuration

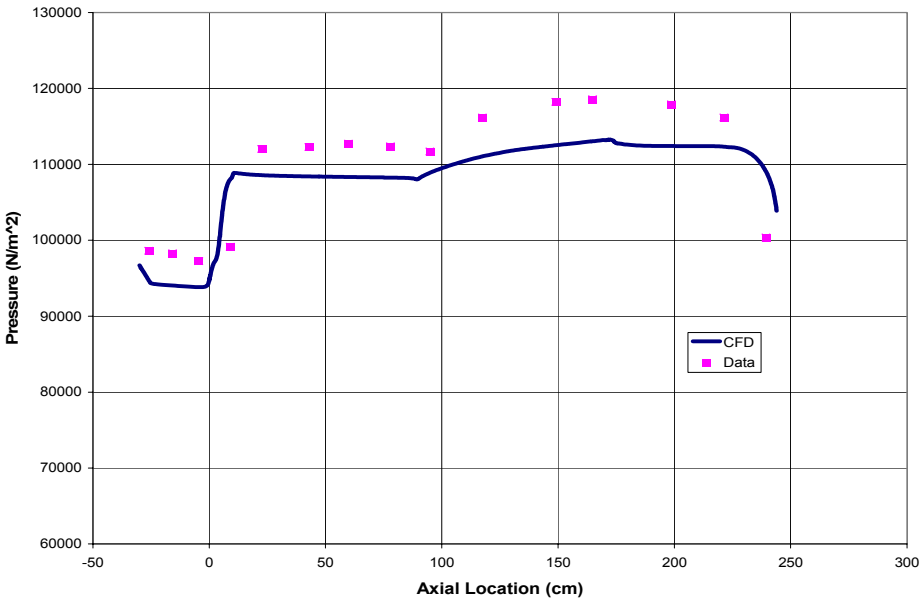

Figure 6: Static pressure comparison for twin-rocket configuration

Major Species Mole Fractions

Figure 7 shows the mole fraction comparison for the single rocket configuration at an axial distance of 23.75 cm from the primary thruster exit. The solid lines represent CFD data and the lines with the markers represent experimental data. The CFD predictions are found to be flatter than the experimental data. The reason can again be attributed to the lower entrained flow in the CFD simulation. An increased flow entrainment would increase the mole fraction of N2 near the wall and decrease them at the centerline. Similarly the effect on the mole fraction of H2O would be just the opposite, i.e., increase at the centerline and decrease towards the will. This would make the prediction much more comparable than the current predictions.

Conclusions

Initial simulations of RBCC flow path physics were performed with the newly developed code Chem. Two cases, namely, single-rocket sea-level static configuration with primary thruster and twin-rocket sea-level static configuration were simulated. The CFD results provided good qualitative agreement. Further grid refinements and parameter adjustments are required to get better quantitative agreement. The Chem code generally was found to be robust on both computing clusters used for simulation in Marshall. The Department of Mechanical Engineering at Prairie View A&M University is expected to acquire a computing cluster by the end of September, 2003. The current simulation work will be continued on that cluster for further assessment of Chem in the next several months at Prairie View.

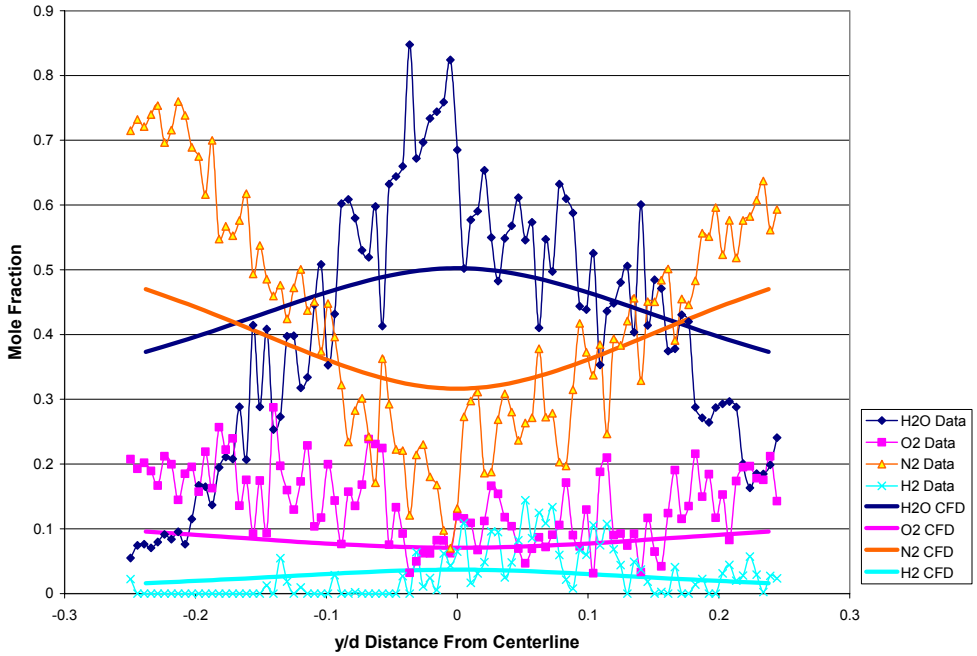

Figure 7: Mole fraction comparison for single-rocket configuration at an axial distance of 23.75 cm from the primary thruster exit.

Acknowledgements

The author would like to thank Robert Garcia of TD 64 for all the support and time and being instrumental in providing the opportunity for an educational and productive summer at Marshall Space Flight Center. The author also wants to extend heartfelt thanks to Jeff West and Francisco Canabal for their time and patience. Thanks are also due to Joe Ruf for providing information whenever requested.

References

[1] Escher, W. J. D., ed., The Synerjet Engine: Airbreathing/Rocket Combined-Cycle Propulsion for Tomorrow's Space Transports, Society of Automotive Engineers, Warrendale, PA, 1997.

[2] Lehman, M., Pal, S. and Santoro, R. J., "Experimental Investigation of the RBCC Rocket-Ejector Mode," AIAA 2000-3725, 36th Joint Propulsion Conference, Huntsville, AL, July 17-19, 2000.

[3] Lehman, M., Pal, S., Broda, J. C. and Santoro, R. J., "Raman Spectroscopy Based Studies of RBCC Ejector Mode Performance," AIAA-99-0090, 37th AIAA Aerospace Sciences Meeting, Reno, NV, January 11-14, 1999.

[4] Lehman, M., Pal, S. and Santoro, R. J., "Experimental Studies of the RBCC Rocket-Ejector Mode," Joint Meeting of the United States Sections: The Combustion Institute, Washington, DC, March 15-17, 1999.

[5] Santoro, R. J. and Pal, S., "Experimental and Analytical Modeling of the Rocket Ejector Mode of a Combined Cycle Rocket-Based Engine," Final Report for NASA Contract Grant NAS8-40890

[6] Cramer, J. M., Pal, S., Marshall, W. M., and Santoro, R. J., "Recent Experimental Results Related to Ejector Mode Studies of Rocket-Based Combined Cycle (RBCC) Engines," NASA Spring Workshop on Fluids – 2003, Birmingham, AL, April 22-24, 2003.

[7] Ruf, J., Lehman, M., Pal, S., Santoro, R. J., and West, J., "Experimental/Analytical Characterization of the RBCC Rocket-Ejector Mode," JANNAF-2003.

[8] Tucker, K., "Validation of a CFD Code for Heat Flux Predictions in Small Thrusters Used in RBCC Testing," MSFC Internal Report.

2003

NASA FACULTY FELLOWSHIP PROGRAM

MARSHALL SPACE FLIGHT CENTER
THE UNIVERSITY OF ALABAMA IN HUNTSVILLE

ADAPTIVE INVERSE CONTROL OF X-33 FOR TAEM APPROACH/LANDING

Prepared By:	Leehyun Keel
Academic Rank:	Professor
Institution and Department:	Tennessee State University Center of Excellence in Information Systems & Department of Electrical Engineering
NASA/MSFC Directorate:	Transportation
MSFC Colleague:	Charles Hall

Introduction

The entry/Terminal Area Energy Management (TAEM) phase of the Reusable Launch Vehicle (RLV) starts at roughly 100,000 feet and Mach 3 and ends with main gear touch down at the landing site when the speed is about 200 knots. Maneuvers are commanded by guidance to dissipate excess energy from entry/TAEM interface to the Heading Alignment Cone (HAC). A typical TAEM and Approach and Landing (A/L) trajectory can be a relatively straight path, or a series of "S" turns depending on the vehicle's speed and distance from the runway. The vehicle is maneuvered to align the heading to a point tangent to the HAC, and continues to turn until it is aligned with the runway. During the approach and landing phase, the vehicle must maintain a desired glide slope and heading, then smoothly flare to reduce descent rate before touchdown. In this phase of flight, significant disturbances due mainly to winds can occur. Thus, it is necessary to design a controller that provides closed-loop stability, robustness, and accurate tracking for the vehicle [1].

On the other hand, conventional controllers such as that used on the Space Shuttles [2] rely heavily on linear analysis, computation of transfer functions and gains at many operating points. To avoid numerous point-wise designs and analysis, a nonlinear control method can be used. Typically, dispersions, trajectory changes, and failure conditions of the vehicle require a redesign of the control system. Since such situations requiring a redesign of the control system often occur during a mission, a redesign of the control system must be done preferably on-line or at least much simpler than the current practice of control design. From these considerations, we study a controller design problem for a RLV to achieve a technique that adaptively determines the controller parameters so that the overall controlled vehicle maintains robust stability against system uncertainties and external disturbances while satisfactory tracking is obtained. The adaptive controller must also have ability to quickly adapt its parameters to optimal values when the vehicle model changes drastically due to dispersions or failure conditions. In this study, we consider the flight control problem of a RLV during TAEM only.

Our approach to this problem is adaptive inverse control that achieves open-loop-like control of the system by using a series controller whose transfer characteristic is the inverse to that of the plant to be controlled. The adaptive inverse controller is adaptive, and adjusts itself with respect to the plant output response. A notable difference between the adaptive inverse control architecture from the conventional feedback structure lies in the use of feedback. Unlike conventional control structures, the adaptive inverse controller is not derived by feedback signal. It uses feedback to control the variable parameters of the controller. Since changes in the plant parameters take place much more slowly than changes in the signals, feedback in an adaptive inverse control system can be relatively slow acting, only fast enough to keep up with plant parameter changes. The result is that system stabilization and regulation with adaptive inverse control is in many cases easier than with conventional feedback control [3]. In this study, we will develop an intelligent adaptation algorithm to produce an adaptive inverse controller for a given nonlinear model of a RLV. In this report, we give some results of a preliminary study in developing a control scheme for the RLV TAEM A/L phase that automatically (adaptively) designs a controller for dispersions, change of trajectories, and failure conditions. We will also show that the controller is robust with respect to plant uncertainties and disturbances.

X-33 Description and the Mathematical Model for TAEM A/L Phasel

The X-33 is a lifting body airframe with two vertical rudders, two body flaps and two elevons on each of its small wings as shown in Figure 1. During TAEM and A/L phase of flight only the aerosurfaces are used.

Figure 1: X-33 Vehicle

Assuming rigid body, constant mass, and constant inertia, the standard 6DOF equations of motion in body axes for TAEM and A/L phase are as follows [4]:

$$\begin{aligned} \dot{p} &= -L_{pq}pq - L_{qr}qr + L & \dot{u} &= rv - qw + X + G_x \\ \dot{q} &= -M_{pr}pr - M_{r^2p^2}(r^2 - p^2) + M & \dot{v} &= pw - ru + Y + G_y \\ \dot{r} &= -N_{pq}pq - N_{qr}qr + N & \dot{w} &= qu - pv + Z + Gz \end{aligned} \tag{1}$$

where *L, M,* and *N* are angular accelerations generated by aerodynamic moments including basic aerodynamic moments due to flight condition (α, β, Mach) plus moments due to aerosurface deflections. The aerodynamic forces C_x, C_y, C_z are nondimensional quantities scaled to units of force:

$$\begin{bmatrix} X \\ Y \\ Z \end{bmatrix} = \frac{\bar{q}S}{m} \begin{bmatrix} C_x \\ C_y \\ C_z \end{bmatrix} \tag{2}$$

where $\bar{q}$ (lb/ft^2) is the dynamic pressure; S (ft^2) is a reference area and *m* is the mass in slugs. Similarly, the aerodynamic moments on the body are

$$\begin{bmatrix} L \\ M \\ N \end{bmatrix} = \bar{q}S \begin{bmatrix} \dfrac{b}{I_{XX}I_{zz} - I_{xx}^2}(C_{lT}I_{zz} + C_{nT}I_{xz}) \\ \dfrac{c}{I_{yy}}C_{mT} \\ \dfrac{b}{I_{xx}I_{zz} - I_{xz}^2}(C_{nT}I_{zz} + C_{lT}I_{xz}) \end{bmatrix} \tag{3}$$

Adaptive Inverse Control Implementation

Unlike conventional feedback systems shown in Figure 2, the basic idea of adaptive inverse control is to derive the system with a signal from a controller whose dynamic characteristic is the inverse of that of the system as shown in Figure 3. In effect, it is an open-loop control structure in controls point of view and feedback is used only for adaptation of the controller.

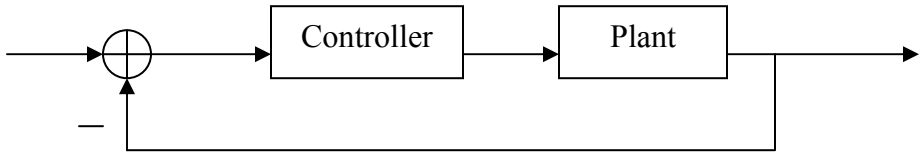

Figure 2: A conventional feedback system

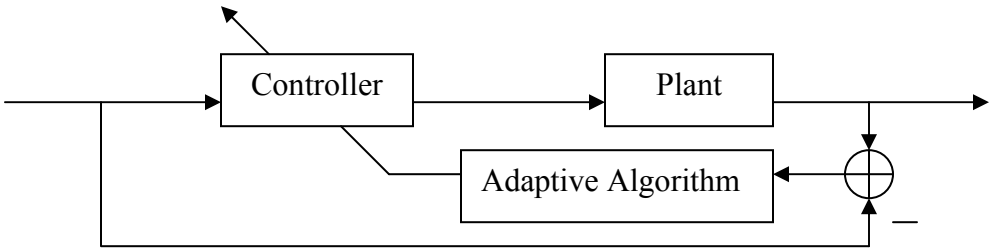

Figure 3: Basic adaptive inverse control

Clearly, the plant must be stabilized if it is unstable. Since the RLV model is unstable, we design a robust, stabilizing nonlinear feedback gain for each of the six plant states. An adaptation algorithm is developed to adapt controller parameters so that the controller parameters converge to those of the inverse of the stabilized plant. The main complication is to achieve a causal and stable controller (or inverse model). Since the RLV model is non-minimum phase, the direct inverse will be unstable. Such a controller is not acceptable for the open-loop-like configuration we use here. Thus, we approximate the stabilized system as a delay (with appropriate amount time) plus a minimum phase plant. Then use the inverse of the minimum phase plant as the controller. Causality of a controller is obtained by using the future trajectory information. Figure 4 shows our control scheme.

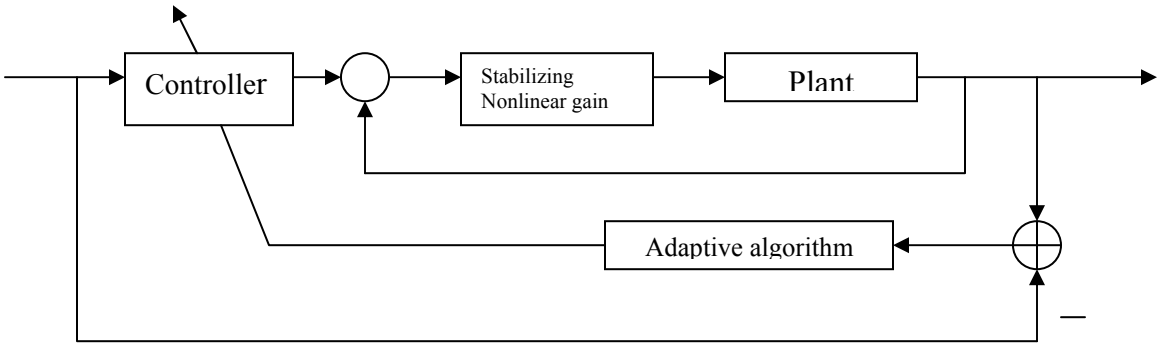

Figure 4: Proposed adaptive inverse control scheme

Results

Computer simulations have been performed with the given guidance commands (normal acceleration (Nz), roll angle (ϕ), and yaw velocity (r)). Due to the unavailability of information of control allocation to convert commanded torque and acceleration to actuator deflections, an ideal condition is assumed. Under this assumption, satisfactory tracking has been achieved. Many open problems are observed and some of them are discussed in the next section.

Resources

The project requires two software tools. Matlab with Simulink and appropriate toolboxes was the main software tool for verification of models and design and testing of the controllers. Several sets of data were collected from the Maveric simulations. Maveric is a 6 DOF vehicle software simulation for analysis of guidance and control systems and is an ongoing development project of the Vehicle Design Group (TD54) and Control Systems Group (TD55).

Future Works

Once control allocation information is obtained, the control algorithm will be modified appropriately. The control algorithm will be tested under more realistic environment to study the effects of plant parameter changes, new guidance commands, and presence of disturbances on performance. Non-minimum phase behavior of nonlinear systems will also be studied further to improve the adaptive inverse controller performance. Different inversion techniques will also be examined. The controller will later be tested in the Maveric to further examine its capabilities. Other adaptive control schemes are also subject to study.

Acknowledgements

The author would like to thank Mark Whorton of TD54 for encouraging him to participate in the summer program and for showing genuine interests in his research. A special thanks to Charles Hall of the TD54 for providing us with models, teaching us flight dynamics, and working with us in the midst of his busy schedule.

References

[1] Hall, C. E. and Shtessel, Y. B. (2003), "RLV Sliding Mode Control System Using Sliding Mode Observers and Gain Adaptation,"

[2] Moore, T. E. (1991), "Space Shuttle Entry Terminal Area Energy Management," NASA TM 104744.

[3] Widrow, B. and Walach, Walach (1996), *Adaptive Inverse Control*, Prentice-Hall PTR.

[4] Wise, K. A. and Broy, D. J. (1996), "Agile Missile Dynamics and Control," *Proceedings of AIAA Guidance, Navigation, and Control Conference,* San Diego, CA, July 28-31.

2003

NASA SUMMER FACULTY FELLOWSHIP PROGRAM

MARSHALL SPACE FLIGHT CENTER
THE UNIVERSITY OF ALABAMA IN HUNTSVILLE

TENSEGRITY RESEARCH FOR GENETIC ALGORITHM OPTIMIZATION

Prepared By:	Kenneth R. Kimble
Academic Rank:	Associate Professor
Institution and Department:	University of Tennessee Space Institute Mathematics
NASA/MSFC Directorate:	Engineering
MSFC Colleague:	Jim Steincamp

Introduction

A project was begun at Marshall Space Flight Center (MSFC) in 2001 to investigate the optimization of tensegrity structures using genetic algorithms[7]. The MSFC interest in tensegrities stemmed from its charge to develop advanced technologies for space telescopes. There has also been some interest in using this technology in several other applications, which require very large and light weight structures. Since tensegrities consist of continuously connected tensile members (wires) connecting a discontinuous set of compressible elements (bars), and since stiffness can be adjusted by adjusting the tensions in the tensile elements, these structures provide the extreme in strength to mass ratio and have evident advantages in space construction.

An artist initially noticed the system of compression and tension, which constitutes a tensegrity. Figure 1 shows the "trigonal tower" tensegrity designed by Kenneth Snelson, the inventor of tensegrity structures[6]. This one has 12 stages of 3 bars and 9 wires each. Large-scale towers similar to this one of heights above 160 feet have built as artistic structures in several places around the world. Tensegrities also seem to occur at the opposite extreme of scale in the physical world. Figure 2 shows a sketch of a model of the structure of spider silk[9], the strongest natural fiber. The red and blue straight segments surrounded by green boxes represent beta-pleated protein structures, which serve as compression elements. The coiled blue curves are amorphous chains of proteins, which serve as tension elements. A variety of natural forms including viruses, carbon atoms, cells and tissues are similarly thought to behave mechanically like a tensegrity[2].

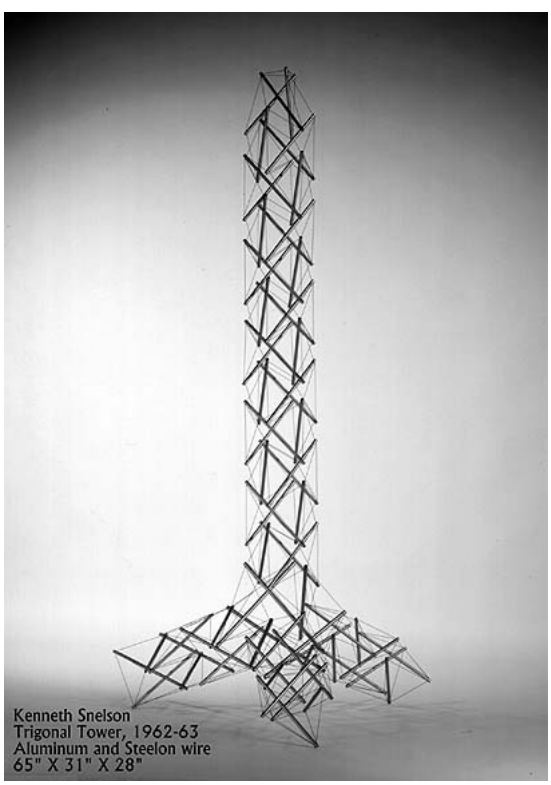

Figure 1. Snelson's trigonal tower.

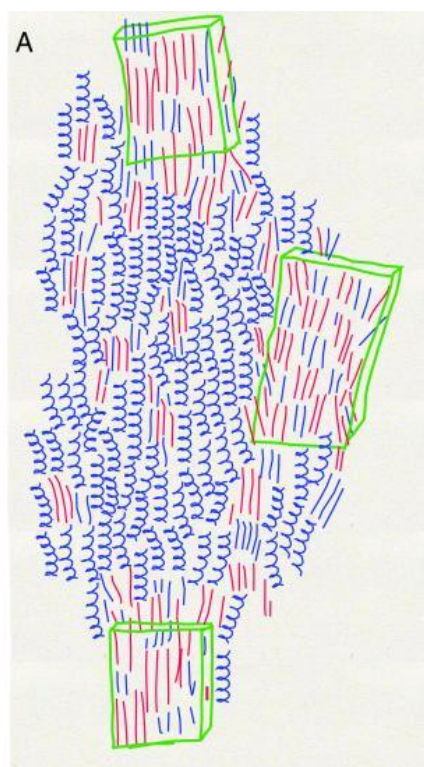

Figure 2. Spider silk.

The motivation to use a genetic algorithm[1,10] to aid in the design of tensegrities originated in a very promising study on trusses. A. Keane and S. Brown[4] used a genetic algorithm to optimize the design of at truss with respect to its vibration performance. Figure 3 shows the original standard truss, while Figure 4 shows the truss optimized using the genetic algorithm for vibration performance. An improvement of over 20,000% in frequency-averaged energy levels was obtained using this approach[3].

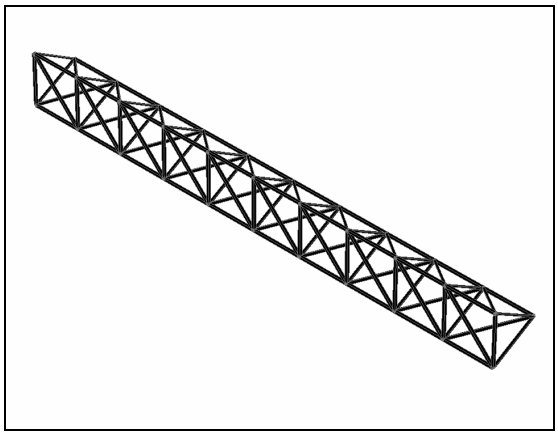

Figure 3. Baseline Truss Structure.

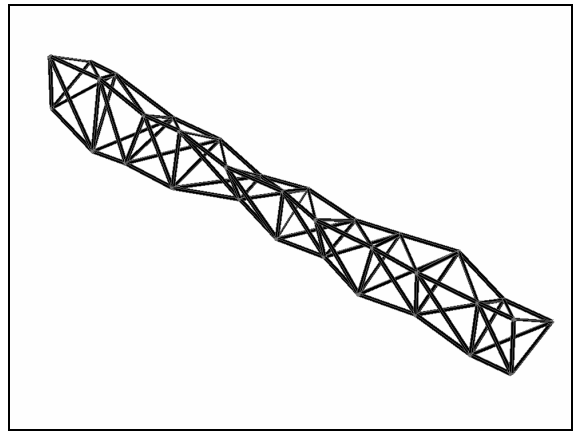

Figure 4. Performance Enhanced Structure.

Efforts were made to optimize the vibration behavior of the tensegrity structures using genetic algorithms. However the "form finding" calculations available at the time of the first study were based on truss calculations based on small disturbances from equilibrium. Unlike the truss, tensegrities execute moderate excursions to reach equilibrium and therefore a linearized theory is inadequate to find an equilibrium shape. However, once the equilibrium configuration is found, the vibrational behavior can be once again predicted from linear small disturbance theory. This study shows how a non-linear "form finding" calculation can be used to find the equilibrium configuration of arbitrary tensegrities.

Finding the Shape

A MATLAB procedure was designed which generates a cylindrical tensegrity topology and suitable initial positions for the nodes of the tensegrity. Figure 5 shows the generated structure, which is not in equilibrium. Figure 6 shows a tensegrity map, which is an aid in setting and checking the wire connections.

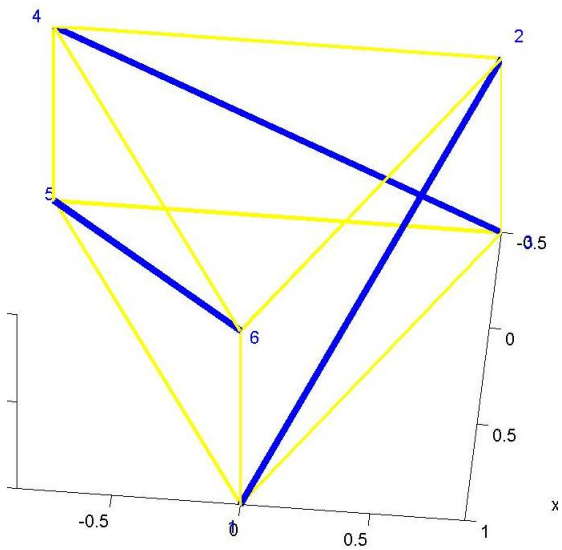

Figure 5. Initial 3 bar 1 stage tensegrity.

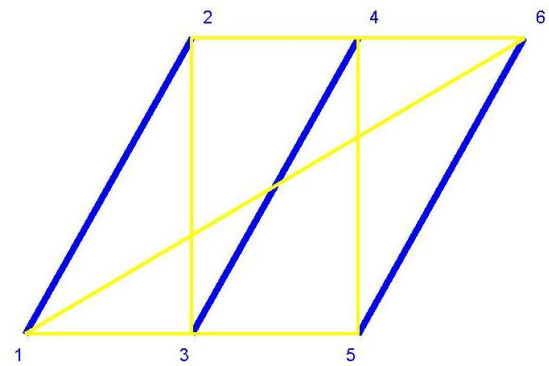

Figure 6. Tensegrity map.

It was assumed that the bars would maintain a fixed length and hence contribute nothing to the total potential energy P. The wires were assumed to have unstretched lengths L and to obey a simple Hooke's law in terms of the difference between the length |w| of the wire and L so that the potential energy of one wire was given by $k(|w|-L)^2/2$ where k is the Hooke's law constant. Using a sum of such expressions and the connection matrix A allows w to be represented as A' x where x is the vector of nodal coordinates. If P is minimized while keeping the bar lengths constant, the equilibrium position of x will be found.

In order to minimize P, the gradient of P, dP, was calculated. It represents the negative of the net tension forces appearing at the nodes of the tensegrity and is also the direction for steepest descent to minimize P. However, applying -dP to x directly will change the bar lengths. In order to prevent this and approach equilibrium as fast as possible, dP was expressed first in terms of the central forces Fcm and the couples Fcp on each bar. See Figure 7 where the bars are shown in red, Fcm in green and Fcp in purple. Then the Fcp was reduced by its projection on the bar, which effectively removes the compressive component leaving Frp in yellow. Finally in order that the bar not be changed in length Frp was slightly decreased in length to Fcorr in blue to compensate for truncation error. The final correction is then Fcm +- Fcorr. Rather than use dP for the step, a small fraction (typically 1-2%) of dP was used, because, if the step was too large, a wire often went slack. The converged 3 bar single stage tensegrity is shown in Figure 8. Note that the top triangle is rotated 5 pi/6 with respect to the base triangle as is predicted by theory.

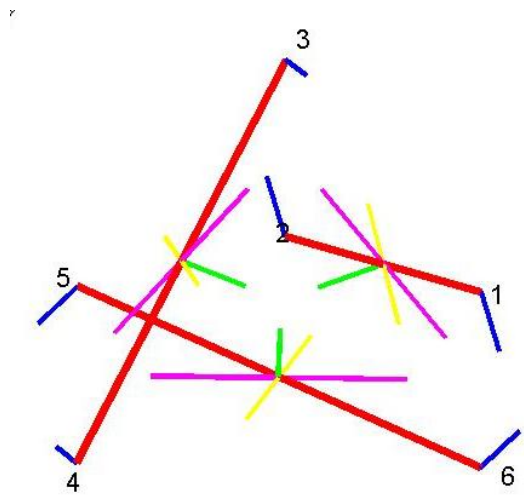

Figure 7. Wire forces.

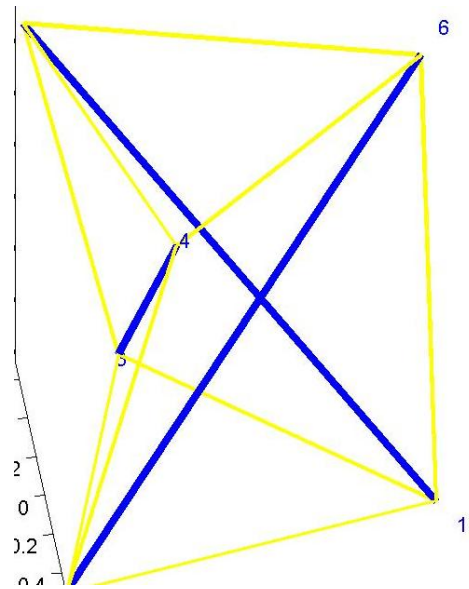

Figure 8. Converged C3,1 tensegrity.

The C6,6 (6 bars per stage, 6 stages) tensegrity was generated and converged. Figure 9 shows the resulting spherical shape, not at all like the cylinders seen in the literature. However, the cause of this anomaly has been traced to the assumption that all wire lengths L were assumed to be the same, whereas in reality, to obtain a cylinder, these lengths must be made greater in the longitudinal direction and smaller in the radial direction of the cylinder. Figure 10 shows the result of experimenting with these parameters.

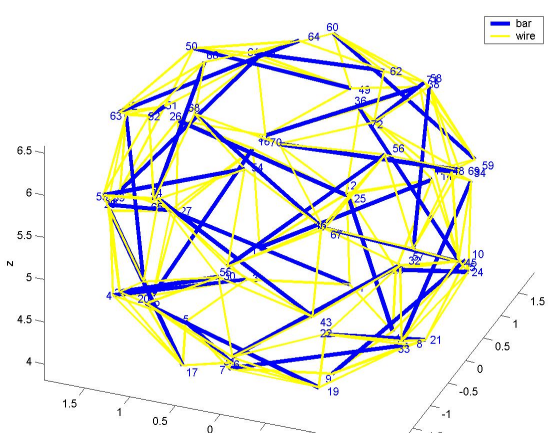

Figure 9. C6,6 equal wire length.

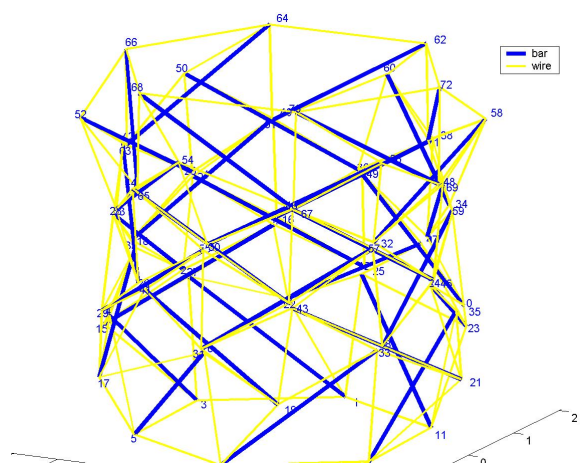

Figure 10. C6,6 adjusted wire lengths.

Structional Vibration Modes

In order to avoid a second order theory, it was assumed that the bars have very high Hooke's law constant and the corresponding energy terms were added to P. This allowed a straightforward derivation of the traditional truss equations for the linearized small disturbance motion. The eigenvalues of the resulting matrix were then computed giving the required frequencies as the square roots of the eigenvalues. This method avoids the complications of fixed bar length. Free

motions and the force balance give zero eigenvalues while the stiff bar contributes high frequency spurious frequencies. But the first non-zero eigenvalue gives the square of the fundamental frequency which is all that is needed for genetic algorithm optimization.

Experimental Work

The "NASA Tensegrity Model" (NTM) was previously built and instrumented to provide physical verification of the theory. Figure 11 shows the model equipped with accelerometers. A sonic digitizer was used to locate the nodes (ends of the bars) and the tensions in the individual wires were measured as in Figure 12. Initial data input and preliminary analysis has been performed on the equilibrium data for the NTM and preparations are underway to do dynamic Measurements. These should serve to prove the computational techniques described above.

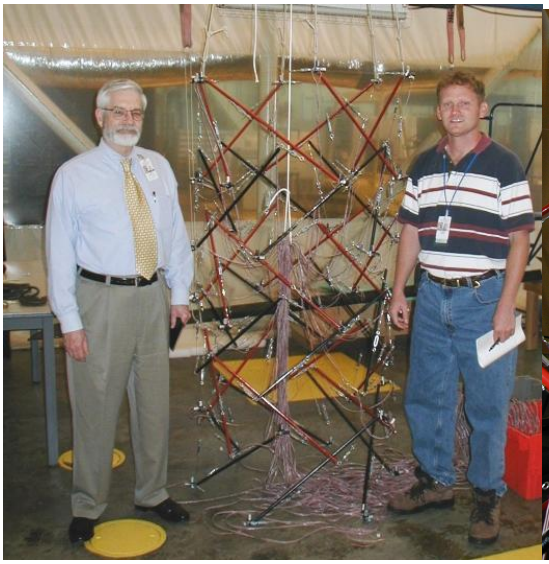

Figure 11. The NASA tensegrity.

Figure 12. Measuring the wire tensions.

Conclusions and Future Work

A viable "form finder" for tensegrity research has been constructed. Fundamental frequencies can be approximated accurately enough to allow genetic optimization and comparison with experiment to proceed.

A second order theory is essential for several reasons. Firstly, the modified gradient technique is sensitive to the scaling factor and requires manual intervention. Secondly, the accuracy of the frequencies is very dependent on choosing the bar stiffness; too small and the results are inaccurate; too large and sever convergence difficulties occur. Finally, computation of the full dynamic motion of the tensegrity requires the second order corrections.

Acknowledgements

The author would like to thank Dr. Jim Steincamp for providing the opportunity to work on this problem. The author wishes to express his appreciation to Russel Parks for providing the data from the NASA tensegrity model. The author is in debt to Jaime Taylor for his earlier efforts on this project and for kindly sharing his results.

References

[1] Goldberg D., *Genetic Algorithms in Search, Optimization and Machine Learning,*Reading, MA, Addison Wesley Longman, Inc.; 1989.

[2] Ingber D. E., "The Architecture of Life," Scientific American: Feature Article, January 1998, pp 48-57.

[3] Kanchanasaratool N and Williamson D, "Modelling of class NSP tensegrity structures", 6th Int. Conf. Control, Auto. Robotics & Vision, Singapore, Dec 2000.

[4] Keane A. and Brown S., "The Design of a Satellite Boom with enhanced Vibration Performance using Genetic Algorithm Techniques," pp. 107-113 in Proceedings of the Conference on Adaptive Computing in Engineering Design and Control 1996, ed. I. C. Parmee, P.E.D.C., ISBN 0-905227 61 1, Plymouth.

[5] Murakami H. and Nishimura Y., "Initial Shape Finding and Modal Analysis of Cyclic Right-Cylindrical Tensegrity Modules," Computers and Structures, 79, 2001, pp. 891-917.

[6] Snelson,K, "Trigonal Tower", http://www.grunch.net/snelson/trigonal.html

[7] Taylor J., "Genetic Optimization of a Tensegrity Structure", NASA/ASEE Summer Faculty Fellowship Report, Marshall Space Flight Center, 2001.

[8] Skelton R, Pinaud J, and Mingori D, "Dynamics of the Shell Class of Tensegrity Structures," Journal of the Franklin Institute, 338, 2001, pp. 255-320.

[9] van Beek J, Hess S, Vollrath F, and Meier B, "The Molecular Structure of Spider Dragline Silk: Folding and Orientation of the Protein Backbone", PNAS , August 6, 2002 , vol. 99, no. 16, pp 10266-10271.

[10] Whitley D, "A genetic algorithm tutorial," Tech. Rep. CS-93-103, Department of Computer Science, Colorado State University, Fort Collins, CO 8052, March 1993. http://citeseer.nj.nec.com/article/whitley93genetic.html

[11] Williamson D and Skelton R, "A general class of tensegrity structures: topology and prestress equilibrium analysis", AIAA, Journal of Guidance, Control & Dynamics, (under review).

2003

NASA FACULTY FELLOWSHIP PROGRAM

MARSHALL SPACE FLIGHT CENTER
THE UNIVERSITY OF ALABAMA IN HUNTSVILLE

MSFC IN THE CONTEXT OF GRANULAR MATERIALS RESEARCH IN SUPPORT OF THE IN-SPACE FABRICATION AND REPAIR INITIATIVE

Prepared By:	Emir Macari
Academic Rank:	Professor
Institution and Department:	Louisiana State University Civil Engineering Department
NASA/MSFC Directorate:	Science
MSFC Colleague:	Dr. Ron Porter

Introduction

Studying the behavior of granular materials has been part of NASA's planetary and lunar missions since the early years of the agency. Common materials that occur in a granular form include sand, rocks, coal, powders, agricultural grains, and pharmaceuticals. Some of the most important space exploration missions have been based on findings of these studies. The Surveyor mission to the Moon, for example, had as a principal objective to understand the behavior of the granular lunar surface. Surveyor was equipped with instruments to measure the response of granular materials (regolith) to external loading. The soil mechanics investigations were performed by surface samplers and instrumentation, which were carried onboard *Surveyor 3* and *7.* The sampler proved to be an extremely versatile and useful piece of equipment to help assess the mechanical properties of the granular soils. The early Apollo missions also focused on the behavior of the regolith on the lunar surface. Neil Armstrong, after stepping on the surface of the Moon, focused his observations to the way the regolith behaved.

" The surface is fine and powdery. I can kick it up loosely with my toe. It does adhere in fine layers like powdered charcoal to the sole and insides of my boots. I only go in a small fraction of an inch -- maybe an eighth of an inch, but I can see the footprints of my boots and the treads in the fine sandy particles. "
Neil A. Armstrong, July 20, 1969

Soil mechanics and soil science have played an historical role in space exploration. From the initial tests, which facilitated the design of lunar and Mars landing craft, and the development of mobility vehicles, to the tests conducted to determine the mineralogy of lunar and Martian soils for understanding the origin of the moon and Mars, much has been learned on the properties of lunar soils and Martian soils.

The lunar soil has been found to contain resources that would be useful on the Moon and in space exploration (e.g. oxygen); as well as valuable for use on Earth (e.g. helium-3). The latter could be used in nuclear fusion reactors and would be a clean, economic source of energy. It has been estimated that there is enough helium-3 on the Moon to provide at least 1000 years of world energy consumption. In view of the concern for development of future energy sources, a recommendation might be to initiate mining on the Moon, which should ideally begin in the early part of this century.
Martian analog soils, known as JSC Mars-1 have been mined from a location in Hawaii. These soils have been studied to help in the design of the original and the current Mars Rovers (to land in Mars on January, 2004).

In the past decade, granular materials have become a very active area of research for physicists and engineers. The macroscopic phenomena that emerge from grain interactions in granular materials have not been successfully described by statistical mechanics, as is the case with bulk fluids and solids. The proper mathematical description of these materials is not only of intellectual interest, but also has potentially immense economic impacts.

In addition to the static or quasi-static behavior of granular materials, rapid flow of particulates has great practical interest in manufacturing industries, including pharmaceuticals, chemical, bulk processing, etc. in addition to the physics community, where it is frequently viewed as a complex fluid or system. One of the hallmarks of complexity is the ability of individual interacting agents to produce collective behavior, such as self-assembly or evolution. In view of the broad potential and numerous applications, the study of the behavior of granular materials has now also become a research initiative of the Department of Energy.

A granular material is a collection of discrete, solid particles dispersed in a vacuum or containing an interstitial pore fluid. These materials are ubiquitous or all around us - a few examples include food products such as rice, corn, and breakfast cereal flakes, building materials such as sand, unhydrated cement, gravel, and soil, and chemicals such as coal, plastics, and pharmaceuticals. A distinguishing feature between flows of granular materials and other solid-fluid mixtures is that in granular flows, the direct interaction of particles plays an important role in the flow mechanics. A significant fraction of the energy dissipation and momentum transfer in granular flows occurs when particles are in contact with each other or with a boundary.

Purpose

This white paper attempts to present a rational for the development of a strategic direction for Marshall Space Flight Center involving the study of the behavior of granular materials, without interfering with the mission of other NASA centers.
One important branch of MSFC's "In-Space Fabrication and Repair" initiative is In-Situ Resource Utilization. This area fits in very well in the historical mission of MSFC having a tradition of a strong Civil Engineering and Planetary Geology workforce. However, that is history as some of this workforce has retired or moved into other areas since manned planetary exploration has not been at the top of NASA's mission in the past few decades. The NASA 2003 Strategic Plan specifically calls for reaffirming NASA's mission to planetary exploration. It is within this context that this white paper is presented. This initiative also fits within the HEDS strategic plan.
The proposed program is in support of the In-Space Fabrication and Repair initiative but also addresses all three mission statements in the NASA 2003 Strategic Plan (namely, To understand and protect our home planet; To explore the universe and search for life; and To inspire the next generation of explorers.) It promotes collaboration with universities but also with industry, which has not traditionally worked on projects with NASA, such as Caterpillar Corp., John Deere Industries, and other earth moving equipment manufacturers, as well as construction companies such as Brown and Root, Bechtel Corporation, and others.

This initiative calls for a strong interaction between the Science and Engineering Directorates at Marshall Space Flight Center and to create an environment of collaboration that supports each other's missions.

Physicists alone cannot advance NASA's mission regarding these classes of materials. A successful plan will require extensive collaboration with engineers, who are trained to put to use fundamental principles, including findings of the physics community to support NASA's missions in the context of Human Exploration of Space and the colonization of Moon and Mars.

Planetary Geology and In-Situ Resource Utilization

Further research on granular materials may also lead to a greater understanding of geological processes where landslides, erosion, and on a larger scale, plate tectonics determine much of the form and structure of the Earth and other planets in our Solar System. This will help us understand how best to use the natural resources from other planets, when these are within reach and become available. In situ Resource Utilization is a NASA initiative devoted to the understanding and use of such resources. In situ resource utilization (ISRU) is one of five areas with the highest cost leverage for manned missions to Moon and Mars. Specifically, ISRU applied to the manufacture of the propellant for the return journey reduces earth-to-orbit mass, thereby increasing the cost-effectiveness of the mission. NASA plans to establish chemical manufacturing plants on the Moon and Mars prior to the arrival of the first astronauts.

Exploration of other planets will require the utilization of in situ resources. It is not cost-effective to try to carry all fuels, materials and other chemicals from Earth. Therefore, it is essential to develop capabilities to extract, mine and process materials to support future lunar landing missions and longer-term planetary missions. The Martian atmosphere, consisting mostly of carbon dioxide, can be processed to release oxygen for life support or propellant use. By combining this oxygen with small amounts of hydrogen, water could be obtained for only a fraction of its mass as compared to attempting to bring it from Earth. The carbon monoxide by-product of this process could also be used for rocket propellant or fuel.

Marshall Space Flight Center's researchers have been involved in ISRU for some time now and have developed the needed capabilities to help lead this effort on behalf of the entire agency. The table presented below shows some of the groups that are collaborating with MSFC in ISRU.

In-Situ Resource Utilization (NASA 2003 Taskbook)

P.I. Name	Project Title & Task Book Link	Institution
Kenneth Debelak	Recovery of Minerals in Martian Soils via Supercritical Fluid Extraction	Vanderbilt University
Edward Dreizin	High Temperature Phases and Phase Equilibria In Reactive Molten Metal-Based Systems	New Jersey Institute of Technology
Andrienne Friedli	Development of Anionic Polyelectrolytes for Solid State Battery Applications	Middle Tennessee University
Larry Mason	CO2 Acquisition Membrane (CAM)	Lockheed Martin Space Systems Co.

Eric Rice	Carbon-based Reduction of Lunar Regolith (CRLR)	Orbital Technologies
Donald Sadoway	From Oxygen Generation to Metal Production: In Situ Resource Utilization by Molten Oxide Electrolysis	Massachusetts Institute of Technology

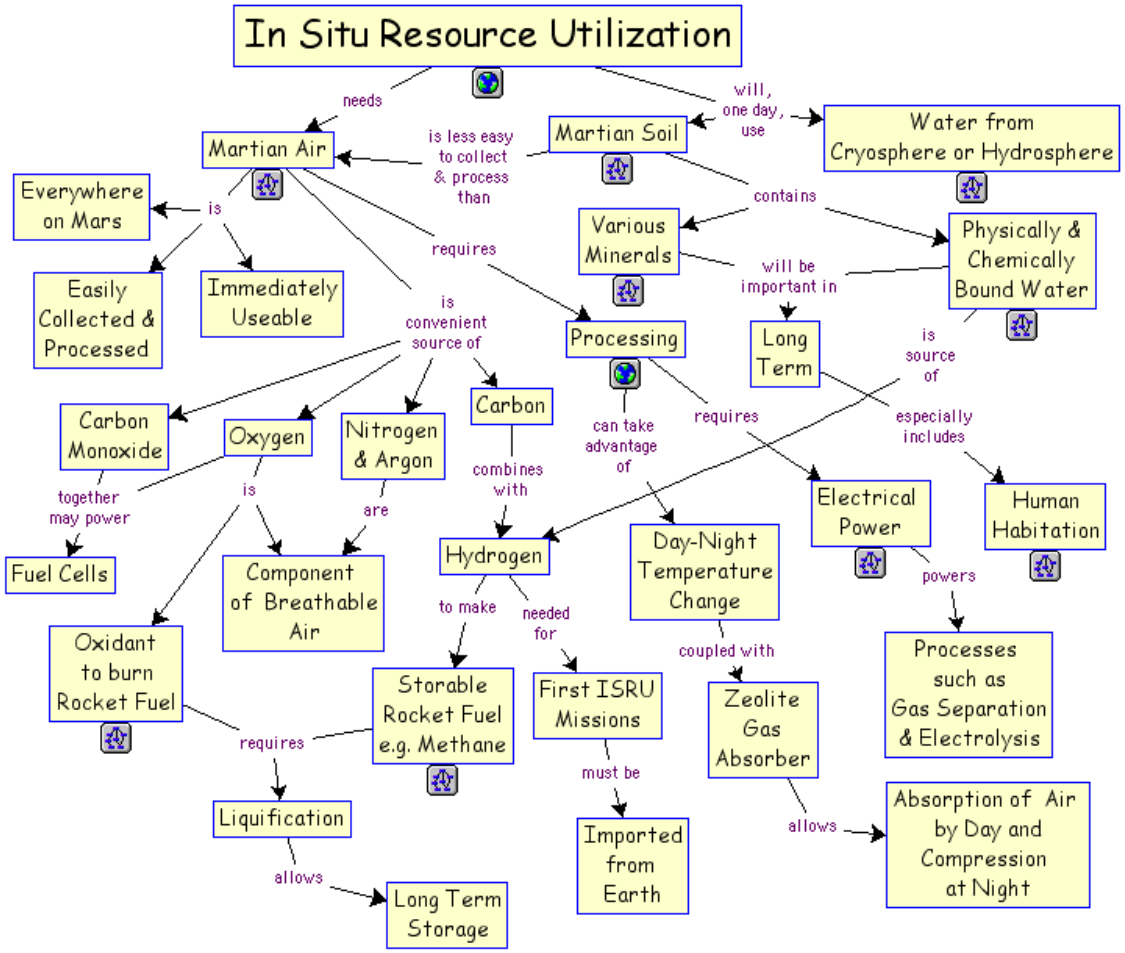

Figure 1: CMEX and Institute of Human and Machine Cognition (IHMC)

References

"Workshop on Research for Space Exploration: Physical Sciences and Process Technology," NASA/CP-1998-207431.

"NASA Ames Center for Mars Exploration (CMEX) and the Institute for Human and Machine Cognition (IHMC) at the University of West Florida" CD-ROM, Grant Number NCC 2-1036 from NASA Ames to IHMC.

“Workshop on In-Space Fabrication and Repair: MSFC” July, 2003.

Disclaimer:
This is a working document that will be formalized during the next six months. It attempts to advice MSFC leadership of areas where MSFC personnel involvement would be warranted.

2003

NASA FACULTY FELLOWSHIP PROGRAM

MARSHALL SPACE FLIGHT CENTER
UNIVERSITY OF ALABAMA IN HUNTSVILLE

REVERSE ENGINEERING WITH GEOMAGIC STUDIO 5 AND THE POLYGON EDITING TOOL SOFTWARE

Prepared By:	Angela Lawson-Macklin
Academic Rank:	Undergraduate Student
Institution and Department:	Alabama A&M University Civil Engineering
NASA/MSFC Directorate:	Engineering
MSFC Colleague:	Ken Cooper

Introduction

This summer has been a great experience. I have had the honor of working in the Advanced Manufacturing building in the Rapid Prototyping Lab with Ken Cooper. There, I studied two sets of software and worked with a 3-D digitizer scanner. The lab itself was interesting. There were several machines and several gadgets lying around. Each machine had a specific purpose. There wasn't nearly enough time to master the software that was given to me. But a better understanding of the purpose and features of the software were achieved.

My assignment was to get a handle on how the software worked and figure out the kinks so that I could then report it back to my department. My mentor Ken was very open with me on things that would make learning the software a little easier. The software was a little difficult to master considering the amount of time I had to spend with the software. I did several tests to understand the concept of the actually process of scanning an object to transform into and actual 3 D figure. The all-purpose of the rapid prototyping scanning was to help out the issues of space travel and making parts for the shuttle or needed parts that could be made virtually out of powders, like sugar and cornstarch!

Reversed Engineering

Originally the Japanese used reverse engineering to improve on competitors' products and, thus, avoid original design effort. Observing and testing a product initiated the redesign process. Thereafter, it was disassembled and the individual components were analyzed in terms of their form, function, assembly tolerances, and manufacturing process. The intent of this process step was to fully understand the execution of a product. Based on this understanding, an improved product was evolved, either at the subsystem (adaptive) or component (variant) level.

Now, Americans have reverse engineered the reversed engineering process and developed powerful tools to further compress development cycles. These tools are relevant for industries in those countries where production engineers are faced with the problem of reproducing parts directly from samples. Making spares for obsolete equipment, fabricating copies of old tooling, or redesigning a foreign-licensed product to come up with a new look are examples of how reverse engineering can be successfully employed. Powerful expert software is giving new meaning to reverse engineering. Computers can now be used to capture the geometry of a part, visualize it in 3D form, carry out design changes, test it for engineering performance, and simulate its manufacturing and inspection cycle. In effect, most of the reverse engineering process can be carried out without actually making a prototype.

Geomagic Studio 5 Software

The software that I have had the opportunity to work on was Geomagic Studio 5 and Minolta polygon Editing Tool. Studio 5 came with a training CD that went over some basic how to on the software. The Geomagic Studio is to automatically generate an accurate digital model from any physical part. Geomagic is also ideal for emerging applications such as mass productions of customized devices, build- to- order manufacturing, and automatic recreation of legacy parts. Geomagic Studio allows you to work with both physical objects and digital models, closing the loop between clay and software modeling. You can import surface layouts created by a CAD software expert as templates and apply them to points obtained from scanning the clay model created by an artist. Without the barrier between physical and digital, design changes take much less time and effort. (Figure 1: conversion of points to polygons using Geomagic Wrap.)

With Geomagic Studio, it comprises three integrated modules that provide a complete solution for reverse engineering and custom design. There were several different features in which all had a very important purpose**.** One feature was the Geomagic Capture. It is compatible with any 3-D scanner or digitizer. Capture works the way you work, with the tools you already use. Whether using white light, laser, or touch probe scanners, Capture will improve your workflow. It has Ultra-fast triangulation algorithm, which is if the surface is extremely large, ultra-dense data sets with unprecedented speed and ease. With Multi-threaded operations, you can tap in to the full power of your multi-processor system and get even more speed gains from key functions like Reduce Noise, Shade Points, and Register. You can register scans manually by selecting three points or a single point, then let Capture's AutoFit function fine-tune the alignment, or let Capture do all the work using Global Registration to fully automate the registration process.

The next feature was Geomagic Wrap. It automatically converts points to polygons. It has automated 3D model creation that creates watertight polygonal models and volume meshes from point cloud data, automatically, without approximation. Its 3D photography integration integrates with 3D scanning technologies, including those that capture color data, such as scanners from Minolta and Arius3D. The Curvature-based hole filling allows holes to be filled in both point and polygon models while maintaining surface

curvature, enabling removal of large blemishes and letting you create more precise scan data. The process of Extensive point processing actually edits large, sparse, or noisy point cloud data with ease. Uses intelligent data filtering to handle very large data and preserve sharp features. Geomagic also has an Automatic edge sharpening that automatically reconstructs sharp or creased edges lost during the scanning process. The last focus of the Geomagic Wrap is the Primitive identification and segmentation; it automatically detects, fits, and replaces planes and cylinders with rational representations. This allows you to concentrate on free-form shapes while preserving fit and function of the model. (And this is shown in Figure 2.)

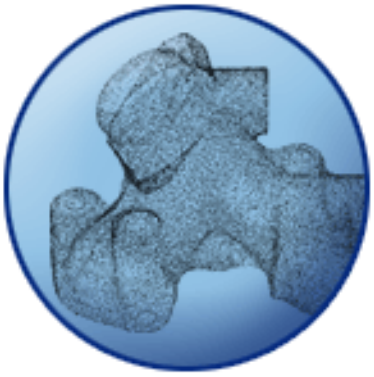

Geomagic Shape creates a network of watertight patches automatically over standard polygonal formats. Eliminates the need to create cross-sections or patches one by one. The Automatic detection feature detects feature lines on hard edges in one mouse-click. Allows you to edit, add, or delete feature lines .The True template-based work flow lets you reuse surface patch layouts by dragging and dropping templates from one model to the next. Then the Automatic edge sharpener follows that, in which automatically reconstructs sharp or creased edges lost during the scanning process. Accurately reproduces prismatic models for export to your CAD/CAM/CAE systems. The Geomagic Shape software's Automatic texture and displacement map generation for streaming 3D content**,** automatically generates texture, displacement, and bump maps for creating rich, streaming 3D content. It produces lightweight, infinitely detailed models.

Minolta Polygon Editing Tool

The second software, Minolta Polygon Editing Tool, was not as user friendly. The Minolta 3D digitizer accompanied this software. This is a 3D scanner with the simplicity of a point and shoot camera that scans over 300, 000 points in less that 4 seconds. With the software you can select specific points on a target object to be viewed, modified modeled, or scaled. And the scanner can also be used into conjunction with the Geomagic Studio 5 software.

Conclusion

The Project required the use of two software tools. The main software, Geomagic Studio was used the most due how user-friendly it was. The software finds success in capturing figures architecture with 3D laser scanning technology and geometry processing software that automatically generates an accurate digital model from the scan data. The Polygon-Editing Tool can also be essential, but given the lack of time that I had to spend with it, there was just not enough time for me to master the software. There are several conventions and training classes for Geomagic Studio software taking place in their home region of North Carolina. They give you a list of local hotels and give you hands on training with the software along with demos. I was really interested in going to a training session, but school will hinder me attending. I would like to thank My mentor, Ken Cooper, for making time to allow me to use the software and Amir Mobasher, faculty, for giving me the encouragement to seek more Mechanical Engineering education and to explore the field.

References

[1] "Geomagic Studio 5." Products. http: //www.geomagicstudio.com/products

[2] "Minolta 3D Digitizers". Software. http: //www.minoltausa.com/vivid

2003

NASA FACULTY FELLOWSHIP PROGRAM

MARSHALL SPACE FLIGHT CENTER
THE UNIVERSITY OF ALABAMA IN HUNTSVILLE

EXPERIMENTING WITH THE (FAST) FRC ACCELERATION SPACE THRUSTER EXPERIMENT

AN OVERVIEW OF MOMENTUM-EXCHANGE ELECTRODYNAMIC-REBOOST (MXER) TETHER TECHNOLOGY

Prepared By:	Lionel Macklin
Academic Rank:	Undergraduate Student
Institution and Department:	Alabama A&M University Electrical Engineering
NASA/MSFC Directorate:	Transportation
MSFC Colleague:	Jeff Richardson

2003

NASA FACULTY FELLOWSHIP PROGRAM

MARSHALL SPACE FLIGHT CENTER
THE UNIVERSITY OF ALABAMA IN HUNTSVILLE

THE TESTING DESIGNS AND DATA ANALYSIS OF NEW COMPOSITE MATERIAL FOR RADIATION SHIELDING AND STRUCTURAL CARRYING LOADS

Prepared By:	John W. Martin III
Academic Rank:	College Senior
Institution and Department:	Alabama A & M University's Department of Mechanical Engineering
NASA/MSFC Directorate:	Science Directorate
MSFC Colleague:	Dr. Nasser Barghouty

Introduction

Recently, composite materials have gained tremendous attention. This has been attributed to it's high strength to weight ratio. Moreover, their properties could be tailored to meet specific applications. This makes composite materials very attractive for the space applications.

This research project is to design the needed experiments for determining the physical and the mechanical properties of a new composite material that has dual application:

a) radiation shield
b) structural carrying loads.

The ASTM standard test databases have been used in determining the required composite specimens (geometry, ply count, fiber orientation, and number of specimens for each test). After finishing the proposed tests, a statistical data analysis will be used to determine the mechanical properties of the new composite material. The experimental and theoretical results would be compared to develop the basic knowledge of the new material.

Pictures of the New Material

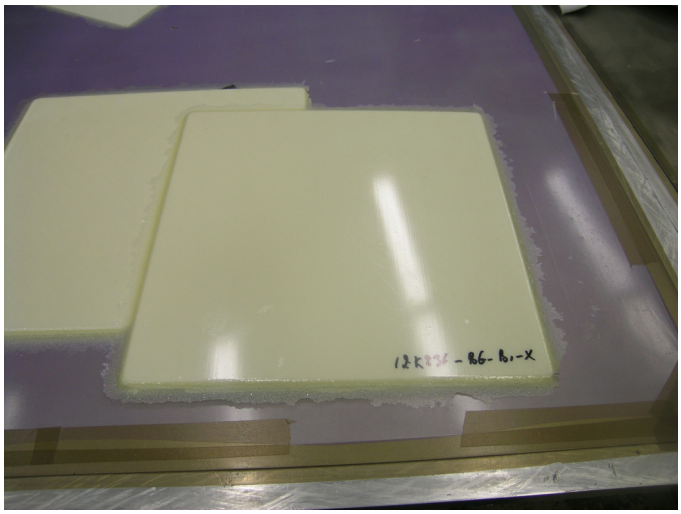

Figure 1: Picture of the manufactured composite material.

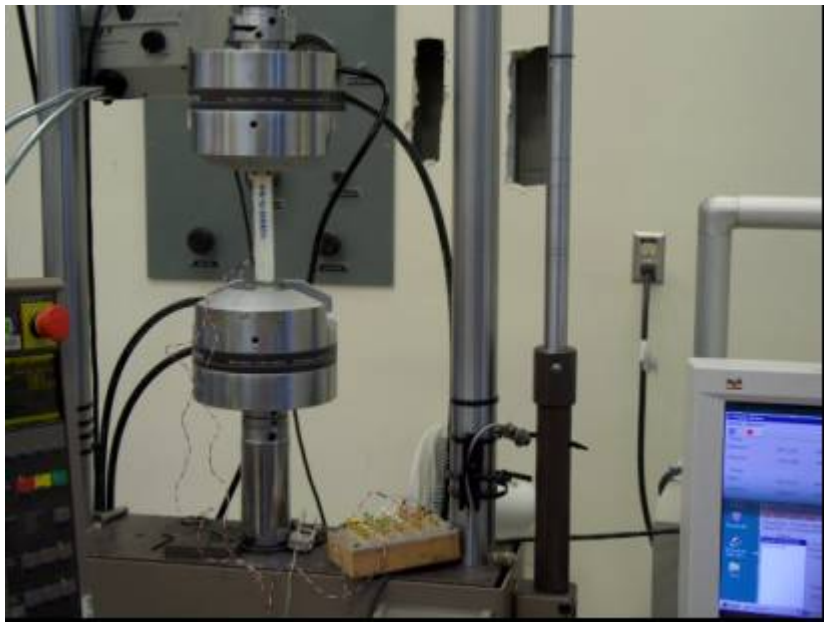

Figure 2: The picture above is a new composite specimen during a tensile test.

Results of the Standard test methods

Table 1: Summary of the standard test methods

ASTM Standard	Fiber Orientation	Ply count	Specimen Geometry (Recommendations)	No. of Specimens
D 3039 Tensile Properties (σ_{ut}, ε_{ut}, E_1, ν_{12}, ν_{21}, σ_y, ε_y)	0 unidirectional	8	Width: 0.5 in Overall length: 10.0 in Tab Length: 2.25 in Tab Thickness: 0.062 in Tab Bevel Angle: 7 or 90	3x7x3
	90 unidirectional	16	Width: 1.0 in Overall length: 7.0 in Tab Length: 1.0 in Tab Thickness: 0.062 in Tab Bevel Angle: 90	3x7x3
D 3410 Compressive Properties	0 unidirectional	8	Width: 0.5 in Overall length: 5.5-6.0 in Gage Length: 0.5-1.0 in Tab Length: 2.5 in Tab Thickness: 0.062 in	3x7x3

(σ_{uc}, ε_{uc}, E_1, ν_{12}, ν_{21}, σ_{yc}, ε_{yc})	90 unidirectional	16	Width: 1.0 in Overall length: 5.5-6.0 in Gage Length: 0.5-1.0 in Tab Length: 2.5 in Tab Thickness: 0.062 in	3x7x3
D 3518 In-plane Shear properties (τ, γ, G)	± 45° Laminate	16	Width: 1.0 in Overall length: 7.0 in Tab Length: 1.0 in Tab Thickness: 0.062 in Tab Bevel Angle: 90	6x7x3
D 3846 Interlaminar Shear (τ, γ, G)	0 unidirectional	42	Width: 0.5 in Overall length: 3.13 in Notch Width: 0.040-0.065 in Notch Depth: Half specimen thickness Notch from the edge: 1.43 in Distance bet. Notches: 0.25 in	6x7x3
D 5961 Bearing Response (σ_{bu}, ε_{bu}, E_b)	$[0,\pm45, 90]_{4S}$	32	Pin diameter, d: 0.25 +0.000/-0.001 in Hole diameter, D: 0.25 +0.001/-0.000 in Thickness range, h: 0.125-0.208 in Length, L: 5.5 in Width, w: 1.5 ±0.03 in Edge distance, e: 0.75± 0.03 in	7x3
D 5766 Open Hole Tensile Strength (σ_{hut})	$[0,\pm45, 90]_{2S}$	32	Width: 1.5 ±0.05 in Length range: 8.0-12.0 in Hole diam.: 0.25 ±0.003 in ***Note:*** while tabs may be used, they are not required and generally not needed.	7x3
D 6484 Open Hole Compressive Strength (σ_{huc})	$[0,\pm45, 90]_{2S}$	32	Width: 1.5 ±0.01 in Length: 12.0±0.01 in Hole diam.: 0.25 ±0.003 in ***Note:*** while tabs may be used, they are not required and generally not needed.	7x3
D 2990 Flexural Creep (δ)	$[0,\pm45, 90]_{4S}$ or $[0,\pm45, 90]_{8S}$	32 or 64	Preferred specimens sizes are: 2.5x0.5x0.125 in or 5.0x0.5x0.250 in ***Note:*** Close tolerances are not critical as long as actual dimensions are used.	2x7x3

E 1545 Thermo-mechanical Analysis (Tg, α)	0 unidirectional	24	Length, width, Height ≈ 0.125 in - Glass Transition Temperature, Tg - Coefficient of Thermal Expansion, α	7x3

Discussion

The summary of the standard test methods chart above gives different ASTM standard test methods, geometry, ply count, fiber orientation, and number of specimens for each test.

Future work with the New Composite Material

The next logical step should be to finish doing the different mechanical test with the appropriate testing. Doing ballistic Impact tests would be good also for future work.

Conclusion

A basic knowledge about this new composite material will be more complete after mechanical testing the specimens. A statistical data analysis can be used to determine the mechanical properties of the new composite material from the proposed test results. The experimental and theoretical results would be compared to develop the basic radiation shielding as well as mechanical properties of the new material.

Acknowledgements

The author would like to thank the Education Program at NASA – NASA Accompany Student Program (Dr. Jeanelle Bland, Dr. Shelia Nash-stevenson, Dr. Razi Hassan, and Dr. Gerald Karr) - for giving him the opportunity to work with this rising technology. Special thanks to Dr. Mohamed Seif of Alabama A & M University's Mechanical Engineering Department, Dr. Nasser Barghouty of the science directorate, and Dr. Raj Kaul of the engineering directorate for their guidance and support during the period of this program.

Reference

[1] (2003), ASTM International: http://standards.nasa.gov/.
[2] Abrate, S., Impact on Composite Structures, Cambridge University Press, 1998.
[3] Anderson, V.L. and McLean, R. A., Design of Experiments: A Realistic Approach, Marcel Dekker, 1974.
[4] Department of Defense Handbook, MIL-HDBK-17-1E, Polymer Matrix Composites, Volume 1-3, 23 January 1997.

2003

NASA FACULTY FELLOWSHIP PROGRAM

MARSHALL SPACE FLIGHT CENTER
THE UNIVERSITY OF ALABAMA IN HUNTSVILLE

GROUND-LEVEL OZONE AIR QUALITY ISSUES AND PUBLIC POLICY CHALLENGES

Prepared by:	Dr. William K. McAllister
Academic Rank:	Associate Professor
Institution and Department:	Alabama A & M University Department of Community Planning and Urban Studies
NASA/MSFC Directorate:	Earth Science SD-60
MSFC Colleague:	Dr. Dale Quattrochi

Introduction

Ground-level ozone, a toxin to humans in large doses, has been resistant to government efforts to mitigate it in many metropolitan areas. Ozone results from the chemical mixing of nitrogen oxides (NOx) and volatile organic compounds (VOCs) in the presence of sunlight and hot summer days. This gas is also difficult for humans to sense due to its mostly clear and odorless qualities, thus there is very little public outcry for its reduction to safe levels. Personal and commercial vehicle exhaust contributes much to the ozone problem and tail pipe emission inspections can present controversial issues relating to equity and repair costs. Additional factors such as coal-fired power plant emissions located upwind, stagnant high pressure weather systems, low wind speeds and air inversions add to its concentration in different ways in particular metropolitan areas. These toxic concentrations also persist late into the summer nighttime hours where massive amounts of urban materials typical of downtown areas collectively hold heat and disrupt natural climatic cycles – a process known as the heat island effect. The Los Angeles, Houston and Atlanta metropolitan areas, for example, are having a particularly difficult time controlling the ozone problem given their latitudinal positions that deliver high levels of both warmth and sunlight, and their history of successful economic growth that has produced large concentrations of slow moving vehicles, heat absorbing materials, and the need to produce new energy. Each metropolitan area's air quality ultimately results from a unique mix of land uses and other spatially inter-connected factors that present a complex set of public policy challenges for planners, policy analysts, public managers, and local elected officials.

Health Aspects of Ozone as a Basis for a National Standard

Epidemiological studies show significant associations between daily ambient concentrations of ozone and a wide range of adverse health outcomes, and past time-series studies may have underpredicted the premature mortality effects of ozone. [1] Low-level ozone (in contrast to Stratospheric ozone at a high level that protects living things and property from harmful effects of the sun's ultraviolet light) in concentrations above a certain threshold is toxic to humans and destructive to crops. Ozone concentrations react chemically with internal body tissues, such as those in the lung. Children are particularly susceptible, especially when exercising outdoors in the summer.

Based on widespread research, evaluated by an appointed science advisory panel, the U. S. Environmental Protection Agency (EPA) established a revised ozone standard of 0.08 parts per million averaged over an 8-hour day and measured by ozone monitors sparsely scattered throughout metropolitan areas. Compliance within any given area is based on the fourth highest reading per year averaged over three years. This 1997 regulation was challenged by the trucking industry. In 2002 all challenges, both procedural and substantive, were set aside by the U. S. Supreme Court in an unanimous decision. New listings of nonattainment areas under the more strict standard will be published by EPA in early 2004. Over 230 counties, including many to be newly designated, will be expected to put in place measures that will improve health outcomes.

The setting of a particular standard was not without professional arguments among the members of EPA's own scientific advisory committee. In the end, EPA made a policy choice to protect

children as a group and others more susceptible to the effects of ozone at the lowest level where sufficient studies report harmful effects. [2]

The Urban Planning Challenges of Some Air Pollution Solutions

Urban planners work for the public interest in an advisory capacity. Their role requires them to involve and educate the public on carefully considered options designed to solve problems that are sometime not obvious. Planners must present convincing arguments to elected officials who make final policy. Ozone and another pollutant, carbon monoxide, are invisible and without smell, yet they are very toxic in certain doses and must be mitigated from present levels in many areas. How do planners and other land use professionals educate the general public about a problem that is invisible? Generally speaking, needed changes with direct costs are viewed as unwarranted unless the problem is clear and has a personal effect, e.g. my vehicle's exhaust is contributing to my child's asthma.

Another challenge for comprehensive planning is to attract residents, visitors and workers back to the central city and out of the suburbs at the same time that research is increasingly clear about the air quality problem in all metropolitan areas, especially in the historical downtowns. Whatever the tailpipes of vehicles and the smoke stacks of industries contribute to the problem throughout the year, in the heat of summer the urban heat island effect exacerbates the condition, especially for ozone production. [3] There are many strategies to consider to solve the multifaceted air quality problems of our larger and medium sized areas. One of these is the encouragement of planned urban villages with mixed uses, diverse housing, and modern energy conserving construction. The reduction of vehicle miles traveled (VMT) and roadway congestion, and the addition of cleaner burning and more fuel-efficient vehicles promise hope, but public choices recently have not always been in those directions.

Roadway Congestion and Ozone

Some would say that roadway congestion is a failure of proper planning. But land use plans and regulations only speak in general terms about what groups of uses, not specific uses, are best suited for a certain location. Rarely do plans and regulations do a good job controlling the timing of land development. Thus, many urban governments find that they must build roads and other urban facilities after development has exceeded current infrastructure capacities.

Table 1 and Table 2 show that short-term congestion is about the same or worse than in the longer-term in some cities known to have air quality problems. Houston's congestion index

Urban Area	Congestion Index *	Short-term: 1994-2000. Rank out of 75 Based on Change for Time Period *	Long-term: 1982-2000. Rank out of 75 Based on Change for Time Period
Los Angeles	1.59 (highest)	31	35
Houston	1.09	31	4
Atlanta	1.32	67	73

* Texas Transportation Institute. *2002 Urban Mobility Study*

Table 1: Trends in roadway congestion for selected metropolitan areas

shows a big change for the worse. Its air quality is also deteriorating. At the same time, the Los Angeles area and the remaining southern California air shed are gradually improving air quality.

Urbanized Areas	Population per Square Mile*	Daily Vehicle Miles per Capita*	Vehicle Miles per Square Mile*	Ozone 1-hour Maximum Averaged over 3 years** (U. S. Standard is 0.12 ppm)
Los Angeles	5380	23.1	124,170 (2nd)	0.17 ppm
Houston	1537	37.1	58,100	0.19 ppm
Atlanta	1629	34.2	55,719	0.16 ppm

* Texas Transportation Institute. ** EPA National Air Quality Emissions Report

Table 2.: Ozone emission compared to roadway use and population density

What Can Urban Researchers Do to Help Practitioners?

The Best Available Science should drive environmental policy and practices. Since scientific conditions, especially concerning air quality, vary from day to day, and even hourly (ozone), professionals working at the regional and local levels often do not know which set of strategies are appropriate to use. Further, the expert's understanding of air quality is evolving, leaving the busy urban officials confused and perplexed about highly technical problems.

Best Practices Manuals need to be agreed on by the scientific community and published. These manuals serve as a menu from which appropriate practices can be selected and refined locally.

What Can Planners Do to Help the Urban Air Quality?

Planners can continue to study the literature and educate the public about certain connections between land use patterns and air quality. For example, nationally in 1999 over 55% of nitrogen oxides (NOx), a major ingredient of ozone, came from transportation sources. Industrial sources contributed almost 40% to NOx. Between 1990 and 1999 NOx emissions increased 5%. [4] Geographic Information Systems (GIS) can help officials and the public see mapped relationships among such factors as the location of coal-fired power plant plumes, urban heat islands, the direction and strength of prevailing winds (wind roses for metropolitan areas are found on the Internet), and other spatial information. Monitor readings for ozone and other criteria pollutants allow officials to tailor Best Management Practices to local conditions.

Planners can also build a strong case for regional planning and implementation where environmental problems involve many local jurisdictions. The State of Georgia established the Georgia Regional Transportation Authority (GRTA) in the late 1990s to attach the increasing air quality problem, much of which is traceable to transportation sources. GRTA is an organizational model worth watching for ideas to use in other metropolitan areas.

Finally, planners can make a strong case for energy conservation through more efficient and effective land use planning and structural construction standards. Planned mixed uses reduce VMTs by positioning common trips for convenience shopping and entertainment close to living areas. In a small way, the juxtaposition of complimentary uses reduces ozone by reducing traffic. Using similar logic, energy conserving home construction and the use of cooling techniques in site plans not only save on utility costs for landowners, but these techniques also help reduce NOx and other air pollution emissions from nearby coal fired power plants. Reducing NOx also reduces ozone, a common problem in large metropolitan area downtowns. Due to the upper air transport of ozone, sometimes from several states away, ozone concentrations can build to higher levels than local land uses and transportation generate in peak summer periods. Local elected officials and planners and other urban environmental practitioners have a big set of challenges. Air quality can be a major factor in daily quality-of-life decisions of residents. Air quality is increasingly a factor in deciding where industry locates and can affect the cost of doing business in different ways in different metropolitan areas.

References

[1] Thurston, G. & Ito, K.. (2001). Epidemiological studies of acute ozone exposures and mortality. *Exposure Analysis and Environmental Epidemiology Journal*. July-Aug. 11(4) retrieved 08-07-03 from
www.ncbi.nlm.nih.gov/entrez/ query.fcgi?cmd=Retrieve&db=PubMed&list_uids=11571608&dopt=Abstract

[2] Anderson, A. Revising the air quality standards. An RFF briefing paper. Retrieved 08-06-03 from http://www.rff.org/issue briefs.pdf files/NAAQS primer.htm

[3] Estes, M., Quattrochi, D., and Stasiak, E. (2003) The urban heat island phenomenon: How its effects can influence environmental decision making in your community. *Public Management*. 85/3 pp 8-12.

[4] American Lung Association (2002) *Trends in Air Quality*. Retrieved 08-07-03 from
http://www.lungusa.org/data/aqp/AQI.pdf

2003

NASA FACULTY FELLOWSHIP PROGRAM

MARSHALL SPACE FLIGHT CENTER
THE UNIVERSITY OF ALABAMA IN HUNTSVILLE

AN OVERVIEW OF MOMENTUM-EXCHANGE ELECTRODYNAMIC-REBOOST (MXER) TETHER TECHNOLOGY

REPORT NOT AVAILABLE

Prepared By:	William Miller
Academic Rank:	Undergraduate Student
Institution and Department:	Alabama A&M University Civil Engineering
NASA/MSFC Directorate:	Transportation
MSFC Colleague:	Kirk Sorensen

2003

NASA FACULTY FELLOWSHIP PROGRAM

MARSHALL SPACE FLIGHT CENTER
THE UNIVERSITY OF ALABAMA IN HUNTSVILLE

REFINEMENT OF A PLATFORM TO COMPUTE FOURIER TRANSFORMS

Prepared By:	Terrence A. Mizell
Academic Rank:	Professor
Institution and Department:	Alabama A&M University Department of Computer Science
NASA/MSFC Directorate:	Flight Projects
MSFC Colleague:	Dr. Jonathan Campbell

Introduction

A brief discussion of Fourier Transforms is in order, though space limitations do not allow a complete discussion of calculation strategies used in this report. Fourier Transforms have been widely used in solving problems in science and engineering since the early 30's. Recently, with the advent of computers, their applications have been widely expanded to include signal processing, process modeling, probability theory, pattern analysis and so on. Data patterns can be readily ascertained, giving a more thorough understanding of a problem solution. The transform decomposes a function into different frequencies allowing identification or distinction of hidden patterns by analyzing their respective amplitudes. Briefly, the Fourier transform of $f(x)$ is defined as

$$F(s) = \quad f(x) \exp(-i\, 2xs)\, dx. \qquad [1]$$

Applying the same transform to $F(s)$ gives

$$f(w) = \quad F(s) \exp(-i\, 2ws)\, ds. \qquad [2]$$

If $f(x)$ is an even function of x, that is $f(x) = f(-x)$, then $f(w) = f(x)$. If $f(x)$ is an odd function of x, that is $f(x) = -f(-x)$, then $f(w) = f(-x)$. When $f(x)$ is neither even nor odd, it can often be split into even or odd parts. To avoid confusion, it is customary to write the Fourier transform and its inverse so that they exhibit reversibility:

$$F(s) = f(x) \exp(-i\, 2xs)\, dx \quad \text{and} \quad f(x) = F(s) \exp(i\, 2xs)\, ds \quad \text{so that} \qquad [3]$$
$$f(x) = f(x) \exp(-i\, 2xs)\, dx \exp(i2xs)\, ds \qquad [4]$$

With a modern graphics interface, the patterns can be displayed visually, which gives an instantaneous interpretation of the data. In the past, literally thousands of Fourier Transform "Commercial Off-the-Shelf" (COTS) software systems have been developed using virtually every coding tool. They address a multitude of scientific and engineering problems, especially if there is repetition in the data. Some of the better models, mathematically speaking, were developed in FORTRAN, most of which were mainframe based. However, while modern desktop computers can outperform the older mainframes, FORTRAN compilers for these computers are expensive, inefficient and clumsy. Therefore, most of the FORTRAN systems have become obsolete – not because their computations are erroneous but based on the limitations of P.C. hosted FORTRAN. Other Fourier models in "C" and "C++" abound, but they have limited utility also. Efficient and inexpensive C++ environments are available for desktops, but the C++ language depends on imported externals via the "include" feature. Each C++ environment has standard imported externals, but the language also supports 'user defined' externals, the absence of which incapacitates the model. Thus, if the 'user defined' external is not available, that software is less than useful

Why Another Fourier Transform Model

Given the difficulty of working with most COTS software, especially that developed with C++, a more user-effective solution was in order. It should be remembered at this juncture that most engineers and scientists refrain from delving into the internals of coded systems, working out the 'kinks' and fitting some data to a model for which the model

was not intended. The solution was simple and straight-forward – almost every P.C. hosts Excel, a spreadsheet supplied with Microsoft office tool suite. It was felt that if a data set could be entered into an Excel spreadsheet, then a simple Visual Basic model could analyze the data and give a graphics or visual representation. While Visual Basic executes much slower than C++, the disadvantage is recovered many times over in human time – the spreadsheets can be rapidly populated and analyzed by the interested parties, without having to spend an inordinate amount of time 'tweaking' a COTS program nor would they be required to develop a custom model, which is very time consuming. Cost is recovered in minimizing the time needed to run the system.

The Model Tableau

The first step in the analytical process is to enter data into an Excel spread sheet. This is a simple procedure, but care must be given to identification of the "X" and "Y" axes and the data to be charted. Once data are entered, the "Interface" is run, giving a path into the model. The Interface will display a menu tableau, Figure 1 that allows selection of a number of Fourier Transforms. The variety includes various matrix sizes, functions, and a facility to enter data from inside the model, if the user doesn't desire to import the data.

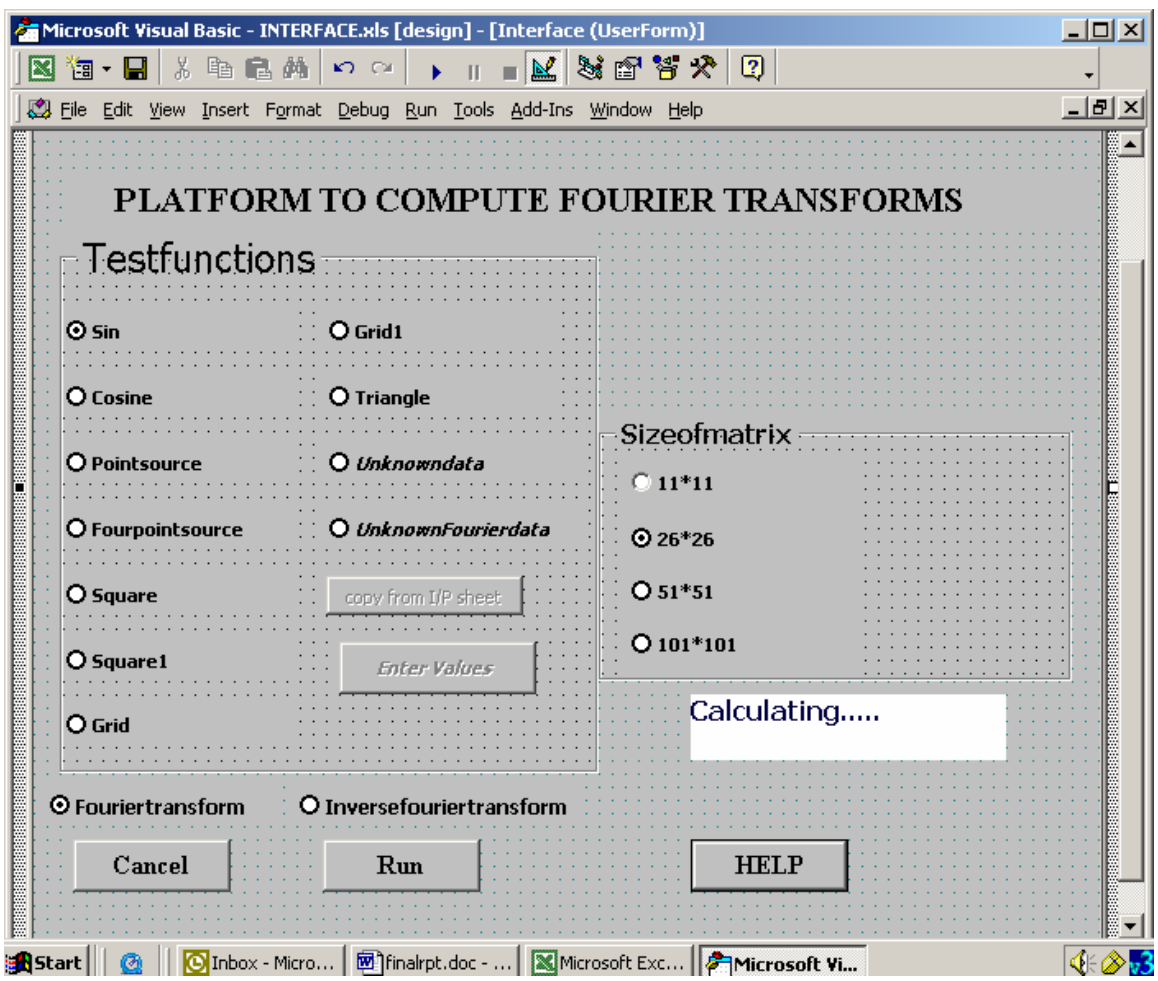

Figure 1: The Fourier Interface Tableau

Once the data have been analyzed, the Excel software can produce a graphical output, similar to the ones in Figures 2 and 3, below. The data can be viewed at any desired angle and rotation about the "z" axis. As noted above, an important point about Fourier Transforms is that the processes are designed to 'summarize' data, and graphics is one convenient way of doing so. As the Interface indicates, matrices can run from ten by ten to a hundred by hundred. The data in Figure 2 shows the 50 x 50 resolution of some known "uv" data. The graphics output is effective in showing data patterns. In Figure 2, the perspective is rotated 15 degrees for more effective view of the data.

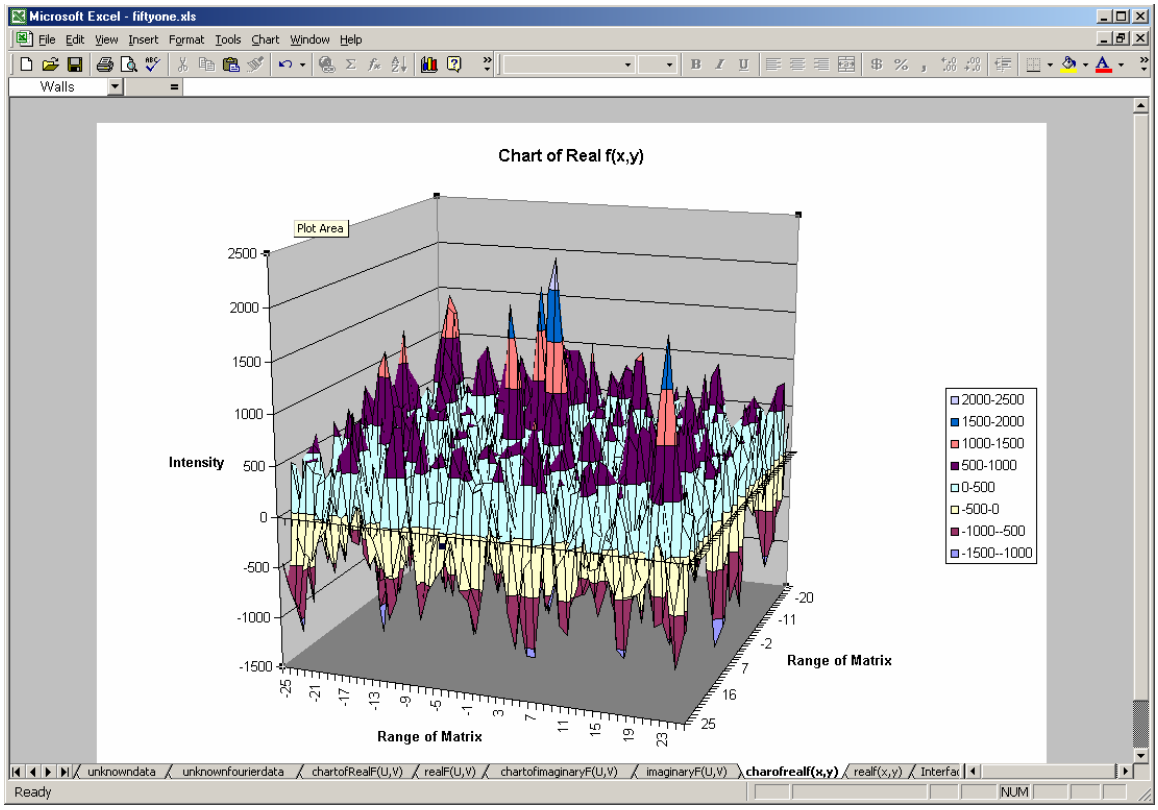

Figure 2: Inverse Fourier 50x50 Matrix Using Real f(u,v) Data

An additional feature of the model is a facility to enter data from the Tableau. In the event that the user does not desire to enter data from an external Excel table, the user can enter data into the matrix by pressing the unknown data button on the Tableau. That procedure will transfer the user to a blank table that can be populated and then accessed from inside the platform.

Other features include the facility to select not only the size of the matrix, but also the test function and the viewing angles. These represent a significant advance in the ability to analyze numerical information that lends itself to Fourier Transforms. For instance, Figure 3, below, shows a 100x100 matrix viewed from the top. The data pattern is clearly visible, which is consistent with earlier work by Campbell [1] with the data set.

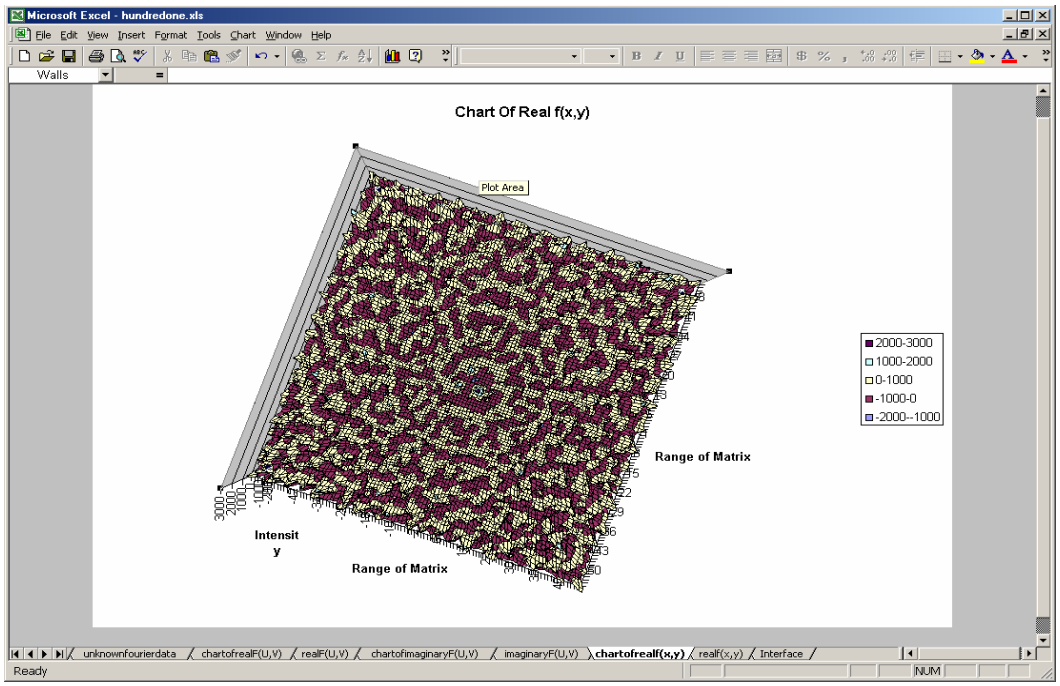

Figure 3: Top View of 100x100 Matrix Displaying Real f(u,v) Data

Conclusions

This platform represents a first release of the system. At this writing, performance is something of an issue. The results can be analyzed in a few minutes if the size of the matrix is small, in this case less than 50x50. But, if a larger matrix is exercised, as in Figure 3, above, the number of iterations becomes so great that a typical run will require several hours on a machine with at least a 2.5 GHz processor. In addition, the system does not run in background, so that any other use of the computer becomes virtually impossible while the system is running. The running process consumes 100% of the processor resources, rendering use of the computer impossible while calculations are in operation. Therefore, the prototype code used in Version 1 of the model should be examined to identify points where the code can execute faster.

Acknowledgements

The author would like to thank NASA for the opportunity to work in the Advanced Concepts Directorate, and to Dr. Jonathan Campbell who developed the idea for this model. It is based on some of his earlier work at NASA.

References

[1] Campbell, J. Imaging the Sun in Hard X-rays Using Fourier Telescopes." MSFC, NASA Technical Memorandum, NASA TM-108390

2003

NASA FACULTY FELLOWSHIP PROGRAM

MARSHALL SPACE FLIGHT CENTER
THE UNIVERSITY OF ALABAMA IN HUNTSVILLE

A NOVEL APPROACH TO FABRICATING SAMPLE CONTAINMENT ASSEMBLIES FOR MICROGRAVITY MATERIALS PROCESSING

Prepared By:	Amir A. Mobasher
Academic Rank:	Assistant Professor
Institution and Department:	Alabama A&M University Mechanical Engineering Department
NASA/MSFC Directorate:	Engineering
MSFC Colleague:	Mr. Keneth G. Cooper

Background

Over the course of the next decade, NASA has planned the time-phased deployment of the Materials Science Research Facility (MSRF), a multi-rack facility for the International Space Station (ISS). The MSRF is designed to accommodate NASA's current and evolving cadre of peer-reviewed science investigations. The facility will provide the apparatus for satisfying near-term and long-range Materials Science Discipline goals and objectives to be accomplished in the microgravity environment of the U.S. Laboratory on the ISS. Each rack will consist of multiple experiments, dedicated to various aspects of materials processing. In some cases, a rack may support a single furnace system with modular, replaceable furnace modules. To date, no requirements for geometrical commonality have been imposed on these furnace systems. Therefore, each of these configurations will require the development of unique Sample Containment Assemblies (SCA).

A SCA is used to contain and support sample ampoule/crucibles during the crystal growth or solidification process. These ampoule/crucibles are typically hermetically sealed tubes made of quartz, alumina, boron nitride, or other similar materials. Because these materials are subject to breakage and other high temperature failure, reliable safe containment of the experimental science sample materials is not assured by the use of ampoule/crucibles made of these materials. Typical crystal growth/solidification science materials include GaAs, HgCdTe, CdZnTe, PbSnTe, Pb-based alloys, Si, etc. Many of these materials have high vapor pressures of known toxic materials (As vapor in GaAs, for example) and many are known to be carcinogenic. Because the MSRF racks will be installed in the manned environment of the ISS, assurance of safe containment of these hazardous chemicals is required by ISS flight rules. To meet this requirement, the ampoule/crucibles are typically sealed into a uniquely designed metal cartridge to preclude crew exposure to sample materials.

The use of a metal cartridge, and in some cases even the ampoule/crucible, is unique to the microgravity environment. In terrestrial crystal growth practices, the use of toxic gas monitors, chemical exhaust cabinets, and equipment isolation is more routinely used to protect personnel. Therefore, while the development of microgravity-based furnaces requires modifications of well-established terrestrial technologies, the SCA fabrication problem is a relatively new technical requirement imposed by the safety concerns and flight rules for microgravity experimentation. Three principal requirements for acceptable SCA performance have thus been identified:

1) The ability of the SCA to contain the pressure associated with the sudden rupture of an ampoule/crucible during performance of a crystal growth/solidification experiment. Implicit in this requirement is also the requirement to contain the pressures associated with processing a SCA containing an undetected fractured ampoule/crucible.
2) Assessment of the probability of ampoule/crucible failure or fracture through an approved ampoule/crucible qualification and test plan.
3) Determination that the selected SCA cartridge material would exhibit sufficient chemical passivity in the event of its high temperature exposure of the sample chemicals such that it will maintain absolute containment, and not permit chemical breach of the safety level of containment required of a qualified SCA.

Laser Engineered Net Shaping (LENS) is a unique manufacturing process recently developed at Sandia National Laboratories. The process uses additive fabrication techniques to deposit steel powders and thus form a fully dense three-dimensional object directly from computer-generated drawings; therefore no tooling or fixturing is required. MSFC has one of only ten of these LENS systems available in the world, thus providing a unique advantage in accomplishing the goals of this proposal. The objective of this project will be to successfully demonstrate that hermetic (non-porous) Sample Containment Assemblies can be fabricated using Laser Engineered Net Shaping at the MSFC at a substantial time or cost savings over the currently employed techniques of Chemical Vapor Deposition (CVD) and Vacuum Plasma Spray (VPS).

Methodology

Initial trials were conducted on the LENS machine at MSFC using materials already known to the process, primarily stainless steel 316 (SS316), and then progressing through the materials needed for the final flight hardware: Inconel and Tungsten. Sample Containment Assemblies were laser deposited of a standard geometry: 1/2-inch diameter cylinder with 0.030-inch wall thickness. The length of the tubes required for porosity testing were determined and established during the experiment. (It should be noted that the current system setup at MSFC will allow for the fabrication of a maximum 10-inch length, whereas the end-use cartridges for the International Space Station will need to be 24-inches long. Successful demonstration of shorter samples, however, will warrant further seed funding from the project offices to adapt for a larger size capability). The deposition of such thin-walled structures introduced a new set of challenges; therefore a process to determine deposition parameters for even known materials was established. Once a set of SS316 sample tubes were successfully deposited, then they were tested by Morgan Research to determine if the strength and porosity meet the requirements for SCAs.

Results

The current cost for fabricating SCAs range typically from $1000-$1500 for an extruded Inconel cartridge with a welded end cap. For a Chemical Vapor Deposited (CVD) tungsten cartridge the cost increases to $5000-6000 each. For a Vacuum Plasma Sprayed (VPS) tungsten cartridge the cost is only $500-1000, but it is difficult to obtain samples that are hermetic. Also, VPS is very fast compared to CVD (1 day vs 5 days). It took only 1 hour to build a 6 inch sample on a LENS machine for a total height of 6 inches. Therefore for the processing time of Inconel it is anticipated to build the samples on the LENS machine within 4 hours. Some additional time is allocated for finishing and testing of the samples. Table 1 depicts the final parameters selected for the processing of the Stainless Steel and Inconel samples.

Table 1. Final parameters that was established for building of the SCA samples.

Material	Laser Amperage (AMP)	Laser Power (Watts)	Oxygen Level (ppm)	Feed Rate (ipm)	Feeder Speed (rpm)	Mass Flow (lpm)	Layer thickness (in)
SS316	42	265	60	15	9	5	0.01
In 718	45	290	55	40	6	5	0.01

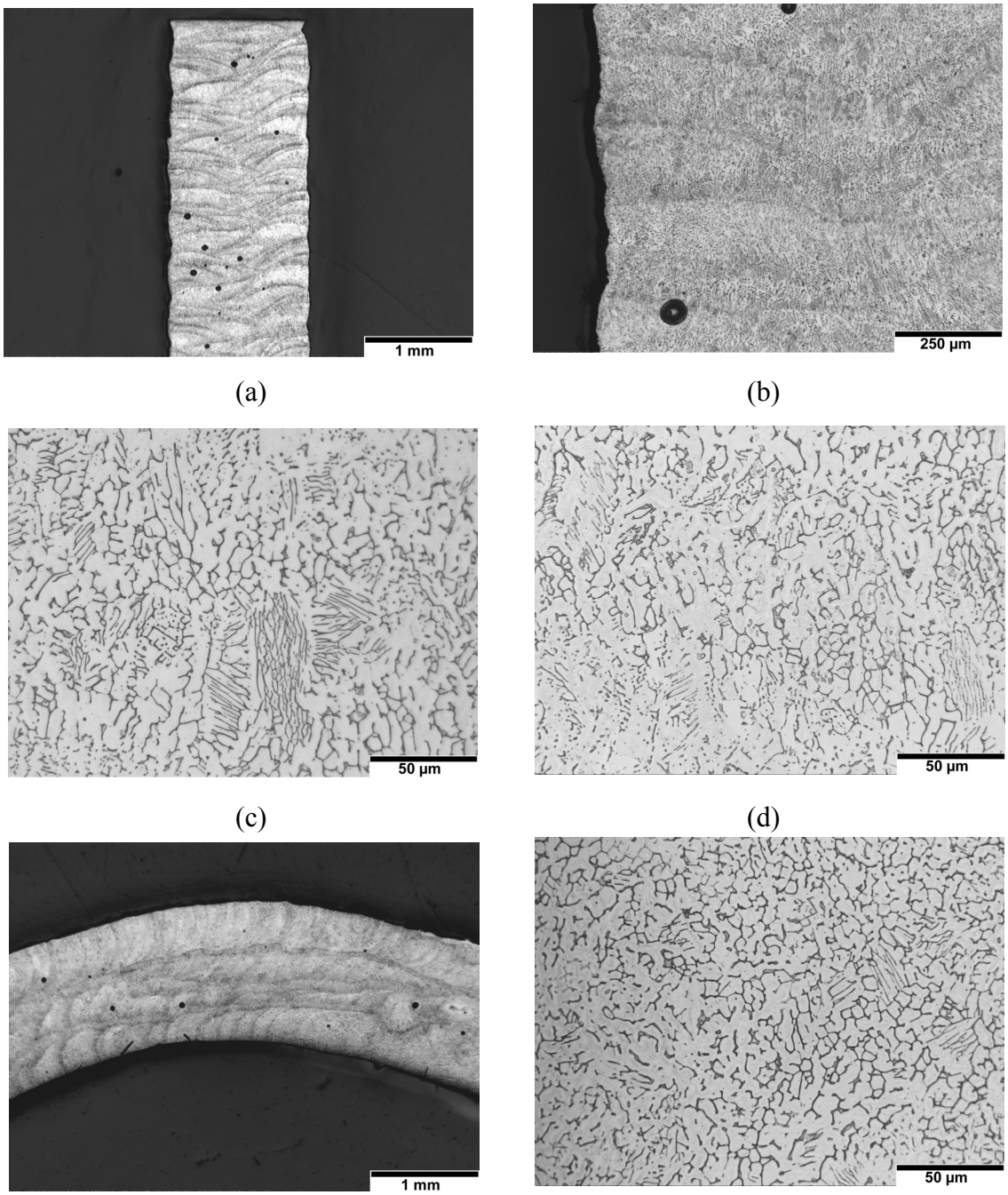

Figure 1. Pictures of cross section of the sample at various magnifications in both radial and axial directions: (a) axial picture at 25 X magnification, (b) axial picture at 100 X magnification, (c) Axial picture at 500 X magnification, (d) Axial at 500 X magnification- sample is etched, (e) Radial picture at 25 X magnification, (f) radial picture of the sample at 500 X magnification.

Resources

This Project utilized the Optomec Machine with appropriate software. Modeling and design of the parts to be built were performed via the Magics, a solid modeling software utilized in the Rapid Prototyping lab.

Discussions/Conclusion

This research project was proved to be a success. The initial results obtained from testing of the Stainless steel samples showed permeability of 1 part in $1x10^8$. This indicates a much lower permeability level as obtained by other methods ($1x10^6$). One main advantage of this method is attributed to the fact that the entire tube (tube and cap) maybe built from the same material (Inconel), while in the CVD and VPS processes, the tube is made and the cap is attached to the tube through a welding process. Samples build by the LENS process took nearly 4 hours for Stainless steel and 1 hour for Inconel. This is a significant improvement in terms of processing time as compared with CVD and VPS methods. The cost of building the samples is anticipated to be far less that of the CVD process.

Acknowledgements

The author would like to thank the entire team of engineers and scientists in the Manufacturing research area of the Marshall Space Flight Center's Engineering Directorate for their support and for providing this research opportunity. Special thanks goes to Gail Gordon (Group Lead), Tim Lawrence (Team Lead), Chris Manning (RP Group) and Glen Williams (Rp Group) and Mike Fiske (Morgan Research) for their support. I am indebted to Ken Cooper (Rapid Prototyping Group) for his guidance and patience in the course of this research. Many thanks goes to Jerry Karr and Mike Freeman for their efforts in Coordinating the Summer Faculty Fellowship Program.

References

Rapid Prototyping technology, selection and Application. Kenneth G. Cooper, Marcel Deker, Inc., New York, 2001.

2003

NASA FACULTY FELLOWSHIP PROGRAM

MARSHALL SPACE FLIGHT CENTER
THE UNIVERSITY OF ALABAMA IN HUNTSVILLE

SOLAR-POWERED PULSED GAS LASERS FOR IN-SPACE FABRICATION

REPORT NOT AVAILABLE

Prepared By:	Jamiu Adeola Odutola
Academic Rank:	Associate Professor
Institution and Department:	Alabama A. & M. University Department of Natural & Physical Sciences/Chemistry
NASA/MSFC Directorate:	Science
MSFC Colleague:	Dr. Don Frazier

2003

NASA FACULTY FELLOWSHIP PROGRAM

MARSHALL SPACE FLIGHT CENTER
THE UNIVERSITY OF ALABAMA IN HUNTSVILLE

INCORPORATING MISSION RISK IN THE CONCEPT SELECTION PROCESS

Prepared By:	Dr. Madara Ogot
Academic Rank	Associate Professor
Institution and Department	Rutgers, The State University of NJ Department of Mechanical and Aerospace Engineering
NASA/MSFC Directorate	Safety and Mission Assurance Office QS10
MSFC Colleague	Vyga Kulpa

Acronyms

CRC Concept Risk Chart
FMEA Failure Mode Effect Analysis
MLD Master Logic Diagram
HST Hubble Space Telescope

Introduction

Various methods are currently available for the selection of promising low fidelity design concepts that warrant further development from an initial concept pool. These methods include Pugh charts, decision matrices, and trade studies. Each method evaluates the concepts based on several criteria, tabulation of which yields the most promising concepts. Typically absent from the evaluation criteria at this early stage of the design process is the inclusion of mission risk. This may be due to the lack of detailed information that traditional methods such as Probabilistic Risk Assessment require and the dynamic nature of the conceptual stage of the design process itself. Previous efforts at introducing risk into the conceptual phase of the design process have been applied to higher fidelity concepts where a lot more detailed information is available [1,2].

Further, as ideas are discussed, accepted and rejected, the form the concepts take change at a fast rate leaving insufficient time for traditional risk assessment to be performed on each one. What are required, therefore, are simple, fast tools and methodologies to assess relative mission risk for low-fidelity concepts in this dynamic design environment. The results would provide additional evaluation criteria for use with the available concept selection methods.

This study develops such a tool, Concept Risk Charts (CRCs). A variation of Pugh charts, CRCs allow design teams to determine *relative* mission risk, i.e. conceptual risks are assessed relative to each other, NOT on an absolute scale. The approach is presented in the context of the design of a space vehicle described in the next section. It illustrates the advantages of including risk early in the design process, and demonstrates potential pitfalls that could result from its exclusion.

De-Orbit Stage for the Hubble Space Telescope

Designed in the 1970s and launched by the space shuttle Discovery in 1990, the Hubble Space Telescope – HST (Figure 1) operates from a low earth orbit – 600 kilometers (375 miles) above the earth's surface – capturing images of distant stars and galaxies that would be impossible from earth due to distortions from the earth's atmosphere.

Figure 1 – Hubble Space Telescope (*Courtesy NASA, hubble.nasa.gov*)

As the HST approaches the end of its useful life, conceptual studies are underway at NASA to determine ways to safely de-orbit and crash it into the Pacific Ocean. One such study was conducted in May-August 2003 at NASA's Marshall Space Flight Center to develop and evaluate several De-Orbit Stage (DOS) concepts that would be launched, attached to the HST, activated and used to safely de-orbit the HST.

One of the subsystems that had to be designed was secondary power used to power systems that are always on, for example avionics, heaters, on-board computers systems, etc. Three concepts were considered:

1. Use of non-rechargeable batteries.
2. Use of solar arrays and rechargeable batteries.
3. A hybrid of the first two concepts.

Detailed descriptions of all three concepts are presented in Table 1. The three concepts were evaluated on four criteria:

1. *Size* – the effect of each concept on the de-orbiting stage size (smaller, better).
2. *Cost* – the lower the cost the better.
3. *Weight* – contribution by each concept to the overall stage weight (lighter, better).
4. *Power* – duration of available secondary power (longer, better).

Table 1. Description of the three secondary power supply options for the Hubble Space Telescope De-Orbit Stage, Shuttle Option

Concept	Description	Duration of available secondary power (days)
1 – All Batteries	Bank of *x* non-rechargeable batteries. Other conditions dictate a stage height of ~6 feet (Figure 2).	m
2- Solar panel and rechargeable batteries	*y* rechargeable batteries and *z* body mounted solar panel area. The area required for the body mounted solar panels forces an increase of the stage height from ~6 feet to ~9 feet (Figure 3).	'Infinite'
3- Hybrid	Bank of *x* non-rechargeable batteries AND *y/2* rechargeable batteries with *z/2* solar panel surface area. The required surface area is 1/2 that of Concept 2 and the stage height is ~6 feet, dictated by other conditions.	2m+

Notes:
For the same voltage output characteristics, deliverable battery capacity increases as the discharge current decreases. As the current discharge of the non-rechargeable batteries for Concept 3 is cut in half (as compared to Concept 1), battery capacity and therefore duration of power supply will more than double.

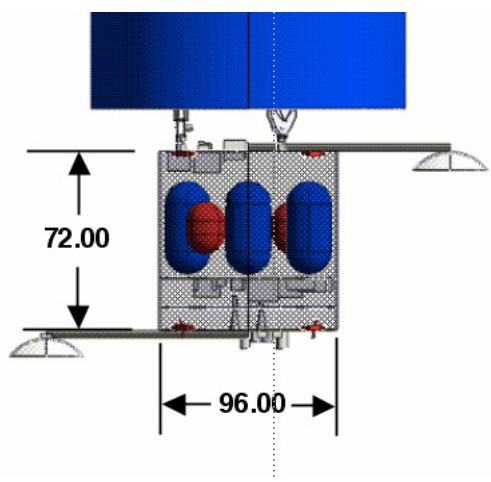

Figure 2. Illustration of the Hubble Space Telescope De-orbiting stage sized for use with only batteries. The overall length of the stage is ~6 feet dictated by factors other than the solar panel area (*Drawing Sharon Fincher, NASA MSFC)*

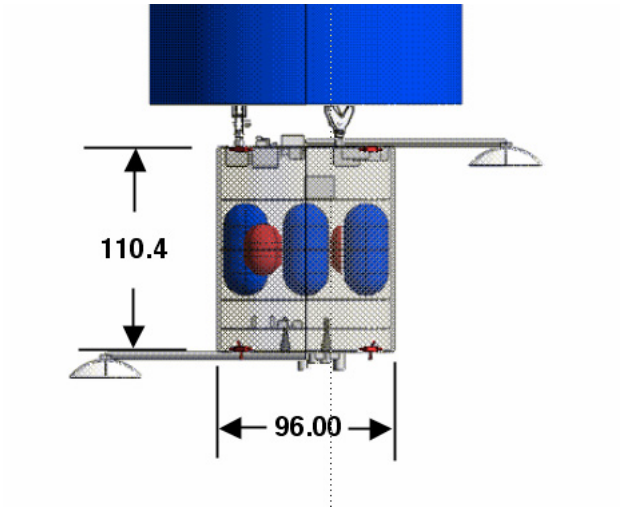

Figure 3. Illustration of the Hubble Space De-Orbiting Stage sized for use with body mounted solar panels and rechargeable batteries. The overall length of the stage is ~9 feet dictated by the area required by the solar panels (*Drawing Sharon Fincher, NASA MSFC)*

Pugh Charts

Pugh charts allow design teams to select concepts in an orderly fashion, reducing the likelihood of selecting the wrong concept or eliminating promising ones [3]. The technique is an iterative process based on the generation of *concept evaluation matrices* with each concept listed on a separate row in the first column and evaluation criteria, derived from the problem statement, listed as headings of the successive columns. One of the concepts is selected as the baseline, against which the relative strengths and weakness of the others are evaluated. The basic six steps in using Pugh charts are outlined below in the context of the secondary power example.

1. Develop all concepts to the same level of detail and create a concept evaluation matrix.
2. Choose one of the concepts as the reference or baseline against which the other are compared. Evaluate each concept/criteria combination against the baseline, using +, - or S ratings where:
   - `+' is superior to the baseline
   - `-' is inferior to the baseline
   - `S' is similar to the baseline

   For our example, Concept 3 was selected as the baseline (Table 2).
3. Sum the `+', `-' and `S' ratings, and evaluate the net score for each concept. The '+', '-' and 'S' column headings refer to each rating's total. 'Net' is the overall rating obtained by assigning each '+', '-' and 'S' rating a numeric value of '+1', '-1' or '0'.
4. Re-examine concepts whose positive net scores seem to be unusually high. If they still remain that way, these are most likely your strong concepts.

5. Change your baseline and repeat steps 2 - 4. A pattern of one or more strong concepts should begin to emerge. If not, your criteria are probably too ambiguous or one or more concepts are subsets of each other. For our example, Concept 2 was selected as the second baseline. The generated Pugh chart is displayed in Table 3. Comparing Tables 2 and 3, one observes that after two iterations Concept 1 emerges as the strongest concept.
6. If one or more concepts remain strong, make them the baseline (if they have not been already) and redo the chart. If they still remain strong, they are your likely candidate(s) to move to the detailed design stage. Concept 1 was strong after the first two iterations and is now made the baseline. Repeating steps 2-4 a third Pugh chart is generated – Table 4. Comparing Tables 2-4, Concept 1 still remains the strongest candidate after three iterations. Note that although Concept 1 fared slightly better than Concept 3, both should be further investigated due to the small difference between them. Based on all four stated criteria – size, cost, weight and power – Concept 2 clearly comes out as the weakest candidate in all three iterations.

Based on these evaluations alone, it would seem clear that Concept 1 and perhaps Concept 3 should undergo further detailed design, and Concept 2 should be abandoned. Yet, engineers and program managers would be 'uneasy' about launching a spacecraft whose critical systems were powered solely by batteries. There is always the *concern* (*read* risk) that the craft may run out of power due to an unforeseen event requiring a pause in the mission while a solution is sought, or if a change in the original mission schedule is necessary. *Accounting for unforeseen events, i.e. taking into account mission risk* ***early*** *in the concept assessment and selection process would allow designers, engineers and managers to make better decisions on which concepts to purse further for detailed design, and which ones to abandon*.

Table 2. Pugh chart for Hubble De-Orbit Stage concepts – Concept 3 baseline

Concept	**Size**	**Cost**	**Weight**	**Power**	**+**	**-**	**S**	**Net**
1	S	+	+	-	2	1	1	**+1**
2	-	-[1]	-[2]	+[3]	1	3	0	**-2**
3	B	A	S	E	L	I	N	E

Notes:
1. All solar requires double the surface area of concept 3. The craft height needs to be increased to account for this.
2. Solar panels are more expensive than batteries, and increased cost from larger craft size.
3. Large craft with more solar panels may extra battery weight

Table 3. Pugh chart for Hubble De-Orbit Stage concepts – Concept 2 baseline

Concept	**Size**	**Cost**	**Weight**	**Power**	**+**	**-**	**S**	**Net**
1	+	+	+	-	3	1	0	**+2**
2	B	A	S	E	L	I	N	E
3	+	+	+	-	3	1	0	**+2**

Table 4. Pugh chart for Hubble De-Orbit Stage concepts – Concept 1 baseline

Concept	Size	Cost	Weight	Power	+	-	S	Net
1	B	A	S	E	L	I	N	E
2	-	-	-	+	1	3	0	**-2**
3	S	-	-	+	1	2	1	-1

Assessing Relative Mission Risk: Concept Risk Charts

Numerous definitions of risk exist in the literature varying primarily based on the context in which they appear. In the framework of concept selection, we will employ the definition that views risk as a set of triplets: What can go wrong (scenarios)? How frequently does it happen (likelihood)? And what are the consequences (severity)? [4]

Attempting to assess and include risk in the concept selection process presents three big challenges:

1. Detailed data required by traditional methods are typically not available.
2. The forms of the concepts themselves keep changing rapidly from one design meeting to the next.
3. How do you handle the dual risk axes: *likelihood* of an event occurring and *its severity*?

In this study we have developed *Concept Risk Charts* (CRCs), a variation of Pugh charts, to rate the relative risk of different concepts as compared to the baseline. The CRCs list all concepts in the first column and different failure modes as headings for successive columns. Each concept is then rated against the baseline on the risk associated with each of the failure modes. The *relative mission risk* ratings are:

- + less risky than the baseline
- - riskier than the baseline
- *s* similar risk as the baseline or unable to differentiate between the current concept and the baseline

These relative ratings are determined from any numerical data that may be available on current or similar systems, or they may be based on the design teams intuition and experience with similar systems.

Severity vs. Likelihood

A qualitative grid comparing severity of an event versus the likelihood of the event occurring is illustrated in Figure 4. Severity ratings are defined as [5]:

1. Catastrophic – complete loss of system or mission

2. Critical – severe reduction of functional performance resulting in change of operational state.
3. Major – degradation of functional item output.

The (severity, likelihood) pairs are grouped into zones with Zone 1 presenting the highest risk to the system and Zone 3 the least. For this study, we will only focus on Zone 1 risk events.

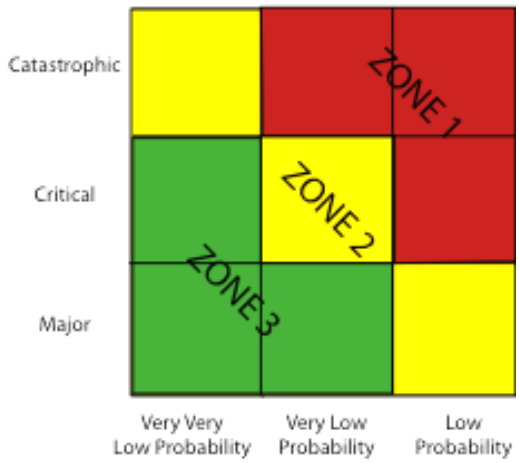

Figure 4. Qualitative grid illustrating the three risk zones

<u>Generation of Concept Risk Charts</u>

The following approach is proposed for the assessment of the relative mission risk of concepts using CRCs. The approach will be described in the context of the secondary power example.

1. For all the concepts perform a Failure Mode and Effects Analysis (FMEA) at the lowest system level available to all concepts. Tabulate your results in a modified FMEA worksheet as illustrated in Tables 5-7. The qualitative categorization for *likelihood* and *consequence* are based either on any numeric data that may be available for the system (or similar systems) or on the design team members experience and intuition.
2. From the worksheets, identify Zone 1 failure modes. These are the failure modes that will populate the CRCs.
3. For each concept develop a Master Logic Diagram (MLD) based on the Zone 1 failure modes. When concepts have identical MLDs, only one is used. MLDs for Concept 1/3 and 2 are shown in Figures 4a and 5a, respectively.
4. Failure modes based on hardware and or software similar in all concepts can be discarded from the MLDs, as they would have the same level of risk in all concepts. Since they do not assist in differentiating *between* the concepts, there is no reason to include them in the CRC*s*. The Power Control Unit, for example, is similar in all concepts, and can therefore be pruned from the MLDs. The revised MLDs are shown in Figures 4b and 5b.

5. In the first column of the initial CRC, list all the concepts. From all the MLDs, list all the failure modes as headings of subsequent columns. Add four additional columns for the +, - and S totals, and 'Net'.
6. Pick one of the concepts as the baseline and then rate the others against it. Not all failure modes apply to all concepts. Concepts that do NOT have a particular failure mode should be rated less risky than those that do. Using Concept 1 as the baseline, the generated CRC is displayed in Table 8.
7. Pick the concept that appears the strongest as the baseline and repeat step 6 and 7 as necessary. In our example, Concept 2 then 3 was selected as the baseline with the corresponding CRCs displayed in Tables 9 and 10, respectively.
8. From the generated tables rank the concepts with respect to risk. Where you cannot differentiate between the concepts, assign a similar rank. For our example, Concept 2 is the least risky, followed by Concept 3 then 1.
9. Incorporate the relative risk information from the CRCs into the original Pugh charts by adding risk as an additional evaluation criterion. With the risk information, update the overall totals. Tables 11-13 display the modified Pugh charts originally presented in Tables 2-4, and provide a better picture of the relative strengths and weaknesses of all the concepts.

Concluding Remarks

From the original Pugh charts, Concept 2 was *clearly* the weakest of the three. But by adding risk as an evaluation criterion, all three concepts are now pretty similar. Implicit in the use of Pugh charts and by extension the CRCs is that each evaluation criterion has equal weight, which may not necessarily be the case. These methods, however, allow design teams to focus on clearly promising design concepts and drop weaker ones early in the design process. The promising designs can then be developed further and evaluated using more sophisticated methods such as decision matrices that can explicitly account for relative importance of evaluation criteria.

What this simple example shows is how the exclusion of risk during the low-fidelity conceptual phase of the design process can lead to the acceptance of concepts that may be technically promising, but present additional risk to the mission that must be accounted for. Future work will investigate how risk in Zone 2 and 3 can be incorporated into the analyses.

References

[1] Smith, N., and Mahadevan, S., "Probabilistic Methods for Aerospace System Conceptual Design" Journal of Spacecraft and Rockets, Vol. 40, no. 3, pp 411-418, 2003.

[2] Elrada, H., Maggio, G., Yazdpour, S.J., Packard, T.W., Hack, K.J., "Probabilistic Risk Assessment on an Orbital Maneuvering Vehicle (OMV)" Proceedings of 39th AIAA/ASME/SAE/ASEE Joint Propulsion Conference and Exhibit , 20-23 July, Huntsville, Al., AIAA 2003-4471., 2003

[3] Pugh, S., "Concept Selection-A Method that Works", Proceedings of the International Conference on Engineering Design, Rome 1981.

[4] Kaplan, S. and Garrick, B.J., "On the Quantitative Definition of Risk" *Risk Analysis,* Vol. 1, pp. 11-37, 1996.
[5] Andrews, J.D. and Moss, T.R., *Reliability and Risk Assessment* Longman Group, Essex, UK, 1993.

Table 5. FMEA Worksheet for Concept 1 – Only non-rechargeable batteries

Identification	Function	Failure Mode	Failure Effect
1.1 Power Control unit	Provides interface between power generation units – batteries – and the power distribution units	Power control unit failure	Loss of power to the De-Orbit Stage
1.2 Non-rechargeable Batteries	Provide all the secondary power to the stage	1.2/1 Failure of single battery or connections to the battery	Reduced duration that secondary power is available
		1.2/2 Failure of back-up battery or connections to the battery	Insufficient power to complete mission
		1.2/3 Prolonged mission duration	All batteries are fully drained and system runs out of power

ID	Compensating Provisions	Severity	Likelihood	Zone
1.1	None	Catastrophic	Very low probability	1
1.2/1	Back-up battery comes on line	Minor	Very low probability	3
1.2/2	None	Catastrophic	Very very low probability	2
1.2/3	None	Catastrophic	Low probability	1

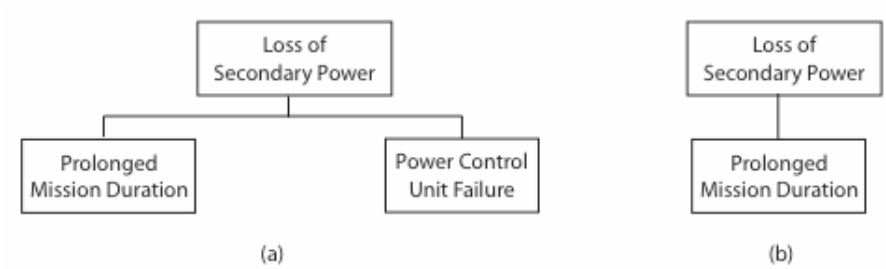

Figure 4 – Master Logic Diagrams for Concept 2: (a) Original and (b) Pruned to remove 'Power Control Unit Failure' end state that represents a system common to all concepts

Table 5. FMEA Worksheet for Concept 2 –Solar Panels and rechargeable batteries

Identification	Function	Failure Mode	Failure Effect
2.1 Power Control unit	Provides interface between power generation units – batteries – and the power distribution units	Power control unit failure	Loss of power to the De-Orbit Stage
2.2 Rechargeable Batteries	Provide all the secondary power to the stage when solar arrays not exposed to the sun	2.2/1 Failure of single battery or connections to a single battery	None
		2.2/2 Failure of back-up battery or connections to the back-up battery	Insufficient power to complete mission
2.3 Solar arrays	Provides secondary power when exposed to the sun and recharges the batteries	Failure/degradation of 'significant' number of panels, failure of connectors	Inability to provide sufficient power nor recharge batteries

ID	Compensating Provisions	Severity	Likelihood	Zone
1.1	None	Catastrophic	Very low probability	1
1.2/1	Back-up battery comes on line	Minor	Very low probability	3
1.2/2	None	Catastrophic	Very very low probability	2
2.3	None	Catastrophic	Very very low probability [1]	1

Notes: 1. For short duration missions

Figure 5 – Master Logic Diagrams for Concepts 1 and 3: (a) Original and (b) Pruned to remove 'Power Control Unit Failure' end state that represents a system common to all concepts

Table 6. FMEA Worksheet for Concept 3 –Hybrid: Solar Panels, rechargeable and non-rechargeable batteries

Identification	Function	Failure Mode	Failure Effect
3.1 Power Control unit	Provides interface between power generation units – batteries – and the power distribution units	Power control unit failure	Loss of power to the De-Orbit Stage
3.2 Rechargeable Batteries	Provide half the secondary power to the stage when solar arrays not exposed to the sun	3.2/1 Failure of single battery or connections to a single battery	None
		3.2/2 Failure of back-up battery or connections to the back-up battery	Insufficient power to complete mission
		3.3/3 Prolonged Mission Duration	All batteries are fully drained and system runs out of power
3.3 Solar arrays	Provides half the secondary power when exposed to the sun and recharges the batteries	Failure/degradation of 'significant' number of panels, failure of connectors	Inability to provide sufficient power nor recharge batteries
3.4 Nonrechargeable batteries	Provides half the secondary power to the stage	3.4/1 Failure of single battery or connection to a single battery	None
		3.4/2 Failure of back-up battery or connections to back-up battery	Insufficient power to complete mission

ID	Compensating Provisions	Severity	Likelihood	Zone
3.1	None	Catastrophic	Very low probability	1
3.2/1	Back-up nonrechargeable battery comes on line	Minor	Very low probability	3
3.2/2	None	Catastrophic	Very very low probability	2
3.3	None	Catastrophic	Very very low probability	2
3.4	None	Catastrophic	Very low probability	1
3.4/1	Back-up nonrechargeable battery comes online	Minor	Very low probability	3
3.4/2	None	Catastrophic	Very very low probability	2

Table 8. Concept risk chart for Hubble De-Orbit Stage concepts – Concept 1 baseline

Concept	Prolonged Mission	+	-	S	Net
1	B	A	S	E	
2	+	1	0	0	**+1**
3	+	1	0	0	**+1**

Table 9. Concept risk chart for Hubble De-Orbit Stage concepts – Concept 1 baseline

Concept	Prolonged Mission	+	-	S	Net
1	-	0	1	0	**-1**
2	B	A	S	E	
3	-	0	1	0	-1

Table 10. Concept risk chart for Hubble De-Orbit Stage concepts – Concept 3 baseline

Concept	Prolonged Mission	+	-	S	Net
1	-	0	1	0	**-1**
2	+	1	0	0	**+1**
3	B	A	S	E	

Table 11. Enhanced Pugh Chart for Hubble De-Orbit Stage concepts with risk criteria – Concept 2 baseline

	Totals without risk					Totals with risk			
Concept	**+**	**-**	**S**	**Net**	**Risk**	**+**	**-**	**S**	**Net**
1	3	1	0	**+2**	-	3	2	0	**+1**
2	B	A	S	E	L	I	N	E	
3	3	1	0	**+2**	-	3	2	0	**+1**

Table 12. Enhanced Pugh Chart for Hubble De-Orbit Stage concepts with risk criteria – Concept 3 baseline

	Totals without risk					Totals with risk			
Concept	**+**	**-**	**S**	**Net**	**Risk**	**+**	**-**	**S**	**Net**
1	2	1	1	**+1**	-	2	2	1	**0**
2	1	3	0	**-2**	+	2	3	0	**-1**
3	B	A	S	E	L	I	N	E	

Table 13. Enhanced Pugh Chart for Hubble De-Orbit Stage concepts with risk criteria – Concept 1 baseline

	Totals without risk					Totals with risk			
Concept	**+**	**-**	**S**	**Net**	**Risk**	**+**	**-**	**S**	**Net**
1	B	A	S	E	L	I	N	E	
2	1	3	0	**-2**	+	2	3	0	**-1**
3	1	2	1	**-1**	+	2	2	1	**0**

2003

NASA FACULTY FELLOWSHIP PROGRAM

MARSHALL SPACE FLIGHT CENTER
THE UNIVERSITY OF ALABAMA IN HUNTSVILLE

EMISSIVE PROBES

REPORT NOT AVAILABLE

Prepared By:	Harold Penn Jr.
Academic Rank:	Undergraduate
Institution and Department:	Alabama A&M University Physics Department
NASA/MSFC Directorate:	Transportation
MSFC Colleague:	Dr. Jonathan Jones

2003

NASA FACULTY FELLOWSHIP PROGRAM

MARSHALL SPACE FLIGHT CENTER
THE UNIVERSITY OF ALABAMA IN HUNTSVILLE

DESIGN AND FABRICATION OF A FORCE MEASUREMENT TABLE FOR FSW STUDIES

Prepared By:	Joseph A. Querin
Academic Rank:	Graduate Student
Institution and Department:	Mississippi State University Mechanical Engineering
NASA/MSFC Directorate:	Materials
MSFC Colleague:	Dr. Art Nunes

Introduction

To produce quality welds using friction stir welding (FSW) process variables such as rpm, travel speed, and plunge force must be chosen correctly. A rotating dynamometer or a table dynamometer could be used during the welding process to quantify welding loads and torque, which would aid in correlating them to weld quality and help in choosing process variables. Also, by measuring the forces that are induced during the welding process, these devices could aid in the design of FSW machinery. Commercially available dynamometers are expensive, so it is more cost effective to design and fabricate a table instrumented with strain gauges to determine the forces during FSW.

Geometry and Assumptions

The table is designed on the premise that forces applied to the table will elastically deform the legs; this deformation can be measured by strain gauges. Forces can then be calculated based on the strains in the legs and the geometry and dimensions of the table. Figure 1 shows the basic geometry of the load table. Notice that there are nine strain gauge locations available, three positions on each of the three legs. Not all of the strain gauge locations are needed to determine forces applied to the table.

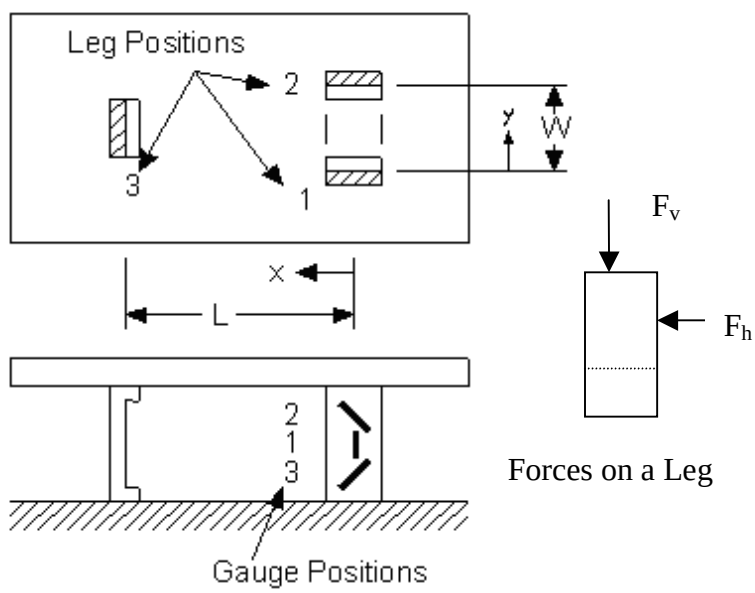

Figure 1: Instrumented Table Geometry

Each leg is assumed to support only two forces, a vertical force (F_v) and a horizontal force (F_h) in the wide direction of the cross section. Other potential force or moment reactions of the legs are dismissed with the assumptions that: the flexibility of the leg is to large in those other dimensions for forces to build up and the geometry and placement of the legs produces a F_v and F_h force system that is sufficiently rigid to prevent substantial deformations in those other dimensions [1].

Equilibrium Equations

Based on the previously stated assumptions, equations of equilibrium can be derived which allow for the component forces and moments to be calculated. This system is represented in terms of forces only. Later strain derivations will be added to relate the strains to the forces. The equilibrium equations are shown in Figure 2. Note that the first number subscript is the leg and the following letter subscript is the direction either horizontal or vertical.

$$
\begin{aligned}
F_L &= F_{1h} + F_{2h} \\
F_t &= F_{3h} \\
F_d &= F_{1v} + F_{2v} + F_{3v} \\
M_d &= yF_{1h} - (W - y)F_{2h} + (L - x)F_{3h} \\
M_t &= x(F_{1v} + F_{2v}) - (L - x)F_{3v} \\
M_L &= yF_{1v} - (W - y)F_{2v}
\end{aligned}
$$

Figure 2: Equilibrium Force Equations

Strain Derivations

The loads reacted by the table will develop two types of strains in the legs. A uni-axial strain exists because of the vertical force, and shear strain exist because of horizontal forces. Equations relating the forces to the strains are based on material properties and geometry.

A unit square subjected to a axial tension force would deform in such a way that one side would be lengthened by ε_1 and the other side would be shortened by $1\text{-}v\varepsilon_1$ (see Figure 3), where (v) is the Poisson's ratio of the material. The axial strain, ε_1, can be related to the strains across each diagonal of the unit square, ε_2 and ε_3. This is done by the use of the Pythagorean theorem and the definition of strain. Equation 1 shows the relation ship between the diagonal strain ε_2 and the axial strain ε_1.

Equation 1

$$\varepsilon_2 = \frac{[(1+\varepsilon_1)^2 + (1-\nu\varepsilon_1)^2]^{1/2} - \sqrt{2}}{\sqrt{2}}$$

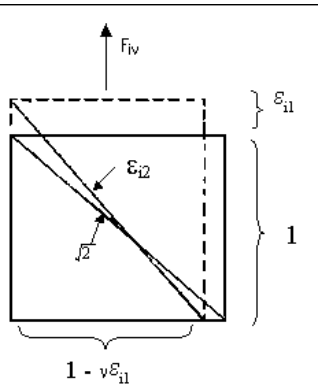

Figure 3: Unit Square Subjected to F_v

A MacLuarin series expansion can be applied and ε_2 can be combined with ε_3 to yield Equation 2.

Equation 2

$$\varepsilon_2 + \varepsilon_3 = (1-\nu)\varepsilon_1$$

Now using Hooke's law and substituting Equation 2 in for the axial strain, Equation 3 is derived for the vertical force on a leg. Note that (E) is the modulus of elasticity of the material and (a) is the cross sectional area.

Equation 3

$$F_v = \frac{-Ea}{(1-\nu)}(\varepsilon_2 + \varepsilon_3)$$

The horizontal force is derived in similar fashion. Equation 4 shows the relationship between the horizontal force and the diagonal strains.

Equation 4

$$F_h = \frac{(\varepsilon_2 - \varepsilon_3)Ea}{2(1+\nu)}$$

Combined Equilibrium Equations and Strain Derivations

The equilibrium equations and strain derivations can be manipulated in such a way that only four strain gauges are needed to determine the forces of interest. The fact that the moments M_L and M_t are zero is used to reduce the number of equations and strain gauges. M_L and M_t are equal to zero because they represent moments at equilibrium taken about the pin tool on the longitudinal and transverse axis with respect to position. The adverse affect of simplifying the equations to use only four strain gauges is that position must be known to input into the equations to calculate the forces. Figure 4 shows the set of equations that are manipulated in this manner, except that position y is held at W/2 to further simplify. In Figure 4 and Figure 5 the first subscript number denotes the leg and the second subscript number denotes the strain gauge.

$$F_L = \frac{Ea}{(1+\nu)}(\varepsilon_{12} - \varepsilon_{23})$$

$$F_t = \frac{Ea}{(1+\nu)}[\varepsilon_{32} - \frac{x}{L-x}(\varepsilon_{22} + \varepsilon_{23})]$$

$$F_d = \frac{-2Ea}{(1-\nu)}\left(\frac{L}{L-x}\right)(\varepsilon_{22} + \varepsilon_{23})$$

$$M_d = \frac{EaW}{2(1+\nu)}(\varepsilon_{12} - \varepsilon_{22}) + \frac{(L-x)Ea}{(1+\nu)}[\varepsilon_{32} - \frac{x}{L-x}(\varepsilon_{22} + \varepsilon_{23})]$$

Figure 4: Four Strain Gauges

The equilibrium equations can also be manipulated so that the forces can be calculated without knowing the x and y position of the pin tool. This set of equations, shown in Figure 5, requires the use of six strain gauges.

$$F_L = \frac{Ea}{2(1+\nu)}(\varepsilon_{12} - \varepsilon_{13} + \varepsilon_{22} - \varepsilon_{23})$$

$$F_t = \frac{Ea}{2(1+\nu)}(\varepsilon_{32} - \varepsilon_{33})$$

$$F_d = \frac{-Ea}{(1-\nu)}(\varepsilon_{12} + \varepsilon_{13} + \varepsilon_{22} + \varepsilon_{23} + \varepsilon_{32} + \varepsilon_{33})$$

$$M_d = \frac{Ea}{2(1+\nu)}\left[y(\varepsilon_{12} - \varepsilon_{13}) - (W - y)(\varepsilon_{22} - \varepsilon_{23}) + (L - x)(\varepsilon_{32} - \varepsilon_{33})\right]$$

Where y and x are defined below :

$$\therefore y = \frac{W(\varepsilon_{22} + \varepsilon_{23})}{\varepsilon_{12} + \varepsilon_{13} + \varepsilon_{22} + \varepsilon_{23}}$$

$$\therefore x = \frac{L(\varepsilon_{32} + \varepsilon_{33})}{\varepsilon_{12} + \varepsilon_{13} + \varepsilon_{22} + \varepsilon_{23} + \varepsilon_{32} + \varepsilon_{33}}$$

Figure 5: Six Strain Gauges

Conclusion

In designing the legs, yield strength criteria and buckling criteria were used to help optimize the leg dimensions. The legs are designed so that they are not so rigid that strain gauges cannot accurately measure the strains, but they are sufficiently rigid not to plastically deform or buckle. Deflections for the tabletop as it is subjected to F_d, the plunge force, were calculated using Castigliano's method, to help choose a thickness. The legs and tabletop were made from Al 2219-T87. Many things that were considered in the design of the instrumented table were left out of this report do to its brevity.

The instrumented table should be validated with a calibrated load cell to determine the uncertainty of the calculated forces. This can be done by applying known forces from the load cell and comparing them to the forces calculated from the strain gauges. Several different locations should be used to compare the actual applied forces F_L, F_t, F_d and M_d to the calculated values.

Reference

[1] Nunes, A. "Load Table – Calibration Effort"

2003

NASA FACULTY FELLOWSHIP PROGRAM

MARSHALL SPACE FLIGHT CENTER
THE UNIVERSITY OF ALABAMA IN HUNTSVILLE

DEVELOPMENT OF A ROCKET ENGINE COMBUSTION CHAMBER COOLING MODULE FOR THE ROCETS MODELING SYSTEM

Prepared By:	S.S. Ravindran
Academic Rank:	Assistant Professor
Institution:	University of Alabama in Huntsville
NASA/MSFC Directorate:	Transportation
MSFC Colleague:	Timothy Olive

Introduction

Primary focus of this project is to develop regenerative/film cooling model for combustion chamber that will be incorporated into the ROCETS modeling system. The goal is to develop a relatively simple, integral boundary layer type film-cooling model for use in preliminary analysis/design of rocket engine combution chambers. This report describes our initial efforts in that direction.

Regenerative Cooling

A typical regeneratively cooled rocket engine consists of a thrust chamber and a converging-diverging nozzle. To cool the walls of these engines, cryogenic fuel or cryogenic oxidizer is passed through cooling channels that are machined in the wall. The pressure drop for the flows of coolant through the coolant tubes is estimated by solving the conservation of mass, momentum and energy

$$\left.\begin{aligned} &\rho_2 V_2 A_2 - \rho_1 V_1 A_1 = 0\,, \\ &\tfrac{V_{avg}}{g_c}(V_2 - V_1) + \tfrac{1}{\rho_{avg}}(p_2 - p_1) + \tfrac{f V_{avg}^2 dz}{2 g_c D_h} = 0\,, \\ &\dot{m}(h_{T_2} - h_{T_1}) - \tfrac{dq}{dt} = 0\,. \end{aligned}\right\} \tag{1}$$

Film Cooling

For film cooling in flows with non-uniform main stream velocity, the momentum integral method of Nicoll and Whitelaw[2] has been chosen. This method provides a convenient way for calculating the film cooling effectiveness based on the boundary layer integral equations. The momentum integral equation when written in terms of the momentum thickness Reynolds number $Re_2 = \delta_2 u_s/\nu$ yields

$$\frac{dRe_2}{dRe_x} + (2 + H_{12} - M^2) K Re_2 = \frac{C_f}{2} \tag{2}$$

where $H_{12} = \frac{\delta_1}{\delta_2}$, δ_1 is the boundary layer displacement thickness, δ_2 the momentum thickness, M the mach number, $K = \frac{\nu}{u^2}\frac{du}{dx}$ the acceleration number and $C_f = 2BRe_x^{-b}$ the skin friction coefficient. The calculation of the film cooling effectiveness requires a second thickness Reynolds number $Re_{\theta,1}$ which is defined from the conservation equation for enthalpy in the coolant film

$$\frac{d(\eta Re_{\theta,1})}{dRe_x} = 0 \tag{3}$$

where

$$Re_{\theta,1} = \frac{u_s}{\nu}\int_0^\infty \frac{u}{u_s}(\frac{h-h_s}{h_{aw}-h_s})dy\,. \tag{4}$$

The mach number M in equation (2) is computed from

$$\frac{A}{A_t} = \frac{1}{M}[(\frac{2}{\gamma+1})(1+\frac{\gamma-1}{2}M^2)]^{\frac{\gamma+1}{2(\gamma-1)}} \tag{5}$$

Assuming a relation between Re_2 and $Re_{\theta,1}$, the film cooling effectiveness under arbitrary distributions of mach number and acceleration can be computed. We further assume that both velocity and enthalpy profiles are straight lines [3]

$$\frac{u}{u_s} = \zeta + (1-\zeta)\frac{y}{y_m}$$

and

$$\frac{h-h_s}{h_{aw}-h_s} = 1 - \frac{y}{y_h}.$$

The auxiliary relationship between Re_2 and $Re_{\theta,1}$ then becomes

$$Re_{\theta,1} = \frac{Re_2}{(1-\zeta)(1+2\zeta)}[(\zeta-1)(3-\frac{1}{\Delta})+3\Delta]. \tag{6}$$

The dimensionless thickness $\Delta(=\frac{y_h}{y_m})$ has been experimentally found to be $\Delta = 1.25$; see [2]. Equations (3) and (5) now yields

$$(\eta Re_{\theta,1}) = constant = Re_c$$

and

$$\eta = \frac{Re_c}{Re_2}\frac{(1-\zeta)(1+2\zeta)}{[(\zeta-1)(3-\frac{1}{\Delta})+3\Delta]}\,. \tag{7}$$

Assuming the effectiveness as being unity at the slot, we get the initial value

$$Re_{2,x=0} = Re_c\frac{(1-\zeta)(1+2\zeta)}{(\zeta-1)(3-\frac{1}{\Delta})+3\Delta}\,.$$

To find the adiabatic wall temperature T_{aw}, we define the effectiveness as

$$\eta = \frac{T_{aw}-T_0}{T_c-T_0}\,, \tag{8}$$

where T_0 is the main stream temperature and T_c the temperature of the coolant as it leaves the injection slot.

Heat Transfer Characteristics

Assuming a steady-state condition is attained very shortly and thermal radiation is negligible, we can write the local heat flux at any axial station in the chamber as

$$q = h_g(T_{aw} - T_{wg}) = h_c(T_{wc} - T_c), \tag{9}$$

where h_g is a function of T_{wg} and is computed from the Bartz equation [1]

$$h_g = \frac{0.026}{D_t^{0.2}}(\frac{\mu^{0.2}C_p}{Pr^{0.6}})_0(\frac{(P_c)_0 g}{c^*})^{0.8}(\frac{D_t}{R})^{0.1}(\frac{A_t}{A})^{0.9}\sigma\,, \tag{10}$$

where

$$\sigma = \frac{1}{[\frac{1}{2}\frac{T_{wg}}{(T_c)_0}(1+\frac{(\gamma-1)}{2}M^2)+\frac{1}{2}]^{0.68}[1+\frac{(\gamma-1)}{2}M^2]^{0.12}}\,.$$

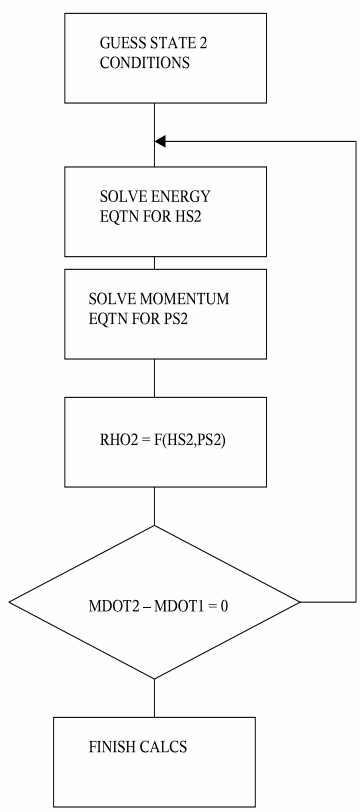

Figure 1

Numerical Model

An outline of the numerical algorithm is shown in Figure 1. In this model, the combustion chamber is subdivided into a number of stations along the longitudinal direction. The station numbering starting with the inlet of the cooling channels and ends at the exit in a counter flow nozzle liner cooling arrangement. The mach number at the stations first calculated using equation (5) via Newton's method and this was then used in equation (2) to compute Re_2 via the Backward-Euler method. The film cooling effectiveness η was computed from equation (7). The adiabatic temperature T_{aw} was computed from (8). Finally the wall temperature T_{wg} and heat flux were computed using equations (9) and (10) via Newton's method. Our preliminary numerical predictions were in good agreement with available data.

References

[1] D.K. Hazel and D.H. Huang. Modern Engineering for Design of Liquid Propellant Rocket Engines. *AIAA* 1992.

[2] W. B. Nicoll and J. H. Whitelaw. The Effectiveness of the Uniform Density, Two-Dimensional Wall Jet. *International Journal of Heat and Mass Transfer* 1967; bf 10: pp. 623–639.

[3] H. Ziebland and R.C. Parkinson. Heat Transfer in Rocket Engines. *AGARDograph*; No 148-71.

2003

NASA FACULTY FELLOWSHIP PROGRAM

MARSHALL SPACE FLIGHT CENTER
THE UNIVERSITY OF ALABAMA IN HUNTSVILLE

MICROGRAVITY EDUCATIONAL OUTREACH

Prepared By:	Denise Richardson
Academic Rank:	Assistant Professor
Institution and Department:	Jacksonville State University Department of Educational Resources
NASA/MSFC Directorate:	Science
MSFC Colleague:	Mr. Dan Woodard

Introduction

The National Science Education Standards, (2003) states: "Becoming an effective science teacher is a continuous process that stretches from preservice experiences in undergraduate years to the end of a professional career (p.1)."

This quote from the National Science Education Standards notes the movement many states are participating in across the nation. Science education, driven by the standards, needs reform. Professional development can greatly support this reform by providing resources and new pedagogy that will inform educators about the need for inquiry learning, real-world application of objectives, and authentic laboratory experiences for their students.

NASA's Physical Sciences Research (PSR) in Microgravity provides professional development opportunities and resources for teachers. The goal statement explains that:

> A primary goal of Physical Sciences Research (PSR) in microgravity is to effectively communicate the results, benefit and value of the nation's investment in microgravity research. We recognize our responsibility to communicate the results of our efforts and to share the wonder of space exploration with our customers. NASA's Physical Sciences Research Outreach and education customers include the general public, the educational community from kindergarten through twelfth grade, university undergraduate and graduate students and faculty, the scientific academic and research community and industry (p. 1).

The objectives for the summer faculty fellow project with PSR included editing and enhancing two educational publications, Protein Crystallization, Structural Biology and Space Travel-What's the Connection? and NASA's Bioreactor: Growing Cells in a Microgravity Environment. Additionally, an evaluation plan was written for NASA's professional development workshops. This evaluation will help ensure that NASA met their goals and objectives. Further, brainstorming began on plans to take NASA's interests and develop a course for pre-service teachers. This course would strengthen both science and pedagogy. Last, future publication ideas were discussed.

Educational Briefs and NASA

According to the Curriculum Support Product Development Layout and Dissemination Guide published by NASA (2000):

> an educational brief is targeted toward educators at specific grade levels (K-4, 5-8, 9-12, and Higher Education) focusing on mission discoveries/results as they support curriculum content. Classroom activities are an essential element of Educational Briefs. Educational Briefs may also include hands-on aerospace-related construction activities as well as background information (p. 19).

NASA uses the abbreviation EB to refer to Educational Briefs. Many can be found at (http://teacherlink.ed.usu.edu/tlnasa/briefs/).

Also in this source, the description of an Educational Guide (EG) is given. Relating:

> Educator Guides are directed at specific grade levels and provide materials for educators that allow them to incorporate aerospace-related topics into existing curriculum. Classroom activities that utilize problem-solving, hands-on, and critical thinking skills should be incorporated for the educator to use with the students. Classroom activities are included within the Guide so that they can be reproduced by the educator and used for classroom instruction with students (p. 21).

Many of the Guides can be found at (http://www2.semo.edu/nasaerc/pubs.asp?what=7).

The Protein Crystallization, Structural Biology and Space Travel-What's the Connection? Guide provides background information on the purpose to NASA's Protein Crystallography program. An experiment is included that teaches students, grades 9-12, about the chemical composition of proteins and their role in cell metabolism. Further, students will learn how proteins form from the processes of gene expression and why enzymes and proteins are important to medical research. Questions from the Guide include, "What is a crystal? How and why do molecules form crystals? Why do we want to grow crystals of proteins at all, and in particular, why do we want them to grow in space?" The summer faculty fellow project enhanced this brief by editing, adding the National Science Education Standards, Mathematics Principles and Standards and the Technology Educational Standards all for grades 9-12. Additionally, photographs were added throughout the Guide, particularly for the laboratory equipment. Teachers can copy this page and distribute to help visual learners follow the experiment.

NASA's Bioreactor: Growing Cells in a Microgravity Environment is a brief that was a part of the summer faculty fellow project in 2002. This brief, which eventually will become a Guide, was also written for a target audience of teachers and students grades 9-12. Background information includes the description of a Bioreactor and its role in NASA research. Further, a discussion of microgravity and its affects on cell growth helps students and teachers understand how the Bioreactor helps NASA learn more about cells. Instructions on how to build a student Bioreactor and an experiment are included. The summer faculty fellow project enhanced this brief through editing, the addition of the National Science Education Standards, Technology Education Standards, and the Mathematics Principles and Standards. All of these standards are for grades 9-12. Additionally, the Brief was enhanced with diagrams to support instructions on how to build a Student Bioreactor.

Evaluation Recommendation for NASA's Workshops

Workshops are widely utilized by school districts to renew and add to skills of teachers. Many require teachers to obtain continuing education units to keep their teaching license current. Thus, NASA's workshops and the goals are greatly needed in the educational community. However, conducting a workshop does not ensure that the goals and objectives will be met. Therefore,

evaluation needs to be conducted. Evaluation can be described as "a systematic process designed to gauge the quality and effectiveness of a program" (Yap, Aldersebases, Railsback, Shaugnessy, Speth, 2003; p. 2). The summer faculty fellow project included writing a recommendation for evaluation of NASA's workshops. When an evaluation is conducted on a workshop, it means that evaluators collect data, organize it, analyze then draw conclusions. Last, data and findings are reported. A summary of the evaluation strategy is:

1. Identify stakeholders.
2. Write a list of goals and objectives.
3. Select who will be responsible for conducting the evaluation.
4. The use of external and internal evaluators.
5. Data collection
6. Organizing and Analyzing Data
7. Interpretation of Data
8. Conclusions and Recommendations

Project Plan for New Course

The summer faculty fellow project generated an idea that NASA's workshops, which currently support continuing education units (CEU's), would benefit all stakeholders if college credit could be given. Dr. Bill Carswell, a NASA/UAH materials scientist, and this paper's author, Dr. Denise Richardson, Jacksonville State University assistant professor, will write a project plan to submit to NASA's Microgravity Educational Outreach manager, Dan Woodard. The goals of this course will include the content of all five microgravity disciplines: Biotechnology, Fundamental Physics, Fluid Physics, Materials Science and Combustion Science. Use of existing NASA education products will be considered. Many of these can be found on (microgravity.nasa.gov). Course flow will focus on fundamentals of science in preparation for space phenomena descriptions with consideration given to the National Science Education Standards. Inquiry learning techniques will be employed. The course will be developed as a distance learning course with a few on-site visits. The university that will pilot this program is Jacksonville State University located in Jacksonville Alabama. This is approximately 128 miles from Marshall Space Flight Center located in Huntsville, Alabama. Long-term vision for this course includes extending to universities all over the nation.

Conclusion

NASA's Physical Sciences Research (PSR) Educational Outreach provides opportunities for teachers and students to incorporate the National Science Educational Standards in their course of study. Further, teachers and students are exposed to the dynamic world of NASA's microgravity research. Through the efforts of PSR Outreach, educators have the tools necessary to increase understanding of science, increase motivation for science learning, and inspire our greatest resource, young students.

Acknowledgements

The author would like to thank the Microgravity Team, in particular, Dan Woodard and Betty Grisham, for the opportunity to be involved in the Summer Faculty Fellow Program.

References

[1] Microgravity Research Program. (2003). [Online] Available: http://www.microgravity.nasa.gov

[2] National Aeronautics and Space Administraton (2000). *Curriculum Support Product Development, Layout, and Dissemination Guide.* Washington, DC: Author.

[3] National Science Education Standards (2003). Retrieved from http://www.nap.edu/readingroom/books/nses/html/4.html.

[4] Yap, K., Aldersebaes, I., Railsback, J., Shaughnessy, J., and Speth, T. (2003). *Evaluating Whole-School Reform Efforts: A guide for district and school staff.* (2nd ed.). Portland, OR: Northwest Regional Educational Laboratory.

2003

NASA FACULTY FELLOWSHIP PROGRAM

MARSHALL SPACE FLIGHT CENTER
THE UNIVERSITY OF ALABAMA IN HUNTSVILLE

NEW HYDROPHILIC, COMPOSITE MEMBRANES FOR AIR REMOVAL FROM WATER COOLANT SYSTEMS

Prepared By:	Stephen Ritchie
Academic Rank:	Assistant Professor
Institution and Department:	University of Alabama Department of Chemical Engineering
NASA/MSFC Directorate:	Flight Projects
MSFC Colleagues:	Jon Holladay Dallas Clark

Introduction

The introduction of gas bubbles is inevitable in fluid coolant loops containing orbital replacement units (ORUs). Non-evacuated gases in the ORUs and dead-spaces in quick disconnects (QDs) are the primary sources of gas bubbles. These must be removed from the coolant loop, as their presence can have several negative effects, including: loss of centrifugal pump prime, interference with sensor readings, and blockage of fluid flow to remote systems. The removal of gas bubbles in microgravity is non-trivial because of the lack of buoyancy. Therefore, alternatives must be used to remove these non-condensable gases from the system.

One current design involves the use of a dual-membrane system (SAE #932162). In this case, one membrane is used to retain gas bubbles, while the other membrane is used to vent the bubbles from the system. This gas trap is currently being used on the International Space Station (ISS). It is important to note that the need for gas traps is not exclusive to the ISS; rather, they are needed in the logistics module and in future NASA projects such as the Strategic Launch Initiative (SLI) and the Orbital Space Plane (OSP). Although the original gas trap design was effective in ground tests, it has demonstrated decreased performance and susceptibility to fouling on orbit.

There is a demonstrated need to find replacements for the existing gas traps on the ISS and in other NASA applications. This work builds on a redesign of the dual-membrane gas trap performed during the Summer 2002. The redesign involved two major changes: the hydrophilic membrane material was changed to permit better bubble retention with similar coolant fluid pressure drop, and the venting membrane was reconfigured (SAE #2003-01-2569). In both cases, changes where made to address specific issues faced by the original design during operation on the ISS.

In this work, the first major change was addressed by examining the formation of a composite membrane. The membrane is formed by deposition of a thin coating of polyethersulfone (PES) in the bore of a porous polyethylene (PE) tube. The PES provides the separation ability for selective passage of water and retention of gas bubbles, while the PE tube provides the structural stability. Both the polymer and the tube are available commercially. Methods of formation, problems encountered and resolved, and preliminary results will be provided in this report.

Background

A dual-membrane gas trap is currently used on the ISS. This trap is composed of an array of 84 tube sets. Individual tube sets are composed of an outer hydrophilic membrane, and an inner hydrophobic membrane. A schematic of the tube set is shown in Figure 1. Note that coolant enters the bore of the hydrophilic membrane, passes through the wall, and then exits the gas trap. Gas bubbles retained by the hydrophilic membrane adhere to the hydrophobic membrane, where they are subsequently vented to the cabin. The hydrophilic membrane has larger pores than the hydrophobic membrane. However, since its pores are filled with water, air bubbles must

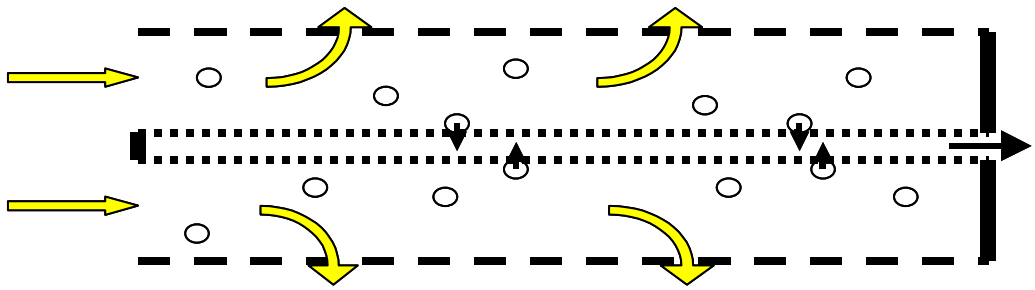

Figure 1: Schematic of membrane tube set. Outer dashed lines represent the hydrophilic membrane. Inner dashed lines represent the hydrophobic membrane.

overcome the membrane bubble pressure to displace this fluid before they can bypass the gas trap. As long as the bubble pressure is greater than the actual pressure drop across the gas trap, bubbles are retained.

The hydrophilic membrane is critical for the capture of gas bubbles, and the bubble pressure and overall pressure drop are direct functions of the membrane material and pore size. For a fixed mass flux and membrane pore size, a more hydrophobic material will have lower water permeability than a more hydrophobic material. For example, the nylon-11 membranes (3.6 μm pore diameter) used in the original gas traps have a water permeability of 186 lb/ft^2 hr psi. A more hydrophilic polymer, such as PES, has approximately the same permeability (167 lb/ft^2 hr psi) at a pore diameter of only 0.22 μm. Therefore, a PES membrane with the same pore size as the nylon-11 membrane would have substantially higher water permeability.

The bubble pressure is a stronger function of pore size than membrane material. It can be calculated directly using equation 1,

$$\text{Bubble Pressure} = \frac{4k\cos\theta}{d}\sigma \qquad (1)$$

where k is a shape factor (unitless), θ is the contact angle (degrees), d is the pore diameter (μm), and σ is the liquid surface tension (mN/m). The true value of this equation is the relationship between the bubble pressure and d, since the other parameters are constant. Reported data modeled by this equation are shown in Figure 2. The model fits the data exceptionally well, and predicts bubble pressures of 7.3 and 51 psi, respectively, for the nylon-11 and PES membrane discussed above. Given the similar water permeability of these membranes, a switch to PES membranes would result in a much higher tolerance for the pressure increases observed during operation of the gas traps on orbit.

In the course of this research, hydrophilic, composite membranes were formed by deposition of PES in the bore of a porous PE tube. Advancements have been made on coating procedures and methods for testing and comparison of different composite membranes. This report will focus on lessons learned during preliminary coating experiments, observed decreases in membrane permeability after coating, and some preliminary work demonstrating improved bubble pressure over the substrate tube.

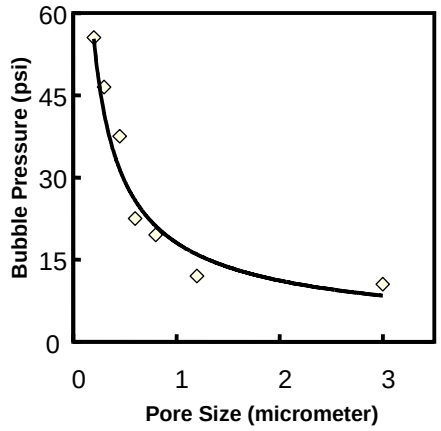

Figure 2: Bubble pressure dependence on membrane pore diameter.

Experimental

Materials

The two samples of PE tubes used in this study were obtained from PoreX Corporation (Fairburn, GA) and Interstate Specialty Products (Leicester, MA). The PES was a commercial grade Radel A obtained from Solvay (Brussels, Belgium). Reagent grade dimethylformamide (DMF) was purchased from Fisher Scientific (Pittsburgh, PA) and used as received. Polymer solutions were made by dissolution of 10 g of polymer in 45 or 90 mL DMF, degassed, and stored in the cooler at 10 ^{o}C until needed.

Tube Preparation

Early studies used the PoreX tube as received. The majority of coated membranes were made by first soaking the PE tube in DMF. Soak times varied between 20 minutes to 2 hours. The tubes were removed from the solvent and the exterior surface was wiped dry prior to polymer coating.

Tube Coating

Typical membrane tube coating was performed by placement of the dried (see previous) tube in a tube holder assembly. This permitted hands-free application of the polymer solution to the bore of the tube. Once placed in the holder, 1-2 pipettes of the polymer solution (~ 4 mL) were applied to the bore side of the tube. Visual inspection verified uniform surface coating as evidenced by the presence of a smooth, glistening coating in the tube bore. Excess polymer was allowed to drain for one minute, and residual polymer at the base of the tube was wicked away with a paper towel.

Phase Inversion and Membrane Drying

The coated tubes were next placed in a beaker of still water. Immersion in water permits leaching of the solvent DMF from the coating followed by precipitation, or phase inversion, of the polymer. Distortions in the beaker liquid headspace were evidence of solvent leaching from the tube. After two minutes in the bath, the tube was rinsed directly with flowing water for 3 minutes. The tube was then allowed to soak in flowing water for 25 minutes. Flowing nitrogen through the bore dried the coated tube.

Nitrogen Flux Testing

Tubes were tested for nitrogen permeability to get a relative feel for decrease in membrane pore size after coating. Tygon tubing was attached to each end of the coated tube with hose clamps. One end of this assembly was closed with a second clamp, while the other end was attached to the nitrogen supply. A pressure regulator in the line allowed for application of a constant pressure difference across the tube. The nitrogen flow rate was measured by collecting permeated gas in a water-filled graduated cylinder. As gas displaced water in the cylinder, the volume of nitrogen could be measured versus time. The flow rate was normalized by the membrane cross-sectional area to calculate the nitrogen flux. Further normalization with the applied pressure results in a membrane permeability that offers an objective comparison between different coated tubes. The nitrogen flux was determined in the same way after permeation of 100 mL water through some of the membranes.

Results

Past experience with homogeneous PES membranes indicated that a moderately viscous polymer solution, properly degassed, results in very uniform and repeatable membranes. In this study, differences in surface energies between the polymer film and substrate resulted in non-uniformities. Subsequent work focused on improving interactions between the two materials, and finally resulted in fairly repeatable and uniform coated tubes. The tubes do not yet have the desired properties, however, significant advancements have been made toward that end.

Thick-Coated Membranes

Initial studies were performed by coating dry tubes with a thick (10 g PES:45 mL DMF) polymer solution. Efforts were made to ensure even coating of the tube; however, pooling of the polymer solution generally resulted in significant inconsistencies in the coated membranes. A comparison of the flux behavior for the uncoated (upper line) and coated membranes is shown in Figure 3. Clearly there is a significant drop in membrane permeability caused by a decrease in membrane pore size. This is shown in better detail in Figure 4. Note that pore size of the PES coated is much smaller than for the substrate.

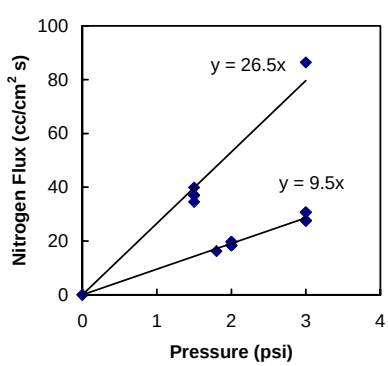

Figure 3: Nitrogen permeability decrease for the thick-coated composite membranes.

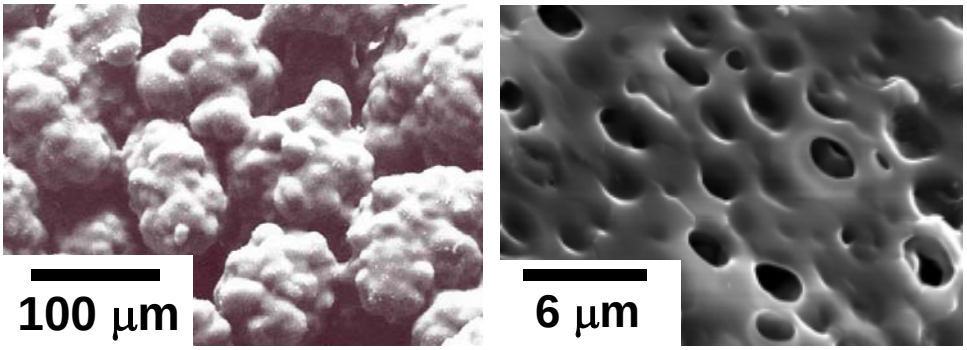

Figure 4: Raw PE tube (left) and surface of thick-coated membrane.

The thick-coated membranes were not stable, with coatings delaminating from the tube. In one case, the added PES coating completely delaminated and was removed from the bore of the tube. This phenomenon is a function of two effects. First, the PES is hydrophilic, and contact with water (during phase inversion) results in swelling of the material. As the tube is allowed to dry, the coating will shrink. The PE tube is rigid, and has no affinity for water, so as the PES coating shrinks, there is no comparable change in PE tube conformation. Consequently, stresses at the interface become too large and the coating pulls away from the tube surface. An SEM analysis of the interface (Figure 5) shows very few contact points between the surfaces that may have inhibited the delamination. Seeding the pores of the PE tube with PES, thereby altering the surface energy of the PE, may permit better bonding between the materials and may help mitigate this process.

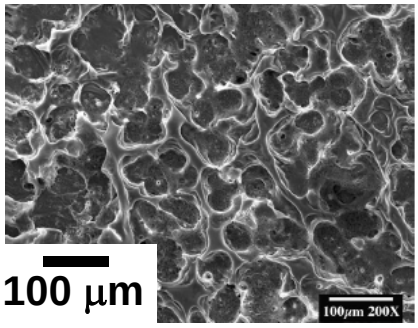

Figure 5: PES interface with PE tube after delamination.

Thin-Coated Membranes

Initial studies were performed to eliminate observed problems with the thick-coated membranes. Issues with delamination of the PES coating were eliminated by using a thinner PES solution (10g PES:90 mL DMF). Problems with pooling of excess polymer solution were eliminated by allowing the excess to drain and wicking away residual solution with a towel. A representative SEM of the tube surface is shown in Figure 6.

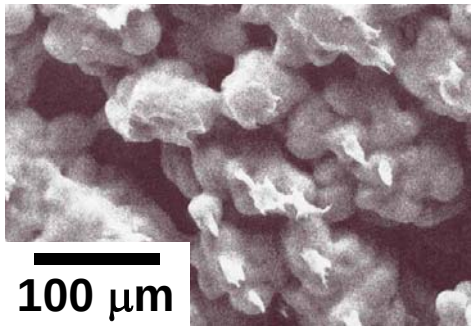

Figure 6: Thin-coated PES tube.

The most obvious conclusion here is that the thinner solution is not resulting in a coating that lies on the surface like in Figure 4. Rather, combination of a thinner solution and presoaking of the PES tube in DMF results in better pore penetration and a coating of the porous structure of the substrate. What may be more important is that seeds of PES in the porous PE structure will increase the surface energy of the substrate and allow for more uniform secondary coating of the membrane.

The nitrogen flux behavior was similar to that observed with the thick-coated membranes. A typical result for the thin-coated membrane is shown in Figure 7. In this case, the new permeability is approximately half of the raw tube permeability. The membrane permeability varied ± 30% for different thin-coated membranes. The most likely sources of error are the cross-sectional area for nitrogen flow (±10%) and time keeping during testing (±10%). Secondary coating of PES generally resulted in an additional 33-75% decrease in nitrogen permeability.

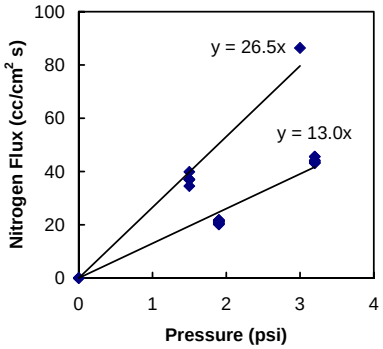

Figure 7: Representative nitrogen flux data for the thin-coated membranes (lower line) versus the uncoated tube.

Thin-Soaked Membranes

Intimate contact between the applied PES coated and the PE tube is critical to long-term stability of the composite material. In an effort to improve this contact, several membranes were soaked in the thin PES solution. The membranes had previously been soaked in DMF. It was hypothesized that long-term contact would allow more of the PES chains to diffuse into the PE tube porous structure. Representative nitrogen permeability data for the thin-soaked membrane is shown in Figure 8. The nitrogen permeability of these membranes was lower than all of the

single-layer coated tubes. Repeatability was also improved, with ±20% between all permeability values. There was no delamination of the applied PES.

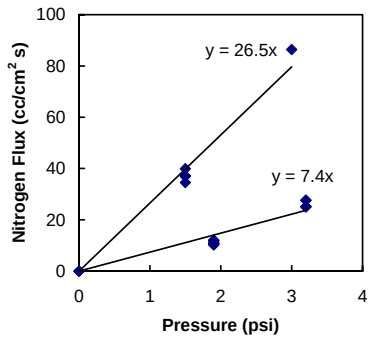

Figure 8: Typical nitrogen permeation data for the thin-soaked PES membranes.

Coated and soaked membranes were also permeated with water, followed by measurement of nitrogen permeability. In all cases, there was a significant decrease in nitrogen permeability. There may be two causes for this observed decrease. First, the PES coating may absorb water, causing it to swell. Much as inflammation will cause constriction of blood vessels, swelling of the polymer would constrict flow pathways, resulting in decreased nitrogen permeability. A second possibility is that water is retained in the porous structure. This is akin to the phenomenon that allows bubble retention in the gas trap. The nitrogen flux was measured multiple times for a wetted thin-soaked membrane. Over time, the nitrogen permeability improved and approached a steady value, as shown in Figure 9. However, that permeability is still only 33% of the dry membrane permeability. Given that the water contact time is very small (about 1 minute), it is unlikely that a significant amount of water is absorbed. Rather, water in large pores is displaced at the permeation conditions (3.3 psid) and smaller pores retain water. The cross-sectional area for nitrogen flow is reduced, resulting in lower apparent permeability.

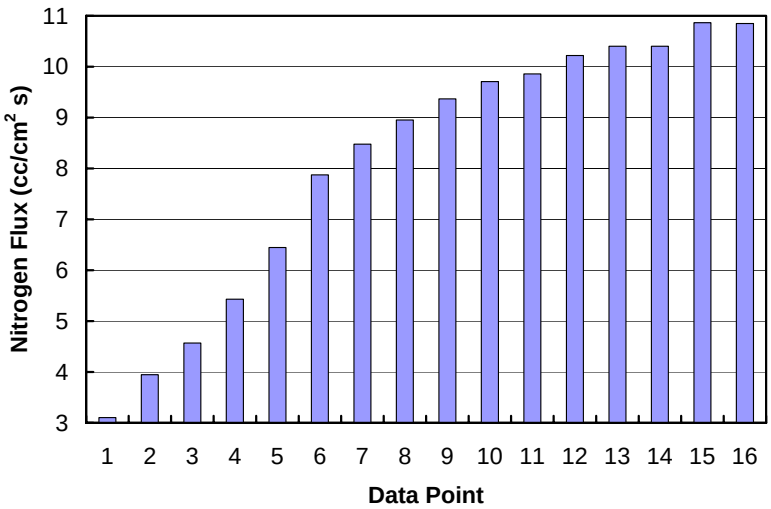

Figure 9: Partial nitrogen flux recovery for post-water contacted thin-soaked membrane.

Conclusion and Future Work

Deposition of a layer of PES on the bore surface and in the porous structure of a PE tube will alter the tube permeability. Optimization of the coating process is imperative to create reproducible membranes with desired characteristics. Thick polymer solutions are ineffective because of inconsistencies and material disconnects between the dried polymer coating and the substrate. These issues have been partially addressed by presoaking the PE tube in the solvent to increase the surface energy at the interface. The use of a thinner solution has also been found to generate membranes with similar permeability characteristics, but without delamination. Soaking the tube may also be beneficial, as the coating can better penetrate the porous substrate. In the latter two cases, there is some evidence of increased bubble point due to probable retention of water in smaller pores of the material.

Future work will address improving the deposition procedure to produce hydrophilic, composite membranes with desired properties. Successful formation of the hydrophilic membrane will be followed by creation of a prototype for testing bubble retention properties at normal operating conditions. The hydrophobic membrane reconfiguration will also be examined.

Acknowledgements

This work is the result of the collaboration of an excellent group of researchers across the Marshall Space Flight Center and the University of Alabama. First, I would like to express my sincere thanks to the Pressurized Carriers Group/FD24 for all of their support. I would especially like to thank my colleagues from FD24, Jon Holladay and Dallas Clark. Lab space was provided by FD21, with special help from Gene Hartsfield and a lot of advice from Bill Barnett. SEM pictures were provided with the help of James Coston in ED33. I am also grateful for the help of Kimberly Wasser who will begin her studies in Aerospace Engineering at the University of Alabama in Huntsville this Fall, and to my graduate student, Tapan Shah, for his help on SEM pictures of the thin-coated tubes. Finally, I would like to thank the NASA Summer Faculty Fellowship Program for financial support during the summer of 2002 for the design work, and this summer for the experimental work.

References

Faust, M.B., Zhou, S.J., and Brubaker, I.M., "Dual-Membrane Gas Trap for the Space Station Freedom Internal Thermal Control System," SAE Technical Paper #932162, 23rd International Conference on Environmental Systems, Colorado Springs, Colorado, July 1993.

Ritchie, S.M.C., Holladay, J.B., Holt, J.M., and Clark, D.W., "An Improved Design for Air Removal from Aerospace Fluid Loop Coolant Systems," SAE Technical Paper #2003-01-2569, 33rd International Conference on Environmental Systems, Vancouver, British Columbia, July 2003.

2003

NASA FACULTY FELLOWSHIP PROGRAM

MARSHALL SPACE FLIGHT CENTER
THE UNIVERSITY OF ALABAMA IN HUNTSVILLE

LIGHTNING DETECTION EFFICIENCY DETERMINATIONS FOR LIGHTNING NETWORKS OF LIMITED SCOPE

Prepared By:	John T. Rompala
Academic Rank:	Professor
Institution and Department:	University of Wisconsin-Stout Physics Department
NASA/MSFC Directorate:	Science
MSFC Colleague:	Richard Blakeslee

Introduction

Lightning strike detection and locating relies on the registering of the event's emitted electromagnetic impulse. Variations in signal time of arrival at grid detection sites permit a triangulation solution of the event's impact time and site. Solutions can also be arrived at using detector directional antenna data. Event range information, once formulated, leads to the determination of each event's peak current. This determination is based on the strength of the observed signal extrapolated to the event's position using the well established 'transmission line' model of electromagnetic signal attenuation for lightning strike phenomena.

Event peak currents for a statistically significant number of events range from below a kiloamp to beyond a hundred kiloamps. The fractional distribution for events lowering negative charge from cloud to ground and that for events lowering positive charge each has their own recognizable but, hitherto, uncodified form.

The signal from a fraction of events attenuates to levels below detector threshold and as a result, goes undetected. The straight forward, though impractical, way to avoid this detection inefficiency is to increase the population density of sites. Make all location in the service region within range of at least two detector sites even for events of low peak current. An alternative is to determine the fraction of events that can be expected to be in the class of events having peak currents below detectable levels. The development of an analytical and functional technique for enhancing detection efficiency of sparse density networks has been the ongoing effort of this researcher, his mentor, and colleagues at NSTTC [1,2].

Peak Current Distribution and Range Effects

The focus of this effort has been the utilization of the dependence of both the peak current distribution and range effects on event signal strength. The basic premise is that the knowledge of grid and detector characteristics determines the minimum event strength at any point in the service grid prompting a detection/location solution. Referring this lower limit to the peak current distribution fixes the fraction of events at this service grid location going undetected. It also gives the probable peak currents of these missed events.

The application of this premise relies on two basic assumptions. First, it is possible to obtain a statistically significant and complete peak current distribution of events. This complete data set would be representative of results form a sub-region of the service grid with a nearly ideal detection efficiency. Data from a centralized sub-region of the service grid should serve this purpose. Second, though that data may be representative of only a nearly ideal detection efficiency, it can serve as a control data set for the entire service grid. It can be at least considered a zeroth order approximation to such a standard.

Bi:Gamma PDF Representation of the Peak Current Distribution

Though it is possible to carry out this process using the peak current distribution based on empirical data, it is advantageous to find a mathematical model for this distribution. Such an

analytical formulation, if chosen appropriately, offers the programming flexibility. It also provides a possible link to the physics associated with the processes involved.

Initially the peak current distribution was characterized as a gamma probability distribution function (pdf). This was especially attractive since the gamma pdf has been found utility in describing a wide variety of physical phenomena. The comparison was close but warranted modification. In order to obtain a working model of the peak current distribution, it became necessary to sum two gamma pdf's, one associated with the low current portion of the distribution and a second associated with the high current portion. The resulting spectral representation is referred to as a bi:gamma formulation.

The peak current distribution for the standard central section is modeled by a two element spectral representation of gamma probability distributions.

$$Bi:GPDF = m_A \frac{\left(x/\beta_A\right)^{\alpha_A - 1} e^{-\left(x/\beta_A\right)}}{\Gamma(\alpha_A)\beta_A} + m_B \frac{\left(x/\beta_B\right)^{\alpha_B - 1} e^{-\left(x/\beta_B\right)}}{\Gamma(\alpha_B)\beta_B}$$

Equation 1: Bi:Gamma Probability Distribution Function

Each term dominates an opposite end of the current spectrum.

Rondonian Lightning Detection Network Data

The process has been formulated around the data from, and characteristics of, a four-station lightning detection network in the Rondonian region of Brazil. It is intended that the process' first full scale application will be directed to data from this network. Data from strikes detected by the network during November 1999 was used as the reference data set. The distribution of negative cloud to ground (CG) events in the 10° X 10° region serviced by this network is shown in the figure 1 below. The scaling is in 'events per (1.0^oX1.0^o)'.

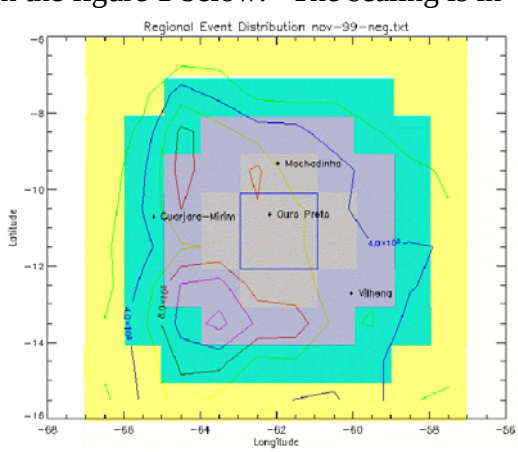

Figure 1: Negative CG Events

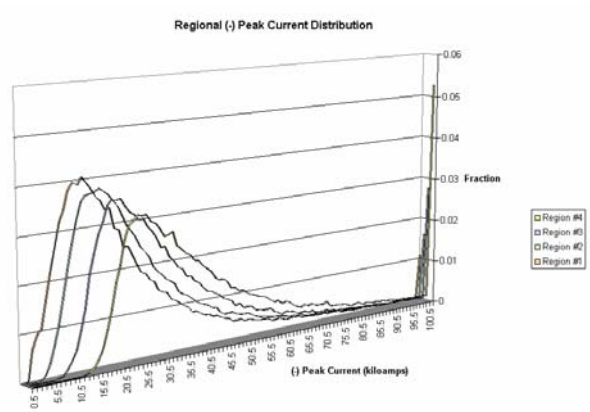

Figure 2: Monitored Regional Peak Current Distribution

Highlighted in that figure is a $2.0^{o}X2.0^{o}$, central quad, region in which the network is taken as having a nearly perfect detection efficiency. Also shown are four arbitrarily defined sub-regions used in this study. The peak current distributions in these regions are shown in the figure 2

Regional Detection Efficiency Determination

The distribution appearing in the central quad is considered representative of the actual distribution experience over the full region. The distribution spectra segment with currents falling below detection criteria account for detection inefficiency. The set of criteria not only includes signal attenuation but also detector sensitivity and solution type. Detection sensitivity is monitored through a sensor's gain and threshold settings. Consideration is also given to the number of detectors required to be within range of the event in order to prompt a solution.

Process Poster Presentation

The detection efficiency evaluation process has been compiled in two formats, IDL and Excel spreadsheet with Visual Basic macros. Each format was used in developing a summary of the process in a poster presentation at the 12th International Conference on Atmospheric Electricity [3]. This duality in format was an outgrowth of the dual development efforts carried out at MSFC and UW-Stout. This flexibility however necessitated an eventual correlation and verification to insure that the independent processes produced common results using common input data and parameters.

Process Utilization

In order to facilitate utilization of this process as a research and data analysis tool, the IDL and Excel packages were reformulated and expanded to offer future investigators maximum flexibility in two major areas: selecting data input/output and establishing analysis parameters.

Data Input/Output

The IDL package initially was framed about the bi:gamma probability distribution model of the central quad peak current distribution. This facilitated determination of the feasibility of the process and the complexity of the analysis. This background showed that it is possible to use empirical data from the central quad in the analysis as well as it analytical form. Both formats were expanded to incorporate this aspect of the process.

The Excel package spreadsheets offer a more immediate and detailed presentation of intermediate graphical and analytical steps. This is especially useful to investigators when determining the bi:gamma parameters which model the central quad peak current distribution. There is no direct analytic process for determining these parameters. The Excel graphics are currently the best way to arrive at the parameter set visually. The graphics in this package were also reformulated to make them compatible with the IDL package displays

Analysis Parameters

In either package the user has the capacity to interactively vary, the detector threshold, bi:gamma parameters, the members of the active detection network, and the caliber of the solution type. This capability can easily be extended to include detector gain, transition line model parameters and attenuation coefficient. One of the outcomes of using the bi:gamma model is to employ its spectral character in data analysis. As an example, one way of eliminating low current events from the distribution is to assume that they have their own gamma distribution and to set its amplitude to zero in the analysis. That is what is done with positive events below.

Sample Application

The intent of determining the regional detection efficiency is to ultimately determine the actual distribution of events using the full spectrum of peak currents. This is a straightforward process and functioning code carrying out that step of the analysis has been written.

.

Conclusion

The packages are now functional and in a utilitarian form. This now offers a variety of directions for further study. The physical implications of the gamma probability distribution function form taken by the peak current distribution are numerous. Relating the parameters spectral form to physical processes is warranted. Enhancing data sets should lead to more meaningful and more cogent interpretation of meteorological patterns over time and local. A graphical representation of the impact of network operational parameters should foster more efficient network operation.

Acknowledgements

The many NSSTC members contributing to this effort and their support is much appreciated especially that of Richard Blakeslee and Jeff Bailey. The NFFP staff fostered and facilitated this work during all stages of its development. That proactive effort is highly valued.

References

[1] Rompala, J. T. (2000), "Characteristics of the Rondonian Lightning Detection Network", Report LIV, NASA/MSFC, Research Reports, NASA/ASEE Summer Faculty Fellowship Program.

[2] Rompala, J. T. (2000), "Lightning Current Distribution Simulations for the Rondonian ALDF Network", Universities Space Research Association, Earth System Science Program.

[3] Rompala, J. T., Blakeslee, R. J., and Bailey, J. C. (2003), ”Detection Efficiency Contours for Regions Serviced by Lightning Detection Networks of Limited Scope”, Poster Presentation, 12th International Conference on Atmospheric Electricity.

2003

NASA FACULTY FELLOWSHIP PROGRAM

MARSHALL SPACE FLIGHT CENTER
THE UNIVERSITY OF ALABAMA IN HUNTSVILLE

DEVELOPMENT OF A FUZZY LOGIC CONTROLLER FOR USE IN THE APPROACH AND LANDING PORTION OF DESCENT

Prepared By:	Curtis A. Schmitt
Academic Rank:	Graduate Student
Institution and Department:	Rose-Hulman Institute of Technology Department of Mechanical Engineering
NASA/MSFC Directorate:	Space Transportation
MSFC Colleague:	Dr. John Hanson

Introduction:

In conjunction with the Next Generation Launch Technologies (NGLT) program, there has been a large motivation to develop Advanced Guidance and Control (AG&C) algorithms for Reusable Launch Vehicles (RLV). These algorithms offer additional autonomy as well as the capacity to account for large dispersions in initial conditions and aero-surface failures during the flight. The major impetus for AG&C is to create more cost effective, reliable, and safety based programs for the exploration and development of space initiatives.

During the return flight from orbit, there are three distinctive phases of flight: entry, terminal area energy management (TAEM), and approach and landing (A/L). This paper will present work conducted in the A/L phase of the return flight. The A/L phase of flight is divided into four distinct phases: steep glide slope, pre-flare, shallow glide slope, and final flare. For the duration of these A/L flight phases, there are only small changes in heading angle and the fact that the range-to-go is monotonically decreasing allow for many simplifications and tend to lead to a straightforward optimization. The work presented in this paper considers approach and landing without imposing these simplifications.

Fuzzy inference systems provide for direct application of human knowledge without analytically deriving a complicated control surface to determine the appropriate action.

Fuzzy Logic & Simulation Development

Everyday of our lives people take on and complete extremely complicated tasks without ever making any kind of measurements and/or mathematical calculations. An appropriate example is when a major league baseball pitcher is pitching. He/She does not have to know the exact finger placement on the baseball or angular rotation rate to throw a strike. The pitcher can quickly adapt to any situation and throw a variety of pitches to achieve the desired result; a strikeout. Fuzzy Logic supplies a methodology that allows for the combination of a large variety of information into a self-sufficient algorithm, making precise knowledge of the mathematical model or specific knowledge of the plant superfluous.

The dynamics used, to create the simulation in MATLAB, were gathered from Grantham's "Adaptive Critic Neural Network Based Terminal Area Energy Management/Entry Guidance," [1] and are listed below.

$$\dot{V} = -\frac{D}{m} - g\sin\gamma \qquad \dot{\gamma} = \frac{L\cos\phi}{mV} - \frac{g\cos\gamma}{V} \qquad \dot{\psi} = \frac{L\sin\phi}{mV\cos\gamma}$$

$$\dot{x} = V\cos\gamma\cos\psi \qquad \dot{y} = V\cos\gamma\sin\psi \qquad \dot{h} = V\sin\gamma$$

Applying the conservation of linear momentum to the vehicle, as a point mass system, in three-dimensional space reveals these equations of motion (eom). Using these equations a Fuzzy Logic Controller (FLC) was developed in MATLAB with two main channels (at right). The first channel uses the error in the y-position, varying from –2500 to 2500 ft., and the rate of change in

the y-position, deviating from –2500 fps to 2500 fps, to dictate the bank angle (ϕ) of the vehicle. The bank angle, phi, can vary from –30 degrees to 30 degrees in the roll plane. The second channel of the controller was developed using the error in altitude, the error in rate of change of the altitude, and the error in velocity to determine the negative z-axis acceleration (N_Z) and the speed brake position (spdbrk). The limits placed on the three errors involved in the second channel are as follows: altitude error between –2500 and 2500 feet, rate of change in altitude between –5000 and 5000 fps, and velocity error between –1000 and 1000 fps. The resulting commands dictated by this channel, N_Z and spdbrk; vary between –0.8 g and 0.8 g and 0 and 20 degrees respectively. This two channel Mamdani FLC uses some 253 rules to ascertain the proper output signals to be fed into the simulation. When the Mamdani controller is implemented the two channels act independently of one another in this 3-DOF simulation. The rule base has no cross term rules to take into account the velocity when determining the bank angle and vice-versa. The error values in this case are found by comparing the actual values given by the FLC (in green below) and the desired trajectory (in red below) within the MATLAB simulation: developed in SIMULINK.

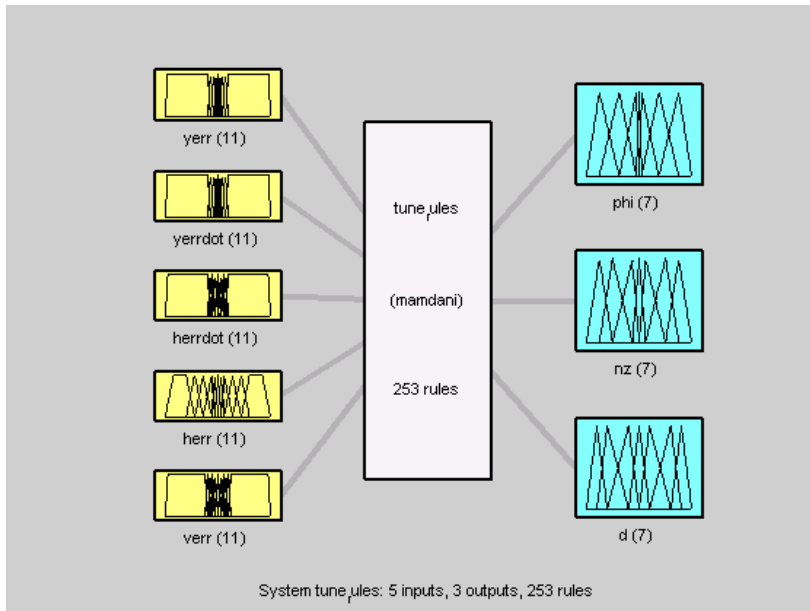

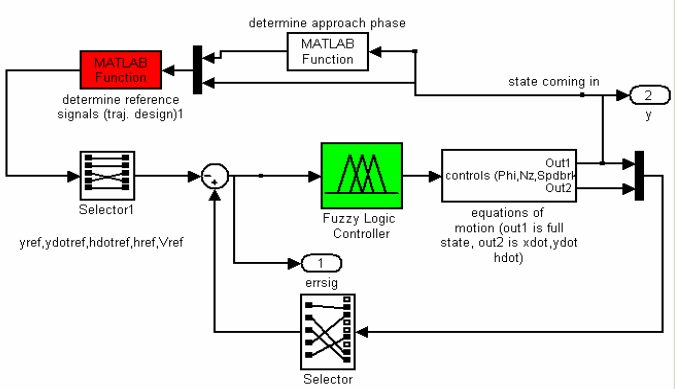

The trajectory designer (red block) implements the trajectory design from the current shuttle systems. This block sets forth the path that is to be followed and includes the four sections of A/L: steep glide slope, pre-flare, shallow glide slope, and final flare. As one can see from the block diagram the states of the system ('y') and the error signal ('errsig') are returned to the workspace for analysis.

Genetic Algorithm Development

The genetic algorithm (GA) allows for timely turn around in testing and developing the fittest FLC for the simulation. The genetic algorithm is very similar to natural selection in the

biological world. The population is the group of possible solutions and consists of thirty chromosomes, which are the consequents of the FLC. Each of the chromosomes is fed into the FLC via MATLAB and each is judged against the cost functions. Those with the lowest cost/highest fitness level have the greatest probability of mating and remaining in the gene pool. The mating pairs are chosen at random and are considered "asexual partners". Once the mother and father have been chosen, a random cross over site is chosen and the father and mother switch their chromosomes with the other (as can be seen below). These new chromosomes then become part of the next generation.

	Chromosome	Mutation Site (*)	New chromosomes
Mom	1100101110110011111	110010111011*0011111	1100101110110101100
Dad	0001100101000101100	000110010100*0101100	0001100101000011111

Once, the generation has been reproduced the process of finding the fittest chromosome begins again. The purpose of using a GA is to reach a near-optimal solution as quickly as possible: which is generally reached between ten and fifteen generations.

One of the stumbling blocks of using GAs is developing the cost function. The cost function is what determines the fittest chromosome. The reason that the cost function is so important is because the GA can actually "out-smart" the operator. It is extremely important that one is careful in preparing the cost function. I have seen this on two different occasions during my research this summer, which will be presented in the Results section.

Results

In this section, results of the simulation using two different cost functions are being presented. The first cost function is the mean squared error of the velocity, altitude, and y-distance. One can see the plots of its performance in Figures 1 and 2. In Figure 1, the FLC does not follow the predicted trajectory (green line) well at all and is unable to complete the pull-up/circular flare maneuver to land on the runway and Figure 2 shows large dispersions from the predicted velocity (pink line).

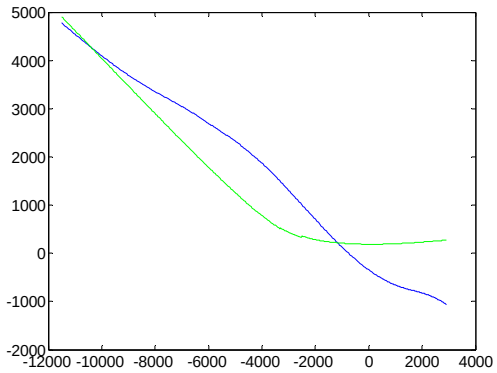

Figure 1: Altitude vs. Range-to-go Knowledge based

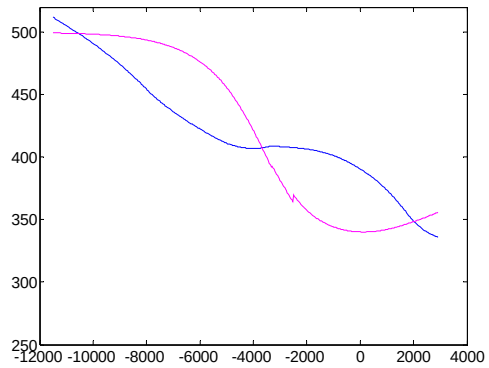

Figure 2: Velocity Profile-Knowledge Based

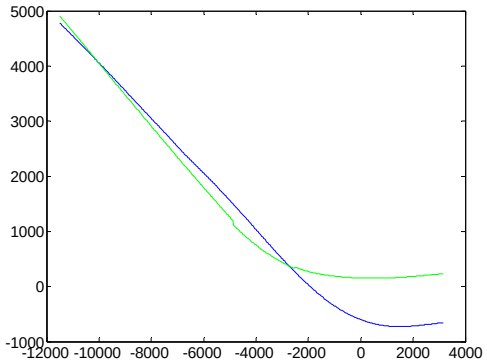

Figure 3: Altitude vs. Range-to-go G.A. Tuned

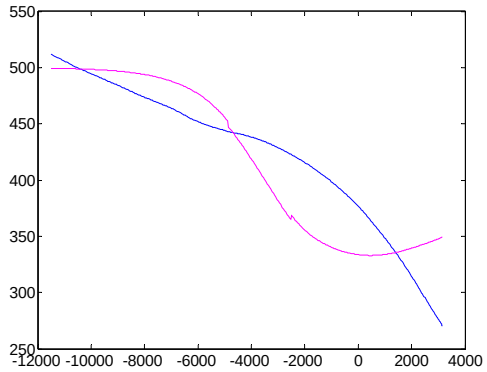

Figure 4: Velocity Profile-G.A. Tuned

Figures 3 and 4 are depictions of the second cost function: the mean squared error in energy height and mean squared error in the y-position. As one can see from the graphs the vehicle has much greater stability in the vertical plane. Unlike, the performance of the FLC in Figure 1, The GA tuned results show that the FLC is able to perform the pull-up/circular flare (blue line). In much the same manner the velocity profile shows improved behavior after implementing the GA: there is a decrease from approximately 100 fps dispersion to less than 50 fps dispersions in the velocity channel. This reinforces the idea of carefully choosing the cost function to evaluate each candidate FLC. As is evident in Figures 3 and 4, the vehicle has not yet reached the point of landing safely at the runway. However, this research has not yet matured to its full potential but great strides have been made this summer to reach that point.

Reference

[1] Grantham, K., "Adaptive Critic Neural Network Based Terminal Area Entergy Management/Entry Guidance," 41st AIAA Aerospace Sciences Meeting and Exhibit, Reno, NV 2003.

[2] Hanson, J., Coughlin, D., Dukeman, G., Mulqueen, J., and McCarter, J., "Ascent, Transition, Entry, and Abort Guidance Algorithm Design for the X-33 Vehicle," AIAA Paper 97-4409.

[3] Karr, C. L., (1999), "Practical Applications of Computational Intelligence for Adaptive Control," *International Series on Computational Intelligence*, CRC Press L.L.C., pp. 29-40, 85-98.

[4] Moore, T. E., "Space Shuttle Entry Terminal Area Energy Management," NASA Technical Memorandum 104744, Lyndon B. Johnson Space Center, Nov 1991.

[5] Phillips, M., "Terminal Area Energy Management (TAEM) and Approach and Landing (A/L) Design," NASA-MSFC TD54, Oct 2001.

[6] Class Notes, "Mechanical Engineering Course # 597: Intelligent Methods", Dr. Bradley Burchett, Rose-Hulman Institute of Technology, Spring Quarter—2002/2003.

2003

NASA FACULTY FELLOWSHIP PROGRAM

MARSHALL SPACE FLIGHT CENTER
THE UNIVERSITY OF ALABAMA IN HUNTSVILLE

USE OF MARKER STUDIES TO STUDY MATERIAL FLOW IN THE FRICTION STIR WELD PROCESS

Prepared By:	J.A. Schneider, Ph.D.
Academic Rank:	Assistant Professor
Institution and Department:	Department of Mechanical Engineering Mississippi State University Mississippi State, MS 39762
NASA/MSFC Directorate:	ED 33 Materials and Manufacturing Processes
MSFC Colleague:	A.C. Nunes, Jr.., Ph.D. R.W. Carter

Introduction

FSW is a solid state joining operation that was invented in 1991 at The Welding Institute (TWI) [1]. The process is potentially capable of joining a wide variety of aluminum alloys that are traditionally difficulty to fusion weld. The FSW process joins the material by moving a non-consumable rotating pin tool along a seam between work pieces that are firmly clamped to an anvil. At the start of a weld the rotating pin, shown in Figure 1, is plunged into the material to a pre-determined depth, it then travels the length of the weld seam. The mechanical work of the pin, transformed to heat, raises the temperature thereby softening the weld metal adjacent to the tool. The load on the tool shoulder and the supporting anvil reaction maintain a high hydrostatic pressure as the metal is literally stirred together. To produce a defect free weld, process parameters (RPM, travel speed, and downward force) and tool pin design must be chosen carefully. An accurate model of the material flow during the process is necessary to guide the process variable selection.

Observations of weld macro-structural features and the results of prior tracer experiments have provided a basis for the construction of a plastic slip line model of the friction stir welding process at MSFC [2, 3]. Although the model appears to have captured the main macro-structural features of the process, the micro-structural features and the underlying material specific interactions are not yet understood. In this study, thin longitudinal wires were stirred into the weld zone. X-ray radiography is used to document the resulting wire placement in an effort to interpret the material flow paths. These studies indicate an additional flow field may need to be considered in the modeling efforts at NASA-MSFC.

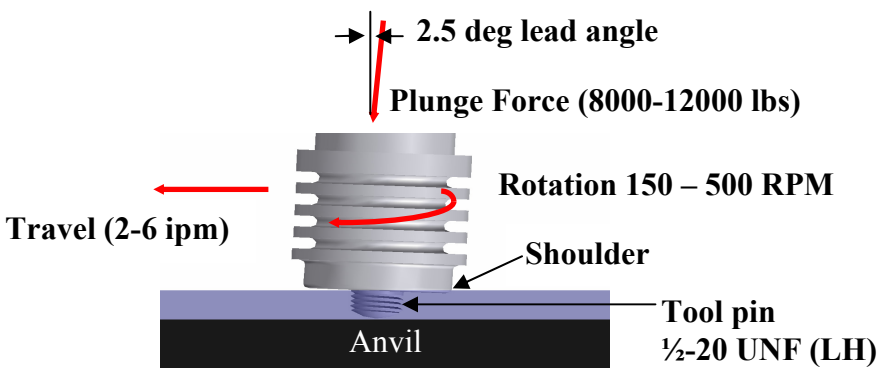

Figure 1. Schematic of conventional friction stir weld process.

Experimental Procedure

Two panels of aluminum alloy 2195-T81 were prepared for welding by scoring a groove 0.001" deep into the longitudinal side as shown in Figure 2. The groove was placed 0.05" below the surface toward the side of the shoulder placement. A thin tungsten wire, 0.001" dia., was placed along the groove and the plates were tack welded together. The tacks penetrated to a depth of 0.01" below the surface and didn't affect the wire. The Vertical Weld Tool (VWT) at NASA-

MSFC was used to make the off-centered weld with the wire located either toward the advancing side or the retreating side of the pin tool. All welds were made at a rotational speed of 200 rpm (CW) and a travel speed of 6 ipm. The weld tool consisted of a pin tool 0.5" in diameter with a smooth shoulder 1.2" in diameter.

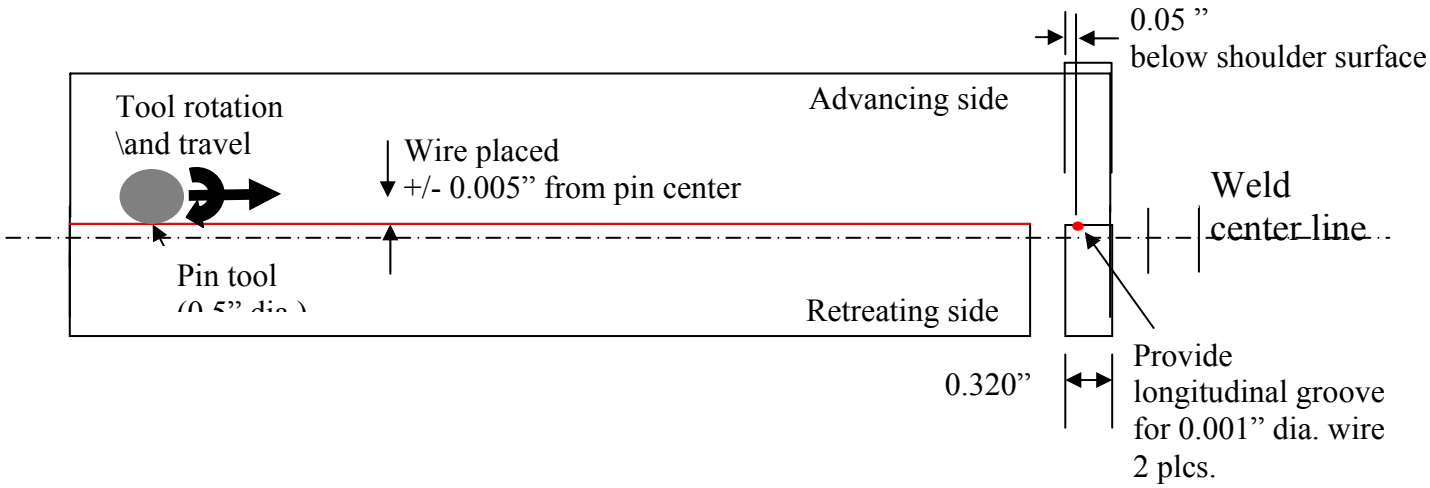

Figure 2. Weld panel geometry for tracer wire studies

Results and Discussion

Figure 3 shows x-ray radiographs of the tungsten wire following a the off-centered FS weld. The segments in Figure 3 show the hole left at the end of the weld as the pin tool is retracted. The

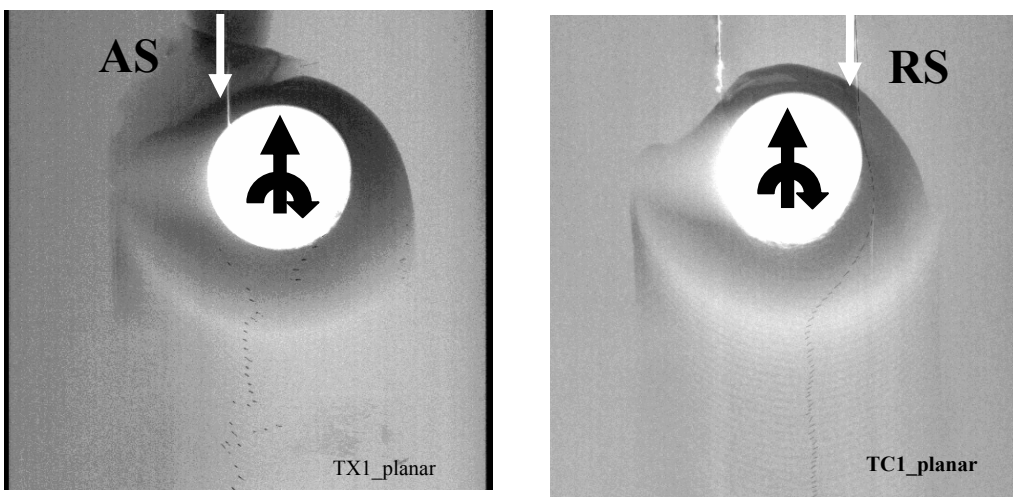

(a) **(b)**

Figure 3 X-ray radiographic images showing wire markers in the wake introduced into the (a) AS and (b) RS. Greater dispersion in position is observed from the marker introduced on the AS.

weld wake in both images show that the fine, 0.001" diameter wire has been broken into segments of uniform length. The wire introduced into the retreating side (AS) of the weld displays a chaotic behavior in the wake. The segments appear to be whisked around the pin tool very rapidly, leaving no trace around the exit hole of the pin tool hole shown in Figure 3 a. In contrast, the wire introduced on the advancing side (RS) of the weld, Figure 3 b, breaks up with the segments following the pin tool closely as it rotates clockwise and are deposited uniformly behind the middle of the off-centered weld seam.

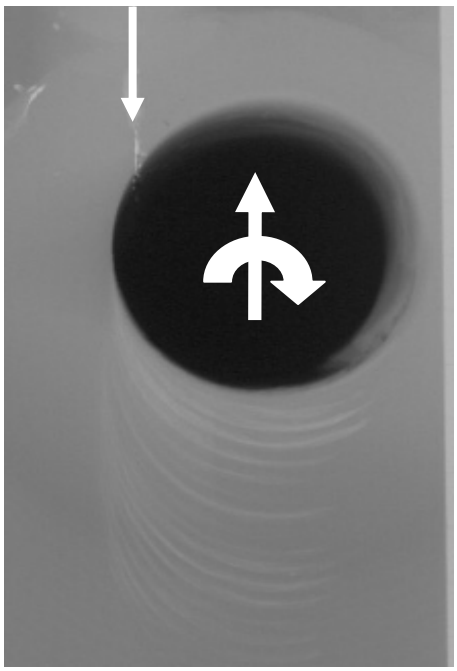

An additional off-centered FSW was performed with a 0.010" diameter lead wire inserted into the groove located 0.05" from the plate surface. The weld was made with the wire on the AS. Lead, with a melting temperature of 327.5º C, was expected to become liquid at the estimated welding temperature of 450º C. Figure 4 shows the paths left in the wake from the molten lead being 'wiped' around the pin tool. The lead marker was only observed in the x-ray radiograph at the end of the 6" weld and in the mid-travel distance of the weld. No evidence of the lead was observed at the start of the weld. As in Figure 3a, the wire introduce on the AS shows a more thorough distribution of the material into the weld wake.

Figure 4. Lead wire, molten at Al welding temperatures, traces out a path in the wake.

In both wire marker studies, the wire introduced on the AS left no evidence of segments around the pin tool exit hole. Whereas, the wire segments were observed to be uniformly distributed around the pin tool exit hole when introducted on the RS. This suggests that the rotating plug model [2] theorized earlier is requires an additional flow component to describe the material movement around the pin tool. In the rotating plug model, a velocity of 400 ipm and a shear rate of 10^8 s^{-1} have been estimated [4] in the shear zone around the plug, or primary rotation. If the wire is caught in this primary rotation, the wire segments would not be expected to be captured around the pin tool at the given weld parameters. However, that wire segments are captured around the pin tool from wire introduced on the RS suggests that a secondary shear, or induced rotation maybe present. From the spacing of the wire segments and weld parameters, a material velocity of 20 ipm can be calculated. If the material is drawn in close enough to the pin diameter, the material is whisked around in the primary rotation field further, resulting in greater distribution. As this material exits the primary rotation, it interacts with the ring vortex, which influences the flow patterns observed in the weld wake. The two rotating plugs are shown schematically in Figure 5.

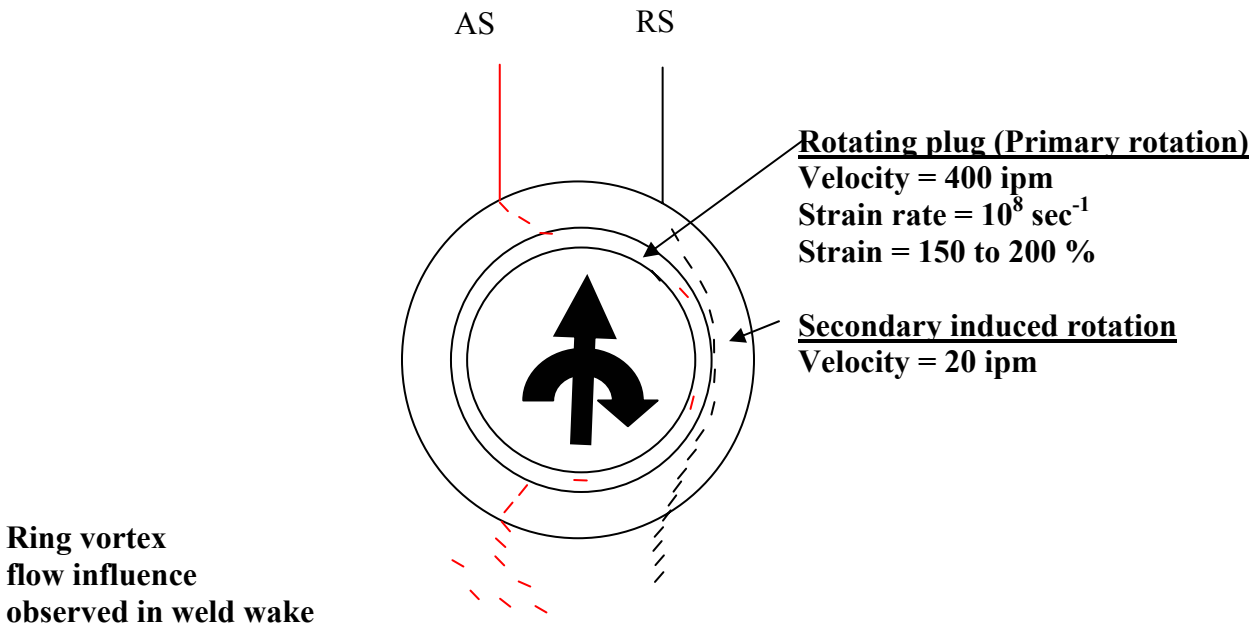

Figure 5. Macroscopic model needs additional rotational flow componenet, i.e. a secondary induced rotation, to explain observations.

Summary and Conclusions

- The distribution of wire segments around the pin tool suggests that the material from the weld AS undergoes greater dispersion than that from the retreating side.
- Secondary entrained flow around primary surface needs to be considered in flow model. It is possible that major down-flow occurs in the secondary flow region.
- Subsequent analysis can be made from the wire segments to calculate tangential and radial velocity profiles.
- Additional x-ray radiography or serial sectioning will be used to interpret the extent of up-and-down flow in the longitudinal plane of the weld.

References

1. W.M. Thomas, et. al., "Friction Stir Butt Welding," (1991) U.S. Patent No. 5,460,317.
2. A.C. Nunes, Jr., "Wiping Metal Transfer in Friction Stir Welding," *Aluminum 2001: proceedings of the 2001 TMS Annual Meeting Automotive Alloys and Joining Aluminum Symposia*, ed. G. Kaufmann, J. Green, S. Das, 2001, p. 235-248.
3. J.A. Schneider and A.C. Nunes, Jr., "Thermo-mechanical processing in friction stir welds," *Friction Stir Welding and Processing II*, ed. K.V Jata, M.W. Mahoney, R.S. Mishra, S.L. Sematin, T. Lienert, 2003, p. 43-51.
4. A.C. Nunes, Jr., Introduction to Friction Stir Welding, Chapter 2, "The Flow Field and the Microstructure of Friction Stir Welds", private internal documentation, March 2003.

2003

NASA FACULTY FELLOWSHIP PROGRAM

MARSHALL SPACE FLIGHT CENTER
THE UNIVERSITY OF ALABAMA IN HUNTSVILLE

DESIGN OF EXPERIMENTS AND DATA ANALYSIS OF NEW COMPOSITE MATERIAL FOR RADIATION SHIELDING AND STRUCTURAL EFFECTIVENESS

Prepared By:	Mohamed A. Seif.
Academic Rank:	Associate Professor
Institution and Department:	Alabama A&M University Mechanical Engineering Department
NASA/MSFC Directorate:	Science Directorate
MSFC Colleague:	Dr. Nasser Barghouty

Introduction

In recent years, high performance composites are widely used in weight sensitive applications such as space shuttles, aircrafts, cars, ships and other various types of vehicles. This has been attributed to their high strength/weight ratio that contributes to reducing fuel consumption and improving performance. With the wide use of composite materials in structural components, it has become necessary to develop new composite materials that meet new conditions.

This project concentrates on developing a new composite material for radiation shielding and structural effectiveness. The work concentrates mainly on the following:

1. Design of Experiments and Data Analysis
2. Failure Analysis
3. Finite Element Analysis

This work will help in establishing a better understanding of the behavior of the new composite material. In addition, the development of engineering models and design charts could be attained, thus contributing to improve basic studies of composite materials under various operational conditions.

Design of Experiments and Data Analysis

In developing a new composite material, a laboratory screening to determine the physical properties should be performed. Table 1 summarizes the standard test methods (ASTM Standards) used in determining the different properties of the new composite material. For Each test, the table provides the recommended specimen geometry, fiber orientation, ply count, number of specimens, and properties determined from the test. Figure 1 shows the experimental set up used in the tensile testing.

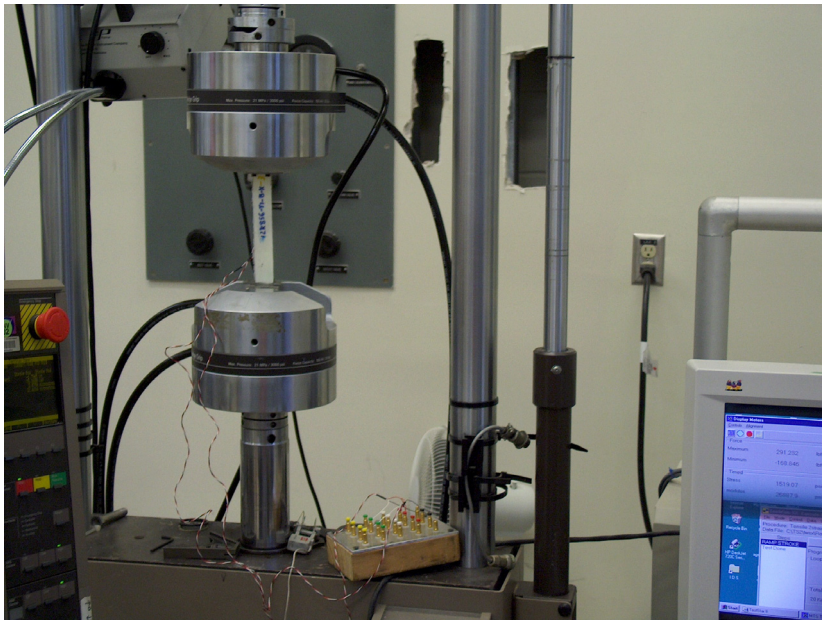

Figure 1: Experimental set up for tensile testing

Table 1: Summary of the standard test methods

ASTM Standard	Fiber Orientation	Ply count	Specimen Geometry (Recommendations)	No. of Specimens
D 3039 Tensile Properties (σ_{ut}, ε_{ut}, E_1, ν_{12}, ν_{21}, σ_y, ε_y)	0 unidirectional	8	Width: 0.5 in Overall length: 10.0 in Tab Length: 2.25 in Tab Thickness: 0.062 in Tab Bevel Angle: 7 or 90	3x7x3
	90 unidirectional	16	Width: 1.0 in Overall length: 7.0 in Tab Length: 1.0 in Tab Thickness: 0.062 in Tab Bevel Angle: 90	3x7x3
D 3410 Compressive Properties (σ_{uc}, ε_{uc}, E_1, ν_{12}, ν_{21}, σ_{yc}, ε_{yc})	0 unidirectional	8	Width: 0.5 in Overall length: 5.5-6.0 in Gage Length: 0.5-1.0 in Tab Length: 2.5 in Tab Thickness: 0.062 in	3x7x3
	90 unidirectional	16	Width: 1.0 in Overall length: 5.5-6.0 in Gage Length: 0.5-1.0 in Tab Length: 2.5 in Tab Thickness: 0.062 in	3x7x3
D 3518 In-plane Shear properties (τ, γ, G)	± 45° Laminate	16	Width: 1.0 in Overall length: 7.0 in Tab Length: 1.0 in Tab Thickness: 0.062 in Tab Bevel Angle: 90	6x7x3
D 3846 Interlaminar Shear (τ, γ, G)	0 unidirectional	42	Width: 0.5 in Overall length: 3.13 in Notch Width: 0.040-0.065 in Notch Depth: Half specimen thickness Notch from the edge: 1.43 in Distance bet. Notches: 0.25 in	6x7x3
D 5961 Bearing Response (σ_{bu}, ε_{bu}, E_b)	$[0,\pm45, 90]_{4S}$	32	Pin diameter, d: 0.25 +0.000/-0.001 in Hole diameter, D: 0.25 +0.001/-0.000 in Thickness range, h: 0.125-0.208 in Length, L: 5.5 in Width, w: 1.5 ±0.03 in Edge distance, e: 0.75± 0.03 in	7x3
D 5766 Open Hole Tensile Strength (σ_{hut})	$[0,\pm45, 90]_{2S}$	32	Width: 1.5 ±0.05 in Length range: 8.0-12.0 in Hole diam.: 0.25 ±0.003 in ***Note:*** while tabs may be used, they are not required and generally not needed.	7x3
D 6484 Open Hole Compressive Strength (σ_{huc})	$[0,\pm45, 90]_{2S}$	32	Width: 1.5 ±0.01 in Length: 12.0±0.01 in Hole diam.: 0.25 ±0.003 in ***Note:*** while tabs may be used, they are not required and generally not needed.	7x3

D 2990 Flexural Creep (δ)	$[0,\pm45, 90]_{4S}$ or $[0,\pm45, 90]_{8S}$	32 or 64	Preferred specimens sizes are: 2.5x0.5x0.125 in or 5.0x0.5x0.250 in ***Note:*** Close tolerances are not critical as long as actual dimensions are used.	2x7x3
E 1545 Thermo-mechanical Analysis (Tg, α)	0 unidirectional	24	Length, width, Height ≈ 0.125 in - Glass Transition Temperature, Tg - Coefficient of Thermal Expansion, α	7x3

Failure Analysis

Stresses around cracks are of great interest in design. The strength of a structure is greatly affected by the development of stress concentrations and damage growth around cracks. Such development results in decreasing the structure strength that reduces its life performance. Therefore, the evaluation of the stresses around cracks is very important in predicting the failure mode and the resistance of the material to the loading conditions.

The stress intensity factor is one of the important properties in fracture criteria. It depends on the state of the applied load and material configurations. The stress distribution around the crack-tip can always be separated into symmetric and skew-symmetric distributions. When the loading axis differs from the crack axis, the crack undergoes mixed mode loading. Symmetric loads cause the crack to open (Crack Opening Displacement, mode I), while skew-symmetric loads lead to forward sliding (Crack Shearing Displacement (CSD), mode II). The importance of measuring COD and CSD arises from their direct relationship to the fracture strength of the material. Once they are obtained, the critical stress intensity factors will be easily determined.

When composite laminates are subjected to biaxial states of stress, it is difficult to predict analytically the response of these laminates on the basis of lamina properties. This is because of the nonlinear behavior of the laminates and the failure-mode interaction. Various approaches have been developed for predicting biaxial properties of composites based on some limiting assumptions. It is necessary to perform extensive testing of composite laminates under biaxial state of stress to validate these theories and to develop useful failure methodology for design purposes.

The stress distributions around a crack-tip in orthotropic materials are given by the following expression:

$$\sigma_x = \frac{K_I}{\sqrt{2\pi r}} f_1\left(a_{ij},\alpha\right) + \frac{K_{II}}{\sqrt{2\pi r}} f_2\left(a_{ij},\alpha\right) \qquad (1.a)$$

$$\sigma_y = \frac{K_I}{\sqrt{2\pi r}} f_3\left(a_{ij},\alpha\right) + \frac{K_{II}}{\sqrt{2\pi r}} f_4\left(a_{ij},\alpha\right) \qquad (1.b)$$

$$\tau_{xy} = \frac{K_I}{\sqrt{2\pi r}} f_5\left(a_{ij},\alpha\right) + \frac{K_{II}}{\sqrt{2\pi r}} f_6\left(a_{ij},\alpha\right) \tag{1.c}$$

Where K_I and K_{II} are the stress intensity factors for mode I and mode II, respectively; r is the radial distance from the crack to the point of interest; α is the angle between the radius r and the axis of the crack; and a_{ij} are the compliance coefficients for the orthotropic plate. The normal stress on the crack is calculated from the following relation:

$$\sigma_n = \sigma_\infty \sin^2(\theta) \tag{2}$$

where σ_∞ is the remotely applied stress, and θ is the crack angle measured from the applied stress axis. The shear stress along the crack is determined by

$$\tau_{n\theta} = \sigma_\infty \sin(\theta)\cos(\theta) \tag{3}$$

The stress intensity factor for mode I is expressed in the following form

$$K_I = \sigma_\infty \sin^2(\theta)\sqrt{\pi a} \tag{4}$$

whereas the stress intensity factor for mode II takes the following form

$$K_{II} = \sigma_\infty \sin(\theta)\cos(\theta)\sqrt{\pi a} \tag{5}$$

From equations 4 and 5, the ratio between the stress intensity factors for mode II and mode I is given by

$$\frac{K_{II}}{K_I} = \cot\theta \tag{6}$$

The damage zone ahead of the crack (a_o) can be determined by using the average stress criterion

$$a_o = \frac{\sigma_f^2}{\sigma_o^2 - \sigma_f^2} 2a\sin(\theta) \tag{7}$$

where σ_f is the failure stress of the notched specimen, σ_o is the unnotched material strength and "a" is the half length of the crack. The strength reduction ratio can also be computed by rearranging equation (7) to take the following form

$$\frac{\sigma_f}{\sigma_o} = \sqrt{\frac{a_o}{a_o + 2a\sin(\theta)}} \tag{8}$$

The stress intensity factor is proportional to the stress component near the crack tip. Once the stress reaches critical value, the material fails, and the stress intensity factor is known as critical stress intensity factor. The critical stress intensity factor for mode I, K_{IC}, is given by

$$K_{IC} = \frac{(COD)_C\ E\sqrt{\pi a}}{4\left(a + a_o\right)} \tag{9}$$

where COD_C is the critical crack opening displacement at the center of the crack, and E is Young's modules of the material. The critical stress intensity factor for mode II, K_{IIC}, is obtained by

$$K_{IIC} = \frac{(CSD)_C\ E\sqrt{\pi a}}{4\left(a + a_o\right)} \tag{10}$$

where CSD_C is the critical crack shearing displacement. From equations 4 and 5, the critical stress intensity factors for mode I and mode II using the linear elastic fracture mechanics (LEFM) solution are given by

$$K_{IC} = \sigma_f \sin^2(\theta)\sqrt{\pi a} \tag{11}$$

$$K_{IIC} = \sigma_f \sin(\theta)\cos(\theta)\sqrt{\pi a} \tag{12}$$

Note that K_I, K_{II} and σ_∞ are replaced by K_{IC}, K_{IIC} and σ_f, respectively.
From equations 6, 9 and 10, the ratio between the critical stress intensity factors for mode II and mode I is

$$\frac{K_{IIC}}{K_{IC}} = \frac{(CSD)_C}{(COD)_C} = \cot\theta \tag{13}$$

The experimental and theoretical values should be compared to confirm the validity of the LEFM model for this material, and the use of COD and CSD as fracture criteria for studying mixed mode fracture mechanics problems.

The critical stress intensity factor for the laminate, K_C, is calculated by using an empirical formula, which is given by:

$$K_C = \sigma_f \sqrt{\pi\left[a\sin(\theta) + a_o\right]} \tag{14}$$

The material critical stress intensity factor, modified to include the projected crack length and a horizontal extension of the damage zone, is found to be nearly constant. This means that it is a constant value for the same materials.

Finite Element Analysis

Finite Element Analysis has been performed to determine the damage zone, the COD and the CSD of a laminate. Due to the lack of the mechanical properties of the new material and the need for more testing, the validity of the finite element analysis could not be confirmed.

Suggested Future Work

Recent developments in fracture mechanics and structural-life management demand that testing techniques not only detect, but also characterize flaws. Flaw characterization is needed to determine flaw criticality and predict the remaining life of components. Criticality of a flaw depends upon the size of the flaw, its shape and location, as well as its nature. Much work is still needed to advance the state-of-the-art of flaw characterization in advanced composite structures. The following summarizes some of the work that could be done to advance the current work:

1. Studying the behavior of bolted joints in composite structures (study the effect of washer size, tightening torque, bolt clearance, diameter/width ratio and hole quality.)
2. Investigate the effect of machining parameters (feed rate, drilling speed, surface roughness) on the performance of the composites
3. Fatigue Failure Analysis
4. Ballistic Impact (ballistic limit, failure modes)
5. Damage prediction and repair

Conclusion

A new composite material for radiation shielding and structural effectiveness has been developed. Using the ASTM standard test methods, design of experiments has been done to determine the mechanical and physical properties of such material. Failure analysis has been performed to determine the material critical stress intensity factor and other failure parameters. Since the project is still in the early stages and most of the material properties are not available, the Finite Element Model could not be tested.

Acknowledgements

The author would like to thank the Education Program at NASA – NASA Faculty Fellowship Program - for giving him the opportunity to work in this emerging technology. Special thanks for Dr. Nasser Barghouty and Dr. Raj Kaul for their guidance and support during the period of this program.

References

1. Abrate, S., Impact on Composite Structures, Cambridge University Press, 1998
2. Anderson, V.L. and McLean, R. A., Design of Experiments: A Realistic Approach, Marcel Dekker, 1974
3. Department of Defense Handbook, MIL-HDBK-17-1E, Polymer Matrix Composites, Volume 1-3, 23 January 1997
4. Hoa, S. V., Computer-Aided Design of Polymer-Matrix Composite Structures, Marcel Dekker, 1995
5. Meyers, M. A., Dynamic Behavior of Materials, John Wiley & Sons, 1994
6. Montgomery D. C., Design and Analysis of Experiments, 4th Ed., John Wiley & Sons, 1997
7. Montgomery D. C. and Runger, Applied Statistics and Probability for Engineers, 3rd Edition, John Wiley & Sons, 2003
8. Reifsnider, K. L. and Case, S. W., Damage Tolerance and Durability of Material Systems, John Wiley & Sons, 2002
9. Seif, M. A. and Shahjahan, M., "Mixed-mode Failure of Graphite/epoxy Composites," ASME Journal of Engineering Materials and Technology, Vol. 123, No. 3, July 2001, pp. 371-376.
10. Seif, M. A. and Dasari, N. B., "Effect of Combined Loading on Crack Opening and Shearing Displacements" Journal of Composite Materials, Vol. 52, March 2001, pp. 539-544.
11. Seif, M. A. and Short, S. R., "Determination of Residual Stresses in Thin-walled Composite Cylinders," Journal of Experimental Techniques, March/April 2002, pp 43 - 46.
12. Weber, D. C., and Skillings, J. H., A First Course in the Design of Experiments, CRC, 2000.

2003

NASA FACULTY FELLOWSHIP PROGRAM

MARSHALL SPACE FLIGHT CENTER
THE UNIVERSITY OF ALABAMA IN HUNTSVILLE

PRELIMINARY DESIGN AND MINIMUM MATERIAL COST ESTIMATES OF 1 TO 8-KILOMETER HEIGHT STEEL TOWERS FOR ELECTRO-MAGNETIC LAUNCH ASSIST SYSTEMS

Prepared By:	Ajay Shanker
Academic Rank:	Associate Professor
Institution and Department:	University of Florida School of Building Construction
NASA/MSFC Directorate:	Flight Projects
MSFC Colleague:	David Smitherman

Introduction

Design and construction of tall towers is a research effort in the Flight Projects Directorate for construction of electro-magnetic launch assist systems. Based on prior NASA research it was decided to construct a tower that has about 60-degrees sloping side and rails for an electromagnetic carriage vehicle. This is continuation of a similar research project on computerized design of tall towers that this author completed in the NFFP program in 2002.

SAP2000 Nonlinear version 8.2.3 (updated to May 2003) FEM structural design software was used for constructing the tower model. SAP 2000 has been used for designing many important structures, e.g., Petronas Towers, Malaysia, Eiffel Tower-II, Nevada, Las Vegas and Safeco field, Seattle, Washington and many other structures throughout the world. This software can generate extremely large structures. A Pentium-4 dual processor computer with 4GB of RAM was provided by NASA for this work. Author initially planned to design a 10-Km tall tower with one 60-degree sloping side but was able to complete only an 8-Km tower because of RAM limitations of 32-bit processors. The 8-Km tower model has 253,400 structural members. It may be noted that the computer processed data for about seven hours and then ran out of memory during construction of ninth kilometer.

Design Procedure

This design process first starts with a basic architectural design that is just sufficient to support its own weight. A modular design was used for completely automating the construction process. A 150mx150mx250m module (Figure1) was used to develop an 8-Km tall steel tower. The module is comprised of sixteen 75m long space truss beams, sixteen 62.5m long columns, four 106m long horizontal braces, eight 123m long diagonal braces and eight 145m long beam braces. Space truss built-up structural members of such lengths are not uncommon and can be easily constructed using existing steel sections produced by the steel industry. The module has an internal spatial node that connects twenty braces to beams and columns (Figure1). This 3D bracing allows for increased shear strength in all three directions and compounds bracing effects when additional modules are added (Figure 2). Calculations were made to find number of modules needed and spatial placement in each kilometer and then module was replicated in 32 different files; four for each kilometer of tower. The replication process allows tall 250m meter sides of the module to be supported by four braces at 90 degrees to each other at every 62.5 meters. Such a bracing system for columns will substantially reduce buckling effects

All 32 files were then combined and a 3D view of the resulting tower is shown in Figure 2. Individual bracing members were then designed for the module. As the structural members are very long in length, deflection criteria was used to calculate the weight per lineal foot for the structural members. An Excel spreadsheet was then used to combine weights of all members and size of columns needed at every 250m. The structural data for all thirty-two files from the software was included in the Excel spreadsheet for basic analysis of the tower (Table 1). The data presented in Table1 is based on use of A913 high strength low alloy steel with a Load Factor of 1.4 and Resistance Factor of 0.85. It may be noted that most of the steel columns will need special fabrication and therefore can be designed and built for slenderness ratio of less than 20. AISC permits 85% of yield stress as critical failure stress for columns with slenderness ration of less than 20. Therefore buckling of columns was excluded in this preliminary analysis.

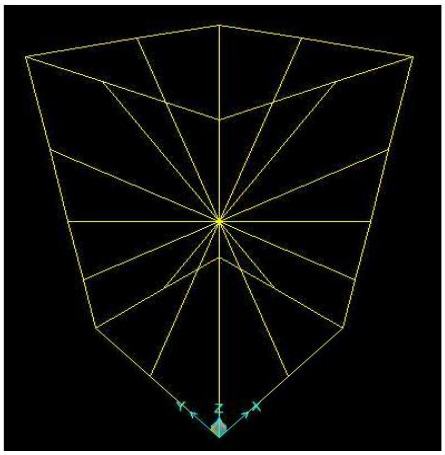

Figure1: Tower Module

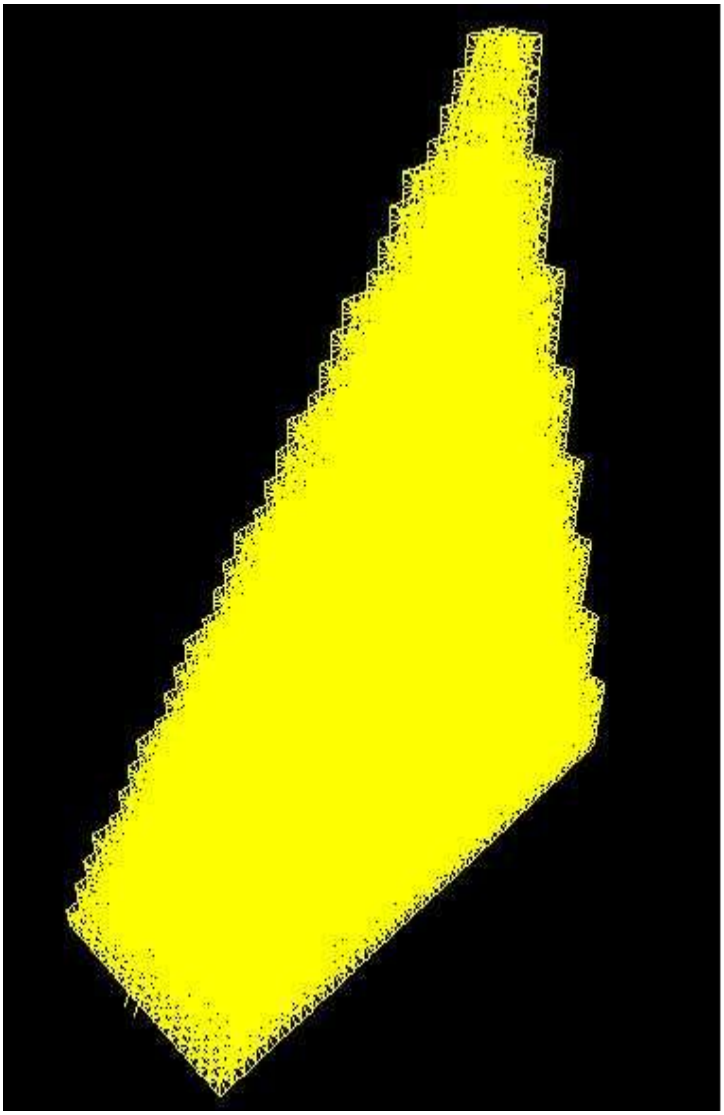

Figure 2: 3D View of 8-Km Tall Tower

.

No	Km	Total Col. Length Kms	Total Beam Length Kms.	Total Beam wt. 1000 kg.	Total Hoz. Brace Length Kms	Total Diag. Brace Length Kms	Total Beam Brace Length Kms	Total Wt. of Hoz. Braces 1000KG	Total Wt. of Diag Braces 1000KG	Total Wt. of Beam Braces 1000KG	Factored Wt of Beams & All Braces 1000KG	Cum Wt of Beams & All Braces 1000KG	Total Cum Wt Needed 1000KG	Cum Cost of Steel Mil $
1	7.75 - 8.00	4.00	3.60	234	3.82	8.86	10.44	420	1,107	1,566	4,657	9,657	10,110	5.561
2	7.50 - 7.75	5.00	4.65	302	5.09	11.81	13.92	560	1,476	2,088	6,196	15,854	17,072	9.389
3	7.25 - 7.50	6.00	5.70	371	6.36	14.76	17.40	700	1,845	2,610	7,735	23,589	25,949	14.272
4	7.00 - 7.25	7.00	6.75	439	7.63	17.71	20.88	840	2,214	3,132	9,274	32,863	36,818	20.250
5	6.75 - 7.00	13.50	13.95	907	16.96	39.36	46.40	1,866	4,920	6,960	20,513	53,376	59,909	32.950
6	6.50 - 6.75	15.00	15.60	1,014	19.08	44.28	52.20	2,099	5,535	7,830	23,069	76,445	86,685	47.677
7	6.25 - 6.50	16.50	17.25	1,121	21.20	49.20	58.00	2,332	6,150	8,700	25,625	102,070	117,270	64.499
8	6.00 - 6.25	18.00	18.90	1,229	23.32	54.12	63.80	2,565	6,765	9,570	28,180	130,250	151,792	83.486
9	5.75 - 6.00	28.00	30.30	1,970	38.58	89.54	105.56	4,244	11,193	15,834	46,537	176,787	206,919	113.805
10	5.50 - 5.75	30.00	32.55	2,116	41.55	96.43	113.68	4,571	12,054	17,052	50,109	226,896	268,073	147.440
11	5.25 - 5.50	32.00	34.80	2,262	44.52	103.32	121.80	4,897	12,915	18,270	53,682	280,578	335,433	184.488
12	5.00 - 5.25	34.00	37.05	2,408	47.49	110.21	129.92	5,224	13,776	19,488	57,254	337,833	409,174	225.046
13	4.75 - 5.00	47.50	52.65	3,422	68.69	159.41	187.92	7,556	19,926	28,188	82,729	420,561	512,401	281.821
14	4.50 - 4.75	50.00	55.50	3,608	72.50	168.26	198.36	7,975	21,033	29,754	87,318	507,879	624,501	343.476
15	4.25 - 4.50	52.50	58.35	3,793	76.32	177.12	208.80	8,395	22,140	31,320	91,907	599,786	745,702	410.136
16	4.00 - 4.25	55.00	61.20	3,978	80.14	185.98	219.24	8,815	23,247	32,886	96,496	696,283	876,230	481.927
17	3.75 - 4.00	72.00	81.00	5,265	107.27	248.95	293.48	11,800	31,119	44,022	129,088	825,371	1,045,627	575.095
18	3.50 - 3.75	75.00	84.45	5,489	111.94	259.78	306.24	12,313	32,472	45,936	134,694	960,065	1,227,241	674.983
19	3.25 - 3.50	78.00	87.90	5,714	116.60	270.60	319.00	12,826	33,825	47,850	140,300	1,100,365	1,421,352	781.744
20	3.00 - 3.25	81.00	91.35	5,938	121.26	281.42	331.76	13,339	35,178	49,764	145,906	1,246,272	1,628,236	895.530
21	2.75 - 3.00	101.50	115.35	7,498	154.34	358.18	422.24	16,977	44,772	63,336	185,616	1,431,888	1,883,871	1,036.129
22	2.50 - 2.75	105.00	119.40	7,761	159.85	370.97	437.32	17,583	46,371	65,598	192,239	1,624,126	2,155,569	1,185.563
23	2.25 - 2.50	108.50	123.45	8,024	165.36	383.76	452.40	18,190	47,970	67,860	198,861	1,822,988	2,443,660	1,344.013
24	2.00 - 2.25	112.00	127.50	8,288	170.87	396.55	467.48	18,796	49,569	70,122	205,484	2,028,472	2,748,470	1,511.659
25	1.75 - 2.00	136.00	155.70	10,121	209.88	487.08	574.20	23,087	60,885	86,130	252,311	2,280,783	3,112,415	1,711.828
26	1.50 - 1.75	140.00	160.35	10,423	216.24	501.84	591.60	23,786	62,730	88,740	259,951	2,540,734	3,496,769	1,923.223
27	1.25 - 1.50	144.00	165.00	10,725	222.60	516.60	609.00	24,486	64,575	91,350	267,590	2,808,324	3,901,912	2,146.051
28	1.00 - 1.25	148.00	169.65	11,027	228.96	531.36	626.40	25,186	66,420	93,960	275,230	3,083,554	4,328,220	2,380.521
29	0.75 - 1.00	175.50	202.05	13,133	273.90	635.66	749.36	30,129	79,458	112,404	329,175	3,412,729	4,824,546	2,653.500
30	0.50 - 0.75	180.00	207.30	13,475	281.11	652.39	769.08	30,922	81,549	115,362	337,831	3,750,560	5,346,128	2,940.370
31	0.25 - 0.50	184.50	212.55	13,816	288.32	669.12	788.80	31,715	83,640	118,320	346,487	4,097,047	5,893,396	3,241.368
32	0.00 - 0.25	189.00	217.80	14,157	295.53	685.85	808.52	32,508	85,731	121,278	355,144	4,452,191	6,466,776	3,556.727

Table 1: Preliminary Weight and Material Cost Data for 8-Km Tower

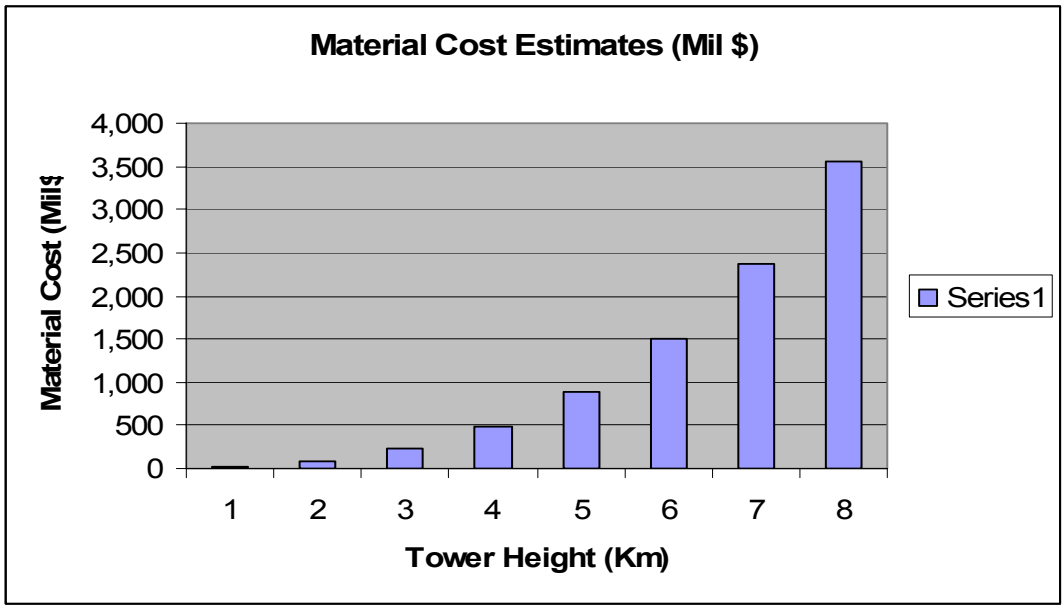

Figure 3: Material Cost Estimates for 1 to 8 Km Tall Towers

Limitations, Conclusions and Recommendations

Based on the tower geometry and other assumptions, it is concluded that construction of an 8-KM self supporting steel tower is possible. The minimum material costs, however, may exceed 3.55 billion dollars. The tower in the present study includes eleven million pounds of static weight for the launch vehicle but not the wind and earthquake analysis. The cost of substructure and labor involved are extremely difficult to estimate but will definitely add additional 4-12 billion dollars. All structural members can be built using existing material sizes with little or no need for specialized design and fabrication. Please send your input to author at shankerajay@hotmail.com.

This research is the first attempt to approximately quantify the steel requirements of 1-8 KM tall steel towers. Future research should address labor and installation costs that include advanced robotic construction techniques. Materials, e.g., composites, aluminum and concrete should also be explored for reducing cost. As the tower files become extremely large (160MB for this example) a faster computer with 4-8MB of RAM and 64-bit processors should be used to do analysis. Number of columns should be increased as a faster rate as we approach lower parts of the tower. Effects of wind, earthquake, temperature changes and equipment thrust and vibrations should be included to modify the structure.

Acknowledgements

The author wishes to extend sincere appreciation to Mr. David Smitherman for reviewing and providing valuable input continuously throughout the project duration. The author would also like to thank Mr. Joe Howell and Mr. Wayne Parks of Flight Projects Directorate, at Marshall Space Flight Center, Huntsville, Alabama, for their help in completing the work.

2003

NASA FACULTY FELLOWSHIP PROGRAM

MARSHALL SPACE FLIGHT CENTER
THE UNIVERSITY OF ALABAMA IN HUNTSVILLE

ANALYSIS OF A ROTATING VAPOR COMPRESSION DISTILLATION SYSTEM FOR URINE PURIFICATION

Prepared by:	Dr. Muhammad A.R. Sharif
Academic Rank:	Associate Professor
Institution and Department:	The University of Alabama Aerospace Engineering and Mechanics Department
NASA/MSFC Directorate:	Flight Projects
MSFC Colleague:	Donald W. Holder

Introduction

NASA Marshall Space Flight Center (MSFC) is developing a urine recovery system for the International Space Station (ISS). The urine recovery system is based on vapor compression distillation process (VCD). The urine is discharged on the inside surface of a slightly tapered rotating cylinder. The component of the centrifugal force drives the urine film up along the tapered surface. The inside space of the cylinder is maintained at a very low pressure and the urine is evaporated from the moving film surface. The resulting steam is compressed by a rotary lobe compressor and is discharged into the annular space between the above-mentioned tapered cylinder and another tapered coaxial and co-rotating outer cylinder. The steam condenses on the inner surface of the outer cylinder and is again driven up along its tapered surface by the component of the centrifugal force and is collected in a circumferential trough at the other end. The condensing steam releases the latent heat of condensation in the annular space, which is conducted through the inner cylinder wall and heats the urine film moving up the inner surface of the inner cylinder thereby assisting the evaporation of the film. The excess concentrated urine (brine) in the inner cylinder, which is not evaporated, is also collected in a circumferential trough at the end. The purified condensed water and the excess brine collected in the circumferential troughs are pumped through stationary tubing by the ramming action of rotation for further processing. The entire assembly is housed in a stationery bowl or cylinder. A cross-sectional view of the assembly is shown in Fig. 1.

The main objective of this report is to develop and analyze a theoretical/mathematical model of the associated thermal-fluid dynamic processes in the above mentioned vapor compression distillation system so that further numerical/mathematical analysis and predictions can be conducted. The developed model can be used to supplement the ongoing experimental investigation and testing of the system at NASA MSFC.

The operation of the VCD system is very similar to the rotating heat pipe operation originally proposed by Gray (1969). A schematic representation of the rotating heat pipe, duplicated from Marto (1973) is shown in Fig. 2. It consists of a sealed hollow shaft, having a slight internal taper from one end to the other, and containing a fixed amount of working fluid. When the shaft is rotated at high speed about its longitudinal axis, the working fluid collects as an annulus at the larger end. Heat added to this end of the shaft (evaporator) evaporates/boils the working fluid, generating vapor, which then flows axially toward the smaller end. Heat removed from this end of the shaft (condenser) condenses the vapor. The component of the centrifugal force along the inside surface of the shaft accelerates the liquid condensate back to the evaporator to complete the cycle. An adiabatic section at the middle separates the evaporator and condenser sections.

Marto and his group did extensive theoretical and experimental analysis of the rotating heat pipe in early 1970 at Naval Post Graduate School in Montery, California [Ballback (1969),

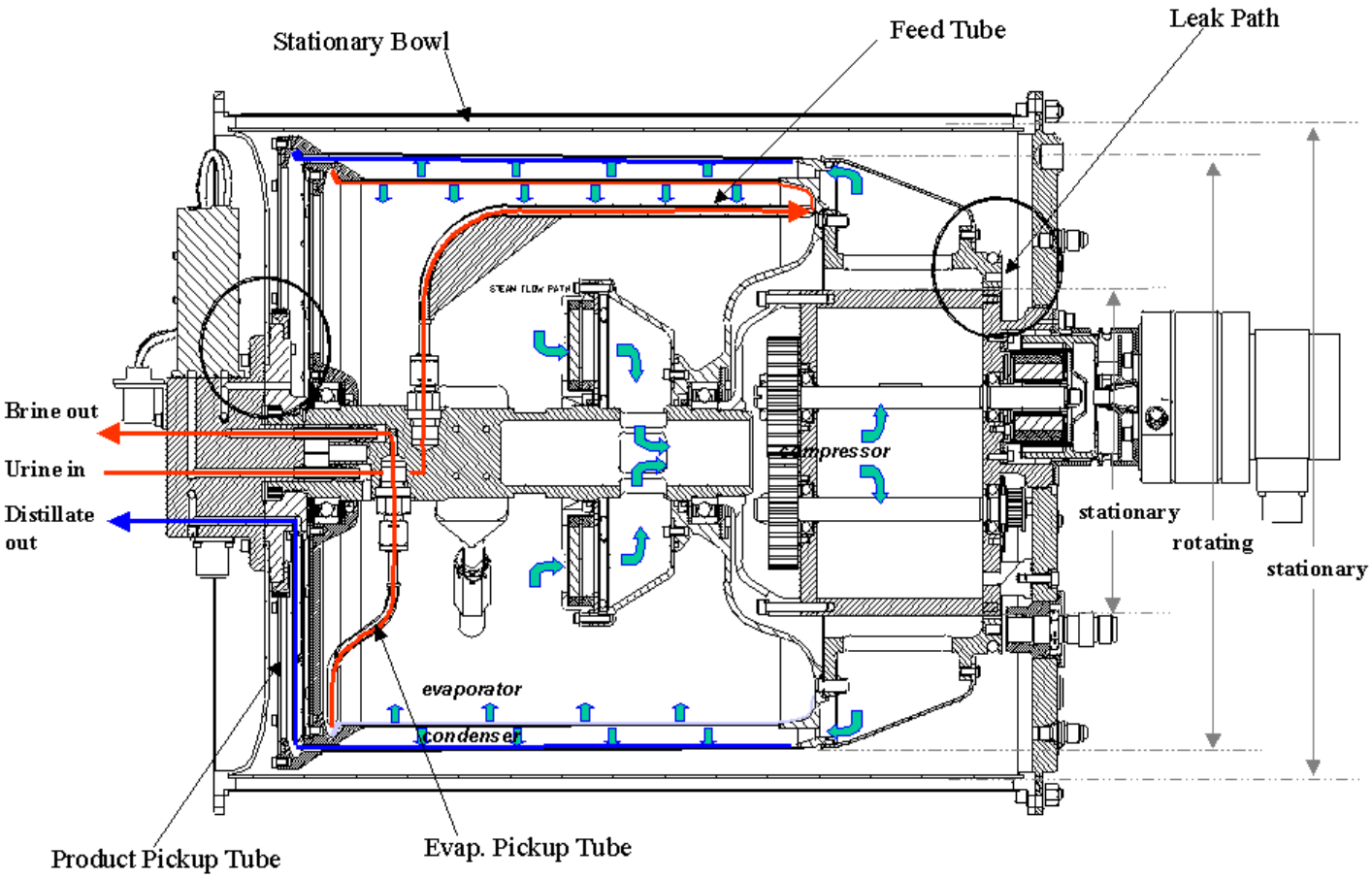

Daley (1970), Newton (1971), and Woodard (1972)]. Further theoretical, experimental, and numerical analysis of the rotating heat pipe system was conducted by Daniels and Al-Jumaily (1975), Roetzel (1977), Daniels and Williams (1977), Daniels and Williams (1978), Daniels and Williams (1979), Faghri et al. (1993), Li et al. (1993), and Harley and Faghri (1995), among others.

Theoretical Analysis

The subsequent theoretical development for the VCD system in this report closely follows that of Marto (1973) for the rotating heat pipe analysis due to the similarity of both systems. The major processes involved in the VCD system are evaporation of the urine film along surface of the rotating inner drum, compression of the vapor by the rotating lobe compressor, and filmwise condensation of the vapor along the surface of the rotating outer drum.

Hydrodynamics of the Moving Liquid Film with Negligible Gravity. The assumptions made here are:

(a) filmwise evaporation or condensation,
(b) the flow in the film is laminar,
(c) the inertial and convective effects are negligible in the liquid film,

(d) the thickness of the film is negligible compared to the radius of the cylinder
(e) temperature variation within the film is linear,
(f) the vapor space is at constant pressure,
(g) fluid properties in the film are assumed constant,
(h) the density of the liquid is much greater than that of the vapor,
(i) gradients in the circumferential direction is negligible,
(j) effect of gravity is negligible,
(k) the taper angle of the cylinder surface is very small, and
(l) the cylinder wall surface temperature is uniform over its length.

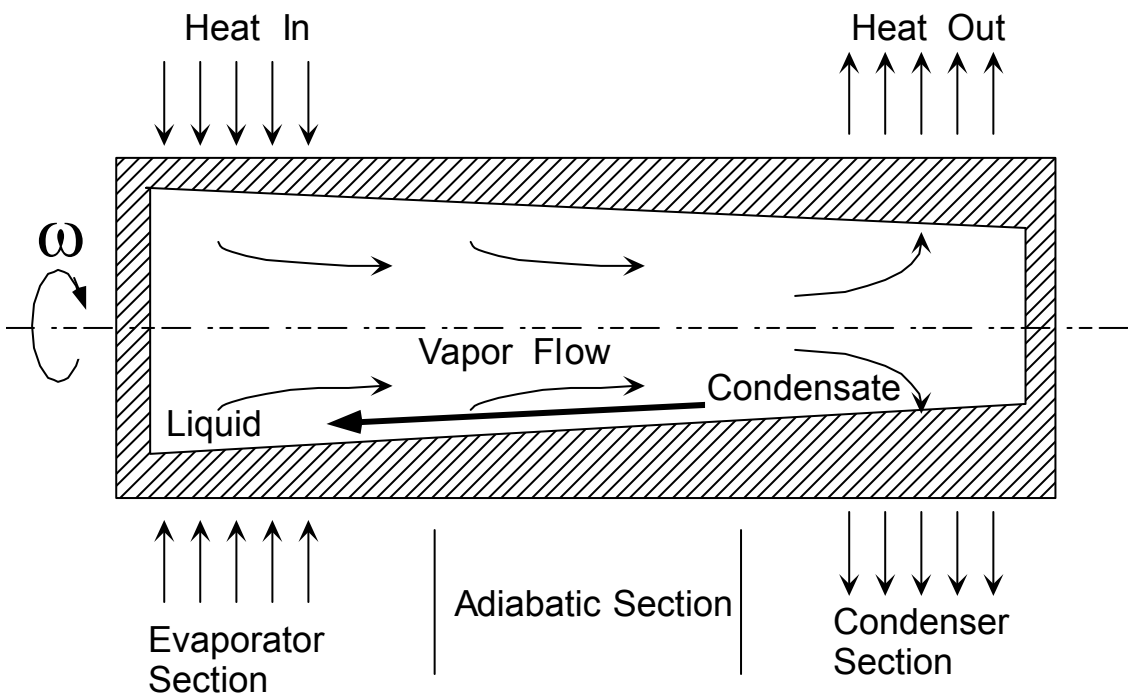

Figure 2. Schematic representation of the rotating heat pipe.

Fig. 3 shows a differential liquid element and the various forces acting on it. The *x*-direction is chosen along the tapered surface while the *y*-direction is perpendicular to the surface. Assuming that the momentum changes within the liquid film are small, a static force balance in the *x*- and *y*- direction gives

$$p\,dy - \left(p + \frac{\partial p}{\partial x}dx\right)dy - \tau\,dx + \left(\tau + \frac{\partial \tau}{\partial y}\right)dx + \rho_f\,dx\,dy\,\omega^2 r \sin\phi = 0$$

and

$$p\,dx - \left(p + \frac{\partial p}{\partial y}dy\right)dx - \rho_f\,dx\,dy\,\omega^2 r \cos\phi = 0$$

which after simplification yield

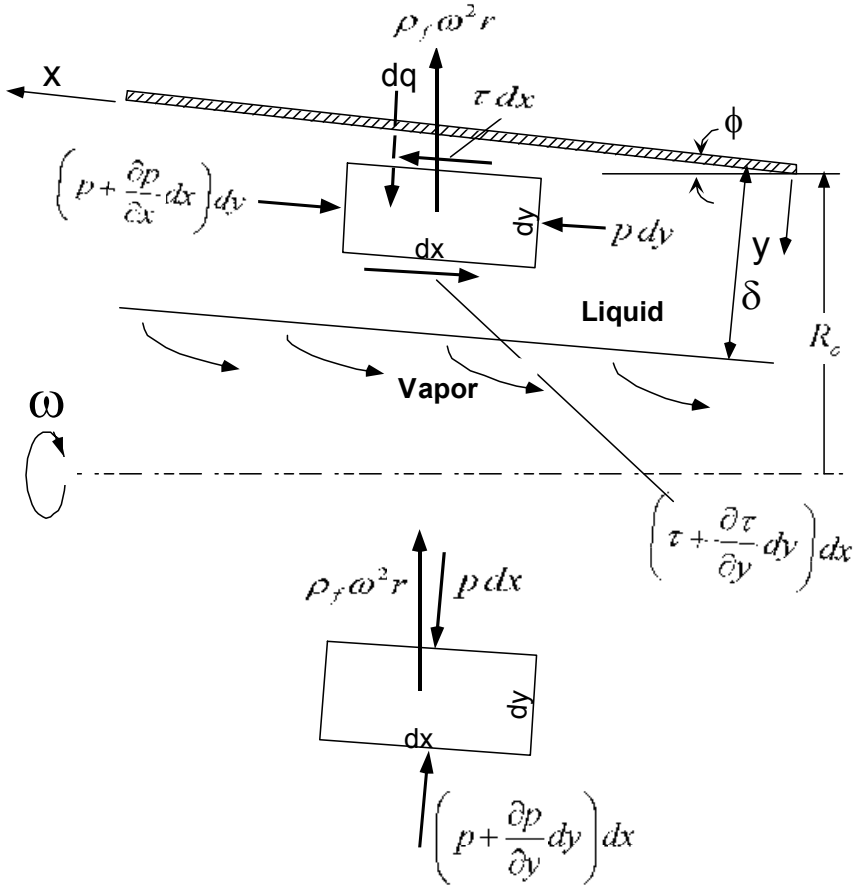

Figure 3. Differential liquid element and the forces acting on it.

$$\frac{\partial \tau}{\partial y} - \frac{\partial p}{\partial x} + \rho_f \omega^2 r \sin\phi = 0 \tag{1}$$

$$\frac{\partial p}{\partial y} + \rho_f \omega^2 r \cos\phi = 0 \tag{2}$$

where τ = local shear stress, p =local pressure, r = local radius to the centroid of the liquid element from the axis of rotation, ϕ = taper angle of the cylinder surface measured from the axis, ρ_f = density of the liquid, and ω = angular speed of rotation of the cylinder. The local radius in the liquid film may be expressed as

$$r(x, y) = R_o + x\sin\phi - y\cos\phi \tag{3}$$

where R_o is the minimum radius to the cylinder wall at the beginning. Substituting Eq. (3) into Eq. (2) and integrating

$$\int_p^{p_v} dp = \int_y^{\delta} -\rho_f \omega^2 (R_o + x\sin\phi - y\cos\phi)\cos\phi\, dy$$

where $\delta(x)$ is the local film thickness and $p_v(x)$ is the local vapor pressure at the surface of the film. After performing the integration we obtain

$$p(x, y) = p_v(x) + \rho_f \omega^2 \cos\phi \left[(R_o + x\sin\phi)(\delta - y) - \frac{1}{2}\cos\varphi(\delta^2 - y^2) \right] \tag{4}$$

Differentiating Eq. (4) with respect to x we obtain

$$\frac{\partial p}{\partial x} = \frac{dp_v}{dx} + \rho_f \omega^2 \cos\phi \left[R_o \frac{d\delta}{dx} + x \sin\phi \frac{d\delta}{dx} + \delta \sin\phi - \delta \cos\phi \frac{d\delta}{dx} \right]$$

Substituting this result into Eq. (1), and integrating from y to $\delta(x)$ where the shear stress varies from τ to $-\tau_v$

$$\int_{\tau}^{-\tau_v} d\tau = \int_{y}^{\delta} \frac{dp_v}{dx} dy + \int_{y}^{\delta} \rho_f \omega^2 \cos\phi \left[R_o \frac{d\delta}{dx} + x \sin\phi \frac{d\delta}{dx} + \delta \sin\phi - \delta \cos\phi \frac{d\delta}{dx} \right] dy$$
$$- \int_{y}^{\delta} \rho_f \omega^2 \left(R_o + x \sin\phi - y \cos\phi \right) \sin\phi \, dy$$

Performing the integration we obtain

$$\tau = -\tau_v - \frac{dp_v}{dx}(\delta - y) + \rho_f \omega^2 \left(R_o + x \sin\phi - \delta \cos\phi \right) \left(\sin\phi - \cos\phi \frac{d\delta}{dx} \right) (\delta - y)$$
$$- \rho_f \omega^2 \cos\phi \sin\phi \left(\delta^2 - y^2 \right) / 2$$

The last term in the right hand side of this equation can be neglected assuming very small film thickness δ and very small taper angle ϕ. Assuming laminar flow the shear stress τ can be expressed as $\tau = \mu_f \partial u / \partial y$ where μ_f is the viscosity of the liquid and $u(x, y)$ is the component of velocity in the liquid film along the tapered surface of the cylinder. Thus the above equation can be written as

$$\mu_f \frac{\partial u}{\partial y} = -\tau_v - \frac{dp_v}{dx}(\delta - y) + \rho_f \omega^2 \left(R_o + x \sin\phi - \delta \cos\phi \right) \left(\sin\phi - \cos\phi \frac{d\delta}{dx} \right) (\delta - y) \quad (5)$$

Integrating Eq. (5) from 0 to y in which the velocity varies from 0 to u gives an expression for the velocity component as

$$u(x, y) = -\frac{\tau_v}{\mu_f} y - \frac{1}{\mu_f} \frac{dp_v}{dx} y(\delta - y/2)$$
$$+ \frac{\rho_f \omega^2}{\mu_f} \left(R_o + x \sin\phi - \delta \cos\phi \right) \left(\sin\phi - \cos\phi \frac{d\delta}{dx} \right) y(\delta - y/2) \quad (6)$$

In the above derivation, surface tension forces due to the curvature of the liquid-vapor interface have been neglected. Thus the analysis is restricted to practical applications where the average radius of the cylinder is not very small. This is the case for the present analysis. Furthermore for the present application, the vapor velocity and the gradient of the vapor pressure is assumed to be negligible. This means the shear stress at the liquid vapor interface, τ_v, and the pressure gradient term dp_v / dx in Eq. (6) can be omitted. With these assumptions Eq. (6) is modified as

$$u(x, y) = \frac{\rho_f \omega^2}{\mu_f} \left(R_o + x \sin\phi - \delta \cos\phi \right) \left(\sin\phi - \cos\phi \frac{d\delta}{dx} \right) y(\delta - y/2) \quad (7)$$

The mass flow rate, $\dot{m}_f$, through the circumferential liquid film of thickness, δ, is given as

$$\dot{m}_f = \int_0^{\delta} \rho_f u \; 2\pi\left(R_o + x\sin\phi - y\cos\phi\right)dy \tag{8}$$

Substituting $u(x, y)$ from Eq. (7) into Eq.(8) and integrating,

$$\dot{m}_f = \frac{2\pi\rho_f^2\omega^2}{\mu_f}\left(R_o + x\sin\phi - \delta\cos\phi\right)\left(\sin\phi - \cos\phi\frac{d\delta}{dx}\right)$$
$$\times\int_0^{\delta}\left[\left(R_o + x\sin\phi\right)\left(\delta y - \frac{y^2}{2}\right) - \cos\phi\left(\delta y^2 - \frac{y^3}{2}\right)\right]dy$$

or

$$\dot{m}_f = \frac{2\pi\rho_f^2\omega^2}{\mu_f}\left(R_o + x\sin\phi - \delta\cos\phi\right)\left(\sin\phi - \cos\phi\frac{d\delta}{dx}\right)$$
$$\times\left[\frac{\delta^3}{3}\left(R_o + x\sin\phi\right) - \frac{5}{24}\delta^4\cos\phi\right] \tag{9}$$

The temperature variation within the liquid film thickness is assumed to be linear, i.e., the heat transfer between the cylinder wall at a temperature, T_w, and the liquid-vapor interface at the saturation temperature, T_{sat}, is by conduction only. This assumption is valid for ordinary fluids with Prandtl number above 1. Thus the heat transfer across the film element of length dx is

$$dq = -k_f A\frac{dT}{dy} = -k_f 2\pi(R_o + x\sin\phi)\,dx\frac{T_{sat} - T_w}{\delta}$$

where k_f is the thermal conductivity of the liquid and A is the peripheral surface area of the film element. This amount of heat is to be provided for evaporation or to be rejected for condensation. Thus $dq = h_{fg}d\dot{m}_f$ where h_{fg} is the latent heat of evaporation or condensation and $d\dot{m}$ is the mass of the liquid evaporated from the liquid element or condensed into the liquid element. Hence,

$$\frac{dq}{dx} = h_{fg}\frac{d\dot{m}_f}{dx} = -k_f 2\pi(R_o + x\sin\phi)\frac{T_{sat} - T_w}{\delta} \tag{10}$$

Differentiating Eq. (9) with respect to x

$$\frac{d\dot{m}_f}{dx} = \frac{2\pi\rho_f^2\omega^2}{\mu_f}\left[\left(R_o + x\sin\phi - \delta\cos\phi\right)\left(\sin\phi - \cos\phi\frac{d\delta}{dx}\right)\frac{\delta^3}{3}\sin\phi\right.$$
$$+\left(\sin\phi - \cos\phi\frac{d\delta}{dx}\right)\left(\frac{\delta^3}{3}\left(R_o + x\sin\phi\right) - \frac{5}{24}\delta^4\cos\phi\right)\sin\phi$$
$$\left.-\left(R_o + x\sin\phi - \delta\cos\phi\right)\left(\frac{\delta^3}{3}\left(R_o + x\sin\phi\right) - \frac{5}{24}\delta^4\cos\phi\right)\cos\phi\frac{d^2\delta}{dx^2}\right]$$

Substituting this in Eq. (10) and rearranging

$$
\begin{aligned}
&\left(R_o + x\sin\phi - \delta\cos\phi\right)\left(\frac{\delta^4}{3}\left(R_o + x\sin\phi\right) - \frac{5}{24}\delta^5\cos\phi\right)\cos\phi\frac{d^2\delta}{dx^2} \\
&+\left\{\left(R_o + x\sin\phi - \delta\cos\phi\right)\frac{\delta^4}{3} + \left(\frac{\delta^4}{3}\left(R_o + x\sin\phi\right) - \frac{5}{24}\delta^5\cos\phi\right)\right\}\sin\phi\cos\phi\frac{d\delta}{dx} \\
&-\left\{\left(R_o + x\sin\phi - \delta\cos\phi\right)\frac{\delta^4}{3} + \left(\frac{\delta^4}{3}\left(R_o + x\sin\phi\right) - \frac{5}{24}\delta^5\cos\phi\right)\right\}\sin^2\phi \\
&= \frac{\mu_f k_f\left(T_{sat} - T_w\right)}{\rho_f^2\omega^2 h_{fg}}\left(R_o + x\sin\phi\right)
\end{aligned}
\tag{11}
$$

Eq. (11) is a second-order nonlinear differential equation for $\delta(x)$, which can be integrated by a numerical method such as the Runge-Kutta scheme. The two required initial conditions are

$$
\text{at } x = 0, \quad \delta = \delta_i, \quad \text{and } \frac{d\delta}{dx} = \tan\phi \tag{12}
$$

The second condition is a consequence of assuming the velocity u being zero at $x = 0$ in Eq. (6).

Gravity Effects. The above analysis for the determination of the film thickness along the tapered cylindrical surface is done with the assumption that the gravity effects are negligible. Consequently the radial film thickness is assumed constant along the azimuthal direction. If the gravity effects are taken into consideration with the cylinder axis being horizontal, the problem is no longer axisymmetric and the analysis becomes considerably more difficult due to the interaction of the gravity and centrifugal forces. The radial film thickness is not axisymmetric during startup conditions or while operating below certain critical rotating speed. Depending on the angular speed of rotation the condition may be annular flow where the film thickness is uniform or rimming flow where the radial film thickness is nonuniform due to the interaction of the gravity, centrifugal, and the wall shear force. Fig. 4, reproduced from Baker et al. (2001), schematically illustrates these conditions where Ω is the rotational speed and Ω_c is the critical angular speed with $\Omega_2 < \Omega_c < \Omega_1$. In their experimental study Baker et al. (2001) observed that as the rotational speed increased during startup the onset of annular flow occurred only at certain axial locations and did not happen throughout the length of the cylinder simultaneously. Complete annular flow along the entire length was observed to occur at a certain critical angular speed. On the other hand, during shut down, the collapse of annular flow occurred at a certain angular speed, which is not necessarily the same as the onset of annular flow due to hysteresis effect. Thus they define three different flow regimes, *vig.*, onset of annular flow, complete annular flow, and collapse of annular flow.

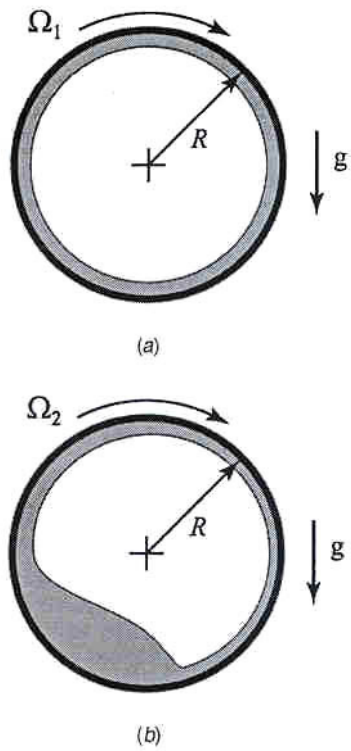

Figure 4. Schematic representation of (a) annular flow and (b) rimming flow.

Theoretical and experimental analysis of annular and rimming flows inside a uniform (axially non-tapered) circular cylinder with horizontal axis and gravity acting vertically downward direction has been done by numerous investigators in the past. Among the theoretical studies the works of Ruschak and Scriven (1976), Deiber and Cerro (1976), Orr and Scriven (1978), Preziosi and Joseph (1988), Johnson (1988), Wilson and Williams (1997), Tirumkudulu and Acrivos (2001), and Wilson et al. (2002) can be mentioned. These studies tried to develop the equation for the film thickness, $h(\theta)$, as a function of the rotational speed and volume of the liquid inside the cylinder. The average film thickness, $\bar{h}$, can be obtained by equating the fluid volume as

$$\pi R^2 - \pi(R-\bar{h})^2 = \int_0^{2\pi} h\frac{R+(r+h)}{2}d\theta$$

which after simplification becomes

$$2R\bar{h} - \bar{h}^2 = \frac{1}{2\pi}\int_0^{2\pi}\left(2Rh - h^2\right)d\theta \tag{13}$$

The dimensionless average film thickness is defined as $\bar{H} = \bar{h}/R$. The loading ratio, L_r, defined as the ratio of the liquid volume inside the cylinder to the total cylinder volume, is given as $\left[\pi R^2 - \pi(R-\bar{h})^2\right]/\pi R^2$, which after simplification becomes $L_r = 2\bar{H} - \bar{H}^2$. The other relevant parameters are the Froude number defined as $\mathrm{Fr} = \Omega^2 R/g$, the Reynolds number defined as $\mathrm{Re} = \Omega\bar{h}^2/\nu$, and the Webber number defined as $\mathrm{We} = \sigma/\rho\Omega^2 R^2\bar{h}$ where ν is the kinematic

viscosity of the liquid, σ is the surface tension at the gas-liquid interface, and ρ is the density of the liquid.

Lin and Groll (1996) provided analytical solution for the critical Froude number for the collapse of annular flow for low viscosity liquids such as water as

$$\mathrm{Fr} = 3/(1-\overline{H})^2 \tag{14}$$

whereas Baker et al. (2001) provided empirical relation for critical Froude number based on their experimental data as

$$\mathrm{Fr} = C_1/(1-\overline{H})^{C_2} \tag{15}$$

where C_1 and C_2 are constants which assumes different values based on whether the flow is in the onset of, complete, or collapse of annular flow regime. The appropriate values of C_1 and C_2 are reproduced here in Table 1.

Table 1. Constants for Eq. (15)

	C_1	C_2	Critical Fr Eq. (15)
Onset of Annular Flow	9.60	2.967	10.8
Complete Annular Flow	20.03	2.421	22
Collapse of Annular Flow	3.32	1.833	3.6

For the present VCD system under development in NASA Marshall, the relevant data are $R = 0.1542$ m, $\Omega = 200$ rpm or 20.93 rad/s, $\rho = 1013$ kg/m^3, and $\sigma = 0.0371$ N/m. Assuming a uniform film thickness of 3 mm, $\overline{H} = 0.02$ and the calculated critical Froude numbers for onset of, complete, and collapse of annular flow are given in the last column of Table 1. The operating Froude number for the present VCD system is 6.9, which indicates that the present system at earth's gravity operates under rimming flow condition. This means that the film thickness on the rising side is larger than the falling side.

The Reynolds number is also an important parameter in this flow configuration, which along with the Froude Number defines different flow regimes that is established for a particular set of variables. Deiber and Cerro (1976) presented a chart defining various flow regimes for this configuration as a function of the Reynolds number and Froude number, which is reproduced here in Fig. 5. For a detailed description of the different flow regimes depicted in this figure see the article by Deiber and Cerro (1976). For the given set of variables the Reynolds number is calculated to be 176. Thus the operating point falls in the collapsing film region in Fig. 5 implying that a stable film will not form. The different flow regimes in Fig. 5 are the result of interactions of the gravity, centrifugal and viscous forces. Under micro-gravity condition (very large Froude number), Uniform film thickness with solid body rotation type flow is supposed to occur.

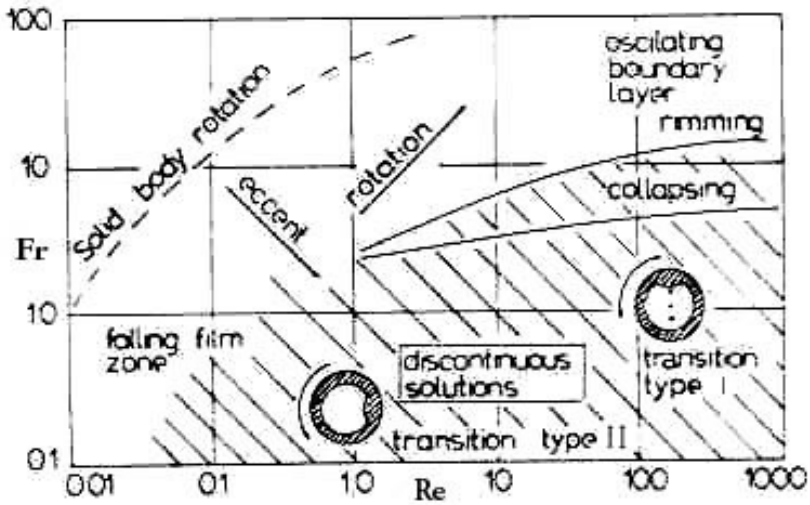

Figure 5. Different flow regimes as a function of the Froude number and Reynolds number.

CFD Modeling. Theoretical solution of the annular/rimming flow is quite complex. Computational Fluid Dynamic (CFD) calculation for this problem was attempted using the CFD-ACE+ software of CFD Research Corporation, Huntsville, AL with the VOF (Volume of Fluid) module turned on which can calculate free surface flow problems. Initial simulations qualitatively predicted the collapsing film phenomenon. Due to time limitation, the computational model could not be tested and refined thoroughly and extensively to obtain accurate solution.

Conclusions

An analysis of the hydrodynamics and associated thermal process for the liquid film movement on the rotating cylinder surface of the VCD system is attempted. An equation for the film thickness along the tapered cylinder surface has been developed assuming negligible gravity effects. A review of the theoretical and experimental analyses about the rimming/annular flow on the inside surface of a rotating cylinder without neglecting the gravity effects are done. It is observed that for the given operating conditions of the VCD system, the flow belongs to the collapsing film regime. A Computational Fluid Dynamic simulation for the rimming/annular flow is also attempted which needs further refinement for quantitatively accurate solution.

References

Baker, J., Oliver, T., Lin, L., Ponnapan, R., and Leland, J., Correlations of Critical Froude Number for Annular-Rimming Flow in Rotating Heat Pipes, *Journal of Fluids Engineering*, Vol. 123, pp. 909-913, 2001.

Ballback, L.J., The Operation of a Rotating, Wickless Heat Pipe, M.S. Thesis, Naval Postgraduate School, Montery, California, 1969.

Daley, T.J., The Experimental Design and Operation of a Rotating Wickless Heat Pipe, M.S. Thesis, Naval Post graduate School, Montery, California, 1970.

Daniels, T.C. and Al-Jumaily, F.K., Investigations of the Factors Affecting the Performance of a Rotating Heat Pipe, *International Journal of Heat and Mass Transfer*, Vol. 18, pp. 961-973, 1975.

Daniels, T.C. and Williams, R.J., Condensation Heat Transfer in Rotating Heat Pipes, *Mec. Appl.*, Vol. 22, pp. 497-521, 1977.

Daniels, T.C. and Williams, R.J., Experimental Temperature Distribution and Heat Load Characteristics of Rotating Heat Pipes, *International Journal of Heat and Mass Transfer*, Vol. 21, pp. 193-201, 1978.

Daniels, T.C. and Williams, R.J., The Effect of External Boundary Conditions on Condensation Heat Transfer in Rotating Heat Pipes, *International Journal of Heat and Mass Transfer*, Vol. 22, pp. 1237-1241, 1979.

Deiber, J.A. and Cerro, R.L., Viscous Flow with a Free Surface Inside a Horizontal Rotating Drum. I. Hydrodynamics, *Industrial and Engineering Chemistry Fundamentals*, Vol 15, pp. 102-110, 1976.

Faghri, A., Gogineni, S., and Thomas, S., Vapor Flow Analysis of an Axially Rotating Heat Pipe, *International Journal of Heat and Mass transfer*, Vol. 36, pp. 2293-2303, 1993.

Gray, V.H., The Rotating Heat Pipe – A Wickless Hollow Shaft for Transmitting High Heat Fluxes, American Society of Mechanical Engineers and American Institute of Chemical Engineers Heat Transfer Conference, Minneapolis, Minnesota, August 3-6, 1969, *ASME Paper No. 69-HT-19*.

Harly, C. and Faghri, A., Two-Dimensional Rotating Heat Pipe Analysis, *Transactions of the ASME*, *Journal of Heat Transfer*, Vol. 117, pp. 202-208, 1995.

Johnson, R.E., Steady-State Coating Flows Inside a Rotating Horizontal Cylinder, *Journal of Fluid Mechanics*, Vol. 190, pp. 321-342, 1978.

Li, H.M., Liu, C.Y., and Damodaran, M., Analytical Study of the Flow and Heat Transfer in a Rotating Heat Pipe, *Heat Recovery System & CHP*, Vol. 13, pp. 115-122, 1993.

Lin, L. and Groll, M., Critical Coditions for Collapse of Annular Flow in a Rotating Heat Pipe with a Cylindrical Wall, Heat transfer Engineering, Vol. 17, pp. 29-34, 1996.

Marto, P.J., An Analytical and Experimental Investigation of Rotating Noncapilary Heat Pipes, NASA CR-130373, 1973.

Newton, W.H., Performance Characteristics of Rotating, Non-Capillary Heat Pipes, M.S. Thesis, Naval Post graduate School, Montery, California, 1971.

Orr, F.M. and Scriven, L.E., Rimming Flow: Numerical Simulation of Steady, Viscous, Free-Surface Flow with Surface Tension, *Journal of Fluid Mechanics*, Vol. 84, pp. 145-165, 1978.

Preziosi, L. and Joseph, D.D., The Run-Off Condition for Coating and Rimming Flows, *Journal of Fluid Mechanics*, Vol. 187, pp. 99-113, 1988.

Roetzel, W., Laminar Film Surface Evaporation with Uniform Heat Flux in a Fast Rotating Drum, *International Journal of Heat and Mass Transfer*, Vol. 20, pp. 549-553, 1977.

Ruschak, K.J. and Scriven, L.E., Rimming Flow of Liquid in a Rotating Horizontal Cylinder, *Journal of Fluid Mechanics*, Vol. 76, pp. 113-125, 1976.

Tirumkudulu, M. and Acrivos, A., Coating Flows within a Rotating Horizontal Cylinder: Lubrication Analysis, Numerical Computations, and Experimental Measurements, *Physics of Fluids*, Vol. 13, pp. 14-19, 2001.

Wilson, S.D.R. and Williams, J., The Flow of a Liquid Film, on the Inside of a Rotating Cylinder, and Some Related Problems, *Physics of Fluids*, Vol. 9, pp. 2184-2190, 1997.

Wilson, S.K., Hunt, R., and Duffy, B.R., On the Critical Solutions in Coating and Rimming Flow on a Uniformly Rotating Horizontal Cylinder, *Quarterly Journal of Mechanics and Applied Mathematics*, Vol. 55, pp. 357-383, 2002.

Woodard, J.S., The Operation of Rotating Non-Capillary Heat Pipes, M.S. Thesis, Naval Post graduate School, Montery, California, 1972.

2003

NASA FACULTY FELLOWSHIP PROGRAM

MARSHALL SPACE FLIGHT CENTER
THE UNIVERSITY OF ALABAMA IN HUNTSVILLE

DUSTY PLASMA SAIL FEASIBILITY STUDY

Prepared By:	Robert Sheldon
Academic Rank:	Visiting Professor
Institution and Department:	Wheaton College Physics
NASA/MSFC Directorate:	Science
MSFC Colleague:	Dennis Gallagher

Magnetic Flux in the Plasma Sail Linked with the Spacecraft

Perhaps it would help to start with some basics, since it seems that the question jumps into the middle of the problem.

The plasma sail concept uses the same mechanism to generate thrust as the "mag sail" concept, as developed by Robert Zubrin and others (see NIAC web site). What Zubrin and many other discovered, was that the size magnet needed to generate a magnetic sail was either too heavy or made of "unobtainium" superconductors. The insight Robert Winglee realized, was that plasma itself is in some ways an obtainable superconductor that can be potentially controlled by adjusting current, temperature, density, ion species, and central magnet strength. In other words, the 30 years of research into plasma physics could be leveraged to make a plasma sail with current technology. He presented and published in JGR his simulation of the plasma sail as an example of what such a technology would look like and the potential uses it had. There have been several reanalyses of his concept, some favorable, some less so. Our own reanalysis suggests that the concept is feasible but should undergo fine tuning that will require further simulations.

The point of all sails is to intercept momentum, so that the area of the sail is directly proportional to the thrust. For a plasma sail to operate on the solar wind (which is roughly 1nPa of pressure as compared to 1mPa for sunlight), it must have about 30 times the diameter of a sunlight sail. Since the smallest useable sunlight sails proposed were roughly 1 km in diameter, a plasma sail needs to be approximately 30km in diameter to achieve comparable performance. So the first goal of the new plasma technology is to produce a bubble 30km in diameter in the solar wind.

Now a vacuum dipole has a magnetic field strength that drops as $1/R^3$. Taking the standoff distance at the nose to be where solar wind magnetic + ram pressure = plasma sail pressure, we get about 50nT for conditions at the Earth's nose. This number will drop considerably as a plasma sail moves out of the solar system, not only because both solar wind magnetic field and ram pressure drop with density ($\sim 1/R^2$), but also because the accelerating sail moves with the solar wind, which reduces the pressure of both. As Winglee points out, this causes the plasma sail to expand as it moves out of the solar system, in such a way as to keep the force constant. Even at the Earth, 50nT is the maximum field, since the flanks of the magnetosphere have much smaller field strengths, nevertheless, a plasma sail will start at Earth orbit, so very conservatively, we can use 50nT for the outer boundary condition. If we set 15km as the radius, and perhaps 1T surface field for the central magnet (presently achievable with NIB magnets), this fixes the radius of our magnet,

$$B = B_0(R_0/R)^3,$$

giving a 55 meter diameter for a 1T magnet. Conversely, if we take a 1 meter radius satellite (typical rocket farings are 2-3 meters in diameter), then the field strength is 170kT, or roughly 1000 times larger than the strongest laboratory magnets ever built. It should be clear why Zubrin's approach was not pursued further. Since a larger diameter magnet would greately reduce the required field strength (e.g. B*A=constant), Zubrin's approach might succeed if the plasma

itself took up the role of the large diameter magnet. In common parlance, we say that the plasma has "inflated" the vacuum magnet field.

Now there are two basic ways to inflate a plasma bubble: plasma pressure, and magnetic pressure. (One might envision kinetic ram pressure or electric field pressure as possible inflationary strategies, but the need for an MHD equilibrium reduce all these possibilities to the two above.) As examples, one might argue that laser ablation plasma (Gekelman 2003) or the AMPTE thermite explosions are examples of pure thermal plasma expansion, whereas the Earth's magnetic Dst storm (Chapman 1931) is a pure example of magnetic pressure expansion. Of course, the two types of expansion are related, such that strong currents and plasma waves are generated in a thermally expanding bubble, and plasmasheet plasma is injected in a Dst storm, but for the purposes of this response we consider them separately.

Now there are some fundamental differences between these two coupled pressure terms. Speaking heuristically, magnetic pressure is non-local, depending on current systems from the entire domain, whereas plasma pressure is local, satisfying local hydrodynamic equilibrium. A full self-consistent description will require careful modelling, but we can make a few simplifications that should give us ballpark limits. We address the global currents first.

Magnetic Pressure

A bar magnet, immersed in a plasma, will exclude the plasma and form a bubble (Chapman 1931). But as we saw above, the vacuum dipole field diminishes too rapidly. Using both the Earth's and Jupiter's magnetospheres as a guide, we argue that injecting plasma into a vacuum dipole field creates currents that expand the bubble diameter so that Earth's field inflates 10-20% during a magnetic storm. Likewise Jupiter's field is inflated 300-400% by Io's injected plasma, that is, Jupiter's standoff distance without plasma would be around 35 jovian radii, whereas Voyager and Pioneer have observed the magnetopause at 120 R_J. The Earth's inflationary field is caused by the ring current, 30-300keV ions located between 3-5 R_E from the Earth. The source of this plasma normally the plasmasheet, which in usually has only weak diffusive access to the ring current except during storms when large electric fields cause direct injection (e.g. Sheldon 1993). Jupiter's plasma source is thought to be Io's volcanos that inject directly into the magnetosphere at 6 R_J. In both cases, the injected plasma rapidly condenses at the dipole equator, forming an equatorial ring current that is primarily responsible for inflating the field.

Note that the ring current plasma can be many R_E from both the earth and the magnetopause, yet still exert a magnetic pressure of inflation, a consequence of the non-local nature of this pressure term. This is also true of Jupiter's magnetodisk, and is expected to be true of Winglee's mini-magnetosphere. That is, much of the plasma injected into the vacuum dipole bubble will redistribute itself into a ring current and provide magnetic pressure that inflates the bubble. Therefore we model this component of the inflation with a ring of current, or in the case of Jupiter, a series of rings that approximate a disk. (A direct integration of a current sheet distribution produces an analytically less tractable form than a sum of rings.) We interpret Winglee's simulation results from his 2000 JGR paper, as well as our own kinetic simulations, as supporting a Jupiter-like magnetodisk, where the magnetic field strength in the dipole magnetic plane diminishes with 1/R dependence. This is strictly a consequence of having a semi-infinite

magnetodisk, or a sum of current carrying rings. We recognize, of course, that at the inner and outer boundary, fringing of the fields will cause a faster decay of the magnetic field, smoothly interpolating to the vacuum dipole solution.

Using this simulation result in it's simplest form, we can now recalculate the required magnet size using the relationship,

$$B = B_0(R_0/R)$$

As before if we use a 1T magnet to create a 15km bubble, the required magnet diameter is an astonishing 0.75mm. Conversely, if we use a 1m radius magnet, we need only a weak 750mT field strength. This result appears too good to be true, nature is never so kind. What physics did we overlook?

There are two places that we have perhaps ignored some crucial data. First, at both Jupiter and Earth, the ring currents exist only over a small radial region of the entire bubble. Thus the 1/R scaling strictly applies only in this ring current region, and $1/R^2$ or $1/R^3$ scaling applies outside. Hints of this were observed in our own kinetic simulations of the plasma sail. Second, at both Jupiter and Earth, the flux in the ring current never exceeds the flux in the central magnet. There are good physical reasons for these observations, which we explore later, but first we estimate the magnet size. This is not to say that an overpumped ring current cannot exist, only that the physics of such a distribution cannot be extrapolated from our limited pool of existing models. Both of these complications put some limits on the simple extrapolation carried out by Winglee.

Magnetic Pressure: RC Contribution

In the near-field, or close to the ring current, the magnetic field might be expected to go as $1/R^2$, rather than a vacuum dipole worst case of $1/R^3$, heuristically because of the finite extent of the ring current. This $1/R^2$ dependence also appears consistent with our simulations. Using the Earth's ring current as a paradigm, we might argue that the magnetic field goes as $1/R^3$ from 10-5 R_E, and then as 1/R from 5-2.5 R_E, and back to $1/R^2$ from 2.5 -1 R_E. This self-similar scaling is awfully suggestive, so we use it without much more justification for the mini-magnetosphere. Here is our model:

Region \ Quantity	Radius	Magnetic field
Magnet R_0, B_0	~1 m	~1 T
Inner edge of RC, R_1, B_1	3.5 km	
Outer edge of RC, R_2, B_2	7.5 km	
Standoff distance, R_3, B_3	15 km	50nT

Applying these boundaries, and using $1/R^2$ between the magnet and the RC, 1/R within the RC, and $1/R^3$ outside the RC, we get the following formulae:

$$B_3 = B_2(R_2/R_3)^3$$

$$B_2 = B_1(R_1/R_2)$$

$$B_1 = B_0(R_0/R_1)^2$$

which can be combined to estimate either B_0 or R_0. If we use R_0=1m, then the 3 expressions can be combined to produce:

$$B_0 = B_3\ R_1R_3^3\ /\ (R_0^2R_2^2)$$

Substituting the values from the table in the expression, we find B_0~10T. Conversely, putting in 1T in the expression for B_0 retrieves 3.2 m for R_0.

This is getting closer to what we intuitively expected, though it is a bit larger than we would prefer to fly. For the level of sophistication of this calculation, it is in the same ballpark as Winglee's estimate, and since we did not include the thermal plasma pressure to this calculation, we have made the ring current do all the work by itself, which is an overestimate of both B_0 and R_0. So we certainly have not demonstrated infeasibility of the approach, but neither have we addressed the more serious 2nd issue, that of the total flux in the RC approximating that of the central magnet.

Magnetic Pressure: RC Cartoons

This stability question is prone to misunderstanding, so we attempt to provide several heuristic cartoons in the hope that we have caged the elusive physics.

Cartoon 1: Imagine that we have laid a loop of fine gauge copper wire on a slick countertop, and pump an ampere of current through it. In addition to getting hot, the wire will billow out into a circular shape. This is because the the repulsion of oppositely directed currents on opposite sides of the loop. Alternatively, the magnetic flux threading the interior of the loop is compressed relative to the flux outside the loop and exerts a magnetic pressure. In a like fashion, the Earth and Jupiter's RC will also expand outward. Two things constrain the unlimited expansion of the RC, the pressure balance at the outer boundary, and the tension force from the inner magnet (which can also be stated as the need to conserve encircled flux). Now if one imagines that the magnetosphere is a water-filled balloon, it is clear that compressing it between one's hands is an instability prone process, whereas the tension force of the latex (or conservation of water volume minimizing the area) is a stable process. That is to say, it is the central magnet that provides the stable confinement of RC, not the solar wind pressure. Even if we were to remove the solar wind (e.g., a DC-glow discharge around a laboratory magnet) the RC would not expand beyond a few magnet radii. Thus if the RC were to produce much more flux than the central magnet could contain, it may not be stable, since the internal contraint would be less important than the external constraint.

Now let us replace the single loop of wire with a three stranded loop and drive an ampere through the strands, what would happen? The 3 strands would expand as before, but in addition,

the strands would coalesce because of the mutual attraction of like currents. Thus in the absence of "tidal" forces of the central magnet or "tidal" forces of centripetal acceleration such as exist at Jupiter, one might expect that the RC would form a single band or current system in force balance with the central magnet tension, and the self-induced expansion.

Cartoon 2: If we imagine that we start with a permanent magnet for the central magnet, and lay a loop of wire some distance away from it, and gradually ramp up the current in the wire loop, what are the forces on the system? As is well known, two magnets repel when their dipole moments are anti-parallel, attract when they are parallel, and experience a torque when they are not parallel. The interaction between loops and magnets is not so intuitive, but perhaps can be reasoned out. Since energy is proportional to B^2, the magnet and loop will be at an energy minimum when their external fields cancel. This means that the permanent magnet will be aligned with the magnetic moment of the loop, and move toward the center of the loop, so that the external fields of the permanent magnet will cancel the field inside the loop. One might imagine the analogous operation of the starter solenoid on an automobile.

Let's test this conclusion with the Earth. The dipole moment of the earth points south, the external field points north at the equator. The RC moves counter-clockwise around the Earth, such that the RC field is southward for all regions inside the RC. Hence the external dipole field cancels the RC field producing a dip in |B| during a Dst storm. That works.

Cartoon 3: Now consider what happens when the RC is made stronger and stronger. At first field strength inside the RC but outside the magnet (Dst) decreases, but at some point, the field would completely reverse direction and grow stronger. Since the external dipole magnet field is northwards, there must be a null boundary, a separatrix between the fields of the RC and the fields of the central magnet. Inside that separatrix, the central magnet is disconnected from the RC field, looking something like a plasmoid, and as the external magnetic pressure is increased, this plasmoid would experiences a repulsive force. Again, this is analogous to a UMd theta-pinch demonstration, in which an empty coke can is placed in a ten-turn coil of 10# wire, through which is dumped the output of a 1 F, 5000V capacitor. The can is ripped in half and forcibly expelled from the device.

Cartoon 4: If we take the above example, turn off the RC, and extend an infinite plane through the equator of the dipole magnet, the integrated flux outside the magnet must equal the flux passing through the center (that's $\nabla * B=0$). If carry out the definite integral, say from the surface of the magnet to twice the loop radii, we will have a constant value. Now as the current in the loop of wire is ramped up, the initial effect on the integrated flux density is nearly neglible, because any contribution from flux inside the ring is balanced by an opposite contribution outside the ring. The loop magnetic moment is aligned with the magnet, so there must be a net increase if our outer boundary were at infinity, but the additional flux is being added outside our outer boundary. Another way of saying this, is that the RC does not add flux in the vicinity of the central magnet, it merely redistributes it.

Obviously this approximation breaks down when the RC carries more flux than the initial magnet, but first let's look at the redistribution. The field lines from the central magnet that extend beyond the RC are stretched outwards, whereas field lines inside the RC are not so much

redirected as weakened, so that magnetic tension force pulls in the ring, and magnetic pressure is reduced inside the ring, also enhancing the pull. This redistribution changes the radial profile of the field such that it goes from a vacuum $1/R^3$ to a magnetodisk $1/R$, but it can only do this as long as there is flux to redistribute. Once the RC flux is comparable to the magnet, the solution reverts to that of a pure current ring, the central magnet field lines no longer encircle the ring current, but close in on themselves, losing both the tension outside and the pressure inside. And the definite integral grows linearly with increasing current.

If our heuristic reasoning is correct, then the RC can carry only an amount of flux roughly comparable to the central magnet before instabilities set in. This inflates the magnetosphere more than a factor of two, however, because the RC is at a much larger radius than the central magnet. Since the placement of the RC is critical to this calculation, which is itself constrained by the central magnet, it requires a self-consistent approach not presently at our disposal, and we cannot do much better than order-of-magnitude in this calculation. Therefore we address a related, but more tractable question: what are the stability criteria for a central magnet trapped in the field of a RC?

Magnetic Stability

Dipole Stability in RC field

From Jackson, we can write that the force between a dipole magnet with magnetic moment, **m**, and a magnetic field is,

$$\mathbf{F} = \nabla(\mathbf{m} * \mathbf{B})$$

Since we have already assumed that the torque is zero and the magnet is aligned with the current ring, we can write this,

$$\mathbf{F} = m\, \nabla B_z$$

where B_z is the z-component of the RC magnetic field. Unlike most books, which take the limit at the center, we keep both radial (ρ in cylidrical coord) and z-components of B_z, and derive the following:

$$F_z = [-3m\, \mu / k^{5/2}]\, z\, (2a^2+2z^2 - 3z\rho^2 - za\rho)$$
$$F_\rho = [-3m\, \mu / k^{5/2}]\, (3a^3+3az^2 + a\rho^2 + 4\rho z^2 + 5\rho a^2 - \rho^3)$$

where m is the magnetic moment of the magnet, μ is the magnetic moment of the RC, $k=(a^2+z^2+\rho^2 + 2a\rho)$, and "a" is the radius of the RC. Note that for $\rho < a$ (in the radial direction) and $z\rho<a^2$ in the z-direction, the force is negative, indicating unconditional stability.

RC Stability in a Dipole Field

By symmetry, this ought to give the same answer as the above section, but as check on the approximation used for the RC field, we carry out this integral. Here we use Ampere's Law,

$$F = -I \int B_d \times dl$$

Since at the dipole equator, the field is purely in the z-direction, and the current is purely in the φ-direction, the resulting force is pure F_ρ, which when integrated around a circle, is zero. So this is an equilibrium point. In order to calculate the stability, we need to show that the force obeys Hooke's Law in both directions, it is always a negative restoring force.

As before, we assume the torques are zero, so we displace the RC perpendicular to the dipole plane to get the z-component of the force, and in the plane to get the ρ-component.

$$\mathbf{F} = \nabla(\mathbf{m} * \mathbf{B}) = \nabla(mB_z) = m\,\mu/(\rho^2+z^2)^{3/2}$$
$$F_z \sim -3\,m\mu\, z/(\rho^2+z^2)^{5/2}$$
$$F_\rho \sim -3\,m\mu\, \rho/(\rho^2+z^2)^{5/2}$$

<u>RC Stability in a RC Field</u>

But when the central magnet cannot be described as a point magnetic dipole we have to carry out an integral to estimate the force between them. We would like to model the finite size of the central magnet as a loop of current of radius b inside the RC of radius with a force due to the interaction between $B_{RC}(a)$ and $B_{RC}(b)$. Unfortunately, the expression for the magnetic field or vector potential of a RC given in Jackson, is either in terms of elliptic integrals, spherical harmonics or Bessel functions. The series expansion for elliptic integrals is not valid outside the RC, nor is the asymptotic expression derived from it particularly accurate in this area. The spherical harmonics are much better, but converge very slowly in the region around the RC. Thus the stability question must be resolved numerically, but should converge to the above results when the inner ring shrinks, a<<b.

<u>RC radius stability</u>

Having ascertained that a RC as a rigid body is stable in the presence of a dipole (and can therefore transmit thrust), the last question to be addressed is the force-free condition for a RC radii. If we consider an element of ring current dl, the two opposing forces are the ixB attractive force of the central magnet, and the self-repulsive force of the remainder of the current ring. The attractive force is straightforward:

$$F_d = i\, B_d(\rho=a) = \mu\, i\, /a^3$$

directed inward, where μ=the magnetic moment of the central magnet.

The self-repulsive force is a bit harder to calculate. A straightforward calculation doesn't seem to converge when the current element approaches our origin. One possibility would be to use the magnetic field solution at r=a to calculate the force. Again, this goes infinite for a infinitely thin current ring. Since the current is not infinitely thin, it might be possible to approximate it with an average of [B(r_inside) + B(r_outside)]/2. Jackson gives an expansion of the B-field due to a ring in terms of associated Legendre polynomials that is valid both inside and outside the ring (unlike the expansion of elliptic integrals). When we take the average of the inside and outside in the

limit that r=a, the expression converges very slowly to an average B-field equal to the B-field in the center of the ring. The force then becomes:

$$F_{RC} = i\ m / a^3$$

directed outward, where m= magnetic moment of the ring. Using the definition of $m = I\ \pi\ a^2/c$, we have

$$F_{RC} = i^2\ \pi / (a\ c)$$

Equating these two forces on a current element, i, we have:

$$\mu = m$$
$$\mu c/(i\ \pi) = a^2$$

If we assume that the central magnet is some sort of electromagnet of radius s, then we have

$$B_0 s^2 = B_{RC} a^2$$
$$B_0/B_{RC} = (a/s)^2$$

If we believe this equilibrium, then we have collapsed R_1 and R_2, leading to the equation:

$$B_3 = B_2(R_2/R_3)^3$$
$$B_2 = B_0(R_0/R_2)^2$$

From this calculation, then, to get a RC of 7.5 km radius from a magnet of 1m radius will require a magnet strength 5.6×10^7 stronger than RC. Working backwards, if the RC is at 7.5 km, and the nose at 15km, then $50nT*(R_3/R_2)^3 = 400nT$, which scale to 22T for the magnet. This seems a bit excessive for a lightweight sail. Using 1T as our largest magnet, and self-similar scaling to place the RC at 1/2 the bubble diameter, we find that 3.2km is the radius of the bubble, or approximately 1/5 of the radius desired.

Note that this calculation essentially collapses the RC to a single current. Neither Jupiter nor Earth have such a concentrated RC, suggesting that diffusion, or centripetal acceleration, or plasma instabilities such as flux-tube interchange might conceivably play a role in the thickness of the RC, which would give an answer more similar to the original calculation up above, with 1/R scaling within the RC.

Plasma Pressure

Up until this point, we have assumed that the plasma exists as a medium to carry a current. In addition, the plasma serves as a medium that transmits a thermal pressure. Now since instabilities tend to occur whenever the plasma pressure dominates over the magnetic pressure, one would

assume that for a plasma sail to maintain integrity long enough for momentum transfer, it will operate in a regime of $\beta \sim 1$. One might, of course, attempt stabilization techniques such as those used in tokomaks, but the selling point of a plasma sail is that it uses simple technology that is presently available, which would suggest that thermal pressures much exceeding $\beta=1$ are unlikely. Since the plasma sail is expanding against a constant solar wind pressure, a new equilibrium is reached when we add in the plasma pressure. Using our RC self-similar model above, we assume that the magnetic field outside the RC region scales as $1/R^3$. So if we include the plasma pressure along with the magnetic pressure, the energy density will double, but the radius will not. There are two equivalent ways to say this, either the standoff magnetic field will drop to 50nT/&root;2, or the bubble will expand to a larger diameter. Since B_0 is linearly dependent on B_3, this has the effect of reducing the required magnetic field strength by 30%.

While significant, this hardly changes the order of magnitude of this calculation, indicating that the whole plasma sail concept hinges on whether a RC magnetic flux, comparable in magnitude to the spacecraft magnetic flux, can achieve 15km radii.

This is actually a three part question, answered with different means. The first part is what is the force exerted by the solar wind on the magnetic bubble. The second part is how that force is transmitted from the plasma to the spacecraft. Complicating this further, our proposal suggested that dust suspended in the plasma (dusty plasma) could intercept sunlight momentum and add an additional force to the plasma.

Solar Wind Momentum

The first part, how solar wind momentum is intercepted by the bubble, is complicated because the bubble is comparable in size to the ion gyroradius in the solar wind. If the bubble were much larger than this, then one could compute simply the solar wind pressure and the area of the bubble, but for small bubble sizes, the ions "slip" past the bubble without transferring much momentum. This is analogous to the problem in optics when a scatterer is comparable to the wavelength of light, because geometric considerations are no longer sufficient to describe the interaction. As we show before, the bubble starts to behave geometrically as an opaque obstruction only when its diameter exceeds about 50km.

Heuristically, when the bubble is smaller than an ion gyroradius, one can view the solar wind ions as unshielded, (ions, not electrons, carry the momentum) interacting with a bare magnet. In this case, the Lorenz force, $F = qv \times B$, causes the ions to deflect sideways if the dipole is oriented perpendicular to the velocity. This change of direction is not necessarily a bad thing, since this is exactly the direction a Δv rocket firing is directed to change orbit characteristics of a spacecraft, but in addition to direction, the magnitude of the force also diminishes. One could integrate an analogous Rutherford scattering law for a magnetic force, but the calculation would be in the unshielded limit, and the actual interaction lies between the two extremes. MHD theorists regard this interaction as a "viscous" interaction, which again, requires a full kinetic simulation to achieve better than order of magnitude estimates. Our own simulations suggest that perhaps 10% of the geometric force is transmitted to the plasma in this regime.

Solar Sunlight Momentum

As our experiments and proposal have shown, it is possible to suspend 3μ sized SiO_2 dust grains in a magnetized plasma, and levitate them against the force of gravity in the laboratory. The laboratory gravitational force is much greater than the calculated solar photon force, indicating that these dust grains could also be stably trapped in sunlight. If they could be likewise trapped and suspended in the plasma sail, they would contribute a force to the plasma in addition to the solar wind force. Since the solar photon pressure is 1000 times larger than the solar wind pressure, a dust ring component need only be 10% of the area and 1% opaque to double the (assumed) geometrical force on the sail. In the laboratory we were able to achieve densities much higher than this, though admittedly in a very different plasma environment. The field of dusty plasmas is young, and whereas models and simulations have been developed, none have addressed the parameter regimes such a sail would operate at. Indeed, many theorists did not think it possible to levitate dust magnetically. The answer, apparently, is that they are trapped electrically to the plasma, and the plasma is trapped magnetically to the magnet.

Recognizing that without further research into the physics of this phenomenon, all our conclusions are extrapolations, we can nonetheless estimate a force from the dust component of the plasma sail. Our laboratory dust may have had several thousand charges per grain, which is a consequence of a very hot electron plasma. If we assume a photoelectron charging source, this number is closer to several hundred charges per grain. Since the plasma neutralizes the dust, the plasma density must be greater than the dust density by this amount, or

$$Q_d \times n_d < n_i$$

Winglee estimates densities of $n_i \sim 10^{12}$/cc in his helicon, which we might argue decrease by 1/R from the source (since they are confined to a 2-D sheet). Taking perhaps 0.1m for the diameter of the helicon, and 5 km for the outer edge of the RC, which is where we observed our laboratory dust ring, the plasma density is down to about 2×10^7/cc. This gives a maximum dust density of about 10^5/cc. Estimating the thickness of dust sheet to be approximately the magnet diameter of 1 m, gives us a column density of $10^{11}/m^2$. Since the mass of a dust grain goes as the cube, whereas the area goes as the square, flight dust will likely have r <1μ to maximize area to weight ratio. Using this dust, our cross sectional area is:

$$\pi(500\text{ nm})^2 * 10^{11}\text{m}^2 = 0.08\text{m}^2 \text{ or 8\% opacity.}$$

The area is hard to estimate from the laboratory, though it seemed it was about 10% of the radial extent as the laboratory RC+magnet but located at the outside of the visible RC. Using this number we estimate the dust ring to extend from 5-5.5 km. Thus the area of this dust ring is

$$(5.5^2-5^2)/15^2 = 2.3\%$$

Combining these figures gives 8% x 2.3% * 1000 photon/wind = 190% boost to the geometric thrust of a plasma sail. Given the conservative estimates and the level of understanding of the physics, we might easily be an order of magnitude off, but clearly, this is an area that can benefit from further research.

Momentum Transfer to the Spacecraft

There have been some concerns that the plasma is not magnetically well connected to the spacecraft, and therefore cannot transfer momentum to the spacecraft. As we addressed in our first section, the magnet is unconditionally stable in a pure RC field as long as the magnet stays "inside" the ring. Likewise a RC is unconditionally stable in a pure dipole field. The "disconnected" topology only exists when the RC is overdriven, and the central magnet appears as a plasmoid compressed in the center of the RC. Under these conditions, the spacecraft is highly stable in the equatorial plane, but unstable along the axis, analogous to a watermelon seed that is squeezed between the thumb and finger. Two obvious solutions to this instability are either not overdriving the RC, or applying the thrust in the equatorial plane of the dipole.

This second solution is not amenable to a dusty sail, however, since the edge-on dust sail has very little area (though it will be completely opaque). Nor does it seem advisable to fly a first generation plasma sail that has inherent instabilities, so it seems again we would argue that the feasibility of the plasma sail hinges on its ability to find an equilibrium RC geometry that is not overdriven. Once again, this is a self-consistent calculation that is somewhat beyond the capabilities of this order-of-magnitude calculation.

In summary then, it appears that a plasma sail on the order of 15 km will generate only 10% of the geometric thrust expected from the solar wind, but 190% can be extracted from the photon flux. To put a number on it, this is,

$$2\,\pi\,(15000\text{m})^2\,(1\text{nPa}) = 1.4\text{ N, or,}$$
$$2\pi\,(3200\text{m})^2(1\text{nPa}) = 0.064\text{ N}$$

Plasma Losses from the Mini-Magnetosphere in the Simulation

Although others may address the plasma experiments, our expertise is with dusty plasma experimentation. For these experiments, there have not been any simulations performed to my knowlege. We are presently working on a PIC simulation of the DC glow discharge, and attempting to calculate the space charge that accumulates at the dipole equator. Direct experimental measurement of this space charge using a floating dipole probe (see Sheldon, AGU 2002 talk) gave inconclusive results of about a volt superposed on a noise signal of about a volt. We are also attempting to upgrade the diagnostics to measure this space charge with better signal to noise ratio. Both of these are ongoing research efforts that are highly manpower limited, but perhaps will return results in 6 months to a year.

2003

NASA FACULTY FELLOWSHIP PROGRAM

MARSHALL SPACE FLIGHT CENTER
THE UNIVERSITY OF ALABAMA IN HUNTSVILLE

GRAPHICAL USER INTERFACE (GUI) USING MATLAB/SIMULINK FOR NUCLEAR ELECTRIC PROPULSION SIMULATION MODELS

REPORT NOT AVAILABLE

Prepared By:	Yeu-Sheng Paul Shiue
Academic Rank:	Professor
Institution and Department:	Christian Brothers University Mechanical Engineering Department
NASA/MSFC Directorate:	Engineering
MSFC Colleague:	Mr. Geoffrey Beech

2003

NASA FACULTY FELLOWSHIP PROGRAM

MARSHALL SPACE FLIGHT CENTER
THE UNIVERSITY OF ALABAMA IN HUNTSVILLE

STRUCTURAL DYNAMICS WEBSITE IN SUPPORT OF AIAA'S EDUCATION OUTREACH PROGRAM

Prepared By:	Michelle Simmons
Academic Rank:	Graduate Research Assistant
Institution and Department:	Alabama A&M University Department of Physics
NASA/MSFC Directorate:	Engineering
MSFC Colleague:	Dr. Mike Tinker Dr. Sheila Nash-Stevenson

Introduction

It has become a common practice for schools today to have computers and Internet access in each classroom. The teacher assigns homework and even in-class assignments to be performed solely on the computer. Computers have become an important tool for obtaining useful information. Long gone are the days of making the weekly trips to the local library, searching through numerous books and newspaper articles, desperately gathering information in order to complete book reports and research papers. All the information you'll ever need is accessible by stroking the keypad of a computer.

Over the past five years, schools have been rapidly acquiring access to Internet telecommunications. Over 90% of schools now have some sort of access to the Internet, someplace in their building [1]. The Internet can be a very resourceful tool when it comes to reaching a vast number of individuals. Most people today turn to the Internet obtain information on different areas of interest. Most information is gain by accessing websites that are readily available on the Internet. Websites are becoming the most common and popular way for educators, advertisers, businesses, and consumers to share information with the world.

Statement of the problem

With the every dwindling number of college students graduating from the school of engineering, there is an immediate need for engineers. This problem was giving great thought by engineers and educators (NASA) Marshall Space Flight Center. Studies showed that although the number of prospective students entering the school of engineering was great, the number of students whom actually graduated with a degree in engineering fell well below the mark, which cause a generation gap between engineers. This problem can be contributed to the fact that once prospective engineering students reach college and began taking engineering courses, they were completely unprepared and ultimately overwhelmed, which, in turn, caused the student to change his or her major.

Purpose of work

Educators and engineers needed to find a solution to this problem. One way to insure that this doesn't happen in the future is to get those students who are interested in engineering to understand the fundamentals of engineering long before entering college. This would prevent students from being bombarded and overwhelmed with subject matters never before discussed in such detail while in high school. By introducing the basics of engineering in high school, students will enter college with some type of foundation or background in engineering.

The engineers in the field aeronautics and astronautics came up with a brilliant idea: design a website dealing with structural dynamics. Any training or educational environment can be greatly enhanced through the use of the Internet. An educational website would help teachers and students to better understand the subject matter by giving them some perspective on what of structural dynamics is all about.

In order for website to be successful, it has to be interactive. The website has to be interesting in order to make the viewer what to visit the website more than once. By adding animation, interactive demos, and movies to website, it is no longer a "boring old website". It becomes a spectacular portal of information that keeps the viewers attention and enthusiasm

Plan of action

In designing a website, one has to take into account its targeted audience. What would my audience like to see? How can I, the author, grab the audience's attention and keep it? The website has to be design to be informative while at the same time being entertaining. How can I make the information on the website understandable to the average person with no background in structural dynamics?

"The contents of your Web page should be brief, while getting across the intended information using clear and simple language with consistent terminology throughout"[2]. Not confusing audience with a bunch engineering and science lingo is the key to keeping your target. The content of the website has to be easy to follow. Visual images is one way to insure that you receive a positive response to the information presented on your website. Visual Images can reach an audience that knows nothing about structural dynamics. Then an engineer can explain what it means in the context of the website.

International Space Station

Another way to get your point across the audience is the use of animations. Any subject matter that is either difficult to explain or understand can always become clearer with an animation. Animations add a creative touch to websites and also give the audience a visual image to relate to the given information.

The website should give the audience some hands experience of the phenomena explained on the website. This can be accomplished by having a section within the website devoted totally to laboratory experiments. The experiments can be carried out within high school laboratories. The materials needed for the experiment are inexpensive and can be purchased at the local hardware store.

Future Work

The next logical step should be to create a CD containing the same content available on the website. The purpose of the CD would be to make information accessible to students and individuals who do not have access to the Internet outside of school or the library. The goal of the website to reach all students interesting in engineering regardless of their financial background. Future possible applications for website limited only to the imagination of the author of the website.

Resources

This project required the use of many software tools. The main software chosen for the project was Macromedia Studio MX. This is a high-end webpage design and animation software used throughout the scientific and entertainment community. The wepages were designed using Macromedia Dreamweaver. The opening flash movie was completed with Macromedia Flash. Most graphics were created in Adobe Photoshop. All other animations, movies and interactive were collected from a vast amount of sources from the Internet. All experiments in the experiments section of the website were written by the author, her colleague Mike Tinker, and several other college professors. All structural dynamics information and material were gathered from engineers throughout the different NASA braches.

Conclusion

The Internet is one most effective ways to reach into the schools and homes of America and educate students on structural dynamics and the importance of it in the design of vehicles, airplanes and spacecrafts. They have the power…to communicate, inspire and move the minds of people. Through this website, it is the intent of the author to help the AIAA (American Institute of Aeronautics and Astronautics) education outreach program to educate and inspire students and teachers about the vast possibilities of engineering and vehicle design using structural dynamics.

Acknowledgements

The author, Michelle Simmons, would like to thank Dr. Sheila Nash Stevenson, Dr. Marilyn Lewis, Mike Tinker, Dr. Razi Hasson, and he entire team of engineers in the structural dynamics area of the Marshall Space Flight Center’s Engineering Directorate. Thank you for the wonderful opportunity to create a website in support of your cause.

References

[1] Internet used by Teachers http://www.crito.uci.edu/TLC/findings/Internet-Use/startpage.htm

[2] Building a Great Web Site, http://www.thejournal.com/magazine/vault/A3879.cfm

2003

NASA FACULTY FELLOWSHIP PROGRAM

MARSHALL SPACE FLIGHT CENTER
THE UNIVERSITY OF ALABAMA IN HUNTSVILLE

Modeling of LH_2/LOX Combustion for Liquid Rocket Propulsion Engines-Enhancement of Generalized Fluid System Simulation Program

Prepared By:	Mehmet Sözen
Academic Rank:	Associate Professor
Institution and Department:	Embry-Riddle Aeronautical University Physical Sciences Department Engineering Physics Program
NASA/MSFC Directorate:	Engineering, ED25
MSFC Colleague:	Dr. Alok Majumdar

Introduction

The Generalized Fluid System Simulation Program [1] (GFSSP) is a general-purpose computer program developed at NASA/MSFC for analyzing steady state and transient flow rates, pressures, temperatures, and concentrations in a complex flow network. The code can handle compressible and incompressible flows as well as phase change and mixture thermodynamics. The program which was developed out of need for an easy to use system level simulation tool for complex flow networks, has been used for the following purposes to name a few: Space Shuttle Main Engine (SSME) High Pressure Oxidizer Turbopump Secondary Flow Circuits, Axial Thrust Balance of the Fastrac Engine Turbopump, Pressurized Propellant Feed System for the Propulsion Test Article at Stennis Space Center, X-34 Main Propulsion System, X-33 Reaction Control System and Thermal Protection System, and International Space Station Environmental Control and Life Support System design. During my summer faculty fellowship at MSFC in summer 2002, I developed a modular FORTRAN code as a subroutine in order to model the combustion of liquid hydrogen (LH_2) with liquid oxygen (LOX). In this code the equilibrium composition of the combustion products and the product temperature are predicted for a given inlet condition and combustion pressure. The details of this work are in reference [2].

The present work was undertaken as the continuation of the work carried out in summer 2002. In the previous work the model was based on chemical equilibrium with the assumption of H_2O, H_2, O_2, OH, H, and O constituting the products of combustion as a mixture of ideal gases. Newton-Raphson method was used to solve the resulting system of non-linear coupled equations. This model did not take into account any kinetic energy effects and considered the thermodynamic properties to be given by ideal gas properties at the corresponding temperatures. The stability of the Newton-Raphson method was shown to be quite well in the vicinity of stoichiometric mixture ratios, but full analysis was not carried out for fuel rich and oxygen rich environments due to time limitations.

Accomplishments of Summer 2003

- Correct Models for Fuel Rich Case(FRC) and Oxygen Rich Case(ORC) Established:

  During the efforts of implementing kinetic energy effects into the model through energy equation, it was discovered that although the stoichiometric model was correct, the FRC and ORC included an error and therefore the overall reaction equation did not satisfy the conservation of mass principle. In the vicinity of stoichiometric case the effect was rather small and was difficult to notice. However as the fuel richness or oxygen richness of the environment increased, this discrepancy became significant and also adversely affected the stability of the solution scheme. The corrected model and the equations that need to be solved simultaneously for the problem shown schematically in Fig. 1 are presented here.

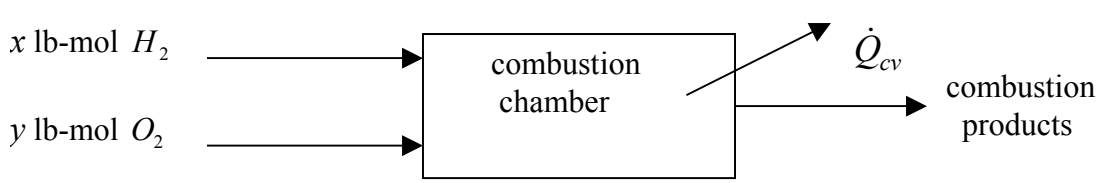

Figure 1: Schematic diagram of the combustion chamber.

Fuel rich case (FRC)

The chemistry mechanism for this case uses the following reactions

$$xH_2 + yO_2 \Leftrightarrow 2yH_2O + (x-2y)H_2 \qquad \text{for } x > 2y$$

$$H_2 \Leftrightarrow 2H$$

$$O_2 \Leftrightarrow 2O$$

$$2H_2O \Leftrightarrow H_2 + 2OH$$

and the changes in each specie in the form of fractions a, b, c, and d can be expressed as

$$\begin{array}{ccccc} xH_2 & + & yO_2 & \Leftrightarrow & 2yH_2O \\ -2ya & & -ya & & +2ya \end{array}$$

$$\begin{array}{ccc} H_2 & \Leftrightarrow & 2H \\ -b & & +2b \end{array}$$

$$\begin{array}{ccc} O_2 & \Leftrightarrow & 2O \\ -c & & +2c \end{array}$$

$$\begin{array}{ccccc} 2H_2O & \Leftrightarrow & H_2 & + & 2OH \\ -2d & & +d & & +2d \end{array}$$

The overall reaction is given by

$$xH_2 + yO_2 \rightarrow (2ya-2d)H_2O + (x-2ya-b+d)H_2 + [y(1-a)-c]O_2 + (2d)OH + (2b)H + (2c)O$$

With the approach detailed in reference [2], the five coupled, non-linear algebraic equations for this case become

$$f_1 = \frac{(2ya-2d)^{2y}[x+y(1-a)+b+c+d]^y}{(x-2ya-b+d)^{2y}[y(1-a)-c]^y}\left(\frac{P}{P_o}\right)^{-y} - K_1 = 0 \tag{1}$$

$$f_2 = \frac{(2b)^2}{[x+y(1-a)+b+c+d](x-2ya-b+d)}\left(\frac{P}{P_o}\right) - K_2 = 0 \tag{2}$$

$$f_3 = \frac{(2c)^2}{[x+y(1-a)+b+c+d][y(1-a)-c]}\left(\frac{P}{P_o}\right) - K_3 = 0 \tag{3}$$

$$f_4 = \frac{[x-2ya-b+d](2d)^2}{[x+y(1-a)+b+c+d](2ya-2d)^2}\left(\frac{P}{P_o}\right) - K_4 = 0 \tag{4}$$

$$f_5 = \dot{Q}_{c.v.} + (\dot{n}_{H_2})_r (\Delta\bar{h}_{H_2})_r + (\dot{n}_{O_2})_r (\Delta\bar{h}_{O_2})_r - (\dot{n}_{H_2O})_p (\bar{h}^o_{f_{H_2O}} + \Delta\bar{h}_{H_2O})_p - (\dot{n}_{H_2})_p (\Delta\bar{h}_{H_2})_p$$
$$- (\dot{n}_{O_2})_p (\Delta\bar{h}_{O_2})_p - (\dot{n}_{OH})_p (\bar{h}^o_{f_{OH}} + \Delta\bar{h}_{OH})_p - (\dot{n}_H)_p (\bar{h}^o_{f_H} + \Delta\bar{h}_H)_p - (\dot{n}_O)_p (\bar{h}^o_{f_O} + \Delta\bar{h}_O)_p = 0 \tag{5}$$

<u>*Oxygen rich case (ORC)*</u>

The chemistry mechanism for this case uses the following reactions

$$xH_2 \quad + \quad yO_2 \quad \Leftrightarrow \quad xH_2O \quad + \quad (y - \frac{x}{2})O_2 \qquad \text{for} \quad x < 2y$$

$$H_2 \quad \Leftrightarrow \quad 2H$$

$$O_2 \quad \Leftrightarrow \quad 2O$$

$$2H_2O \quad \Leftrightarrow \quad H_2 \quad + \quad 2OH$$

and the changes in each specie in the form of fractions a, b, c, and d can be expressed as

$$\begin{array}{ccccc} xH_2 & + & yO_2 & \Leftrightarrow & xH_2O \\ -xa & & -\frac{x}{2}a & & +xa \end{array}$$

$$\begin{array}{ccc} H_2 & \Leftrightarrow & 2H \\ -b & & +2b \end{array}$$

$$\begin{array}{ccc} O_2 & \Leftrightarrow & 2O \\ -c & & +2c \end{array}$$

$$\begin{array}{ccccc} 2H_2O & \Leftrightarrow & H_2 & + & 2OH \\ -2d & & +d & & +2d \end{array}$$

The overall reaction is given by

$$xH_2 \quad + \quad yO_2 \quad \rightarrow \quad (xa - 2d)H_2O \quad + \quad [x(1-a) - b + d]H_2$$
$$+ \quad [y - \frac{x}{2}a - c]O_2 \quad + \quad (2d)OH \quad + \quad (2b)H \quad + \quad (2c)O$$

The five coupled, non-linear algebraic equations for this case become

$$f_1 = \frac{(xa-2d)^x [x + y - \frac{x}{2}a + b + c + d]^{x/2}}{[x(1-a) - b + d]^x [y - \frac{x}{2}a - c]^{x/2}} \left(\frac{P}{P_o}\right)^{-x/2} - K_1 = 0 \tag{1*}$$

$$f_2 = \frac{(2b)^2}{[x + y - \frac{x}{2}a + b + c + d][x(1-a) - b + d]} \left(\frac{P}{P_o}\right) - K_2 = 0 \tag{2*}$$

$$f_3 = \frac{(2c)^2}{[x+y-\frac{x}{2}a+b+c+d][y-\frac{x}{2}a-c]}\left(\frac{P}{P_o}\right) - K_3 = 0 \tag{3*}$$

$$f_4 = \frac{[x(1-a)-b+d](2d)^2}{[x+y-\frac{x}{2}a+b+c+d](xa-2d)^2}\left(\frac{P}{P_o}\right) - K_4 = 0 \tag{4*}$$

$$\begin{aligned} f_5 = {} & \dot{Q}_{c.v.} + (\dot{n}_{H_2})_r(\Delta\bar{h}_{H_2})_r + (\dot{n}_{O_2})_r(\Delta\bar{h}_{O_2})_r - (\dot{n}_{H_2O})_p(\bar{h}^o_{f_{H_2O}} + \Delta\bar{h}_{H_2O})_p - (\dot{n}_{H_2})_p(\Delta\bar{h}_{H_2})_p \\ & - (\dot{n}_{O_2})_p(\Delta\bar{h}_{O_2})_p - (\dot{n}_{OH})_p(\bar{h}^o_{f_{OH}} + \Delta\bar{h}_{OH})_p - (\dot{n}_H)_p(\bar{h}^o_{f_H} + \Delta\bar{h}_H)_p - (\dot{n}_O)_p(\bar{h}^o_{f_O} + \Delta\bar{h}_O)_p = 0 \end{aligned} \tag{5*}$$

The new model was tested for FRC and ORC up to 50% FRC and up to 60% ORC. Fig. 2 depicts the schematic of the problem considered.

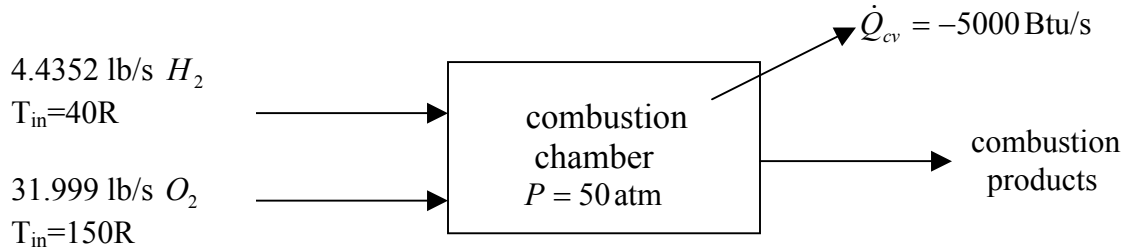

Figure 2 Schematic of the example problem considered

The variations of the adiabatic flame temperature and the flame temperature for the case of $\dot{Q}_{cv} = -5000$ Btu/s with the ratio X/Y (number of moles of H_2 to number of moles of O_2 in incoming reactants) are shown in Fig. 3. The trend in these curves is reasonable and as expected, i.e., the flame temperature decreases as the reactant mixture ratio deviates from stoichiometric ratio.

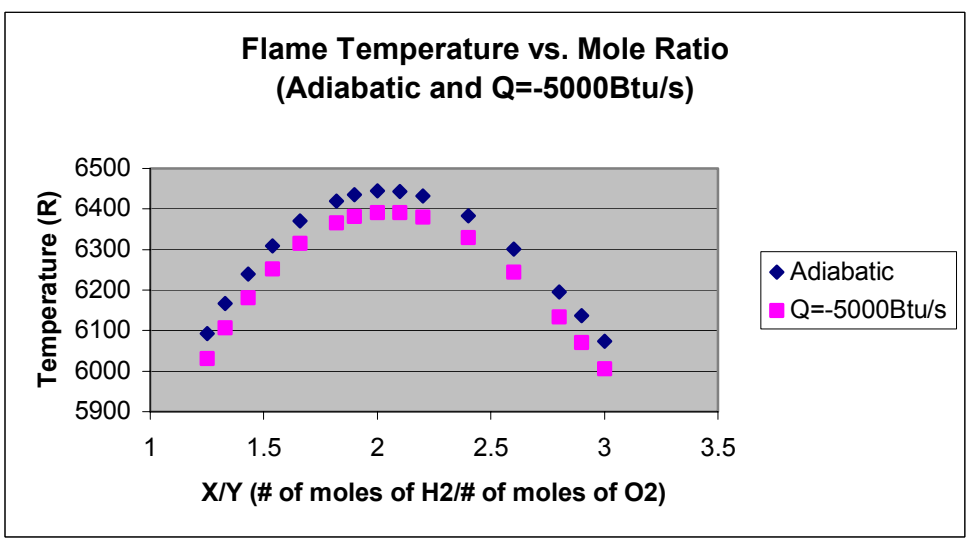

Figure 3. Variation of flame temperature with reactant mixture ratio

- <u>Stability of Newton-Raphson Method</u>

  The stability of Newton-Raphson method is dependent to a certain extent on the initial guess. When kinetic energy effects are neglected, for typical inlet conditions, the only varying parameter that will affect the equilibrium composition and product temperature is $\dot{Q}_{cv}$. For adiabatic case, for a range of X/Y values from 1.25 to 3.25, the range of values for parameter *a* yielding stable solution was determined and average value was correlated to X/Y together with values of parameters *b*, *c*, *d*, and *T* from solutions. This was implemented into the module. Complete stability requires determination of physically possible range of $\dot{Q}_{cv}$ values in conjunction with the effect of X/Y ratio.

- <u>Kinetic Energy Effects and Fluid Thermodynamic Properties</u>

  An enhanced version of the modular code was developed that incorporated the kinetic energy effects into the energy equation. The density of the combustion products was modeled by Amagat's model using the assumption of ideal gas mixture with six species as follows:

Using $$\rho = \frac{\dot{m}}{\dot{V}} = \frac{\dot{m}_{tot}}{\sum_{i=1}^{6} \dot{V}_i} = \frac{\dot{m}_{tot}}{\dot{V}_1 + \dot{V}_2 + \dot{V}_3 + \cdot \cdot \dot{V}_6}$$ where

$$P_p \dot{V}_1 = \dot{n}_1 \overline{R} T_p \qquad \dot{V}_1 = \frac{\dot{n}_1 \overline{R} T_p}{P_p}$$

$$P_p \dot{V}_2 = \dot{n}_2 \overline{R} T_p \qquad \dot{V}_2 = \frac{\dot{n}_2 \overline{R} T_p}{P_p}$$

$$\cdot \cdot \cdot \cdot \cdot \qquad \cdot \cdot \cdot \cdot \cdot$$

$$\cdot \cdot \cdot \cdot \cdot \qquad \cdot \cdot \cdot \cdot \cdot$$

$$P_p \dot{V}_6 = \dot{n}_6 \overline{R} T_p \qquad \dot{V}_6 = \frac{\dot{n}_6 \overline{R} T_p}{P_p}$$

Then

$$\rho_p = \frac{P_p . (\dot{m}_{tot})_p}{\overline{R} . T_p . \sum_i (\dot{n}_i)_p}$$

which is then used for determining the mixture exit velocity from the combustor using

$$V_p = \frac{(\dot{m}_{tot})_p}{\rho_p . A_{out}}$$

The improved module also included provisions for having LH_2 and LOX properties at a variety of combustor inlet conditions. For this provision, the thermodynamic properties at the inlet conditions are now accurately evaluated by use of thermodynamic property program

called GASPAK [3]. Subroutines have been added to call densities and enthalpies from GASPAK. The energy equation would result in the following

$$
\begin{aligned}
f_5 = {} & \dot{Q}_{c.v.} + (\dot{n}_{H_2})_r (\Delta\bar{h}_{H_2} + \frac{M_{H_2} V_{H_2}^2}{2g_c J})_r + (\dot{n}_{O_2})_r (\Delta\bar{h}_{O_2} + \frac{M_{O_2} V_{O_2}^2}{2g_c J})_r - (\dot{n}_{H_2O})_p (\bar{h}^o_{f_{H_2O}} + \Delta\bar{h}_{H_2O})_p \\
& - (\dot{n}_{H_2})_p (\Delta\bar{h}_{H_2})_p - (\dot{n}_{O_2})_p (\Delta\bar{h}_{O_2})_p - (\dot{n}_{OH})_p (\bar{h}^o_{f_{OH}} + \Delta\bar{h}_{OH})_p - (\dot{n}_H)_p (\bar{h}^o_{f_H} + \Delta\bar{h}_H)_p \\
& - (\dot{n}_O)_p (\bar{h}^o_{f_O} + \Delta\bar{h}_O)_p - (\dot{n}_{tot})_p \frac{M_p V_P^2}{2g_c J} = 0
\end{aligned}
\tag{5**}
$$

where M_p and V_p are the combustion product mixture average molar mass and velocity. The subroutines calculating the $\Delta\bar{h}$ values for the species in the combustion products were based on thermodynamic property tables using a reference point of $1\,atm$ pressure and $537R$. For those states for which the $\Delta\bar{h}$ values were obtained from GASPAK, *i.e.,* inlet liquid H_2 and O_2, the $\Delta\bar{h}$ were normalized to the same reference state by using

$$\Delta\bar{h}_{(T,P)} = \left(\Delta\bar{h}_{(T,P)}\right)_{GASPAK} - \left(\Delta\bar{h}_{(537R,1atm)}\right)_{GASPAK} .$$

Hence all $\Delta\bar{h}$ values were based on the same reference state.

<u>SSME Application:</u> A simplified model for the space shuttle main combustion chamber was considered. Figure 3 depicts the schematic of the problem considered. In this example the inlet

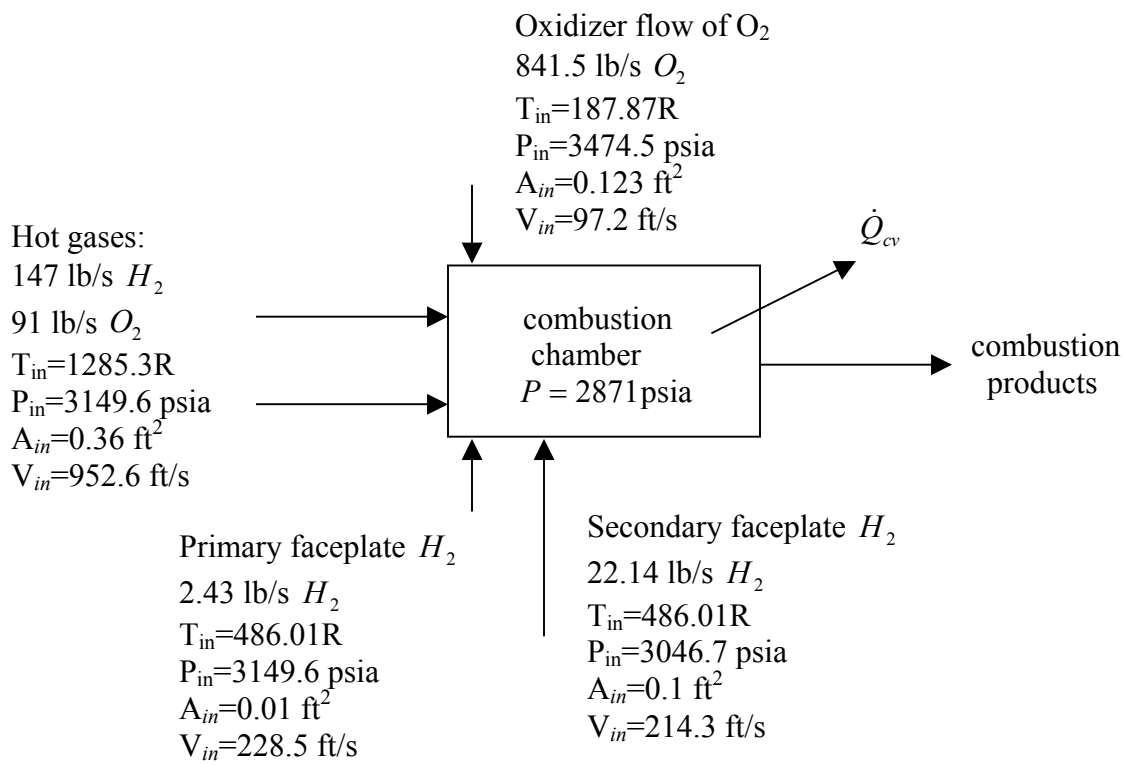

Figure 3. Schematic of the simplified main combustion chamber problem

streams consist of both hot gases coming from the pre-burner as well as streams of liquid phase H_2 and O_2. Several case studies were performed for this configuration for different values of $\dot{Q}_{cv}$ ranging from zero to $1.2 \times 10^6 \, Btu/s$. Figure 4 depicts the variation of combustion product temperature with $\dot{Q}_{cv}$. The qualitative behavior is again as expected, i.e., temperature decreasing with increase in heat transfer rate to coolants.

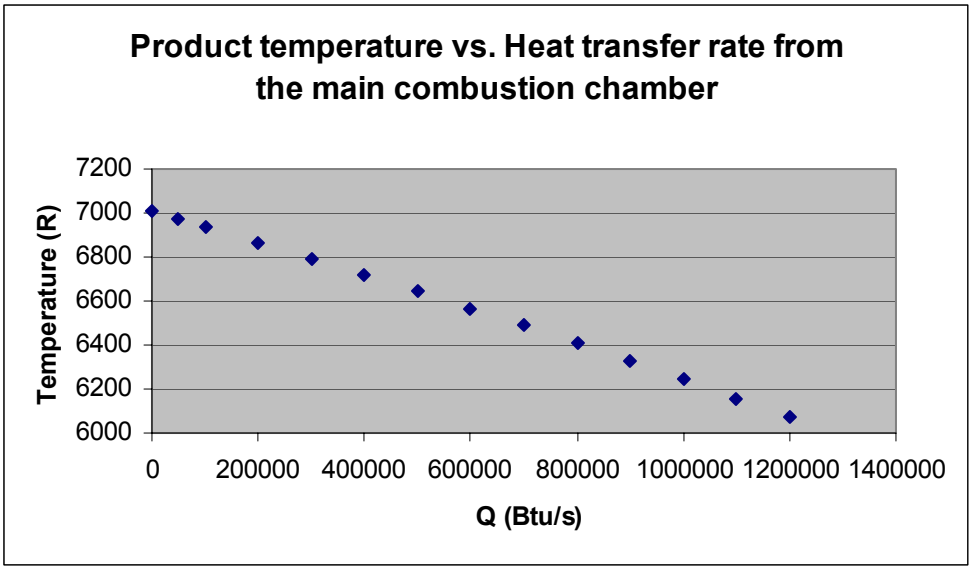

Figure 4. Variation of combustion product temperature with $\dot{Q}_{cv}$

It should be noted that the enthalpies of the species in the mixture of combustion products have been approximated by ideal gas enthalpies at the combustion temperature. The deviation of enthalpy from ideal gas enthalpy at such high pressures (3000-4000psia) may not be negligible and needs further investigation.

Acknowledgements

The author would like to thank Dr. Alok Majumdar for his continuous encouragement and mentorship during the author's NASA Faculty Fellowship appointment at Marshall Space Flight Center.

References

[1] Majumdar, A. (1999), "Generalized Fluid System Simulation Program (GFSSP) Version 3.0", Sverdrup Technology Report No. MG-99-290, Contract No. NAS8-40836.

[2] Sözen, M., "A Computational Method for Determining the Equilibrium Composition and Product Temperature in LH_2/LOX Combustor" Final Report in 2002 NASA Faculty Fellowship Program CR.

[3] Cryodata Inc., "User's Guide to GASPAK, Version 3.2, November 1994.

[4] Saad, M. A., *Thermodynamics, Principles and Practice*, Prentice Hall, Inc., Upper Saddle River, NJ, 1997

2003

NASA FACULTY FELLOWSHIP PROGRAM

MARSHALL SPACE FLIGHT CENTER
THE UNIVERSITY OF ALABAMA IN HUNTSVILLE

A STUDY OF THE SST IN THE COLD TONGUE OF THE NSIPP AND CCSM2 COUPLED CLIMATE MODELS

Prepared By:	Monica Y. Stephens
Academic Rank:	Assistant Professor
Institution and Department:	Spelman College Department of Mathematics
NASA/MSFC Directorate:	Science
MSFC Colleagues:	Dr. Robert J. Oglesby Dr. Franklin Robertson

1. Introduction

An accurate prediction of tropical Pacific sea surface temperature (SST) in coupled simulations is necessary to adequately simulate inter-annual variability within the models, in particular the evolution of the El Nino/Southern Oscillation (ENSO). The El Nino is a warming of the surface waters off the coast of Peru that has implications for weather on a global scale. For example, droughts in Australia and heavy rainfall in South America are associated with El Nino events and the severity of these events is associated with the strength of the El Nino.

This study focuses on the calculation from two climate model simulations of SST in the Nino3 region that includes the central and eastern tropical Pacific Ocean between 150W and 90W longitude and 5S and 5N latitude. The Nino3 index (a time series of monthly SST anomalies averaged over the Nino3 region) is used to determine the time evolution of El Nino events. If the Nino3 index is above a threshold value, generally a warming of 0.5C above "normal" conditions, then an El Nino has occurred. Under "normal" conditions (non-El Nino conditions) there is a region of cold water known as the cold tongue, off the coast of Peru, that is colder than might be expected given the equatorial location of the waters and the warmer surface waters to the west. These colder surface waters are due to northeasterly trade winds that cause a local divergence of waters at the coast. This water is replaced by colder subsurface water that upwells to the surface. The source of the subsurface water is the subtropics where surface water is subducted into the subsurface and travels southwestward towards the tropics where it meets with the strong eastward flowing Equatorial Undercurrent (EUC) and eventually upwells to the surface. During an El Nino the trade winds reduce in strength and the upwelling of cold subsurface waters in the eastern Pacific also reduces and causes warmer surface waters within the cold tongue.

Other studies have revealed problems associated with the SST calculation, in coupled models, in the region of the cold tongue. Mechoso et. al, 1995 reviewed eleven coupled model simulations and found that the cold tongue is too strong and extends to far to the west in most of the simulations. Sun et. al, 2003 shows that the inaccurate prediction of clouds by the atmospheric component of the National Center for Atmospheric Research (NCAR), Community Climate Model v.3 (CCM3) causes the SSTs of the cold tongue to be too cold.

In this study we investigate the SST in the Nino3 region of two coupled simulations, the Goddard - NASA's Seasonal to Inter-annual Prediction Project (NSIPP) model and NCAR Coupled Community Climate System Model v.2 (CCSM2). Although our goal is to eventually look in detail at the seasonal cycle of SST in these two models, we first concentrate on the annual-averaged SST. At a first glance, it appears that the cold tongue in both the NSIPP and CCSM2 models is displaced west of its observed location, although it is more severely displaced in the CCSM2. The SST at the core of the cold tongue in NSIPP model is slightly colder than the observed SST while the SST in the CCSM2 is approximately the same – this is especially surprising given the warmer surface waters in the subtropics of the CCSM2, which are the source of the upwelling water in the cold tongue.

Given the location and the temperature of the cold tongue in the CCSM2 it appears that the source waters of the cold tongue must come from farther poleward in the model than in observations. Evidence that supports this theory is the warmer subtropical surface waters in the CCSM2. Since these waters are the source of the subsurface water that upwell to the surface, in the tropics, the waters must have come from a more poleward location where the waters would be cold enough to make the tropical SST in the CCSM2 agree with the observed SST. Additionally, the westward displacement of the cold tongue in the CCSM2 also suggests that the source waters are poleward of the observed source waters. If waters are subducted farther north, due to the Coriolis acceleration, these waters will have the tendency to travel a more westward path. Water that enters the tropical oceans further to the west will upwell further to the west.

We use the MLOM, a one-dimensional mixed-layer ocean model, to support our theory of a more poleward subduction of tropical source waters as the cause of the difference in SST between the CCSM2 and observations in the cold tongue. This model only contains vertical dynamics and thermodynamics and will therefore be used to access the "local" change in SST. We use this model to (1) determine the SST change associated with having colder tropical subsurface temperatures in the CCSM and (2) determine whether increased entrainment alone could account for the reduction of SST that is present in the model.

2. Model Descriptions

In this study we analyze data from modern control simulations of two coupled climate models, the Goddard NSIPP model and the NCAR CCSM2. For sensitivity analysis we use the MLOM. A brief description of each of the coupled models is given with a more detailed description of the MLOM, which is the focus of the sensitivity studies.

2.1 The NCAR CCSM2

The NCAR CCSM2 is a coupled climate model with atmosphere, ocean, land, and sea ice components. The atmospheric component is the Community Atmospheric Model Version 2 (CAM2). It has T42 (~2.8 latitude x 2.8 longitude) resolution with twenty-six atmospheric layers (Kluzek et. al, 2002). The ocean component is the Parallel Ocean Program (POP) level model that gx3 resolution that contains finer grid resolution in the tropics and a pole over Greenland, with forty vertical levels (Smith and Gent, 2002). The sea ice component is the Climate System Ice Model (CSIM) that has ice dynamics and energy-conserving thermodynamics (Briegleb et. al, 2002). The land component is the Community Land Model (CLM) that has ten soil layers, sixteen vegetation types, and surface hydrology and river runoff (Vertenstein, et. al, 2002). A control simulation of the CCSM2 was run under modern conditions. We use data from the first twenty years of the 600th year of the simulation, which is more than 250 years after model spin-up.

2.2 The Goddard NSIPP

The Goddard coupled climate model NSIPP has atmosphere, ocean, and land components. The atmospheric component is a primitive equation model that can have variable horizontal and vertical resolution that may include stretched grids and grids with rotated poles (Suarez and

Takacs, 1995). The ocean component is the Poseidon ocean model that is a layer model with a turbulent ocean mixed-layer (Shopf and Loughe, 1995, Kraus and Turner, 1967). The land component is the Mosaic land surface model (LSM) that allows for vegetation control and contains three soil types (Koster and Suarez, 1992). A control simulation of the Goddard NSIPP model was run with one-degree horizontal resolution for 100 years. We use the last twenty years of the simulation in this analysis.

2.3 The MLOM

The mixed-layer ocean model (MLOM) is a one-dimensional model of the upper ocean that follows the physics of Kraus and Turner (1967). The model determines mixed-layer temperature (a proxy for sea surface temperature, SST), salinity, and depth from the specification of the pycnocline and the deep ocean and from its interaction with the atmosphere through surface heat, moisture, and momentum fluxes.

The model equations are derived from the equations for ocean momentum, temperature, salinity, and density, which are given in Gill, 1986. The mixed layer is treated as a horizontally homogeneous, Boussinesq fluid that obeys hydrostatics. With these assumptions the equations for the ocean are depth-integrated and Reynolds' averaged to obtain the mixed-layer equations. The MLOM equations are a system of three prognostic ordinary differential equations that describe the ocean temperature, salinity, and depth with an additional linear equation for the density. The governing mixed-layer equations are as follows:

$$\rho_o c_p h_m \frac{dT}{dt} = w_e \Delta T + F_A + F_{sw}(1 - e^{-\gamma h_m}) \tag{1}$$

$$h_m \frac{dS}{dt} = w_e \Delta S + F_S \tag{2}$$

$$we = \frac{2me^{-rh_m} u* + h_m / 2\left[(1-n)B_o + (1+n)B_o\right]}{\Delta b h_m + \Delta u^2} \tag{3}$$

$$\rho = \rho_o \left[1 - \alpha \Delta T + \beta \Delta S\right] \tag{4}$$

where h_m, T, S, w_e, and ρ are the mixed-layer depth, temperature, salinity, entrainment velocity ($w_e = dh/dt$), and density; ρ_o is the mean density of the ocean; c_p is the specific heat capacity; F_A, F_{sw}, and F_s are the surface nonsolar heat flux, solar heat flux and moisture flux, respectively; m and n are the dissipation parameters for winds and buoyancy; γ and r are 1/e-folding scale for solar radiation and wind mixing; ΔS and ΔT are the difference in temperature and salinity between the mixed-layer and the top of the pycnocline; $u*$ is the surface friction velocity caused by winds; Δu is the shear between the mixed layer and the pycnocline, specified as the greater of 3cm/s or the friction velocity; B_o is the net surface buoyancy flux; and α and β are the thermal expansion and haline contraction coefficients. In addition to mixed-layer deepening through entrainment, the model also contains a parameterization for mixed-layer shallowing and mixed-layer deepening caused by convective instabilities that result from the mixed-layer density exceeding the density of the pycnocline. A more complete description of the model may be found in Stephens, 1998 and a description of a control simulation of the MLOM coupled to an atmospheric model under modern conditions may be found in Stephens et. al., 2003.

3. Discussion of Results

In this section we look at the inter-annual variation of the SST in the Nino3 region and then the annual-averaged SST over the longitudinal extent of the Nino3 region, but extend the latitudinal boundaries to include the subtropics. The data are compared the observed data of COADS and Levitus (Woodruff et. al, 1998; Levitus, 1994).

Nino3 Index

Figure 1a,b shows the Nino3 index for the NSIPP and CCSM models for a twenty year period of each model simulation. The Nino3 index uses a time series of monthly SST anomalies averaged over the region 150W to 90W and 2S to 2N. Anomalies larger than 0.5C indicate that an El Nino has occurred. Comparing the model Nino3 indices to observations reveals a more regular El Nino, every 2 to 4 years, in the model than in observations, every 3 to 5 years. Also, the amplitude of the model El Nino is, on average, weaker than observations; no greater than approximately 3C in the models whereas observations contain anomalies that may be as large as 4C. Additionally, the models have a 22 to 25 year modulation in the data that does not appear in the observations.

The question of why the coupled simulations have such disagreement with observations is a topic of great discussion (Mechoso et al., 1995; Latif et al., 1998; Sun et al., 2003). The difference may occur in either the atmospheric component of the model, the ocean component of the model, or in the coupling parameterization between the atmospheric and the oceanic models. The main focus in this paper is on the role of the ocean model in predicting the SST. Particular attention is paid to a significant discrepancy between CCSM2 and observations in the tropical Pacific Ocean where it is clearly evident that the model cold-tongue is displaced west of its observed location. This error in the model SST has a significant affect on the model's ability to accurately predict tropical Pacific climate. We therefore spend time investigating this error, and our theory concerning the error, using the MLOM.

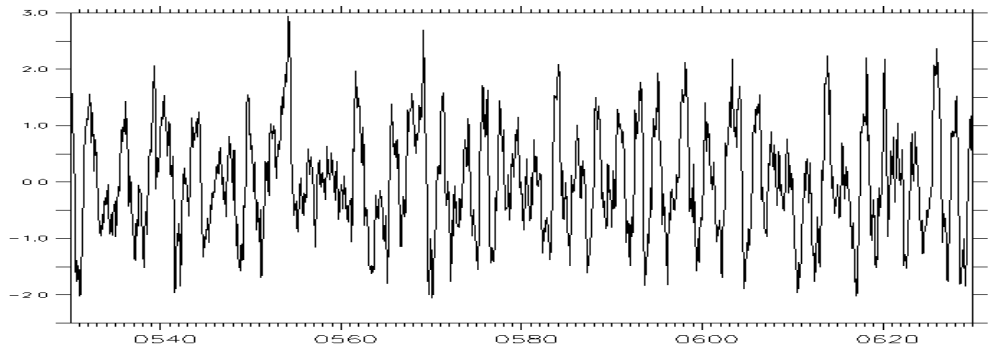

(a)

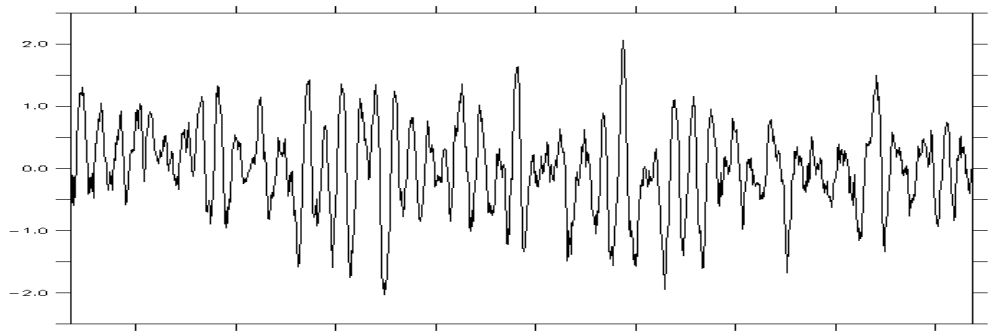

(b)

Figure 1: Nino 3 index (time series of monthly SST anomalies over the region 150W to 90W and 5S to 5N) for (a) the NCAR CCSM2.0 and (b) the Goddard NSIPP models for a twenty year period of each control simulation.

Sea Surface Temperature

Figures 2a,b,c, and d show the annual-averaged SST and SST differences from observations for the NSIPP and CCSM2 models along the longitudinal extent of the Nino3 region and from 20S to 30N. We have included an area larger than the Nino3 region to explore possible remote affects that cause differences between the model and observed SST.

The most striking difference between the CCSM2 SST and the observed SST is the westward displacement of the cold tongue in the CCSM2 model. The upwelling region, generally located directly off the coast of Peru between 105W and 90W, is between 120W and 110W in CCSM2. However, the temperature at the center of the cold tongue, 23C, is approximately the same as the observed temperature. Because of the displacement of the cold tongue, now in a region that would generally be characterized by warmer SST, the SST differences from observations are between 1C and 1.5C near the central Pacific Ocean. The waters of the eastern Pacific, directly off the coast of Peru are slightly warmer than observations. The water is likely warmer because

upwelling is decreased by a reduction in the surface winds or the subsurface waters along the coast are warmer than observations.

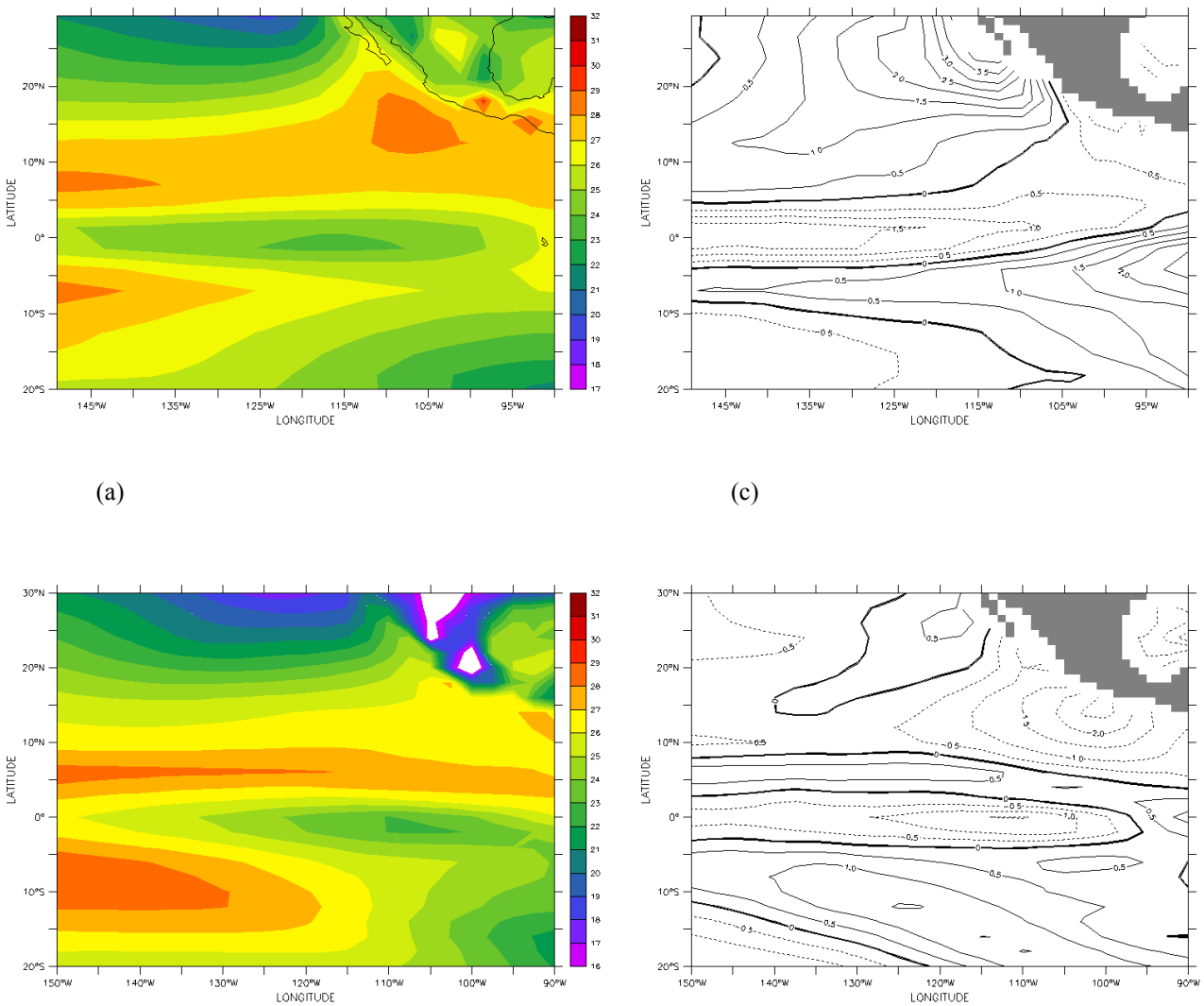

Figure 2: Annual-averaged sea surface temperature in the region Nino 3 longitudinal region for (a) the NCAR CCSM2.0 and (b) the Goddard NSIPP models; Annual-averaged temperature differences from observations for (c) CCSM2.0 and (d) NSIPP. The observed data set is taken from COADS.

The displacement of the cold tongue in the CCSM2 appears to be related to an error in the ocean component of the model that leads to subduction of waters farther north in the model than in observations. It must also be noted that the subtropics of the CCSM2 are warmer than observations, more than 3C warmer off the coast of Central America. The fact that the SSTs of

the subtropics are warmer than observations and that the center of the cold tongue in CCSM2 is approximately the same as observations also suggests that the subducted waters from the subtropics that eventually upwell within the tropics must be from a more northern location.

The NSIPP SST is in much better agreement with observations than CCSM2. The cold tongue of the NSIPP model is also displaced west of the observed cold tongue, although only slightly. The core of the cold tongue is 1C colder than observations. The westward displacement of the cold tongue, between 110W to 102W, and the decreased temperature of the center of the cold tongue cause the SST differences from observations to be approximately 0.5C to 1.0C. The subtropics of the NSIPP model are also in closer agreement with observations. The N.H. subtropics are, on average, colder than observations while the S.H subtropics are slightly warmer than observations.

The Problem with the CCSM Cold Tongue

The Pacific cold tongue is characterized by waters that are approximately 3C degrees colder than waters to the west, at the same latitude, because the source of these waters is upwelling of cold subsurface waters along the equator and off the coast of Peru. Upwelling in the western portion of the basin is suppressed by the piling up of water along the Eurasian coast by the trade winds. Hence, the water in the western half of the tropical Pacific is warmer than that water in the eastern half.

As mentioned previously, the CCSM2 has a cold tongue that is displaced far west of its observed location, although the temperature of the cold tongue is approximately the same as observations. It appears that the westward displacement of the cold tongue is caused by waters that subduct too far to the north in the model. Since the subtropical waters follow a southwestward path to the tropics, water that is subducted from higher latitudes will tend to enter the tropics at a more westward location and therefore upwell farther to the west. Another indication that the waters in the cold tongue of the CCSM2 come from farther north than in observations is that although the subtropical temperatures of the model are warmer than observations, the temperature at the center of the cold tongue is approximately the same as the observed temperature. Since the subtropical waters are warmer the source waters of the cold tongue must have come from farther north to achieve a temperature that is of the same magnitude as observations.

Another possible explanation for the location and temperature of the cold tongue in the CCSM2 is a local increase in entrainment west of the observed cold tongue region. We conduct several sensitivity studies, using the MLOM, to dispel this theory and therefore support our theory that a change in the subduction is the primary cause of the displaced cold tongue in CCSM2.

In the first sensitivity study we use data from observations and from the CCSM2 at 113W and 0N, which is near the center of the cold tongue in CCSM2, to serve as lower boundary conditions for the MLOM. In the MLOM the pycnocline temperature and salinity gradients, the pycnocline depth, and the deep ocean temperature and salinity are specified. Although it is standard to use pycnocline depth as a lower boundary condition in the model, we instead use the thermocline depth, which in the tropics is not much different from the depth of the pycnocline. Table 1 shows the data that are used in the MLOM experiments. We see that the temperature gradient

for CCSM2 and observations are almost the same, although the overall temperature, with depth, in the CCSM2 is colder than observations. The colder subsurface waters of the CCSM2 obviously originate from much higher latitudes than the subsurface waters from observations. We chose the observed salinity profile for both the CCSM2 and observed pycnocline profile since salinity does not play as significant a role as temperature in mixed-layer dynamics at this location. The MLOM, with the profiles specified in table 1 is forced with surface fluxes of heat and momentum from a control simulation of the atmospheric component of the CCSM2 that is not coupled an ocean, but rather contains SSTs that are specified from observations.

	CCSM	NSIPP
T_m	23.5	23
S_m	35.45	35.45
h_m	50	50
T_d	2.5	0.8
S_d	34.6	34.6
h_d	2000	2000
dT/dz	-1.138e-02	-1.077e-02
dS/dz	-4.36e-02	-4.36e-04

Table 1: Mixed-layer temperature (Tm – deg C), mixed-layer salinity (Sm – ppt), mixed-layer depth (hm – meters), deep ocean temperature (Td – deg C), deep ocean salinity (Sd – ppt), pycnocline depth (hd – meters), pycnocline temperature gradient (dT/dz – deg C/meter), pycnocline salinity gradient (dS/dz – ppt/meter)

Figure 3 shows the seasonal cycle of temperature and mixed-layer depth for the CCSM2 and observed pycnocline profiles. The difference in mixed-layer depth between the two runs is, on average, less than 10 meters. This suggests that both profiles undergo approximately the same amount of entrainment. The temperatures for the CCSM2 profile are colder than those for the observed profile. During the winter the temperature difference is largest at 0.4C. Colder subsurface temperature in the CCSM2 therefore accounts for approximately 1/3 of the total cooling of the CCSM2 compared to observations. The remaining temperature difference is likely caused by changes in the surface energy budget.

A second sensitivity analysis was conducted to show that increased entrainment in the CCSM2 could not account for the reduced temperature in the central Pacific. In this analysis we use the observed pycnocline as lower boundary conditions for the MLOM and force the model with the same atmospheric data as in the previous sensitivity study. In this experiment we test the change in SST when entrainment is increased, by increasing the winds. The wind forcing is increased by two, four, and ten times the original wind forcing. Figure 4 shows the mixed-layer temperature and depth for the different wind forcings. The only significant change in temperature and depth occur when the winds are ten times the original wind forcing. This increase in winds is unrealistic and therefore an increase in entrainment alone cannot account for the differences we see in the CCSM2 and the observed temperatures.

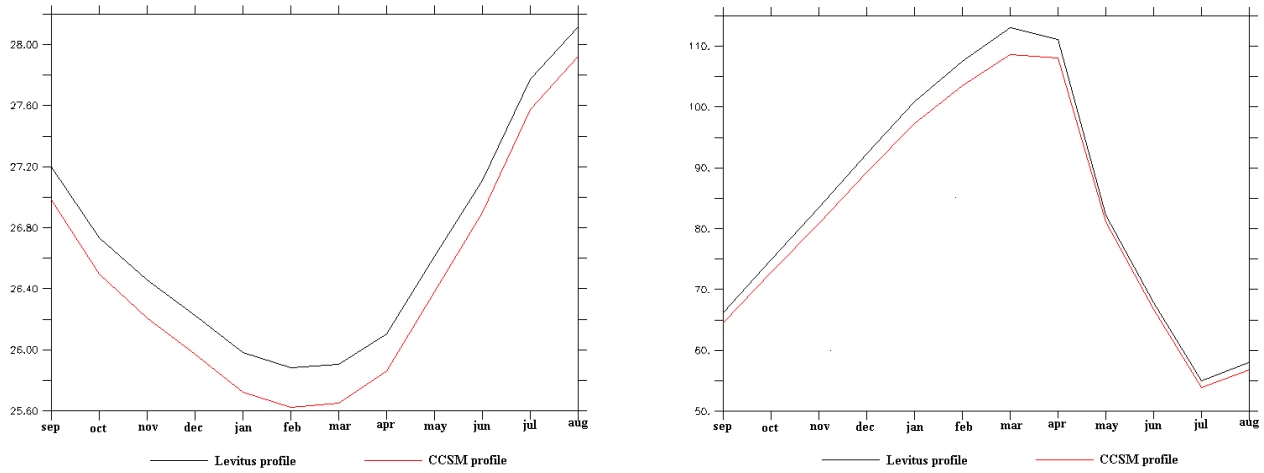

Figure 3: Seasonal cycle of (a) mixed-layer temperature (deg C) and (b) mixed-layer depth (meters) from MLOM. This sensitivity study of the MLOM was conducted with pynocline profiles from Levitus data and the CCSM ocean model. The results show that the difference in profile, colder subsurface temperatures in CCSM, contribute to an over colder SST in the model than in observations. The coldest temperatures are present during Northern Hemisphere winter with an SST difference of approximately 0.4C. This does not give the total temperature difference between observations and the model. The remaining temperature difference may be caused by a reduced surface heat flux and by upwelling (not accounted for by the MLOM).

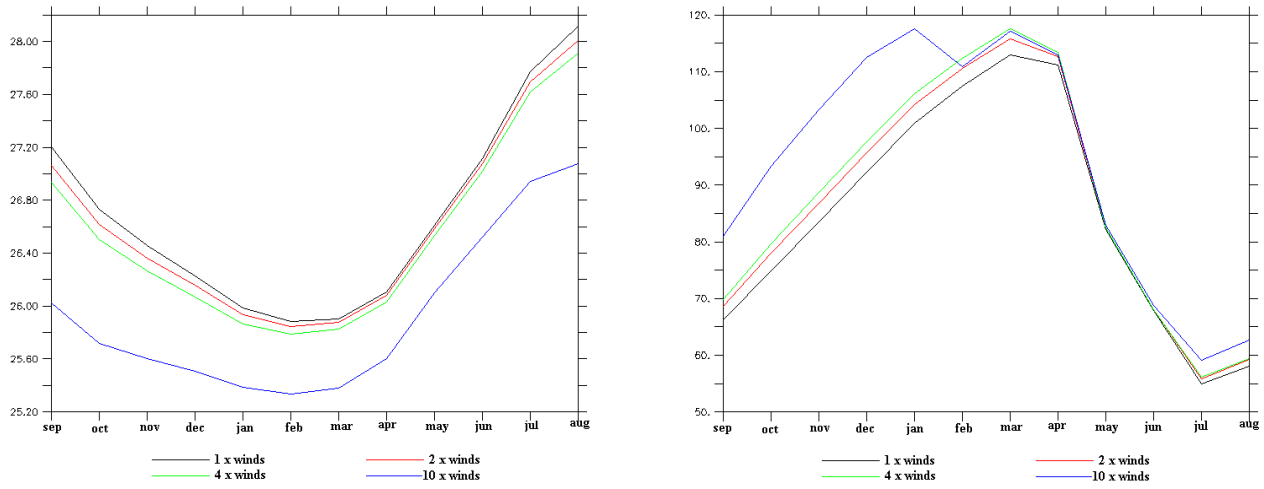

Figure 4: Seasonal cycle of (a) mixed-layer temperature (deg C) and (b) mixed-layer depth (meters) from MLOM. This sensitivity study of the MLOM was conducted with the pycnocline profile from Levitus data. The wind forcing in the model has been increased by a factor of 2, 4, and 10 to increase the model entrainment. With more entrainment, no significant temperature differences occur until the winds are 10 times stronger than the default winds, likely unrealistic.

4. **Conclusion**

This study focuses on the calculation of SST in the NSIPP and CCSM2 climate models in the central and eastern Pacific Ocean, the region were the El Nino has its strongest signal. The Nino3 index in both models reveals an El Nino cycle that is more regular than observations, that is weaker than observations (SST not as warm), and that has a 22 to 25 year modulation of SST that does not occur in observations. The most obvious difference with observations is seen in the annual-averaged SST. In both models the cold tongue is positioned west of the observed location. The NSIPP cold tongue is slightly colder than observations while the CCSM2 cold tongue is of approximately the same temperature. The fact that the CCSM2 cold tongue is the same temperature as observations is fortuitous given the warmer subtropical waters in the model, which are a source for the tropical waters. Overall, the NSIPP model is in better agreement with observation so more emphasis is placed on the prediction in the CCSM2.

The westward displacement of the cold tongue and the temperatures at the core of the cold tongue of the CCSM2 suggest that waters that are the source of the cold tongue subduct too far north in the model. An alternate theory is that increased local entrainment of the model leads to a colder SST. Two sensitivity experiments were performed with the MLOM that give credence to the theory that an error in subduction is the cause of the differences between the observed and model simulated cold tongue. The first sensitivity analysis shows that colder subsurface temperatures in the CCSM2, most probably caused by the subduction of more poleward subtropical waters, account for at least 1/3 of the temperature difference between the model and observations. The rest is likely due to the difference in the surface energy balance. A second sensitivity study in which the MLOM wind forcing was increased shows that entrainment alone cannot account for the difference in temperature between the model and observations.

Further analysis of the CCSM2 data is required to solidify our conclusions. For example, to verify a more poleward source for the cold tongue, it is necessary to look at the ocean flow from a Lagrangian perspective, perhaps by tracking the release of tracers within the model. Additionally, more attention must be paid to the role of the surface energy balance in regulating the SST. In particular, as Sun et al., 2003 suggests, an inaccurate prediction of clouds in the model may be an additional source of error in the model prediction of SST.

References

[1] Briegleb, Bruce, Cecilia Bitz, Elizabeth Hunke, William Liscomb, and Julie Schramm, May 2002: Description of the Community Climate System Model Version 2 Sea Ice Model. NCAR, Boulder, Co.
www.ccsm.ucar.edu/models/ccsm2.0/csim/SciGuide/ice_scidoc.pdf

[2] Kluzek, Erik, Mariana Vertenstein, and Brian Eaton, May 2002: User's Guide to the NCAR CAM2.0. Climate and Global Dynamics Division, NCAR, Boulder, Co. www.ccsm.ucar.edu/models/ccsm2.0/cam/camUsersGuide/index.shtml

[3] Koster, R. D., and M. J. Suarez, 1992: Modeling the Land Surface Boundary in Climate Models as a Composite of Independent Vegetation Stands. *J. Geophys. Res*., 97, 2697–2715.

[4] Kraus E.B. and J.S.Turner, 1967: A One-Dimensional Model of the Seasonal Thermocline II. The General Theory and Its Consequences. *Tellus*, 19, pp.98-105.

[5] Latif, M., D. Anderson, T. Barnett, M. Cane, R. Kleeman, A. Leetmaa, J. O'Brien, A. Rosati, and E. Schneider, 1998: A Review of the Predictability and Prediction of ENSO. *J. of Geophys. Res*., 103, pp. 143756-14393.

[6] Levitus, S. and T. Boyer, 1994: World Ocean Atlas 1994 Volume 4: Temperature. NOAA Atlas NESDIS 4, U.S. Department of Commerce, Washington, D.C.

[7] Mechoso, C.R., A.W. Robertson, N. Barth, M.K. Davey, P. Delecluse, P.R. Gent, S. Ineson, B. Kirtman, M. Latif, H. Le Treut, J.D. Neelin, S.G.H. Philander, J. Polcher, P.S. Schopf, T. Stockdale, M.J. Suarez, L. Terray, O. Thual, and J.J. Tribbia, September, 1995: The Seasonal Cycle of the Tropical Pacific in Coupled Ocean-Atmosphere General Circulation Models. *Mon. Wea. Rev*., pp 2825 – 2338.

[8] Schopf, P., and A. Loughe, 1995: A Reduced-Gravity Isopycnic Ocean Model-Hindcasts of El Nino. *Mon. Wea Rev*., 123, pp.2839-2863.

[9] Smith, Rick, and Peter Gent, Eds., May 2002: Reference Manual for the Parallel Ocean Program (POP): Ocean Component of the Community Climate System Model (CCSM2.0). Los Alamos National Lab, Los Alamos, New Mexico.
www.ccsm.ucar.edu/models/ccsm2.0/pop/doc/sci_ref_manual.pdf

[10] Stephens, Monica Y., 1998: A One-Dimensional Mixed-Layer Ocean Model for Use in Three-Dimensional Climate Simulations, *Ph.D Thesis*. Brown University, Providence, RI.

[11] Stephens, Monica, Robert Oglesby, and Martin Maxey, 2003: A One-Dimensional Mixed-Layer Ocean Model for Use in Three-Dimensional Climate Simulations: Control Simulation Compared to Observations. *J. Climate* (submitted).

[12] Suarez, M. J., and L. L. Takacs, 1995: Documentation of the ARIES/ GEOS dynamical core: Version 2. NASA Tech. Memo. 104606, Vol. 5, 58 pp.

[13] Sun, De-Zheng, John Fasullo, Tao Zhang, and Andres Roubicek, February 2003: A Note on the Radiative and Dynamical Feedbacks Over the Equatorial Pacific Cold-Tongue, *J. Climate* (accepted).

[14] Vertenstein, Mariana, Keith Oleson, and Sam Levis, May 2002: CLM2.0 User's Guide. NCAR, Boulder, Co.
www.ccsm.ucar.edu/models/ccsm2.0/clm2/UsersGuide/UsersGuide/UsersGuide.html

[15] Woodruff, S.D., H.F. Diaz, J.D. Elms, and S.J. Worley, 1998: COADS Release 2 data and metadata enhancements for improvements of marine surface flux fields. *Phys. Chem. Earth*, **23**, 517-527.

Acknowledgements

I would like to thank the NASA Faculty Fellowship Program for the opportunity to work at Marshall Space Flight Center this summer. I would like to thank my colleagues, Robert J. Oglesby, Franklin (Pete) Robertson, Jayanthi Srikishen, and Dan Fitzjarrald for their assistance, their support, and for their guidance on this research.

2003

NASA FACULTY FELLOWSHIP PROGRAM

MARSHALL SPACE FLIGHT CENTER
THE UNIVERSITY OF ALABAMA IN HUNTSVILLE

3-D PHOTONIC BAND GAP CRYSTALS

Prepared By:	Girija Subramaniam
Academic Rank:	Professor
Department:	Chemistry
Institution:	Penn State University-Hazelton
NASA/MSFC Directorate:	Science
MSFC Colleague:	Andrew Keys

Introduction

The hallmarks of current century are miniaturization of devices and high-speed computation. Optical fibers can carry gigabits/second and replaced the slower electronic carriers; however, each of the network nodes requires electronic processing at the end. Transduction from photonics to electronics limits the performance and affordability of the network. One needs optical interconnections to enable high-speed data access and reliability. This will be possible only by optical confinement or by localization of light. Just like electrons are confined within the metallic wire and follow the path of the wire without leaking into the background in an electronic circuit, light needs to be confined and guided in a desired path without leakage into the background.

Research for materials to trap light has grown exponentially over the past decade. Logical deduction supported by theoretical calculations [1, 2] suggests that the only way to trap light is to device/synthesize periodic array of non-absorbing and strongly scattering dielectric structures. Such structures prohibit light propagation over a band of frequencies, called Photonic Band Gap, PBG; this, in turn leads to localization of photons and inhibits spontaneous light emission [3-5]. These dielectric materials are referred to as the Photonic Band Gap Materials, PBGM, in general and as Photonic Crystals, PCs, if they are crystalline. PBGM can also reflect light for any direction of propagation over certain frequencies, which is being exploited in the creation of an all-optical integrated circuit [3]. Depending on whether the periodicity is in 1, 2 or 3 directions, these are classified as 1-D, 2-D and 3-D Photonic Crystals.

Very strong scattering requisite for PBG formation implies that the dielectric material should have a high refractive index and at the same time does not absorb in the region of interest. This, in turn, restricts the choice of materials that can be used in the synthesis/fabrication of PBGM. Commonly used materials are Si, Ge, InP, and GaAs etc.

Fabrication of Photonic Band Gap Materials

Of the numerous varied fabrication methods used, the most commonly used are as follows: layer by layer fabrication, stacking layer by layer, lithography, electrochemical etching of the pattered substrate, two-photon lithography [6-10]. Most of these methods are applicable for small-scale fabrication. They are more involved and complex processes. Mass production of 3-D PCs can be achieved either by 2-photon holographic lithography [11] or from colloidal assemblies [12]. The simpler and easier way is colloidal self-assembly wherein colloidal spherical particles of silica or polymer spontaneously assemble into a face centered cubic (FCC) arrangement. Self-assembly is superior to the other lithographic methods because it is less complex and it can produce thicker materials; further just by changing the diameter of the dielectric spheres, PCs that are active anywhere from UV to Near IR region can be made. Dielectric spheres are usually made of silica or polymer.

PCs via Self-Assembly

Self-assembly of silica spheres lead to a close packing arrangement known as Face Centered Cubic (FCC) packing, which is the Opal structure. Calculations and experiments show that these

opal structures do not have a complete photonic band. However the inverse structures i.e. air spheres in high refractive index background dielectric material have a complete photonic band gap. The goal of this project is to make the inverse opal structure, a PBGM with complete gap.

The strategy to inverse opals involve the following steps:

Synthesis of Monodisperse silica spheres
Self-assembly in Face Centered Cubic (FCC) packing to form the opal template
Infiltration of the interstitial air gaps with high refractive index dielectric material
Removal of the template to form the inverse opal structure

Synthesis of Silica Spheres

Highly Monodisperse silica spheres were obtained by Stober's process, by the ammonia-catalyzed hydrolysis of Tetraethoxysilane, TEOS [13]. The Monodispersity and the size were confirmed by Dynamic Light Scattering experiment and by Scanning Electron Micrograph. Spheres of diameters 380, 480 and 1000 were synthesized.

$$\mathbf{Si(OC_2H_5)_4 + 4\,H_2O \rightarrow SiO_2 + 4\,C_2H_5OH}$$

Methods of Self-Assembly

The most popular conventional method of crystallization of silica spheres is by sedimentation; it works well for heavy spheres, but is very time consuming. Other popular methods lead to polycrystalline material – structures incapable of being incorporated into a device and the presence of too many effects destroy the desired optical property. These defects were overcome by a technique of self-assembly that relies on capillary forces [14, 12]. Our crystals were assembles using these methods and by the faster Electrophoretic methods [15].

The spheres were assembles on a cut silicon wafer substrate, form a 1% v/v ethanolic suspension. The quality of the thicker deposits was amazingly uniform as shown in Figure 1.
The assembly from electrophoresis was also equally good as seen in the SEM image in Figure 2.

Figure 1. SEM image of Capillary Driven Self-Assembly of Silica Spheres

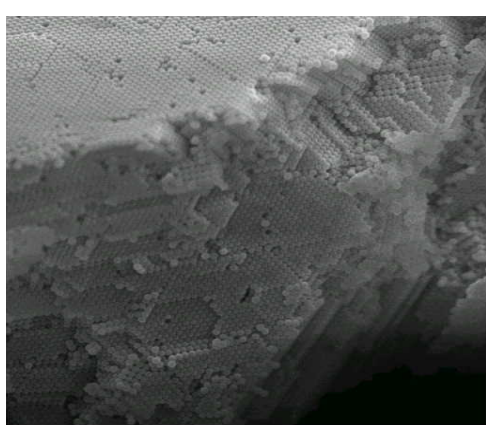

Figure 2. SEM image of Electrophoretic Assembly of Silica Spheres

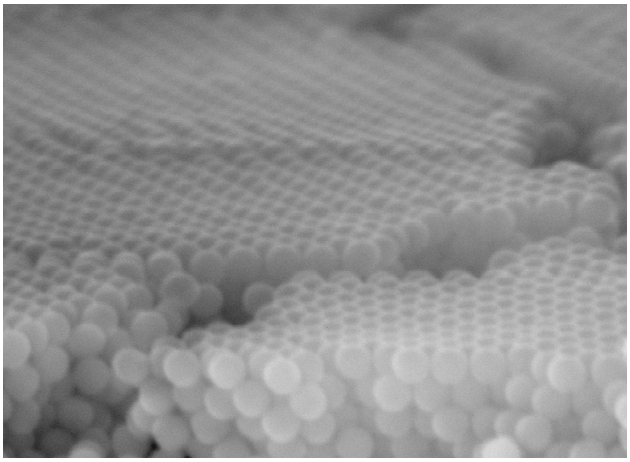

Optical Diffraction in of Opal Template

The transmission spectrum of opal grown on glass-ITO anode is shown in Figure 3. The stop band gap occurs between

Figure 3. Transmission Spectrum of Opal

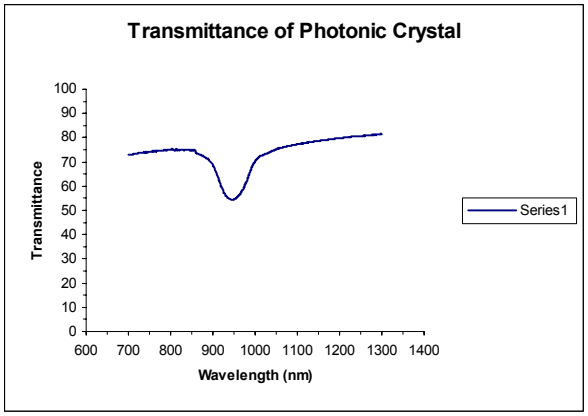

Infiltration by Silicon

The infiltration of silicon into the interstitial spaces was tried by sputtering technique. Sputtering was done for 2 hours at RT. The SEM image of the sputtered template shows infiltration of silicon only on the top layer. Low Pressure Chemical Vapor Deposition (LPCVD) has been shown to infiltrate silicon all the way to the substrate [12] and the future efforts will be using LPCVD.

Infiltration by Diacetylene monomer

In the photonic band gap the linear modes of propagation of light of certain frequencies is prohibited. So it is expected to enhance non-linear properties. To investigate this further, the Diacetylene monomer, DAMNA was chosen. The opal templates were soaked in a dichloroethane solution of the monomer for 3 days at RT and exposed to UV radiation. The silica will be etched away using Hydrofluoric acid to leave PC of NLO polymer. This work is in progress.

Future Efforts

The project is still in progress. Optimization of conditions for Electrophoretic assembly needs to be polished with better polished electrodes, infiltration conditions are to be improved and optical diffraction needs to be studied in more detail with high resolution and at different angles of incidence. We are also investigating strategies to introduce defects controllably to produce micro cavity for lasing.

Acknowledgements

The author gratefully acknowledges Andrew Keys for the sponsorship and for his efforts to make me comfortable at MSFC. Special thanks are to Dave Smith, SD 46 for the constant and untiring helping hand given and for the use of the laboratory facilities. My special thanks are to Curtis Banks, Paul Carpenter, and Palmer Peters for their assistance and all other members of Science Directorate who made my stay very pleasant at MSFC.

References

1. S. John, *Phys. Rev. Lett*. **53**, 2169, **1984**
2. P. W. Anderson, *Phil. Mag*. **B52**, 505, **1985**
3. S. John, *Phys. Rev. Lett*. **58**, 2486, **1987**
4. E. Yablonovitch, *Phys. Rev. Lett*. **58**, 2059, **1984**
5. A. P. Bykov, *Sov. J. Quant. Electron.* **4**, 861, **1975**
6. M. Qui, H. Smith
7. K. Aoki et al, *Appl. Phys. Lett*. **81**, 3172, **2002**
8. S. W. Leonard, H. M. van Driel, A. Bimer, U. gosele and P. R. Villeneuve, *Opt. Lett*. **25**, 1330, **2000**
9. Perry or Ho or Japanese
10. D. N. sharp et al., Quant. *Opt. Elect*. **34**, 3, **2002**
11. Y. A. Vlasov et al., *Adv. Mater*. **11**, 165, **1999.**
12. Y. A. Vlasov Y. A., X. Bo, Z. Strum and D. J. Norris, *Nature*. **414**, 289, **2001.**
13. W. Stober, A. Fink and J. Bohn, *J. Colloid Interface*., **26**, 62, **1968.**
14. P. Jiang, J. F. Bertone, K. S. Hwang and V. L. Colvin, *Chem. Mater.,* **11**, 2132, **1999**
15. A. L. Rogach, N.A. Kotov, D. S. Koktysh, J. W. Ostrander and G. A. Rogoisha, *Chem. Mater.,* **12**, 2721, **2000**

2003

NASA FACULTY FELLOWSHIP PROGRAM

MARSHALL SPACE FLIGHT CENTER
THE UNIVERSITY OF ALABAMA IN HUNTSVILLE

THE EFFECT OF ADVANCED MANUFACTURING TECHNOLOGIES AND TECHNIQUES ON THE COST OF FUTURE EARTH-TO-ORBIT SPACE TRANSPORTATION SYSTEMS

Prepared By:	Meenakshi Sundaram
Academic Rank:	Professor
Institution and Department:	Tennessee Tech University Department of Industrial and Manufacturing Engineering
NASA/MSFC Directorate:	System Management
MSFC Colleagues:	Stephen D. Creech Andy Prince

Introduction

This study presents a method to quantify the potential reduction in costs that NASA can realize through its contractors who use new advanced technologies and techniques in the manufacturing of space transportation systems.

The U.S. Space Shuttle, the first reusable manned space transportation system, is made up of over a million parts [1]. Almost 250 contractors participated in its fabrication and assembly. This one-of-a-kind system was built to provide safe and reliable space transportation.

Since the first Space Shuttle was built over two decades ago, technology and product development methods in design, manufacturing, assembly, and testing have undergone radical improvements, including newer materials with better manufacturability.

The manufacturing philosophy is also changing. Currently, increased outsourcing is the norm and this trend is expected to continue in the near future. Competition is driving the cost down for mass-produced consumer goods. The competitive market is forced to offer whatever the customer demands, including custom-designed products at mass-produced prices.

It is in this context that E. P. Campbell [2], CEO of a large manufacturing company in Ohio, defines manufacturing as “a process of defining products, integrating operations, implementing strategies, and having proprietary rights." This definition is strongly applicable to NASA’s design and development of future human space transportation systems.

Manufacturing cost of a product is usually determined in the commercial world using product data and technical specifications. Since the selling price will be determined based on the profit criterion, production costs must be accurately estimated. In the military and space programs, accurate cost estimation is especially critical in the environment of budget pressures.

Accurately estimating the life cycle cost of future earth-to-orbit space transportation systems is challenging. Typically, the costs of systems to be built are estimated several years before actual manufacturing begins. Limited quantities prevent large volume discounts and take away the opportunity to lower costs with continuous improvement initiatives.

The Systems Management Office (SMO) Engineering Cost Office at Marshall Space Flight Center (MSFC) uses the NASA/Air Force Cost Model (NAFCOM) [3] cost model to estimate development and production costs, along with other software packages such as PRICE [4] and SEER-H [5]. However, these cost models are unable to capture the potential savings from using state-of-the-art manufacturing technologies and techniques such as those employed in the production facilities of NASA prime contractors and their outsourcing partners.

In this study, a reliable methodology has been developed reflecting the advances in manufacturing technologies and techniques. With the approach developed, the cost models may be calibrated to exploit the effect of the recent advances in the design, manufacturing, materials, and tooling of space transportation systems.

The need for the following additional work became apparent during the study. These are:

- Changes in the manufacturing method input in NAFCOM
- A framework for process-based cost modeling.

New technologies, such as exotic materials that are lighter yet are able withstand higher stresses under extreme weather conditions, have created the need for newer manufacturing processes. These new processes, such as water jet cutting and high speed machining, helped encourage the current climate of aggressive collaborating and outsourcing among manufacturers to make better use of limited resources. Competitors often collaborate, thereby making use of their core competencies in designing and developing a cost effective and quality product.

Innovative manufacturing strategies and philosophies such as lean manufacturing, six sigma, and Just-In-Time (JIT) are being implemented in unprecedented levels to improve the product quality and cost, not only in the manufacture of consumer products but also in the production of spacecraft. The prime contractors of the space industry are consortium members of the Lean Aerospace Initiative(LAI) [6] program at the Massachusetts Institute of Technology (MIT) to learn and implement lean manufacturing concepts in all phases of designing and manufacturing.

Since 1993, the Lean Aerospace Initiative has successfully demonstrated that the concepts, principles, and practices of the Toyota Production System (TPS) can be applied to the military aircraft industry [6]. The LAI consortium consists of:

- Airframe, engine, avionics, missile and space companies
- Air Force agencies and System Program Offices (C-17, F-22, Joint Strike Fighter)
- NASA, Army, Navy, National Reconnaissance Office
- Pentagon – Office of the Secretary of Defense, Air Force Secretariat
- International Association of Machinists
- MIT.

The consortium members consider LAI as the venue for collaboration on aerospace challenges.

Impressive gains in manufacturing are reported through the LAI program initiatives. The following are examples of reported success stories:

- Throughput time reduction in the extrusion shop from 12 days to 3 minutes in the production of C-130J
- Reduction in automatic NC code generation time with up to 40% and 80% improvement in quality.
- Cost reduction of 75% in the fabrication of military electronic modules from commercial lines at TRW
- Cycle time reduction of 75% in the F-16 Build-To-Print Center
- Assembly time reduction of up to 47% at Boeing in the production of the 777 floor beam
- Lead time reduction of 67% at Pratt and Whitney General Machining Center
- Reduction in Floor Space in the production of Delta IV launch vehicles.
- One hundred percent on- time deliveries at GE Lynn aircraft engine facility
- Reduction in unit cost of up to 63% in the production of Joint Direct Attack Munitions (JDAM) from an estimate of $68K to $15K
- The C-17 unit price is reported to have decreased from $260M to $178M for the final 80 aircrafts in a total buy of 120.

Since production quantities are limited, this magnitude of cost reduction in the development of future earth-to-orbit space transportation systems may not be possible. However, state-of-the-art manufacturing technologies and techniques will provide some cost savings in the production phase. A general idea is that 30% of the cost of a program is incurred in the design, development, testing, and launching of the first vehicle in orbit. In this case, a method that incorporates the potential cost savings into the cost estimation tools for future earth-to-orbit space transportation systems is needed.

Methodology Used

The first step was to create a survey for the three prime contractors in order to capture the potential cost savings of state-of-the art manufacturing technologies and techniques. An extensive review of contractor presentations and reports related to claimed cost savings available in the public domain was performed prior to creating the survey. This review yielded two sets of questionnaires.

The first questionnaire, attached in Appendix C, is very detailed and was designed to obtain major inputs required for the development of a Process-Based Cost Model underway at Science Applications International Corporation (SAIC). After discussions with many of the engineers and scientists at the Engineering Cost Office, as well as engineers in the Materials, Processes, and Manufacturing department of the Engineering Directorate at MSFC, the ten-week time schedule was deemed too challenging to collect and analyze this amount of data. Hence, a second survey questionnaire, attached in Appendix B, was designed and feedback obtained before it was sent out.

In this questionnaire, twenty-five different technologies were identified and included. These technologies are state-of-the art manufacturing technologies proven in the commercial and military aircraft industry to reduce cost and improve efficiency. A technology is defined as a hardware or software-oriented item that requires a substantial capital investment. The technology may be used exclusively for a specialized function, such as a laser tracking system used for alignment.

Twenty different manufacturing techniques were identified for inclusion in the survey. This list is not an exhaustive by any means -- some techniques such as the "5S Program" were deliberately left out since it would be covered in a continuous improvement program. A manufacturing technique is defined for this study as a manufacturing philosophy or strategy requiring a radical change in the way the business is conducted within an organization. Essentially, a manufacturing technique will require a complete cultural transformation on the shop floor to improve productivity, quality, and reduce cost. An example of this is lean manufacturing.

The basic tenet of lean manufacturing is the elimination of all kinds of wastes. Companies are applying lean concepts throughout the enterprise to eliminate wastes in all areas from sales to warehousing operations. The concepts, principles, and practices of lean manufacturing revolve around the Toyota Production Systems (TPS). Other companies are developing similar production systems, such as FPS at Ford and LM21 at Lockheed Martin.

To speed up response time for the survey, a visit to the three major contractors working to refine requirements and operational concepts for the Orbital Space Plane (OSP) was undertaken. The personal visit provided an opportunity to observe first-hand the continuous and other process

improvement programs in place at contractors' facilities. The contractors were briefed through periodic teleconferences hosted by Andy Prince about the impending visit. Also, the questionnaire was e-mailed a couple days before the visit with a cover letter (attached in Appendix A) explaining the objective of the survey.

The contractors were extremely busy preparing OSP-related documents required by July 7, 2003, so the visit was scheduled after that deadline. Three non-disclosure agreements were signed, one for each of the three contractors. During these visits, the first order of business was to explain each of the technologies and techniques as defined earlier to ensure that each of the contractors had the same understanding.

The second order of business was to gather information about the shop floor capabilities and observe the process improvements at each of the facilities. The personal visit also enhanced the credibility of the survey. The visit provided an opportunity for discussion with the contractors and also to receive suggestions about any relevant technologies and techniques that might have been overlooked. The very busy travel schedule is shown below.

July 7th - Travel to Los Angeles Airport
July 8th – Boeing Plant at Huntington Beach, California
July 9th – Northrop Grumman, El Segundo, California
July 10th - Travel To Denver
July 11th – Lockheed Martin, Denver, Colorado
July 12th - Return to Huntsville

The survey questionnaire in Appendix B shows the cost savings realized by the contractors for each one of the technologies and techniques. These cost savings were planned to be recorded separately if the dollar figures were available, but unfortunately, records were not kept for the individual technologies and techniques.

However, one of the contractors was able to provide an annual cost savings from 1998 to 2002 during the implementation of the advanced manufacturing technologies and techniques. All three contractors reported to have seen productivity improvements such as reduction in floor space, decreased cycle time, and reduced rework with programs like Atlas, Delta, and F-18. The author agreed with the contractors that it would be too difficult to track the cost savings for each of the technologies and techniques individually.

Based on further discussions with all three contractors, it became obvious that cost savings are feasible in the development and production of a new generation of earth-to-orbit space transportation systems but the magnitude will not be the same as that of other programs due to low-quantity requirements. Therefore, it was mutually agreed to rate the technologies and techniques in the questionnaire based on the contractor's capabilities in harnessing them. The contractors were told to be diligent and truthful in assigning the rating and add comments to justify it.

The 5-point rating scale is explained below.

5 – World Class in terms of using the Technology and Technique
4 – Has been in use for some time but has not reached the level of World Class yet
3 – Has been in use for less than a year

2 – Getting started with the use of the technology / technique
1 – Exploring the possibility of using the technology / technique
N/A – Either not available or not applicable

The contractors were also requested to be as objective as possible in rating their capabilities and, during the visit, to demonstrate the use of the technology and techniques, either in their plants or in the plants of their supply chain partners. The courtesy and support extended during the visit was overwhelming. Without such willing cooperation of the participants, the study could not have been completed.

Some of the contractor personnel working in the area of costing were initially apprehensive. They were concerned that the cost saving percentages would be reported to NASA and NASA would expect the contractors to pass on these cost savings during future space programs. These fears were allayed with positive assurances and useful discussions were possible.

About 3 to 4 hours were spent in conferences at each facility with 2 to 3 hours spent on the shop floor looking at the implemented technologies and techniques. A brief wrap-up session ensued at each facility after the shop floor visit. The enthusiastic support of each one of the contractors is very much appreciated.

The personnel that participated in the survey at each of the facilities were extremely knowledgeable and quite willing to talk about the lean initiatives and other continuous improvement projects underway at their facilities. Some of the unique technologies such as friction stir welding, automatic drilling, and one-of-a kind tooling were very interesting to see in use.

Prior to returning to MSFC, one completed survey response was received. The second completed survey arrived at the beginning of the following week with the third one received at the end of the week. Since all three contractors wanted to protect the proprietary data, none of the responses is included in this report. However, for analysis, an average rating is used.

Proposed Approach

i. An Improvement Cost Model Incorporating Two Variables

With the response ratings in hand, the analysis and the development of an approach started falling into place. When the survey questionnaire was designed, the plan was to capture the cost savings and try to develop a cost estimating relationship (CER) for the advanced technologies and techniques. Since the exact cost saving percentage for each of the technologies and techniques is not available, a different approach has been developed.

As one of the three contractors reported an annual cost savings of 4% for the last 5 years with the implementation of advanced manufacturing technologies and techniques, it is fair to assume that similar savings are also realized by the other two contractors as well. Without a reasonable return on investment (ROI), it is unconscionable for a major aerospace company to invest in advanced technologies and techniques.

Extensive brainstorming and analysis was performed to develop an algorithmic approach. It became obvious that the cost savings needed to be captured in the cost improvement (learning)

curve model in use in NAFCOM. The cost estimate can be made not only based on the quantity dependent learning but also on the basis of implementation of advanced technologies and techniques. In order to add the enhancement in the improvement cost model, the rationale used in figuring out the cost slope for the existing single variate learning curve model was explored.

A 95% learning curve model is being predominately used in the Engineering Cost Office at MSFC. Discussions with Spencer Hill revealed that this percentage has been in use for years in the Engineering Cost Office. Therefore, a two-variable cost improvement (learning curve) model shown in equation 1 was developed.

Equation 1

$$C_{x,n} = C_1 x_1^{b1} (1- s)^{n-1} \text{ ---------- } 1$$

Where $C_{x,n}$ – cost of the x -th item produced in year n.

C_1 - cost of the first item produced

x_1 – x-th unit produced

b_1 - exponent of learning curve model

s - average cost savings per unit using advanced technologies and techniques.

n – the year in which the item is made from the base year.

A numerical example is used to illustrate the use of this two-variable improvement curve model.

C_1 = \$10,000

b_1 = ln (0.95) /ln (2) for 95% learning curve

= -0.074

s = 4% or 0.04

If it is to compute the cost of item 3 produced in year 4, it may be computed as below.

$$C_{3,4} = \$10,000 (3)^{-0.074} (1- 0.04)^{4-1}$$
$$= \$8,157$$

The percentage cost savings of 4% is in line with the reported cost savings by one of the contractors during the survey. No adjustment for inflation and cost of money is made in the above computation. It will be interesting to see what happens when these are taken into account.

This will be a challenging assignment to pursue. The next phase will be to calibrate the model against available cost estimates and check the fidelity. A sensitivity analysis may be made to check the effect of the percentage cost savings used on the resulting costs.

ii. Manufacturing Methods Improvement Input

From the NAFCOM training manual and users of the software, it was found that NAFCOM has a manufacturing methods input incorporated into the software. With the ratings available from the survey, an enhancement for the existing manufacturing methods improvement model is possible.

The manufacturing methods definition based on a recent communication between SAIC and Spencer Hill [7] has been very helpful. The choice of manufacturing methods range from "a very low-level to extremely high-level use of advanced manufacturing techniques." It is interesting to note that outsourcing is considered an advanced manufacturing method in addition to JIT techniques.

The number scale currently in use is as described below.

Level of use of Advanced Manufacturing Techniques Such as JIT, Bar Coding, COTS, Outsourcing Etc.	Number scale
Maximum Use	0 -12
Significant Use	13-37
Moderate Use	38-62
Minimum Use	63-87
Limited Use	88-100

The justification for revising the number scale in light of the survey responses is that all three major contractors and their numerous outsourcing partners are using the state-of-art technologies and techniques very significantly. They are also in continuous improvement mode rather than a passive mode. Documented cost savings and productivity improvements are obvious as illustrated at the introduction and based on the survey responses, plant visits, and discussions with contractors. Therefore, the following approach for enhancing this manufacturing input in NAFCOM is proposed.

Due to the proprietary nature of the data and at the request of the contractors, no hard data is included in this report. The data collected reside in a proprietary data depository with the manager of MSFC VS10 who can provide an authorization to look at the data on a need-to-know basis.

The average for the application of manufacturing technologies was computed to be 4.22 and the average for the implementation of manufacturing techniques was computed to be 4.12. The composite average was 4.17. This number indicates that all three contractors have made significant progress in implementing the state-of-the art manufacturing technologies and techniques.

The implementation of technologies requires capital investments with a reasonably good payoff or ROI. The implementation of techniques requires the commitment and management blessing as successful implementation depends on the interest and commitment of the management. As previously mentioned, all three contractors are members of the Lean Manufacturing Initiative consortium at MIT and are aware of each other's involvement and commitment in lean manufacturing.

At the annual meetings, the consortium members get a very good understanding of the levels of their competitions' involvement in lean manufacturing programs. Since the rating for most of the items in the questionnaire ranged from 3 to 5, the manufacturing method scaling currently in use

NAFCOM as outlined above may be modified to reflect the realities on the shop floor of the contractors and their supply chain partners.

It is very encouraging to see the interest and enthusiasm of the contractors in becoming world class in most of the manufacturing technology areas as well as in the implementation and practice of lean manufacturing techniques, six sigma, 5S and other related productivity enhancement techniques. It should be emphasized that these contractors understand that the space-related industry is highly competitive and unless they strive to become world-class leaders, they may not be awarded business.

It is recommended that the following three levels be used as opposed to five different scaling levels currently in use. The new scaling is outlined as below.

Level of the Use of State-of-the Art Manufacturing Technologies and Techniques	Number Scale Author	Number Scale NAFCOM
World Class Capabilities in all areas	5	1-33
World Class Capabilities in Majority of the areas	4	34-66
World Class Capabilities in Some Areas, planning to make progress	3	67-100

iii. Process-Based Cost Development Model

The author has been working with SAIC in the development of a process-based cost model using the historic shuttle data residing in the REDSTAR database. Technical help in the fabrication phase has been provided. The following are some of the major tasks and databases required in the fabrication phase of new space transportation cost model in light of changing technologies and techniques. A complete list will be provided to SAIC for their Process-Based Cost Estimation methodology development.

Task	Database
Make or buy decision and identifying outsourcing partners	Qualified outsourcing partners and their capabilities
For items to be made, selection of material vendors	Qualified vendors and their pricing
Tooling requirements for fabrication as well as testing	Qualified tool designers and fabricators
Development of route sheets for items to be made	Machinablity characteristics of materials. Equipment Capabilities
List of various testing	Testing capabilities
Assembly and testing	Various manpower requirements and their rates

Conclusion

The project was embarked on to capture the cost savings that could be realized using the state-of-the-art technologies and techniques by the three prime contractors of the future earth-to-orbit space transportation systems. Development of an algorithm or a CER to reflect the captured cost savings to be included in the current Cost Estimation models was the primary objective. The objective of enhancing the current cost estimation models to reflect the state-of-the art manufacturing technologies and techniques has been presented through a two-variable cost improvement model. It is important to have the method calibrated to check the fidelity and usefulness of the approach in estimating costs.

The secondary objectives, a spin-off of this study, was a modified approach to input manufacturing method parameters into NAFCOM. Another objective as a spin off of this approach is the framework for Process-Based Costing Model. The comprehensive survey questionnaire attached in Appendix C with the cost drivers may be completed sometime in the future. The responses can also be used to develop a new cost estimation approach such as Process-Based Cost Modeling.

Acknowledgements

The author would like to thank the entire team of dedicated engineers and scientists in the Engineering Cost Office at MSFC. Thanks for all the support and help. Thanks to Dr. Dale Thomas for facilitating travel funds for the author to visit the three prime contractors in times of severe travel budget restrictions. It is very important to recognize the help and support from Boeing, Northrop Grumman, Lockheed Martin and SAIC. You all have been wonderful in helping me out. Last but not the least, the author would acknowledge the help from the cost group at JSC through teleconferencing.

References

[1] Wertz, J.R. and W.J. Larson (1999), “ Space Mission Analysis and Design ”, Space Technology Library, Kluwer Academic Publishers
[2] Campbell, E.P. (2003), "What is Manufacturing? ", Industry Week, June 2003, p25
[3] SAIC (1999), “ NAFCOM 99 Documentation and Users Manual”, SAIC
[4] PRICE (2000), Price estimating Suite 2000, Price Systems LLC
[5] SEER-H (1998), SEER-H Hardware Estimation, Planning and Project Control
[6] LAI (2003), Lean Aerospace Initiative Overview Presentation, MIT
[7] E-mail Correspondence between Spencer Hill (MSFC) and Julie McAfee at SAIC

APPENDIX A
(Survey Cover Letter)

Memorandum

Date: July 1,2003

To: Tom Burns, Boeing; Gregg Nishime, Northrop; Steve Graybeal, Lockheed Martin

From: Meenakshi R.Sundaram, Summer Faculty Fellow at MSFC, VS20

I am a faculty member in the department of industrial and manufacturing engineering at Tennessee Tech University in Cookeville, Tennessee. This summer as a " Summer Faculty Fellow" with the Engineering Cost Group at Marshall Space Flight Center in Huntsville, I am interested in the study of various cost drivers that affect the manufacturing cost of a space transportation system. Specifically, I am hoping that this study will help me assess the impact of the cost drivers or factors of an OSP or any future space transportation systems.

Therefore, I am embarking on a survey of the contractors that are working on defining the requirements and preparing more in-depth cost and performance requirements of such a transportation system. I have designed a one-page survey questionnaire that lists the various state-of-the art technologies and techniques that are relevant in the fabrication phase. A copy of the survey is attached for you to respond. The questionnaire does not cover all the technologies and techniques. Therefore, please feel free to include any relevant technologies or techniques that I may have overlooked. If you have any questions about this survey, please feel free e-mail or call me. My e-mail address is Meenakshi.R.Sundaram@MSFC.NASA.GOV. I may be contacted at either 256-544-6743 or 931-372-3790.

Since there is very short fuse on this study, I plan to visit with you during the week of July 7 to have the survey completed in time for me to compile a report. I would greatly appreciate your cooperation. I will call each one you of individually and have my visit scheduled.

Thank you for your time and I look forward to meeting with you in person during the week of July 7.

Attachments

APPENDIX B
(Simple Survey Questionnaire)

Rating Scale

I. Technologies 1 2 3 4 5

1. CAD/CAM/CAE Systems
2. Integrated Manufacturing
3. High Speed Machining
4. Water Jet Cutting
5. Automated Filament Winding
6. Laser Alignment System
7. Robotic welding and Assembly
8. Auto I.D and Bar Coding
9. Digital Data
10. Computer Aided Process Planning
11. Automatic CNC Code Generation
12. CMMS
13. Manufacturing Execution Systems
14. ERP
15. CRM
16. PDM
17. Product Life Cycle Management
18. Transportation Management Systems
19. On-line Purchasing Systems
20. Mobile Management (Wireless System)
21. Warehouse Management System
22. Virtual Manufacturing System
23. Rapid Prototyping
24. Resin Transfer Molding
25. Automated drilling

II. Manufacturing Techniques

1. Continuous Improvements
2. Synchronized Flow
3. Empowered Teams
4. GT and Part Family Concepts
5. Lean Aerospace Initiative Related Programs
6. Agile Manufacturing
7. Concurrent and Collaborative Engineering
8. SMED
9. Six Sigma
10. Lean Six Sigma
11. Theory of Constraints
12. Toyota Production System or Similar System
13. Outsourcing
14. TPM
15. Integrated Product Development
16. Activity Based Costing
17. QFD
18. Just in Time Delivery
19. Value Analysis and Engineering
20. Cellular Manufacturing
21. Supply Chain Management

APPENDIX C
(Comprehensive Survey Questionnaire)

Questionnaire For Assessing the Relevancy of Tasks	"X" if applies	Chose Cost Drivers from attached list for increased cost	Chose Cost Drivers from Attached List for increased cost
A. Pre-Planning			
1. Make or Buy Decisions			
2. Identify Subcontractors			
3. Develop and issue RFPs			
4. Select Subcontractors			
5. Award Subcontracts			
B. Procurement Analysis			
1. List items to make			
2. List items to purchase			
3. Procure fabricated parts			
4. Procure Materials and supplies			
5. Receive Parts and Purchased Parts			
6. Inspect			
C. Process Planning			
1. Tool Design and Fabrication			
2 Tool Verification			
3. Develop Manufacturing Sequences for Each Subassembly.			
4. Process Planning for items to be made			
5. Development of Manufacturing Specifications as Required.			
D. Production Planning			
1.Capacity Analysis			
2.Master Production Schedules			
3.Detailed Shop Schedules			
4.Material Requirements Planning			
6.Manpower Planning			
7.Sub-Assembly and Assembly Schedules			
8. Procurement of Equipment and Additional Capacity			
9. Progress Control			
E. Quality Assurance			
1. Statistical Quality Control and Process Monitoring			
2. Inspection of tools, parts, and Subassemblies			
3. Inspection of Final Assembly			
4. Repair and Rework			
5. Scrap Disposal if any			
F. Manufacturing			
1. Fabrication of Parts			
2. Inspect Parts and Rework When Necessary			
3. Make Subassemblies			
4. Inspect and Test as Appropriate			

5. Assemble Putting Together
   Subassemblies Made and Bought
6. Perform Final Inspection

G. Engineering and Analysis
1. Design Analysis including Trade Studies
2. Stress Analysis for Load and Thermal
3. Design Analysis for Manufacturing
4. Design Analysis for Assembly
5. Design Analysis for Reliability
   and Maintainability
6. Design Analysis for Quality
7. Mock Up Model Development and Testing
8. Revise Design Based on Mock Up Test
9. Production Drawings
10.Process and Material Qualification
11.Manufacturing Problem Solving
12.Engineering Change Orders
13.Developm Work Methods
14 Develop Performance Management
   Metrics
15.Develop Detailed Facility Layouts
16.Maintenance - Planning and Scheduling

H. Lean Manufacturing
1. Continuous Improvement
2. TPM
3. QFD
4.Value Analysis
5. Waste Removal

Survey Questionnaire Compiled By

Meenakshi R.Sundaram
MSFC- VS20 July 1, 2003
List of Cost Drivers

I. Vehicle Related Factors
1. Propulsion System
2. Launch from ELV or RLV
3. Crew Escape System
4.Crew Size
5. Vehicle Geometry
6. Weight
7. Mass Properties
8. Material –Type
9. Subsystem Complexities
10. % of Expendable Subsystems

II. Mission Related Factors
1. Availability
2. Crew Safety
3. Reduced Turnaround Time Between Missions
4. Increased Orbital Maneuverability
5. Life Cycle in Years

6. Life - certification Requirements
7. Maintainability
8. # of flights per year
9. Overall Flight Duration including Dock Time.
10. # of Redundant Systems / Components
11. Requirement Changes
12. Immature Technologies

III. System Test Hardware Related Factors
1.Mock Up Development
2. Testing and Analysis of Mock Up
3. Number of test articles
4. Fidelity of Test Articles
5. Test - Fail / Fix

IV. System Related Factors
1. System integration
2. System Testing
3. Software Testing and Integration

IV Fabrication Related Factors
1. Work Breakdown Structure
2. Number of Subassemblies To Make
3. Number of Subassemblies To Buy
4. Tool Design
5. Modular Tooling Approach
6. Tool Fabrication
7. Tool Checking
8.Use of Existing Tooling
9. Production Quantity
10. Method of Fabrication - Conventional Vs CAM
11. Concurrent Engineering and Manufacturability Studies
12.Colloboartive Manufacturing Strategies
13. Inspection Methodologies
14. Assembly Techniques
15.Verification Methodologies
16.Past Experience
17. Use of Proven fabrication Techniques
18.Use of New fabrication Techniques Such as Water Jet Cutting and Laser Machining
19.Skilled and Trained Workforce
20. Innovative Technologies Such as Laser Alignment System
21.Equipment Availability
22. Need for Additional Equipment
23. Assembly Flexibility
24.Logistics and Transportation Systems
25. Adequate Material Handling Systems
26. Well Laid Out Facility for Smooth Flow

Survey Questionnaire Compiled By

Meenakshi R. Sundaram
MSFC - VS20 July 2003

2003

NASA FACULTY FELLOWSHIP PROGRAM

MARSHALL SPACE FLIGHT CENTER
UNIVERSITY OF ALABAMA IN HUNTSVILLE

JUSTIFYING TECHNOLOGY TRANSFER AT NASA

Prepared By:	Gary Templeton
Academic Rank:	Assistant Professor
Institution and Department:	Mississippi State University Department of Management and Information Systems
NASA/MSFC Directorate:	Customer and Employee Relations
MSFC Colleague:	Jim Dowdy

Introduction

This manuscript has several purposes designed to assist in decision-making regarding the future of NASA's existing Technology Transfer infrastructure. First, it articulates the mandate the technology function is intended to legally serve. Then it describes the current operations at Marshall's TTD. Finally, I describe the alternative plan, named the 'enterprise engine' model articulated by Dr. Scott Pace.

The words 'Technology Transfer' have become synonymous with NASA's role in encouraging the *commercialization* of technologies derived from the U.S. space program. First, the TTD has the primary purpose of carrying out the following mandates as stated in the Space Act of 1958 (Public Law 85-568), NASA's constituting legislation (see Table 1).

In my judgment, TTD is performing its statutory duties in accordance with Public Law 85-568. TTD does so in several important ways. First, TTD successfully stimulates NASA scientists and engineers to think innovatively and to report those ideas for potential patents and subsequent licensing. Second, TTD provides monetary awards for that activity. Third, through the TT TIPS process, innovators are given an opportunity to develop working prototypes, which greatly increases the likelihood of a patent being granted. Fourth, TTD facilitates NASA spin off technologies (those that reach commercialization), which impact our lives on earth in immeasurable ways. This report includes several such ways, from Home Land security to improved quality of life to medical miracles.

The Current System: The Technology Transfer Department

Second, it is important for NASA and public stakeholders to understand the services currently provided by the Technology Transfer Department (TTD) (see http://www.nasasolutions.com/). Each of the following services is formally described in the TTD's guiding process documentation entitled "Technology Transfer Department Organizational Work Instruction (CD30-OWI-001)." The work instruction is intended to both education NASA employees regarding protocol, and to guide the current operations of TTD personnel in carrying out its mandated purpose.

One compelling repository of evidence on commercialization success is the Space Technology Hall of Fame (http://www.spacetechhalloffame.org). Winners of this award include a myriad of valuable contributing technologies to social well being, including those which have had an enormous economic impact. In fact, economic aspects of candidate technologies are heavily considered in award selection. The award selection criteria distribution is as follows: economic benefit (10 points), public/private/partnership investment (5 points), public awareness (15 points), societal benefit (15 points), and commercial longevity (5 points).

Table 1: Mandates Related to Technology Commercialization in Public Law 85-568

Sec. 102.

(c) The Congress declares that the general welfare of the United States requires that the National Aeronautics and Space Administration (as established by title II of this Act) seek and encourage, to the maximum extent possible, the fullest *commercial* use of space.

Sec. 203.

(a) The Administration, in order to carry out the purpose of this Act, shall-

(3) provide for the widest practicable and appropriate *dissemination of information* concerning its activities and the results thereof;

(4) seek and encourage, to the maximum extent possible, the fullest *commercial* use of space; and

(5) encourage and provide for Federal Government use of *commercially* provided space services and hardware, consistent with the requirements of the Federal Government.

(b) The Administrator, for a period up to 5 years after the development of information that results from activities conducted under an agreement entered into under section 203(c)(5) and (6) of this Act, and that would be a trade secret or *commercial* or financial information that is privileged or confidential under the meaning of section 552(b)(4) of title 5, United States Code, if the information had been obtained from a non-Federal party participating in such an agreement, may provide appropriate protections against the dissemination of such information, including exemption from subchapter II of chapter 5 of title 5, United States Code.

(c) In the performance of its functions the Administration is authorized-

(5) without regard to section 3648 of the Revised Statutes, as amended (31 U.S.C. 529), to enter into and perform such contracts, leases, cooperative agreements, or other transactions as may be necessary in the conduct of its work and on such terms as it may deem appropriate, with any agency or instrumentality of the United States, or with any State, Territory, or possession, or with any political subdivision thereof, or with any person, firm, association, corporation, or educational institution. To the maximum extent practicable and consistent with the accomplishment of the purposes of this Act, such contracts, leases, agreements, and other transactions shall be allocated by the Administrator in a manner which will *enable small-business concerns* to participate equitably and proportionately in the conduct of the work of the Administration;

(6) to use, with their consent, the services, equipment, personnel, and facilities of Federal and other agencies with or without reimbursement, and on a similar basis to cooperate with other public and private agencies and instrumentalities in the use of services, equipment, and facilities. Each department and agency of the Federal Government shall cooperate fully with the Administration in making its services, equipment, personnel, and facilities available to the Administration, and any such department or agency is authorized, notwithstanding any other provision of law, to transfer to or to receive from the Administration, without reimbursement, aeronautical and space vehicles, and supplies and equipment other than administrative supplies or equipment;

Table 2: The Significance of some Space Technology Hall of Fame Winners

Technology	Significance
Visiscreen™ (Ocular Screening System) http://www.spacetechhalloffame.org/inductees.cfm?view=2&id=52	This technology has been placed in pediatric offices and health clinics throughout the United States and has been used to test more than 1.5 million children in 10 states through mass screenings, typically provided free to schools and the students. In a statewide test involving 170,000 Alabama elementary school students, 10 percent were found to have eye diseases or defects requiring medical attention. The early and accurate identification of these eye abnormalities allows for proper medical attention and correction so students maintain good vision while pursuing their education.
Cochlear Implant http://www.spacetechhalloffame.org/inductees.cfm?view=2&id=57	This type of implant has been used to help restore "first time" hearing in many persons who were profoundly deaf from birth and for restoration of hearing in persons who were post-lingually rendered deaf by trauma or disease but who have a responsive auditory nerve. A patient's overall quality of life and range of opportunities are enhanced through the use of this technology. The Cochlear Implant Association estimates over 66,000 patients have received an implant in this multi-billion dollar industry.
Data Matrix Symbology http://www.spacetechhalloffame.org/inductees.cfm?view=2&id=47	During the last year the data matrix symbol has been adopted as the standard for auto parts, medical parts and soon it will be the standard for marking aerospace parts. It is estimated that the data matrix symbol industry will be a multi-billion dollar industry similar to the bar code sector.
Video Image Stabilization and Registration (VISAR) http://www.spacetechhalloffame.org/inductees.cfm?view=2&id=48	Since their first case with the FBI, David Hathaway and Paul Meyer have worked over the years to refine the VISAR technology, improving it so that it could be transferred to companies that produce video enhancement systems for law enforcement, military and even home computers. Incorporation of their commercial technology into various products will enable real-time applications of video stabilization. For example, it could be incorporated into video cameras to reduce or even eliminate jiggle and also to enhance viewing of single frames. VISAR technology has been instrumental in clarifying several video shots of the exploding backpack and its handler just prior to the 2000 Olympic bombing in Atlanta. The inventors (Hathaway and Meyer) and TTD's Sammy Nabors were recognized by receiving the *Federal Lab Consortium's Excellence in Technology Transfer Award* in 2002.
Light Emitting Diodes for Medical Applications http://www.spacetechhalloffame.org/inductees.cfm?view=2&id=6	To date the LED treatment has focused on skin cancers and brain tumors. Several successful cases have been reported. Another NASA need has led to yet another possible application for the use of LEDs. In microgravity, wounds heal much more slowly. The Wisconsin team has conducted experiments that demonstrate that LEDs have help human-cell cultures grow 5 times faster than normal. These results have led to a research program that is testing LEDs capability to increase wound healing. If the experimental results are promising, human clinical trials will follow. The outcome could be a new medical instrument to speed healing in space as well as on earth.

New Technology Reporting- This process involves the identifying and reporting of new technologies and innovations developed by NASA employees, contractors, grantees, and recipients of cooperative agreements. Susan Whitfield (1-256-544-1933) is the current process owner. The following is a list of resources NASA innovators are using in the support of new technology creation and reporting:

"Working with Marshall" Document (includes on-line Customer Request Form):
http://www.nasasolutions.com/working.html

Commercial Technology Office:
http://cto.grc.nasa.gov/

Innovator's Corner (when and how to submit an invention disclosure, incentives, etc.):
http://nasasolutions.com/innovator.html

NASA Commercial Technology Network:
http://www.nctn.hq.nasa.gov/

To access Technical Support Packages (TSP's) older than 6 months:
http://www2.nttc.edu/leads/

To access TSP's that are more recent (you have to search by category here):
http://www.nasatech.com/

Licensing of Patents - The process of managing the licensing of NASA owned patents through active and passive marketing techniques; negotiation and preparation of formal licensing agreements; and receipt of royalty fees for appropriate distribution. Sammy Nabors (1-256-544-5226) currently serves as process owner. For exhaustive information regarding NASA patents, see the United States Patent and Trademark Office (http://www.uspto.gov/web/menu/search.html). Patent information specific to NASA is available at http://webawntts.larc.nasa.gov/scripts/nls_ax.dll/twPatent (user ID: "msfcps" and password: "ntts2000"). Foreign patent information is available at http://www.uspto.gov/web/menu/other.html_ (near bottom of site). Here are two examples of technologies that have been managed through this TTD process:

- NASA High-Strength Aluminum-Silicon Alloy - Innovative new high-strength alloy may help engine manufacturers produce engines that offer more horsepower at lighter weights with less pollutants.
- Video Image Stabilization and Registration (VISAR) - VISAR, developed by Marshall scientists Dr. David Hathaway and Paul Meyer, improves the clarity of video footage by correcting distortion caused by adverse conditions. A video-processing algorithm is used to co-align video image fields by analyzing the picture pixel by pixel and removing the effects of translation, magnification, and rotation.

Commercialization Assistance- The process of assessing NASA owned or funded inventions for commercial potential; resolving intellectual property issues; and implementing formal commercialization strategies, facilitated by the Commercialization Assistance Team (CAT).

Sammy Nabors (1-256-544-5226) is the process owner. The following three examples show how innovations that were created for space science purposes have been adapted for commercial production:

- Use of Scrap RSRM Propellant for a Demining Device - Thiokol has developed a more effective way of demining landmines by using NASA Reusable Solid Rocket Motor (RSRM) scrap propellant.
- Friction Stir Welding Auto-Adjustable Retractable Pin Tool - Introduced and patented by The Welding Institute (TWI) in the United Kingdom, Friction Stir Welding (FSW) has been widely recognized for its ability to provide greatly improved weld properties over conventional fusion welds. The technique utilizes frictional heating combined with forging pressure to produce high-strength bonds. MSFC has made FSW enhancements— which have been commercialized— that improve on the state of the art in FSW
- Ocular Screening - Vision Research Corporation has licensed NASA optics technology and developed VisiScreen™, an eye-screening system for school children. The technology involves simply photographing children's eyes and analyzing the patterns of light reflected in them.

One unique twist to Commercialization Assistance has been the employment of NASA inventors within the TTD offices. Fred Schramm (1-256-544-0823) is a current *inventor in residence* in MSFC's TTD (http://techtran.msfc.nasa.gov/) who had the dual role of inventor and commercialization assistant. This experiment has been a tremendous success for NASA. On May 7, 2003, Schramm was awarded the Federal Laboratory Consortium Excellence in Technology Transfer award, the federal government's most prestigious technology transfer award. He has been working towards the development of *Compressed Symbology* (or *"Data Matrix")* technology, a parts marking technology, in NASA since 1987. It is expected that this technology will replace bar coding, because it is permanent, more efficient, more unified, safer, and easier to scan. When this technology matures, it will result in a tremendous commercial benefit to the national and world economies.

Software Release- The process of formally releasing NASA developed software. Caroline Wang (1-256-544-3887) is the current process owner. One of the key functions within TTD is Software Release process. Software developed by both NASA employees and contractors can be a strategic asset and a valuable NASA technology. The TTD has a streamlined system in place to determine the options and recommendations for release, transfer, collaborative development, partnering and commercialization of the software. This system is called Software Release. The Software Release Authority within TTD has the following responsibilities.

- Ensures that an assessment of commercial potential is made for all contemplated software release.
- Conveys that information to the parties responsible for determining the level of public use
- Works with Center management, the export control officer, the commercialization manager, patent counsel, and information technology security official and assists in the process by maintaining the tracking inventories of reported NASA-funded software that has been submitted for release.
- Mentors and encourages all software developers to report their technology.

The TTD ensures that MSFC is following NASA guidelines regarding the management of

NASA developed software, software-related intellectual property, and software release legal compliance.

External Customer Agreements- The process of coordinating customer agreements made with partners, which may include industry, universities, government agencies, or other NASA Centers for the purpose of advancing technology and technology transfer. Roger Parisa (1-256-544-8949) is the process owner. ECA's purpose to bring in revenue by leveraging NASA's existing unique assets, such as wind tunnels, vibration test stands, and radar range facilities.

Small Business Innovation Research (SBIR)/Small Business Technology Transfer (STTR) (see http://www.sbir.nasa.gov)- Management of the SBIR/STTR programs, providing opportunity and incentive for creative engineering and technology-related small businesses to conduct innovative, high-risk research on important scientific and technical problems. Examples of success in the program include the medical applications of light-emitting diodes. This technology derives from the NASA Space Shuttle plant growth experiments. Through the SBIR program, MSFC is teaming with companies to research how tiny, pinhead-sized light-emitting diodes (LEDs) might treat cancer (http://sbir.gsfc.nasa.gov/SBIR/successes/ss/8-034text.html), flesh wounds (http://sbir.gsfc.nasa.gov/SBIR/successes/ss/8-035text.html), and intestinal damage from chemotherapy (http://sbir.gsfc.nasa.gov/SBIR/successes/ss/8-058text.html).

> MSFC evaluates approximately 350 Phase I proposals for SBIR and 8 Phase I STTR proposals each year. MSFC leads the agency in total number of SBIR/STTR Phase III (contracts funded with Non-SBIR funding-from private industry, NASA program offices, other government agencies and space act agreements. The 144 contracts totaling $76.9M are commercialization successes.
>
> Website for MSFC's SBIR/STTR:
> http://nasasolutions.com/sbir.html

New Technology Reporting Contract Compliance- The organization and administration of a process that ensures contractual obligations pertaining to new technology reporting are being met by MSFC contractors in accordance with applicable new technology or patent rights clause (NASA Federal Acquisition Regulation Supplement 1852.227-70 or 1852.227-11). In 2002, 187 new technology disclosures were made to the TTD. These represent a crucial first step in NASA's role in capturing new knowledge for space applications and commercialization.

Outreach and Education- The process by which information from the major TTD program elements are disseminated to the fullest extent possible. TTD engages heavily in the documentation and dissemination of knowledge regarding NASA technology in the following ways:

1. Edits *NASA Tech Briefs*
2. Maintains the *NASA Technology Inventory Database System* (see http://technology.nasa.gov/), which includes the TechTracS Public Data Set, TOPS, and Success Stories), as required by NASA Headquarters
3. Writes, compiles, and edits articles for *Innovation Magazine*
4. Provides MSFC's input into *NASA Spinoff* Magazine

5. Implemented the "*eNTRe*" Electronic New Technology Reporting

The Marshall Center's TTD utilizes a number of avenues to inform industry, educators and the public about NASA's technology transfer and commercialization mission, and the available mechanisms for working with Marshall – and serve as the facilitators for partnerships/agreements to utilize these technologies. These partnerships drive the need for specific and often unique skills within industry.

Technology Transfer completes the circle by working with area educational facilities to develop curriculum to support these needs. The MSFC's TTD does so in the following four ways:

First, it serves as a sponsor for the New Century Technology High School, located on the Calhoun College Campus in north Alabama's Cummings Research Park. The mission of the school is to connect academic pursuits with business goals. This partnership between business and education will provide skilled workers for the high tech workplace of today and tomorrow.

Second, it provides general support for Center and local educational initiatives. As a partner to the MSFC Education Office, the TTD promotes commercialization by participating in the Bring Your Children to Work Day, Alabama A&M's High School Senior Day, and area school and college visits. The interactions encourage students to consider technical and scientific career paths.

Third, the TTD provides the mechanism for agreements with external partners in support of educational initiatives. The department currently has six agreements with the Educator Resource Centers (info stations for teachers) scattered around the country (AL, TN, LA, AR, IA, MO). Two agreements in process to allow UAH students to work on-site with our technical people and then do papers on what they have observed.

Finally, the TTD provides opportunities through NASA programs for participants to interface dually with in-house personnel to promote commercialization services. It also promotes familiarization with TTD processes that touch external partners. Over the past year, 2 fellowships (NASA Faculty Fellowship Program), two HBCU (Historically Black Colleges and Universities) students, and a SHARP ("Summer High School Apprenticeship Research Program") student have been employed in order to support MSFC's TTD. These efforts fulfill the mission of the TTD to promote space science through community awareness and education.

<u>The Proposed System: The 'Enterprise Engine' Concept</u>

Third, I will briefly describe the 'enterprise engine' concept. In short, very little detailed information regarding the new commercialization proposals have been made available, either internal to NASA or publicly. Based on limited information, it is clear that the new proposals will emphasized the following elements:

A. *Creation of a New Entity*
   1. A new NASA-funded venture capital unit will be created
   2. The unit will attempt to leverage industry resources
   3. The unit will join (through joint investment) with industry participants to create dual use technologies
   4. The Enterprise Engine will have investment (unclear meaning) objectives

B. *Shift in Focus to Dual Technologies*
   5. There will be a shift away from the traditional NASA technical focus
   6. The new focus will be on dual use technologies
   7. These technologies will be relevant to the missions of NASA and collaborating organizations (i.e., "dual" technologies)
   8. Valuation of projects will be enhanced due to NASA's brand name and joint expertise

C. *Joint Venturing vs. Contracting*
   9. The new system aims to increase competition for NASA contracts
   10. The new system will reduce NASA's expense and risk
   11. The new system will provide budgetary flexibility to NASA
   12. The new system will be similar to syndication, which implies that the technology will be licensed to multiple companies simultaneously
   13. NASA will join with multiple contractors focusing on the same technology

At present, no illustrative (process, data, logic, etc.) model of the new system exists. In addition, no example has been presented indicating that it would be relatively advantageous over the current system. Finally, there is no clear evidence that the new system will succeed, nor that it is better than the current system, based on the use of TTD units.

Metrics

The TTD has shown an substantial increase in its effectiveness over the FY01 – FY02 measurement period, and was successful in meeting all mandatory Code R financial metrics.

1. *New Technology Reporting* – New Technology Reports (which document the initial identification of possible inventions) increased from 149 in 2001 to 187 in 2002, an increase of 25.5%.
2. *Innovator Incentives* – Three categories of monetary rewards made to innovators during different stage of a technology's life cycle are made through TTD. Each category increased dramatically from 2001 to 2002, Tech Brief Awards from $13,650 to $26,600 (94.9%), Software Release Awards from $6,400 to $26,850 (419.5%), and Patent Application Awards from $8,760 to $27,000 (308.2%). These awards represent the transfer of budgeted money directly to scientists at various stages of innovation success.
3. *Patents Issued* – Between 2001 and 2002, the number of patents issued through the support of MSFC's TTD increased from 19 to 22, an increase of 15.8%.
4. *Royalties* – Total royalties from NASA-licensed technologies increased from $38,437 to $89,817, a 233.7% increase.
5. *Software Releases* – Through the TTD's software release process, 238 Software Usage Agreements were signed in 2001, compared to 271 in 2002, a 13.9% increase.
6. *SBIR/STTR* – The dollar amount of SBIR Phase I & II Contracts valued $13,258,449 for 2001 and $24,901,660 for 2002, a 87.8% increase. The dollar value of STTR Phase I & II Contracts increased from $399,891 to $449,461, a 12.4% improvement.
7. *Outreach* - The TTD allows NASA to promote NASA and space science through presentations and publications. Between 2001 and 2002, the number of tradeshows, conferences, workshops and speaking engagements increased from 59 to 96, a 62.7% increase. The number of *NASA Tech Briefs* articles published increased from 16 to 27 (a

8. 68.8% increase) and the number of NASA technology *Success Stories* increased from 16 to 18 (a 12.5% increase).

Opinion

In summary, I believe the 'direct cutover' implementation plan, which will simultaneously end TTD operations and begin the 'enterprise engine' initiative, is extremely risky. The following four reasons offer greater insight into this opinion:

Only Radical Failure should Initiate Radical Change - The TTD encourages input regarding incremental improvement of its services. Given recent administrative innovations in MSFC's TTD, I believe that such input will help us reach and maintain a world-class status as providers of Technology Transfer services to U.S. commercial interests. Recent steps taken within the TTD to ensure that new ideas such as the 'enterprise engine' approach are considered for incorporation into its existing structure:

Corrective Action Procedures – The TTD at MSFC has five core processes, each having a 'process owner' or 'process coordinator' who is responsible for the quality and outcomes associated with that process. As stated in the OWI, the owner/coordinator "for each process within TTD is responsible for maintaining a dialog with customers during their respective activities. During such dialog, the PO will have the responsibility for acting upon comments and/or complaints from customers." Further, each issue is managed through n steps: categorization of the issue (formal or informal), provision of evidence, reporting to ISO representative, and recording.

Preventive Action Procedures – MSFC's TTD also has a set of procedures designed to prevent significant deviations from its intended purpose (i.e., as mandated in the Space Act of 1958). Preventive action procedures guide the review and analysis of organizational information to determine 1) if preventive action is necessary and 2) the nature of suggested process changes. All Process Owners/Coordinators are responsible for managing preventive action within their process domain.

Organizational Learning Procedures – The Computer Assisted Organizational Learning (CAOL) system was designed and implemented by Dr. Gary Templeton, Assistant Professor of MIS at Mississippi State University, for the MSFC TTD. It was created to serve as an integrated approach to managing incremental and radical improvement in a more effective way than previously manual methods. This system facilitates group interactions so that change-relevant issues can be better acquired, organized, presented, deliberated, and incorporated into existing processes by owner/coordinators.

Given these process innovations (which are endorsed or encouraged by the International Standards Organization and NASA management) it is inconceivable that change-related issues would not be presented through the appropriate channels.

Alternatives not Comparable - Given the evidence gathered on the two approaches, I do

not believe that the two alternative approaches are functionally comparable. They seem to similarly focus on the management of technology, but that is where the similarities end. I conclude that they are not similar enough to even be considered competing concepts. Even if they are competing alternatives, why assume that one approach to commercialization is better than NASA's?

Elimination of Individual and Collective Intellectual Capital - It would be extremely risky to ignore decades of cumulative tradition embedded in the current TTD services in order for NASA to replace the existing structure with anything new. A great deal of collective and individual experience would be lost if the TTD were deleted.

Loss of Potential Future Benefits - Many TTD services designed to provide efficiency and effectiveness regarding commercialization will be lost before meaningful results can be realized. For example, the return on investment of NASA technologies has just recently been made a concern within the NASA culture. Systems designed to assess the financial impact of technologies are just now being conceived and put into place. I anticipate that NASA's current TTD program is providing a great deal of economic benefit to the U.S. economy, as indicated in the examples above.

I embrace the ideas of the 'enterprise engine' concept and believe it would fit very will with the current portfolio of services. I believe operations designed to fulfill the goals of the 'enterprise engine' can be put into place within one calendar year, given adequate resources are allocated for such an effort. I embrace any new ideas and hope that concepts such as 'enterprise engines' are presented in a manner that will allow current operations (which I believe are highly valuable and fulfill the Space Act of 1958 mandate) to continue. At a minimum, the new approach should be piloted before a commitment is made to the wholesale investment in the new program. I hope that the value of current and any new alternative plans for commercialization will be appraised with the same approaches.

2003

NASA FACULTY FELLOWSHIP PROGRAM

MARSHALL SPACE FLIGHT CENTER
THE UNIVERSITY OF ALABAMA IN HUNTSVILLE

STRUCTURAL HEALTH MONITORING OF COMPOSITE OVERWRAP PRESSURE VESSEL

Prepared By:	Kevin K. Tseng
Academic Rank:	Assistant Professor
Institution and Department:	Vanderbilt University Department of Civil and Environmental Engineering
NASA/MSFC Directorate:	Engineering
MSFC Colleague:	Dr. Michael L. Tinker

Introduction

Composite Overwrap Pressure Vessel (COPV) has increasingly been used in many structural systems for automobile, aerospace, and aeronautical applications. Mackerle [1] reviewed the research work in the analysis of pressure vessels and piping. The composite overwrap increases the pressure carrying capacity of the vessel without adding too much weight on the tank. Experiments at NASA Marshall Space Flight Center show that the burst pressure of an aluminum tank can be increased from 500 psi to 2,850 psi when the tank is wrapped with 5 layers of carbon fiber composites.

The composite overwrap is typically in the form of laminates with multiple layers of uni-directional carbon fibers. This class of composite material is relatively new to the engineering communities and their material behaviors are not as well understood as traditional materials such as metals and metallic alloys. To ensure safe operation of the structural system consisting COPV, an on-line automatic structural health monitoring system is needed to constantly monitor the performance of the structure.

Many structural health monitoring techniques have been proposed. Chang [2] collected references of various structural health monitoring techniques. Most of these techniques are based upon the global or local dynamic characteristics of the structure or the material. The structural health monitoring system identifies the changes in the global or local dynamic characteristics and issues warnings or trigger structural control system to bring the structural performance back to normal. This kind of hybrid sensing/control system can be achieved by using proper smart materials such as the piezoceramics.

The purpose of this project is to test the feasibility of using smart piezoelectric material to serve as the actuator and sensor for a structural health monitoring system for COPV. Two types of piezoceramic materials will be tested: PZT and PMN-PT. PZT is the regular piezoceramics and PMN-PT is a newly developed single-crystal piezoceramics specially designed for low-temperature applications. The COPV will be pressurized by both water and liquid nitrogen.

Composite Overwrap Pressure Vessel

Figure 1: Composite Overwrap Pressure Vessel.

Figure 1 shows the composite overwrap pressure vessel used in this project. The COPV is made of aluminum alloy and the overwrap is laminated uni-directional carbon fibers. The tank is 22.25 in. in length and the center part has an inner radius of 14.92 in. The cylindrical part of the vessel is wrapped with 5 hoop layers of carbon fibers and 2 helical layers cover the entire tank. The picture on the left of Figure 1 shows the helical wrapping and the picture on the right shows the completed COPV.

Dynamic Modeling of COPV

A finite element model was created in NASTRAN to simulate the dynamic characteristics of the COPV. The aluminum liner of the tank has a varying thickness. The middle of the tank has the smallest thickness of 0.12 in. and the thickness increases to the maximum value of 0.37 in. at both openings of the tank. Shell elements with varying thickness were created by the FIELD tool in PATRAN. The composite overwrap was modeled by the LAMINATE MODELER in PATRAN. Overlapping shell elements were created for the composite overwrap. Figure 2 shows first mode shape and the finite element mesh of the analysis model.

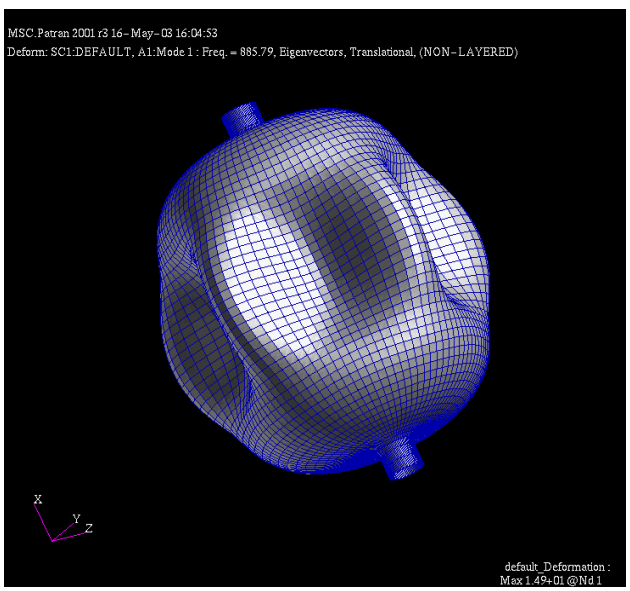

Figure 2: Finite element model of the COPV.

Modal analysis was performed on the finite element model for the aluminum liner tank without composite overwrap. The first 6 mode shapes are shown in Figure 3. Modes 1-5 are bending modes and mode 6 is the first axial mode. It is interesting to note that the number of humps in the middle band of the tank for the bending modes does not start from a small number and increase sequentially for the higher order modes as seen in most of the dynamic characteristics for regular structures. During the analysis, it is also observed that the natural frequencies are very sensitive to the thickness of the tank.

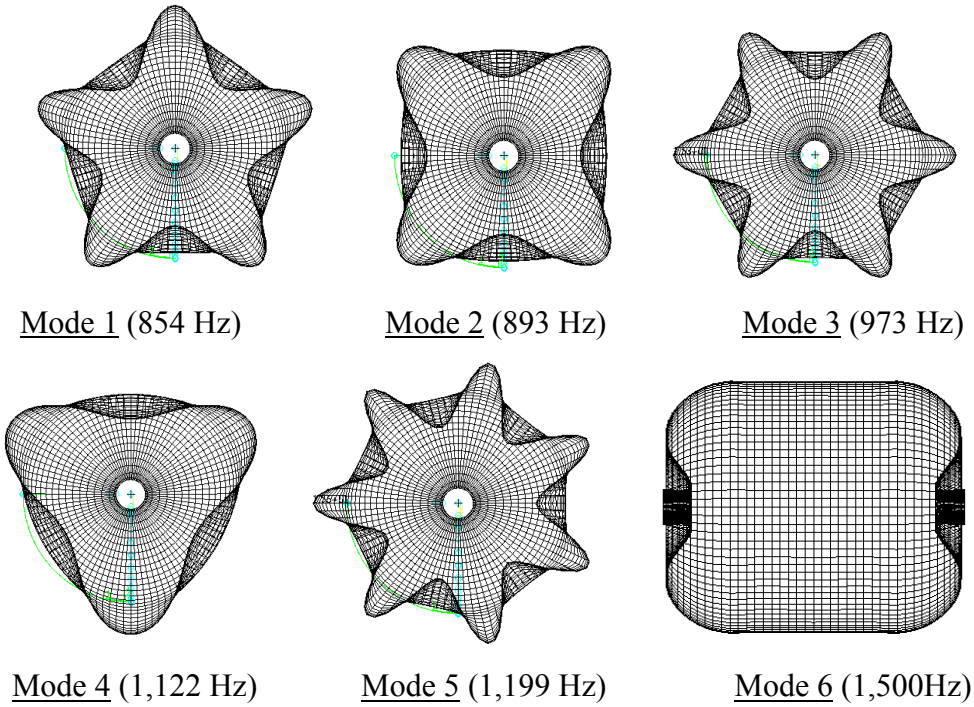

Figure 3: Vibration shapes and frequencies of the first 6 modes.

Comparison with Modal Testing Results

A modal testing was performed by hanging the liner tank to simulate the free-free boundary condition as shown in Figure 4. The natural frequencies from modal analysis as indicated in Figure 3 are compared to the results of modal testing and listed in Table 1.

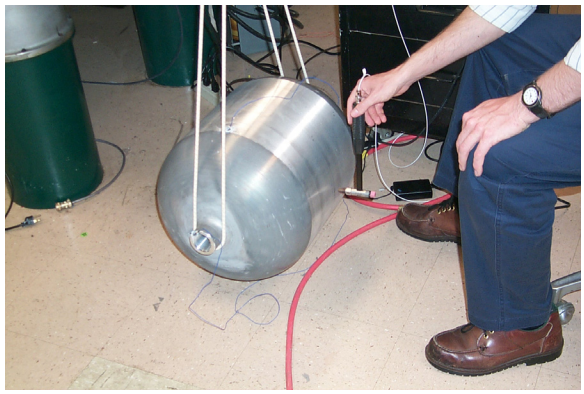

Figure 4: Modal testing of the COPV.

The analysis and testing results agree very well for the first three bending modes as shown in Table 1. The errors are within 3%. It is interesting to note that the vibration frequency of mode 4 (1,199 Hz) is higher than the frequency of mode 5 (1,100 Hz) in modal testing. The errors for mode 4 and mode 5 will be within 1% if the order of these two modes is switched.

Table 1: Comparison between modal analysis and modal testing results.

	Mode 1	Mode 2	Mode 3	Mode 4	Mode 5
Analysis	854	893	973	1,122	1,199
Testing	832	918	949	1,199	1,100
Error	2.6%	-2.7%	2.5%	-6.4%	9.0%

On-going and Future Research

More analysis and testing have been planned for the future for this project. Impedance measurements from the piezoceramic sensors will be taken for the COPV at various pressure levels to assess the feasibility of identifying imminent damage of the tank by the smart sensors. The tank will be pressured by both water and liquid nitrogen. Future analysis work will focus on simulating the impedance response from the piezoceramic sensors attached to the COPV.

Conclusion

The results from modal analysis of the pressure vessel agree well with the results from modal testing except the switching order of modes 4 and 5. The errors are within 3%. It has been observed that the vibration frequencies are very sensitive to the thickness of the pressure vessel. The author and the NASA colleagues are conducting on-going and future research works for this project.

Acknowledgements

The author would like to thank his NASA colleague, Dr. Mike Tinker, and the entire team of engineers in ED21 Structural Dynamics and Loads Group of the Marshall Space Flight Center's Engineering Directorate for their assistance in developing the analysis model. The author is grateful to John Lassiter, Bob Engberg, Tom DeLay, and Sam Russel for their involvement in this project. Financial support through 2003 NASA Faculty Fellowship Program at Marshall Space Flight Center is acknowledged.

References

[1] Mackerle, J. (2002), "Finite Elements in the Analysis of Pressure Vessels and Piping, an Addendum: a bibliography (1998-2001)," International Journal of Pressure Vessels and Piping, 79, pp. 1-26.

[2] Chang, F. K., editor (2001), Proceedings of the 3rd International Workshop on Structural Health Monitoring, Stanford, CA, September, 2001.

2003
NASA FACULTY FELLOWSHIP PROGRAM

MARSHALL SPACE FLIGHT CENTER
THE UNIVERSITY OF ALABAMA IN HUNTSVILLE

ANALYSIS OF ACOUSTIC AND VIBRATIONAL RELATED MEASUREMENTS IN PROPULSION DATA

Prepared by:	Patrick Vitarius
Academic Rank:	Graduate Research Assistant
Institution and Department:	University of Alabama in Huntsville Physics Department
NASA/MSFC Directorate:	Transportation
MSFC Colleague:	John T. Wiley

Introduction

Data collection and analysis of rocket engine tests are critical steps in understanding the physics of propulsion devices that may be used for space exploration. Current sensor technology must be exploited fully and expanded to cover all the classical parameters such as temperature, pressure, and flow rate. Methods must be established to infer such parameters as turbulence and shock that cannot be measured directly. This report will describe several experiments that were performed at the Marshall Space Flight Center, East Test Area, on two different engines. One of the engines was a solid rocket motor and the other was a liquid fuel engine. Neither engine was dedicated to the experiments reported on here, but rather the experiments were added so as to not interrupt scheduled tests.

The research is centered on gathering and analyzing acoustic and vibration data. There were two separate but related reasons for collecting the data. The acoustic experiments were done in preparation for testing a much larger solid rocket motor later in the year and an engine being developed for the NASA Orbital Space Plane (OSP). The testing done over the last few weeks was done on a small experimental engine called the LLT. It has a throat diameter of about 1.5 inches and is made substantially of a laminated material. It is a liquid oxygen/ liquid hydrogen engine. The primary sensors used are model 102A10 manufactured by PCB Corporation, and have a sensitivity of 50 mV/psi and a maximum pressure measurement of 1000 psi. Other sensors used are manufactured by Enderco, model 85108, having a sensitivity of 158.4 mV/psi (millivolts per pound per square inch) and a maximum pressure measurement of 2 psi.

The sensors themselves are quite expensive and cannot be sacrificed every test so a method must be used to move the sensor itself away from the hot engine gasses. A substantial part of the research performed was directed toward determining the most efficient sense line to use for the measure of pressure pulses from the engine. This is not a trivial task because the sense line itself has a unique transfer function that will affect some frequencies more than others. The goal was to determine if hollow tubes, liquid filled tubes, or gel filled tubes would best transmit the actual acoustic spectra. A substantial amount of this work was done in the laboratory before the engine tests were done. Classical linear system concepts were utilized in understanding how the sense lines affected the signal detected by the pressure transducer.

A second task involved designing an experiment to detect off-axis thrust from an engine mounted in a test stand. A test of the 24 inch SPTA engine provided a platform for a simple optical technique that could at least detect an off-axis (torque) component. The experiment was quite simple and involved mounting a mirror on the mounting ring that the engine was hard mounted to. A green solid state laser pointer was obtained and used as the source. The laser was mounted a safe distance away from the motor and the beam reflected from the mirror back to a screen. A digital video camera was then used to record the motion of the green laser spot on the screen. The eventual goal is to use several lasers and mirrors and screens so that a true three-dimensional representation of the off-axis thrust can be created. The goal of this first attempt was to discover the problems and solutions for the method so that the technique would be ready for the OSP tests planned for later this year.

The law of reflection can be used to create a device that accurately measures small changes in angle[1]. A low-power visible range laser is aimed at a small mirror mounted on the test article. The beam is reflected and hits a large screen; a video camera is mounted facing the screen in order to record the path taken by the laser spot. Both the laser and the camera can be mounted hundreds of feet from the test article; only a small mirror need enter the test area.

For Phase I of this experiment, a green laser pointer was used (5 milliwatts, peak wavelength 532 nanometers). The mirror was a first surface gimbaled laboratory mirror mounted onto the thrust structure with epoxy. With an effective dispersion of 0.4 milliradians, the laser spot fit nicely onto the two-inch wide mirror[2]. The mirror was aligned so as to reflect the spot towards a screen staked into the ground in the shade of some pine trees 250 feet from the test engine. The recording device was a digital video camera recording at 30 frames per second, outfitted with an inexpensive green filter.

Motivation

Acoustic Sense Lines

The acoustic phenomena of interest in propulsion applications often occur in harsh environments where heat, high-velocity particulate matter, and volatile chemicals preclude the use of sensitive and expensive sensors. To avoid the compromise between safe distance and useful data range, a sense line may be used to passively transmit information as a conduit. The sense line should either be durable enough to withstand such conditions, or else inexpensive so that it can be replaced periodically.

The variation in parameters at one end of the tube will uniquely determine the condition at the closed end of the tube, where the sensor is to be located. The sense line must have dimensions small enough that it does not affect the parameters of the system it measures. It should be emphasized that a sense line does not automatically transmit temperature, pressure, and other conditions from one end of the tube to the other. Rather, every measurement taken through a sense line must be analyzed in terms of temporal shift and transfer function losses. In addition, any component of the system that alters data introduces potential error into the measurement, and sense lines are no exception. Transfer functions for fluid-filled sense lines fall to zero for high frequencies as this vibrational energy is absorbed by the fluid; any information about these high frequency components is lost. The time delay due to the length of the sense line is a variable quantity that can depend on conditions (e.g., temperature) inside the sense line.

Acoustic resonance is a phenomenon via which certain vibrational frequencies, or modes, are amplified by the resonating structure. In the analysis of the pressure data transmitted through acoustic sense lines, Helmholtz resonance was clearly observed at frequencies corresponding to the lengths of the sense lines.

The resonance condition for a tube opened at one end is

$$(2n+1)\frac{v}{4L} = f \,, \qquad \textbf{(1)}$$

where n is an integer index ranging upwards from zero, f is the frequency of the sound, v is the speed of sound in the resonating tube, and L is the length of the tube[3].

Time of flight analysis depends on the assumption that the transit time for each of the tubes is the same; the offset in signal onset from one sensor to the next is solely a factor of the position of the open end of the sense line. If this is the case, then it is expected that

$$v = \frac{\Delta r}{\Delta t}\,, \qquad \textbf{(2)}$$

where Δr is the difference in distance from the nozzle for any two sensors, and Δt is the time delay between the two sensors[4]. It is possible to calculate a mean value for v by considering the linear fit for the various data points plotted with time on the horizontal axis, and radial distance on the vertical axis.

Optical Off-Axis Thrust Measurements

Axial thrust structures measure displacement along the principle axis and infer thrust on this axis. Most configurations measure off-axis components of thrust poorly, or not at all. A non-invasive, inexpensive technique was desired for measuring these off-axis components of thrust.

A system was developed in which a laser beam is incident on a mirror mounted on the test stand. The laser and mirror were positioned such that the reflected beam struck a Lambertian screen positioned several hundred feet away. Geometry insures that a small change in orientation angle will lead to large displacements of the order

$$\Delta x \approx D\Delta\theta\,, \qquad \textbf{(3)}$$

where Δx is the displacement on the screen, and $\Delta\theta$ is the change in orientation angle of the mirror. A more detailed analysis takes into account the incident angle of the laser beam, the orientation of the screen with respect to the laser and other geometric factors to produce a transcendental equation for Δx in terms of $\Delta\theta$.

Results

Acoustic Sense Line Transfer Functions

Various fluids were explored for use in sense lines. A fluid was desired that would transmit much of the energy to the transducer with a known transfer function. A laboratory experiment was designed to compare short sense lines filled with water, agarose, and air to a control transducer used to measure the unaltered shock. Agarose is a polysaccharide obtained from agar. The preparation used in this experiment is a suspension of agarose in a boric acid buffer with a gelatinous consistency[5].

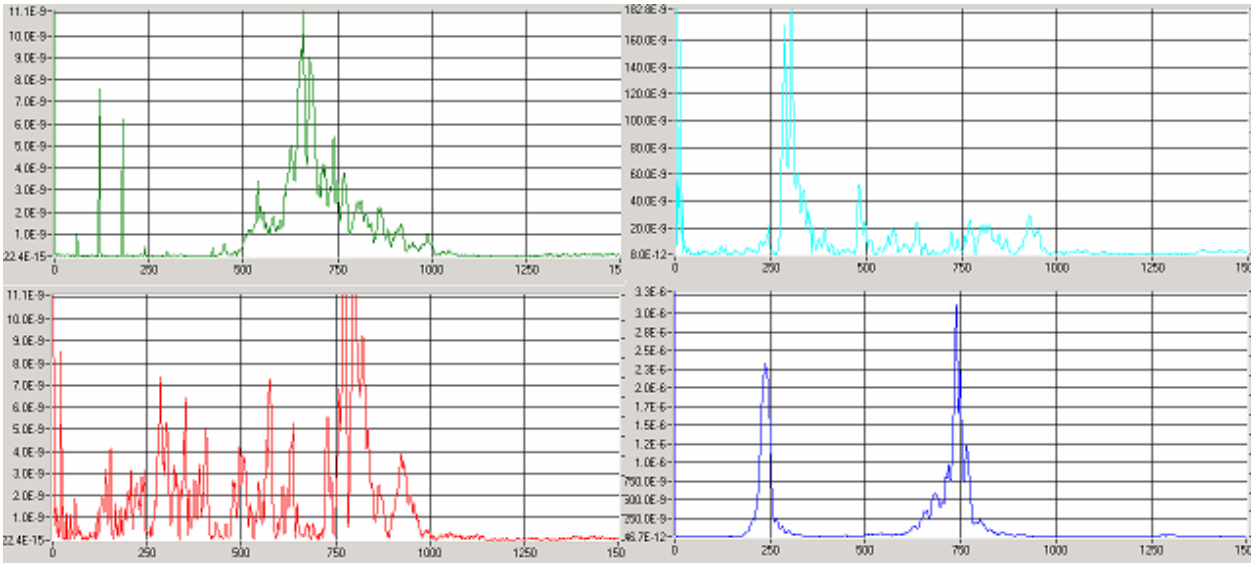

Figure 1: Power spectra of (clockwise from top left): the freestanding transducer, and transducers in sense lines filled with water, air, and an agarose suspension.

The general shape of the transfer functions of the sense lines can be obtained by taking the ratio of each of the power spectra to the power spectrum of the freestanding transducer. This ratio is not the true transfer function, since the power spectra are the squares of Fourier transforms and not the true Fourier transforms, but the general characteristics of the transfer functions should be apparent from such an exercise.

Both water and agarose demonstrate a rough correlation with the freestanding transducer at higher frequencies, in that both mimic the falloff in power at 1000 Hz. But these two sense lines also demonstrate high gain in the lower frequencies that correspond to Helmholtz resonance. This resonance can be seen much more clearly in the air-filled sense line, where the original profile is lost beneath a sharp resonance spike. This resonance is analyzed in more detail in the field tests below.

None of the transfer functions are linear in the sense that no sense line power spectrum differs from the freestanding transducer by a multiplicative constant. All of the sense lines effectively damped out the 60 Hertz (and integer multiple) noise indicated by the sharp, low-frequency spikes in the freestanding transducer.

Acoustic Sense Line Time of Flight Results

The propagation rate of shock wave can be determined by comparing the onset times for each of the sensors. The onset of the shock due to the combustion event appears as a transient spike followed by a rapid rise to a much higher plateau on each of the channels. As all three sensors were separated from the event by identical lengths of Tygon tubing, the time delay can be attributed to the time of flight of the acoustic wave travelling through the air. A linear fit to these three data points indicated a propagation speed of 1100 feet per second, comparing very

favorably to the reference value for acoustic waves, 1086 feet per second at STP. A more extensive array of sensors could detect changes in propagation speed, including regions where the propagation was supersonic, as well as directional difference in propagation speeds.

A qualitative comparison of the signals at each sensor indicates a rather rapid decrease in total energy as distance increase, and a rapid decrease as the sensors are placed further from the axis. A non-directional ($1/r^2$) distribution would be independent of direction, whereas a collimated distribution would not show such a rapid falloff with distance[6]. A more extensive array could determine the shape of the advancing profile by integrating power spectrum of the signal to determine the energy received at each point.

Acoustic Sense Line Helmholtz Resonance

Helmholtz resonance was clearly observed in the acoustic wave tests. By plotting spectral intensity on a time-frequency plane, broad bands could be observed at regular intervals during the combustion event. Each of these events was indexed with an odd integer corresponding to a harmonic for a closed tube, and the value for v_s was used to solve the Helmholtz resonator equation for the length of the tube. A value of 9.5 feet was obtained, very close to the actual length of the tube.

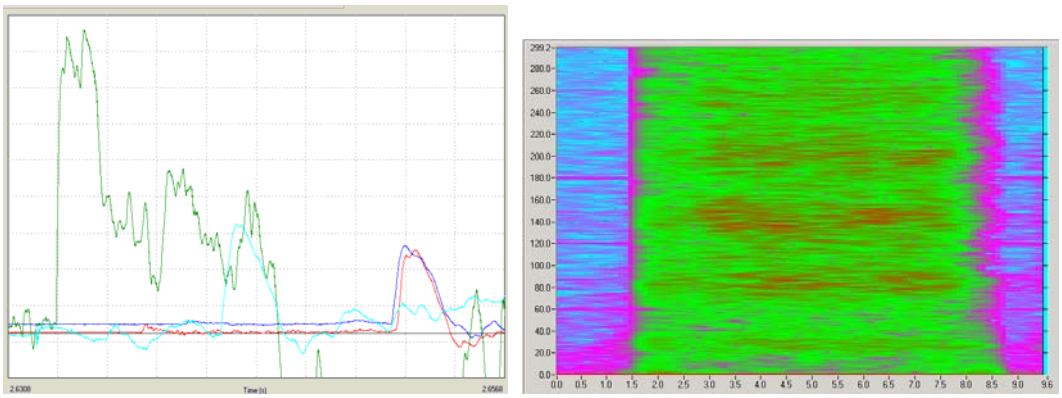

Figure 2: Time-domain data for time of flight measurement; time-frequency plots showing Helmholtz frequencies.

Optical Off-Axis Thrust Measurements

Phase I demonstrated that the recording device could easily detect the full-intensity spot, and in separate experiments it was shown that small changes in angle resulted in measurable shifts in spot location. It was also proven in the laboratory that the formulae developed for calculating change in angle from these shifts was accurate. However, the logistics of test firing resulted in the laser not operating at full strength during the firing of the motor, and as a result the spot was not visible during that time. It will be necessary in future tests to outfit the laser with a remote switch so that it can be turned on immediately prior to the firing.

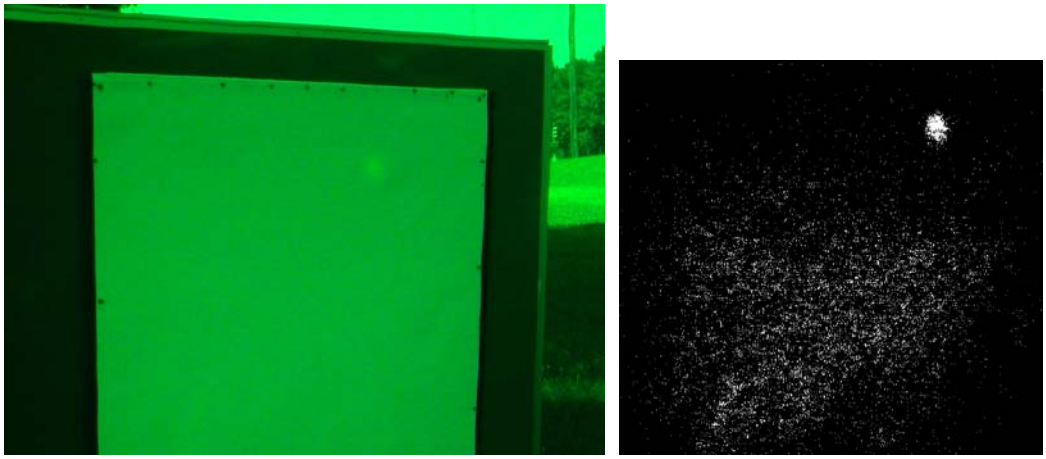

Figure 3: Laser spot on the target screen (left), and an enhanced view of the same image.

CONCLUSION

Thrust and acoustic measurement procedures were proposed and given initial tests with two rocket motors, one solid and one liquid. The liquid tests showed the validity of using sense lines, and the solid test showed the validity of optical techniques in measuring the off axis torque of engines in test stands. Analysis of the liquid tests confirmed the presence of Helmholtz frequencies, and the time of flight analysis was consistent with a shock wave propagating at sonic speeds. Other measurements are planned for engines later in the year.

---

[1] Hecht, E. *Optics*, Addison Wesley, Second Edition. 1987. (83)
[2] Ibid., (422)
[3] Halliday, D. et al. *Fundamentals of Physics*, John Wiley and Sons, Fifth Edition. 1997. (436)
[4] Ibid., (55)
[5] O'Neil, M. (editor) *Merck Index: An Encyclopedia of Chemicals, Drugs, & Biologicals*, Merck Publishing Group. 2001. (**13,** 184)
[6] Griffiths, David. *Introduction to Electrodynamics*, Prentice Hall, Third Edition. 1998. (31)

2003

NASA FACULTY FELLOWSHIP PROGRAM

MARSHALL SPACE FLIGHT CENTER
THE UNIVERSITY OF ALABAMA IN HUNTSVILLE

TALKING HISTORY: ORAL HISTORIES OF MARSHALL SPACE FLIGHT CENTER

Prepared By:	Stephen P. Waring
Academic Rank:	Associate Professor
Institution and Department:	University of Alabama in Huntsville Department of History
NASA/MSFC Directorate:	Customer and Employee Relations
MSFC Colleague:	Mike Wright

Figure 1: Skylab in Orbit

Introduction

For my fellowship, I worked on two projects. I continued research and writing of a history of the Space Shuttle *Challenger* accident, a project I described in my report on my 2002 NASA Faculty Fellowship.[1] This summer I completed drafts of three and a half chapters, all on the accident investigation conducted by the Rogers Commission and by the NASA Data and Design Analysis Task Force. I turned the completed chapter drafts over to my NASA colleague for his comments and reference.

In addition, I conducted several oral history interviews of retirees and employees of the Marshall Space Flight Center. These interviews were recorded; the recordings and written notes of the interviews were turned over to the MSFC History Archives. This report describes this project and discusses some of the stories recorded in the interviews.

Oral History and its Utility

The oral history interview is a standard research technique used by historians of contemporary times. One advantage of doing contemporary history is that participants in past events are still alive and often eager to share their perspectives. As historical accounts, interviews have obvious flaws: the perspectives are biased and reveal the distorted memories that come with the passage of time. However, the limitations of oral history are more than balanced by their advantages.

History interviews are useful to NASA in several ways. They preserve stories that express organizational values. Interviews reveal multiple perspectives on the past and thus show the diversity of the Agency and complexity of its work. They fill gaps in the written record. Finally oral history interviews offer first person accounts of important events in the history of the Agency and its mission.

Methodology

Mike Wright, my NASA colleague and the Marshall historian, and I selected names for possible interviews. The History Archives had interviews of Center personnel, with most of these

conducted for the books in the NASA History Series on Marshall: Bilstein's *Stages to Saturn* [2] and Dunar and Waring's *Power to Explore* [3].

We wanted interviews of people who had not been interviewed before, or who represented aspects of the Center's history that had been neglected. I then contacted these candidates, explained my project, and asked if they wished to participate in a recorded interview for the MSFC archives. Many of the retirees did not respond, but all the current Marshall employees who were contacted consented to interviews. The list included three former Center Directors, and so the Archive now has interviews of all its past leaders. There were 13 interviews with 11 persons totaling 15.5 hours.

I researched the careers of each interviewee and drew up a list of questions for the interview. I sent this list to most of the candidates in advance; two preferred not to receive the questions in advance. The interviews were recorded with a digital device which produced wav files. I took notes during the interviews and used these to write up a summary of the main topics and themes. The recordings and summaries then formed the final products of the interview project.

The interviews necessarily covered a variety of topics and have few consistent themes. The rest of this report uses a few selected stories told by the interviewees to discuss aspects of the Center's history.

Operations and Payload Support

One set of stories from four interviewees (McNair, Kurtz, Steadman, and Craft) dealt with the evolution of Marshall's current capabilities in mission operations, training, and payload support. These overlapping fields of work emerged, not through planning, but as indirect results of hardware projects.

The Center had personnel and facilities for flight operations from its days in the Army Ballistic Missile Agency. For the launch of each Explorer satellite, experts monitored the launch and tracked the spacecraft. They sought to determine the performance of the launch vehicle and predict the lifetime of the satellite. This was a new discipline, the data was incomplete because communication from ground stations was irregular and data came in raw form from teletype machines. When the data came in, it was plotted by hand on charts so long they had to be laid out in the hallway.

By the time of the Saturn launch vehicles, the Huntsville Operations Support Center was established to provide data for Marshall's propulsion engineers. They needed real-time data so they could assist with the "go/no-go" decision of launch and the restart of the S-IVB stage in orbit. The communications technology was still primitive,--telephones, meters, lights, and strip charts. To help direct the S-IVB restart, which occurred when the vehicle was over the ocean, Marshall worked with the Air Force to staff an airplane equipped with monitoring and communications equipment.

Skylab changed the HOSC, both by intention and accident. The Center oversaw construction of Skylab and expected that it would operate nominally. The HOSC had been reconfigured for 24-

hour operation for the six months of the mission, but required immediate innovations after the loss of the meteoroid shield during launch. Marshall had intended to only staff the HOSC with a few people who would send information to spacecraft experts once a day. But with the loss of the shield, Skylab was in crisis and suddenly the experts were living in the HOSC, monitoring spacecraft systems continuously. The HOSC lacked an organizational plan for such a role and even lacked some basic equipment. When Center Director Rocco Petrone learned of the shortage of telephones in the facility, he expressed his frustration by pounding his fists on the wall.

Skylab not only led to upgrades, but also to more Center partnerships with scientists. The Center was responsible for much of the science aboard Skylab and this presaged Marshall's diversification in the 1970s. For the High Energy Astronomy Observatories the Center for the first time had command and control responsibilities for a spacecraft.

In the Seventies, the Center was the lead for Spacelab which further increased its payload support roles. In part because the Johnson Space Center was busy with the Shuttle Orbiter and training astronauts, Marshall offered training facilities for the payload specialists who flew on Spacelab. Soon the Center was providing almost beginning to end of mission operations and payload support for human spaceflight, not only managing science projects and hardware, training specialists in science payloads, integrating payloads, and overseeing launches, but also directing payloads in space. This role in Spacelab continued on the International Space Station.

Figure 2: Marshall women who worked materials science experiments in the General Purpose Lab, an early mock-up of Spacelab—1974

Ironically the interviewees said that Marshall's Center Directors often drug their feet and only reluctantly embraced an extensive operations role. They saw the Center's expertise as being in "smoke and fire" propulsion and often asked "Is this a role for Marshall?" But other managers wanted to extend and protect the operations work, and quietly used money in the budget lines of projects to provide funding to enhance the Center's operations capability. Thus Marshall established operations functions without a mandate from Headquarters or even its own directors.

Lessons Learned

Another common topic of the interviews was "lessons learned" from experience. They offered a myriad of lessons from history that reveal values at the Center and provide directions for learning and achievement.

Some emphasized the importance of individual relationships. Jackie Steadman explained that success in managing projects depends on honesty with people about their work so that information was realistic. Porter Bridwell thought that success for a manager came from listening; "you can get unbelievable feedback," he said, "if you listen."

Some offered lessons learned from problems in project management. Rex Geveden described some difficulties on Gravity Probe-B, warning of how flat-funding led many people on the project to tolerate schedule slippages and how a cost-plus-no-fee contract gave NASA no capability to reward or punish performance. Art Stephenson explained how the failure of the Mars Climate Orbiter revealed problems with "faster, cheaper, better."

Others provided morals learned from failures. Bridwell argued that the *Challenger* accident proved that hardware must be tested in full-scale and in flight conditions so that engineers can find out what they don't know. J. Wayne Littles thought that the accident showed the importance of open communications so that problems and risks could be properly assessed. George Hopson thought that the *Columbia* accident taught the lesson that "recurring problems that seem innocuous must be studied."

Resources

In conducting my research and writing during the fellowship, I mainly worked from the Marshall Space Flight Center's History Archives. The archive has various historical records, including files from past Center Directors, technical reports, photos, videotapes, and news articles. The collection is outstanding and has a marvelous digital finding aid. I also conducted oral history interviews with Center employees and retirees. Those granting interviews were Porter Bridwell, Harry Craft, Rex Geveden, George Hopson, Fletcher Kurtz, Wayne Littles, Garry Lyles, Ann McNair, Jackie Steadman, Art Stephenson, and Ann Whitaker.

Acknowledgements

I would not have progressed as well on my project without the assistance of several people. Mike Wright, my NASA colleague, paved the way with helpful advice about sources and interview subjects; he also helped with computers. Bob Jaques helped me locate information everyday. Mike Leberman not only answered questions, and provided insight into Marshall's culture. Also deserving thanks are Gabrall Yeldell, Susan Eason, Mike Herston, and Steve Durham.

References

[1] Waring, S. P. (2003), "An Accident in History: Challenger in Perspective," NASA Faculty Fellowship Research Reports, NASA/CR-2003-212397.

[2] Bilstein, R. (1980) *Stages to Saturn: A Technological History of Apollo/Saturn*, NASA SP-4206.

[3] Dunar, A. J. and Waring, S. P. (1999) *Power to Explore: A History of Marshall Space Flight Center 1960-1990*, NASA SP-4313.

2003

NASA FACULTY FELLOWSHIP PROGRAM

MARSHALL SPACE FLIGHT CENTER
THE UNIVERSITY OF ALABAMA IN HUNTSVILLE

DUAL PULSE LASER SPARK IGNITION FOR ROCKET ENGINES

REPORT NOT AVAILABLE

Prepared By:	Joseph Wehrmeyer
Academic Rank:	Research Associate Professor
Institution and Department:	Vanderbilt University Mechanical Engineering
NASA/MSFC Directorate:	Space Transportation
MSFC Colleague:	Huu Trinh

2003

NASA FACULTY FELLOWSHIP PROGRAM

MARSHALL SPACE FLIGHT CENTER
THE UNIVERSITY OF ALABAMA IN HUNTSVILLE

INTERNATIONAL SPACE STATION AND PAYLOAD OPERATIONS

Prepared by:	Talicia Williams
Academic Rank:	Accompanying Student
Institution and Department:	Alabama A&M University Department of Arts & Sciences
NASA/MSFC Directorate:	Flight Project
MSFC Colleague:	Mark McElyea

Introduction

I had the opportunity of taking on several tasks during the summer of 2003. Although some were more difficult than others I truly enjoyed working with Mark McElyea in Flight Project Directorate. I worked in the Payload Systems Group - FD 33 and took on several tasks from learning valuable information to doing some hands-on activities. I found it to be an experience like no other. The three hands-on activities were dealing with the International Space Station Express Rack, the Timeliner, and sitting on Console.

Space Station Overview

Station Configuration

The International Space Station (ISS) (Figure 1) is the largest and most complex international scientific project in history. The station represents a move of unprecedented scale off the home planet. Led by the United States, the International Space Station draws upon the scientific and technological resources of 16 nations: Canada, Japan, Russia, 11 nations of the European Space Agency, and Brazil. The completed International Space Station will have a mass of about 1,040,000 pounds, measuring 356 feet across and 290 feet long, with almost an acre of solar panels to provide electrical power to the on orbit laboratories. The U.S. elements include three connecting nodes; a laboratory module; truss segments; four solar arrays; three mating adapters; a cupola; an unpressurized logistics carrier and a centrifuge module. The Payload Support System (PLSS), the Command and Data Handling System; and the Communication & Tracking System (C&TS) provide power and data resources to the ISS payload complement.

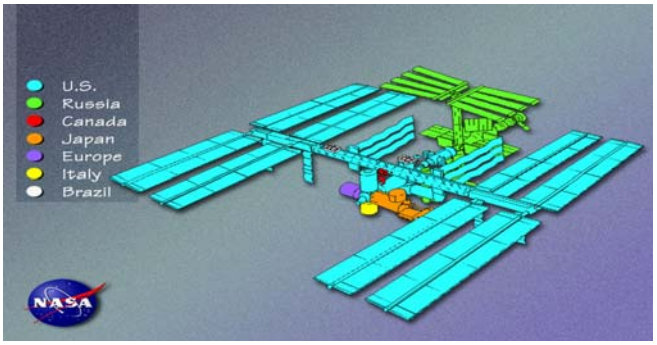

Figure 1: International Space Station

Payload support system (s)

The Electrical Power (EPS) (Figure 2) is a 120 V volt DC system, with 3, 6, or 12 Kw available to the International Standard Payload Racks (ISPRs). EPS consists of the solar arrays, the main bus switching unit, the DC to DC converter unit, the secondary power distribution assembly, and batteries. Three battery assemblies per power channel operate in parallel to store/provide power. Each battery consists of two identical battery subassembly Orbital Replacement Units (ORUs). These nickel-hydrogen (NiH2) batteries store power as required during the insulation portion of an orbit when the arrays can produce power in excess of load demands. During the eclipse portion, the batteries discharge power to provide for ISS load demands. The State of Charge (SOC) of the batteries is constantly monitored and managed to ensure that power is available for

eclipse as well as contingency scenarios. For example, battery SOC is managed to provide power for at least one orbit (with no solar input) in a contingency situation. The Remote Power Control Modules (RPCMs) provide secondary power switching, monitoring, and circuit protection for the U.S. Lab ISPR payloads. The RPCM uses Remote Power Controllers (RPCs) to switch power to the ISPR locations.

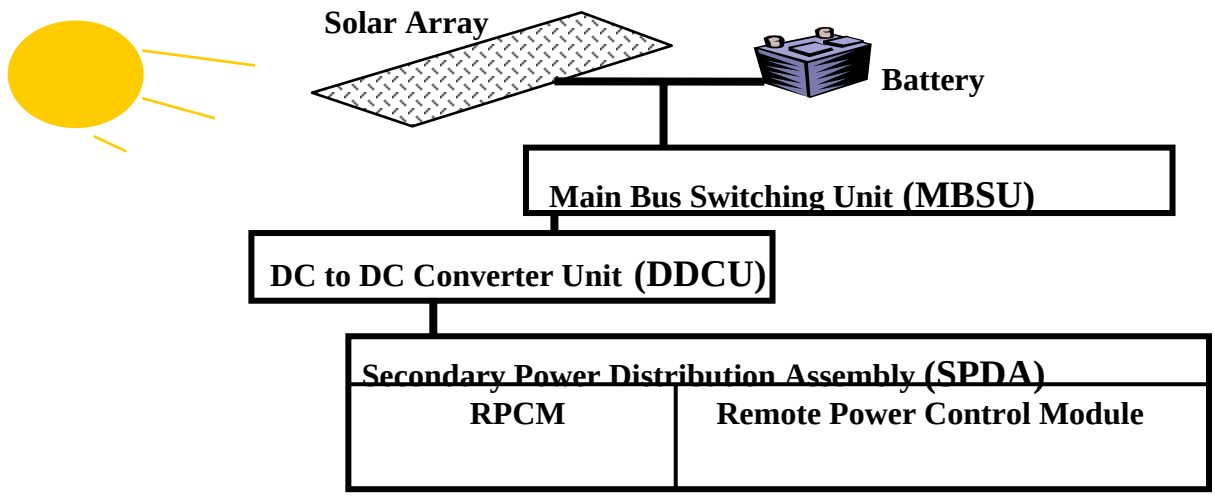

Figure 2: Electrical Power System

The Thermal Control System (TCS) (Figure 3) provides coolant supply to the ISPR interface for active temperature control of payloads. The TCS consists of cold plates, fluid circulation loops, and Avionics Air Assembly Fans. It's functions are heat collection, heat transportation, and heat rejection. The two internal loops provide low temperature (4C) and moderate temperature cooling (17C). Water is the coolant in the internal loops, and it provides direct cooling to payloads and equipment in the ISPR through the cold plates. The AAA provides cooling by air convection and heat exchange with the moderate temperature loop. The Rack Flow Control Assembly (RFCA) provides control of flow rate for one coolant fluid loop (moderate or low). Both loops can be used simultaneously with only one controlled by the RFCA.

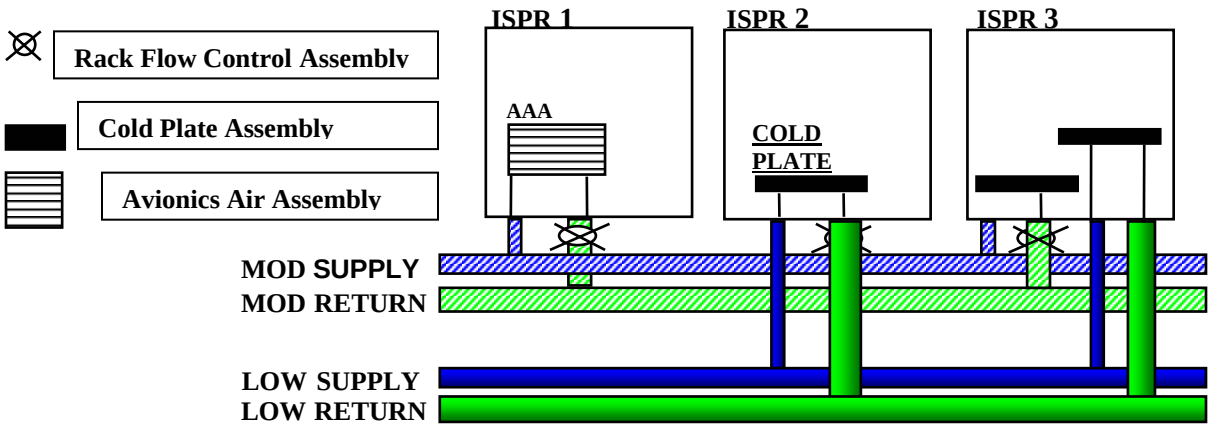

Figure 3: Thermal Control System

The Vacuum Exhaust System (VES) (Figure 4) is used to evacuate waste gases from any payload volume. The VES vents to space and provides total vacuum to the payload volume upon the opening of a servo controlled vent valve. Only one payload may access the VES at a time. The VES attaches to each ISPR location via Quick Disconnect (QD) attachments.

The Vacuum Resource System (VRS) (Figure 4) is used to provide a constant vacuum resource for ISS payloads. A servo controlled valve provides access to the space vacuum. The VRS is manually configured by the crew for the US Lab. The VRS supports constant vacuum for up to six payloads.

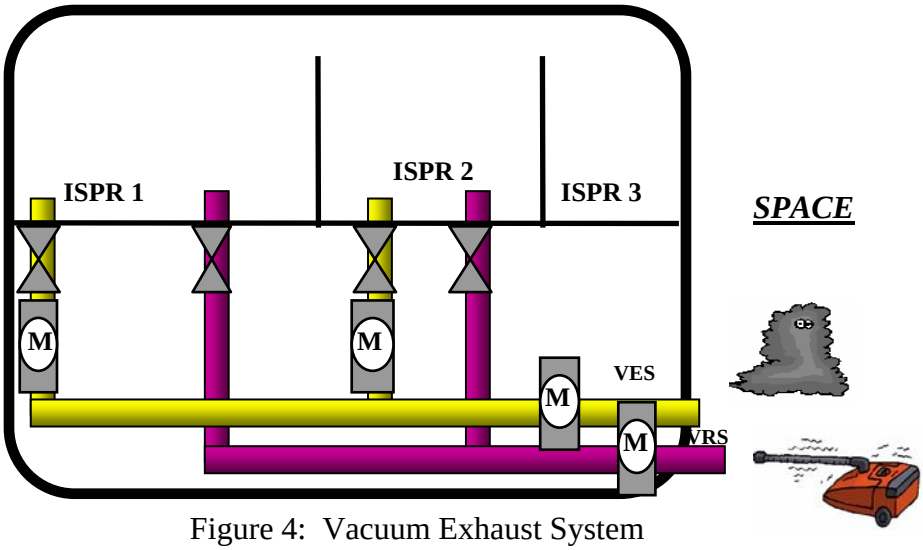

Figure 4: Vacuum Exhaust System

The Lab Nitrogen System (LNS) (Figure 5) has a single gaseous line that is provided as a standard interface to each ISPR. The nitrogen is supplied at a temperature range of 63 to 113 deg F. The nitrogen is used to purge a payload's volume of waste gases or to provide an inert atmosphere for the science experiment. In order to dispose of the waste nitrogen, the VES is

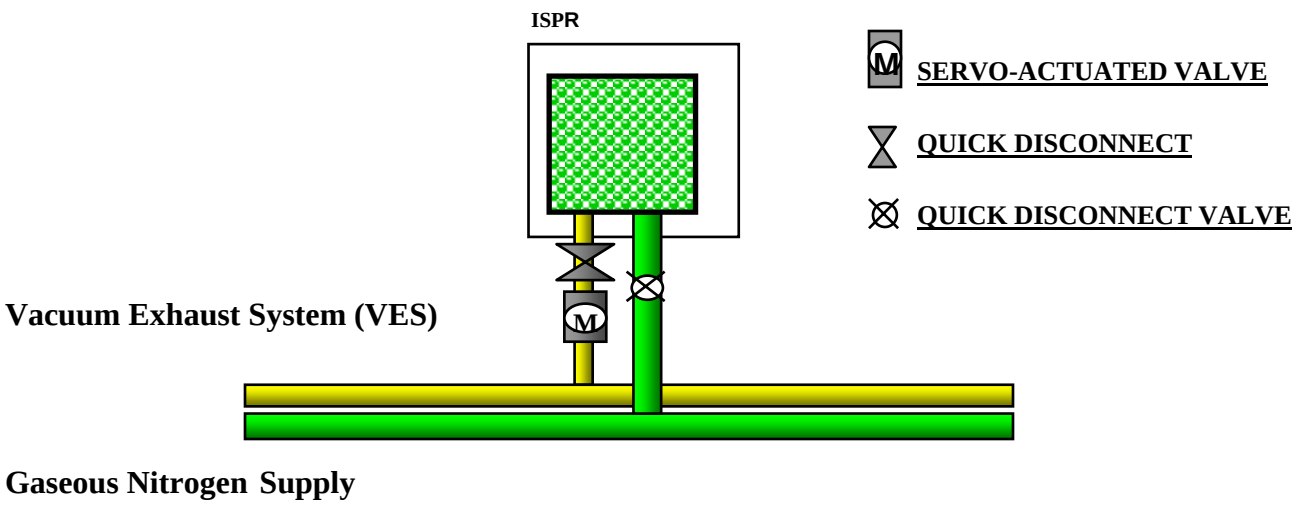

Figure 5: Lab Nitrogen System

used. The ISS crew controls the access to nitrogen by using a manual-shutoff quick disconnect valve at each ISPR location.

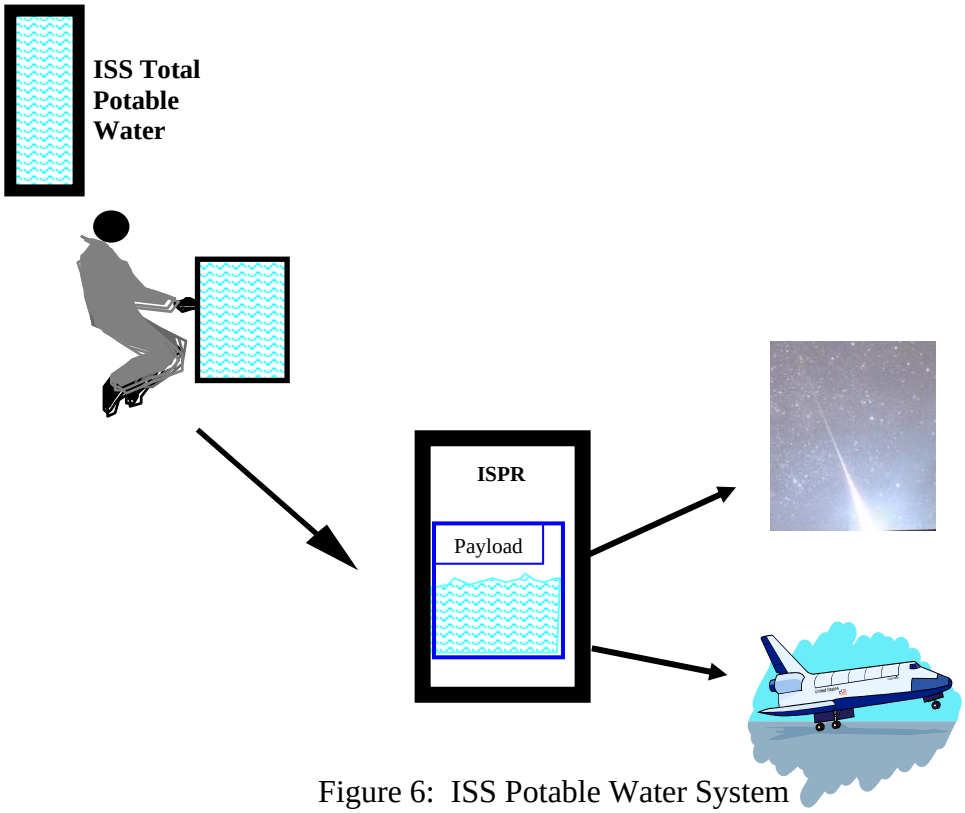

Figure 6: ISS Potable Water System

The potable water supply for payloads is taken from the ISS potable water system (Figure 6). The U.S. Lab has access to up to 5.5 kg/day. The crew must manually transfer water in containers. Waste water is stored in the ISPR and must not be returned to the potable water supply.

Communication & Tracking System

Communication between the ISS and the ground control center occurs through the Tracking and Data Relay Satellite System (TDRSS) that transmits audio, video, and data through S-band and Ku-band frequencies. The S-band system is used for command, data, and audio uplink and for status data/audio downlink. The higher frequency of S-band improves the resolution of the signal and allows it to cut through the ionosphere without reflection. The Ku-band is used because of its ability to transmit large amounts of digital data with sufficient carrier link margin. Data rates range from 0 to 50 mbs for TDRSS data with potential growth to 150 mbs.

TDRSS is a line of sight system (Figure 7) consisting of 6 geosynchronous (appear fixed to an observer on Earth since they orbit at the same speed as the Earth's rotation) satellites. There are times of communication referred to as Acquisition of Signal (AOS) periods and times of no communication referred to as Loss of Signal (LOS) periods. LOS occurs when the ISS Space to Ground Antenna (SGANT) is moved from one satellite to another, whenever ISS structure blocks the line of sight of the SGANT to TDRSS, or when the earth blocks the line of sight to TDRSS. All other periods are AOS. There are 3 satellites online and available for use at any given time. Each TDRSS satellite communicates with the White Sands Complex (WSC) near Las Cruces, New Mexico. Communications from WSC occurs via land lines and Domestic Satellites to the MCC-H and POIC.

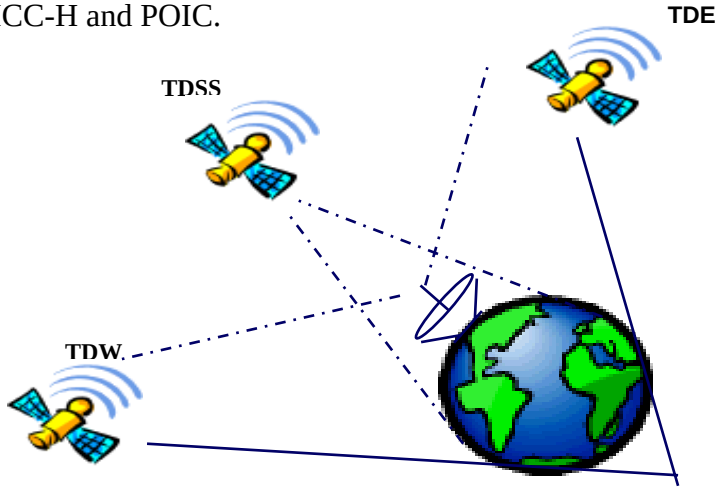

Figure 7: Tracking and Data Relay Satellite System (TDRSS)

On board communications occur through the communications and Tracking (C&T) and the Command & Data Handling (C&DH) systems. Payload data consists of low, medium, and high data rate information. All payload data comes down through the Ku-band system. The C&T and C&DH systems (Figure 8) support both space to ground, space to space (e.g. ISS to shuttle), and internal communication requirements.

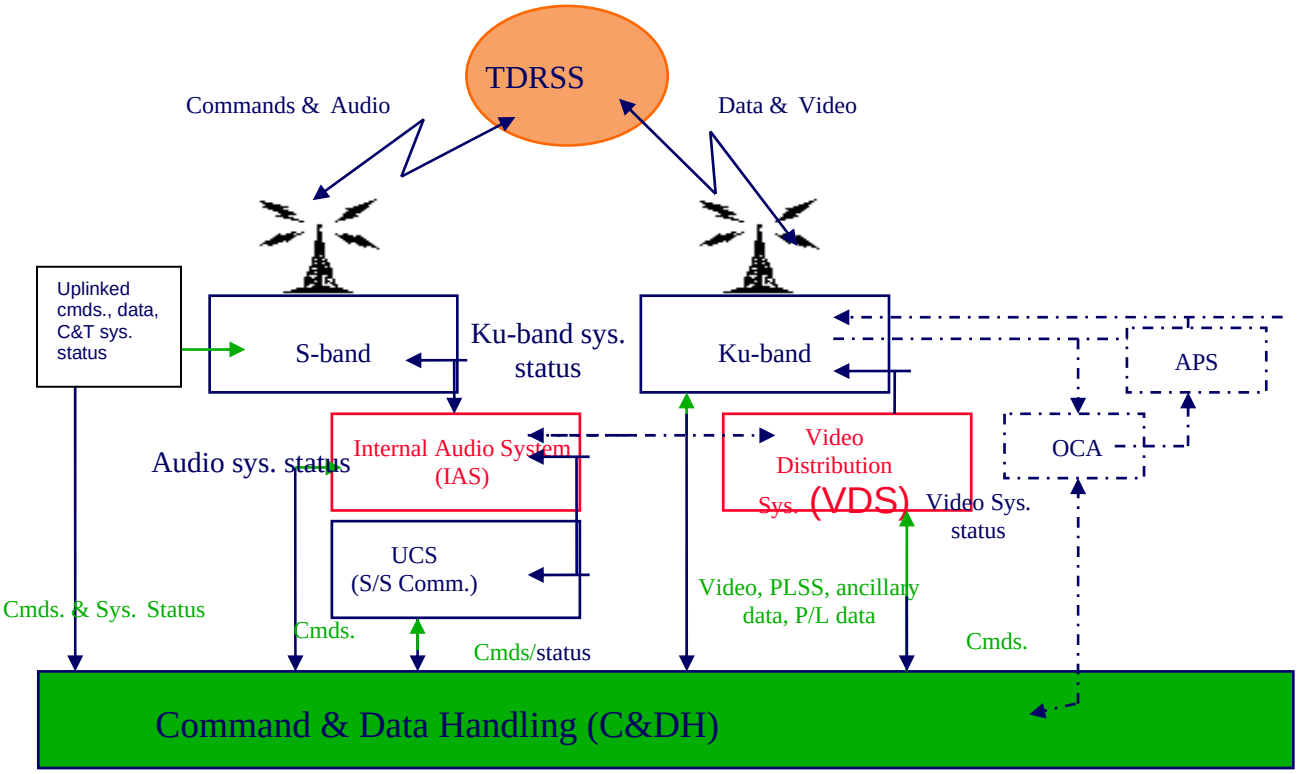

Figure 8: C&T and C&DH Systems

Space Station Operations Overview

Mission Control Center-Houston

Since 1965, the Mission Control Center (MCC) has been the nerve center for America's manned space program. The men and women who work in Building 30 at the Johnson Space Center have been vital to the success of every manned space flight since Gemini 4. These teams of experienced engineers and technicians monitor systems and activities aboard spacecraft 24 hours a day during missions, using some of the most sophisticated communication, computer, data reduction, and data display equipment available.

They watch every movement the crew and spacecraft make, double-check every number to be sure missions are proceeding as expected, and provide the expertise needed to deal with the unexpected. The Mission Control Center-Houston (MCC-H) is responsible for the command and overall safety of the ISS vehicle systems.

2.2Payload Operations Integration Center-Huntsville

The POIC (Figure 8) is an International Space Station (ISS) facility that manages on-orbit ISS payloads and payload support systems in coordination with the Mission Control Center in Houston (MCC-H), the distributed International Partner (IP) Payload Control Centers (PCCs), Telescience Support Centers (TSCs), and payload-unique facilities. The POIC and its supporting systems reside primarily within the Marshall Space Flight Center (MSFC) HOSC. The United States Operations Center (USOC) also resides within the HOSC and provides an ISS host facility

where payload users can choose to control and monitor the operations of the onboard payloads instead of being located remotely. USOC users are provided with access to Enhanced Huntsville System (EHS): workstations, POIC networks, facility space, and POIC voice and video systems.

Figure 8: ISS Control Center

Timeliner

System Components

Timeliner is a Commercial Off-The-Shelf (COTS) software application developed by the Charles Stark Draper Laboratory (CSDL or Draper) to provide automation for procedural types of tasks. The Timeliner system is both a specialized computer language and a development/execution environment. NASA has selected the specialized computer language function of Timeliner to be the Automated Procedure Capability for the ISS program. Timeliner provides the capability for commanding payloads via sequences and commands, and the procedures may be operated automatically or under close monitoring and control of users, and/or crew. The Timeliner application resides in the PLMDM computer onboard. The PLMDM is a component of the ISS Command & Data Handling (C&DH) System. Figure 9 shows a functional diagram of the Timeliner components.

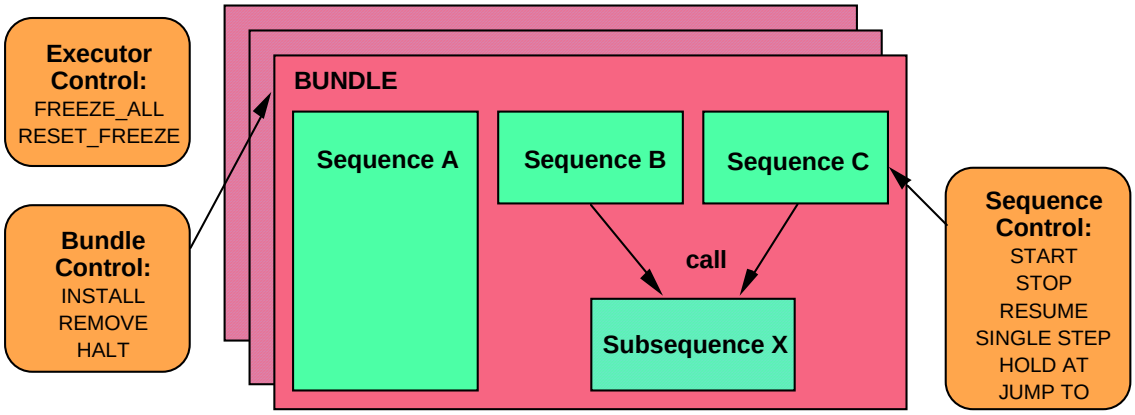

Figure 9: Timeliner Components

Logic Features

The on-board portion of the Timeliner execution environment software resides on the PLMDM. The implementation of Timeliner has two parts, the Compiler and Executor. The Compiler, located in the POIC, prepares procedures for execution. A source procedure is read in as American Standard Code for Information Interchange (ASCII) data. The statements are parsed, data and command references resolved, and error messages are issued if necessary. The output of the Compiler is a listing file, a file of executable data, and an onboard memory address map file. These are uplinked for onboard execution

Procedure Scenario

The Timeliner Executor, located in the PL MDM, executes the commands embodied in a compiled procedure. Up to 50 procedures with a maximum of 10 sequences each may be executed simultaneously. Within each procedure, each sequence is treated as a logically independent "string" or "thread" of execution. The Executor reads and responds to a set of realtime commands that allow a user to control procedure execution and output its status for use in monitoring. An actual procedure to activate and shutdown the Material Science Glove box was developed and tested during this summer internship and is contained in Appendix A. This procedure was run with ground test facilities to demonstrate its capabilities.

Express Rack

Expedite the Processing of Experiments to Space Station (EXPRESS) Rack (Figure 10) has a philosophy of getting small payloads to orbit with a shortened integration period. It provides a set of standard interfaces and resources for subrack payloads. EXPRESS Rack is housed in an International Standard Payload Rack and has the following interfaces with Station: 120 VDC power, Data (MIL-STD-1553, Ethernet, High Rate Link, Internal Video Subsystem), and Fluids (Moderate temperature water, vacuum exhaust, Nitrogen). EXPRESS Rack secondary structure and subsystems include: Structural interface for subsystems and payloads, upper and lower connector panels for payloads to access rack resources (power, data, thermal control systems, vacuum exhaust, gaseous nitrogen), thermal control hardware for subsystems and payloads, the EXPRESS Rack laptop provides local payload command and control capability, and a "utility drawer" at the bottom of the rack for local stowage (potential stowage items include cables, laptop, etc.) The subsystems provide conversion, distribution, and protection for subsystems and payloads, payload and subsystem command, control, and downlink capabilities, initial rack configuration and file transfer capability, rack internal and external ethernet data routing, Rack-level smoke detection tied into the Station C&W System, and the EXPRESS with Active Rack Isolation System (ARIS) Rack, microgravity measurement capability through the Space Acceleration Measurement System (SAMS II). Figure 11 shows a trainee working at the EXPRESS Rack laptop computer.

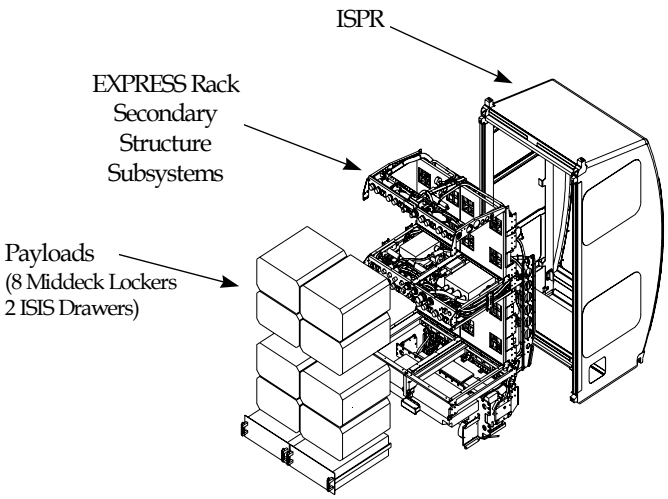

Figure 10: EXPRESS Rack

Figure 11: Trainee working at EXPRESS Rack Computer

Summary

I found this to be a learning experience above any. It showed me that I was capable of doing anything I set my mind out to do. It was an experience like no other because there was so much vital information and things to do. I had the opportunity to work with different people and each person taught me something I didn't know. I feel that I got the opportunity to get a taste of the real world when your boss give you one task with a deadline and you have a million other things to do with a deadline as well.

Acknowledgements

I would like to thank Mark McElyea for being a wonderful mentor and helping me in any way possible; Angela Haddock for being there when I need her; the entire FD 33 crew; Dr. Shelia Nash-Stevenson, MSFC; Dr. John Gregory from the Alabama Space Grant Consortium; Dr. Gerald Karr, NFFP; Dr. Razi Hassan; and anyone I may have missed.

Appendix A

```
Bundle AP_MSG_CPO_STRT_SHUT
--
--*****************************************************************
sequence MSG_STARTUP_NOTIFICATION
--
--The command PUI for the CPO's payload startup notification command tmplt
-- is LAVX961=IM0036K. It has one modifiable field, the payload index is value,
--LAPD10MD0001K

message "   STARTUP MSG-SB "
command LAVX96IM0036K,  --MSG-SB
LAPD10MD0001K => 40       --sensor board
wait 3
--

message "   STARTUP MSG-RPD "
command LAVX96IM0036K,  --MSG-RPD
LAPD10MD0001K => 41       --remote power distribution
wait 3
--

message "   STARTUP MSG-WV1 "
command LAVX96IM0036K,  --MSG-WV1
LAPD10MD0001K => 42       --work volume one
wait 3
--

message "   STARTUP MSG-WV2 "
command LAVX96IM0036K,  --MSG-WV2
LAPD10MD0001K => 43       --work volume two
wait 3
--

message "   STARTUP MSG-ASW "
command LAVX96IM0036K,  --MSG-ASW
LAPD10MD0001K => 44       --application software
wait 3
--

message "   STARTUP MSG-VID "
command LAVX96IM0036K,  --MSG-VID
LAPD10MD0001K => 45       --video
wait 3
--

message "   STARTUP MSG-MLC "
command LAVX96IM0036K,  --MSG-MLC
LAPD10MD0001K => 46       --MSG laptop computer
wait 3
--

message "   STARTUP MSG-LOG "
command LAVX96IM0036K,  --MSG-LOG
LAPD10MD0001K => 47       --archival log
wait 3
--

close sequence--MSG_STARTUP_NOTIFICATION
--
--*****************************************************************

sequence MSG_SHUTDOWN_NOTIFICATION
--
--The command PUI for the CPO's payload shutdown notification command tmplt
--is LAVX96IM0035K.  It has one modifiable field, the payload index value,
--LADP10MD0001K.
```

```
--
message "   SHUTDOWN  MSG-LOG "
command LAVX96IM0035K,  --MSG-LOG
LAPD10MD0001K => 47       --archival log
wait 3
--
message "   SHUTDOWN MSG-MLC "
command LAVX96IM0035K,  --MSG-MLC
LAPD10MD0001K => 46       --MSG laptop computer
wait 3
--
message "   SHUTDOWN MSG-VID "
command LAVX96IM0035K,  --MSG-VID
LAPD10MD0001K => 45       --video
wait 3
--
message "  SHUTDOWN MSG-ASW "
command LAVX96IM0035K,  --MSG-ASW
LAPD10MD0001K => 44       --application software
wait 3
--
message "   SHUTDOWN MSG-WV2 "
command LAVX96IM0035K,  --MSG-WV2
LAPD10MD0001K => 43       --work volume two
wait 3
--

message "   SHUTDOWN MSG-WV1 "
command LAVX96IM0035K,  --MSG-WV1
LAPD10MD0001K => 42       --work volume one
wait 3
--
message "   SHUTDOWN MSG-RPD "
command LAVX96IM0035K,  --MSG-RPD
LAPD10MD0001K => 41       --remote power distribution
wait 3
--
message "   SHUTDOWN MSG-SB "
command LAVX96IM0035K,  --MSG-SB
LAPD10MD0001K => 40       --sensor board
wait 3
--
--
--
--
close sequence--MSG_SHUTDOWN_NOTIFICATION
--*****************************************************************
close bundle -- AP_MSG_CPO_STRT_SHUT
--
*****************************************************************

------  ADAPTER PUI NAME LIST IS IN FILE: AP_MSG_SPO_STRT_SHUT.TLP
------  ADAPTER CONFIGURATION SUMMARY IS IN FILE:  AP_MSG_CPO_STRT.TLC
------  BUNDLE DATA WILL BE WRITTEN TO FILE:  AP_MSG_CPO_STRT.TLX
------  MEMORY USAGE FOR THIS BUNDLE IS AS FOLLOS:
------  category                                                        words
bytes
------  ---------------------------------------------------          -----
-----
------  DATA WRITTEN TO OUTPUT FILE                                     819
3276
------  ADDITIONAL AREA NEEDED FOR EXECUTION                 26
104
------  TOTAL MEMORY REQUIRED FOR EXECUTION                  845
3380


------  COMPILATION WAS SUCCESSFUL
------  BUNDLE CONTAINS 2 SEQUENCES, 0 SUBSEQUENCES, 52 STATEMENTS
------  EXECUTABLE DATA IS IN FILE:  AP_MSG_CPO_STRT_SHUT_TLX
```

2003

NASA FACULTY FELLOWSHIP PROGRAM

MARSHALL SPACE FLIGHT CENTER
THE UNIVERSITY OF ALABAMA IN HUNTSVILLE

ELECTROCOMPOSITE OF ALUMINA IN A NICKEL MATRIX

Prepared By:	Pei Xiong-Skiba
Academic Rank:	Associate Professor
Institution and Department:	Physics and Astronomy Austin Peay State University
APSU Accompany Student:	Ryan Cruz Hulguin
NASA/MSFC Directorate:	Space Science (SD 50)
MSFC Colleague:	Brian Ramsey
UAH Colleague:	Darell Engelhaupt

Introduction

X-ray astronomy involves observing x-rays emitted by astronomical bodies. However, the air surrounding earth absorbs x-rays making it impossible to establish ground-based x-ray observatories. In addition to established space based x-ray observatories such as Chandra, one may also use hot helium balloons to accomplish this goal. X-ray telescopes mounted on helium balloons can reach altitudes 130,000 feet or higher where the x-ray absorbance due to earth's atmosphere is greatly reduced. Currently, the x-ray telescopes used in balloon missions are electroformed nickel-cobalt alloy. Reduction in the weight of the optics can reduce the payload of future missions making the missions more fiscally attractive. This can be achieved by reducing the mass density of the optics material. Thus, developing a material with similar mechanical properties as the nickel cobalt alloy but less mass density is highly desirable.

In the past three decades, a wide range of composite films has been developed for a variety of applications such as wear resistance, corrosion resistance, and lubrication by tailoring the composition via electrocodeposition [3]. Electrocodeposition is a process in which small particles or filaments are suspended in a conventional plating bath and co-deposited into the metal matrix through electroplating. Bath agitation is typically used to keep the particles in suspension. Materials commonly used are carbides, oxides, polymers, and industrial diamonds [2,5]. In these composites, metals are dispersion hardened by the incorporation of particles or filaments. These composites typically have a considerably higher yield strength, hardness, and lower mass density than the pure metals. The amount of particles incorporated into a composite film depends on the particle-matrix system. For electrolytes without bath additives, incorporation levels typically range from 1-10 vol % while the particle concentrations in the plating bath range from 2 to 200 gm/L. It has also been shown that surfactants [1] and periodic reverse pulse plating [4] could be used to enhance particle incorporation.

In this study, nickel aluminum oxide composite was electroformed in a sulfamate bath with 50 gm/L of 0.05-μm aluminum oxide powder. Different plating methods including direct current plating, periodic pulse plating, and periodic reverse pulse plating were used. With conventional direct current plating method, particle inclusion in the nickel matrix remains about 2% (wt). However, much higher particle inclusions were achieved when pulse reversal plating technique was applied. Particle inclusion approaches theoretical maximum when the deposit thickness per cycle approaches the particle diameter size at lower duty cycle. The highest particle incorporation achieved is 23% (by weight) with a composite mass density of 6.4 gm/cm^3.

Experimental

Nickel composite coatings were formed in a 3.5 litter glass beaker. The electrolyte was nickel sulfamte bath as shown in table 1. All of the bath components were mixed with de-ionized water. The plating temperature was controlled manually at 49 ± 2°C. The pH of the bath was adjusted to 4.0 ± 0.1 using sulfamic acid before plating each sample. The alumina powder used was 0.05 μm agglomerate-free (γ phase) polishing powder purchased from Baikalox International Corporation. The concentration of the powder in the plating bath was adjusted when it was estimated to be 3% below the nominal value. The bath was stirred mechanically with a magnetic stirrer to keep the alumina powder in suspension. The anode is a titanium coil in

contact with nickel chips in a cylindrical basket. The cathode is a stainless steel cone rotating at 500 rpm. After each sample was plated, the nickel composite shell (about 220 μm thick) was removed from the stainless steel cone using a mechanical pusher. Then, the cone was washed with Micro-90 concentrated cleaning solution (Cole Parmer) and Webril wipe, rinsed with warm water and de-ionized water, and dried by air-blown. A bipolar power supply (KEPCO, BOP 20-20M) is used in this experiment to enable reverse pulse plating. The power supply was controlled by Labview software via a PC. The densities of the nickel-alumina composites were determined using Archimedes' principle. The density of the alumina powder used in our powder inclusion calculation is 3.3 gm/cm^3, lower than the values (3.7-3.9 gm/cm^3) quoted by CRC handbook. Using a similar method mentioned by Stojak et al [5], we obtained the above density value, in agreement with their measurements. The density of nickel is 8.90 gm/cm^3.

Nickel Metal	100 gm/L
Boric acid	35 gm/L
Sodium Dodecal Sulfate (SDS) wetting agent	0.2 gm/L
Nickel Bromide	2.3 gm/L
Al_2O_3 (0.05 μm, γ-phase)	50 gm/L

Table 1. Chemical composition of the electrolytes

Results and Discussions

DC Plating

The mass density of the composites plated with direct current densities ranging from 3.4 mA/cm^2 to 60 mA/cm^2 is shown in table 2. It peaks at 20 mA/cm^2 current density. The results are consistent with other reports [2,5]. Particle density for 50 gm/L particle loading is 2.3x10^{14}/cm^3 assuming uniform particle distribution in the plating bath. Notice that particle densities of the composites listed in table 2 are all below this value. It's possible that particle density in the double layer (adjacent to the plating part) is lower than the particle density in the solution due to the rotational motion of the plating part.

Sample #	J (mA/cm^2)	ρ (gm/cm^3)	n (1/cm^3)	% Wt
4	3.4	8.5830	1.08x10^{14}	2.13.
5	10	8.6264	9.34x10^{13}	1.82
12	15	8.7130	6.38x10^{13}	1.22
6	20	8.5800	1.09x10^{14}	2.15
8	30	8.6391	8.9 x10^{13}	1.73
9	40	8.7262	5.93x10^{13}	1.23
11	50	8.7075	6.57x10^{13}	1.25

Table 2 Alumina particle incorporation due to variation of plating current density during direct current plating.

Pulse Plating

The average density of the composites plated with 20, 40, and 60 mA/cm^2 with 3.00 seconds on-time and 5.00 seconds off-time pulses is 8.69 gm/cm^3, as shown in table 3. Comparing with densities of the composites plated by direct current, it is clear that the off-time in pulse plating does not attract/remove significant amount of alumina particles to change the mass densities of the composites.

Sample #	J_{on} (mA/cm^2)	t_{on} (sec)	t_{off} (sec)	J_{ave} (mA/cm^2)	ρ_{com} (gm/cm^3)	n (1/cm^3)	% Wt
14	20	3.00	5.00	7.5	8.6964	6.95×10^{13}	1.33
13	40	3.00	5.00	15	8.6431	8.77×10^{13}	1.70
15	60	3.00	5.00	22.5	8.7202	6.14×10^{13}	1.16

Table 3 Pulse plating condition and results

Reverse Pulse Plating

It's been reported that the maximum particle concentration is found when the deposit thickness per cycle approaches the particle diameter size using pulse-reverse plating method [4]. At 20 mA/cm^2 plating current density, it requires 7 seconds to grow 0.05 μm thickness of nickel composite, equivalent to one diameter of the alumina particles. Sample 20 and 21 were plated with 20 mA/cm^2 direct current for 30 minutes (about 0.2 thickness), then followed by reverse pulse plating as described in table 4. For sample 20, composite thickness equivalent to two diameter (2D) of the powder particle is plated, and then thickness close to one diameter (1D) is stripped in each cycle. The density of the composite reduces dramatically. Number of particles incorporated is 5.8×10^{14} /cm^3. Sample 21 is a result of plating 3D and stripping 2D, every cycle. Number of particles included in the composite rises to 8.5×10^{14} /cm^3. Notice that (5.8×10^{14} /cm^3) /2 $\approx$ (8.5×10^{14} /cm^3)/3. It suggests that most particles captured earlier during the plating cycle stay close (within 1D) to the composite during the stripping cycle. These particles are then re-trapped into the first D thickness of the composite in the following plating cycle. It's possible that the alumina particles in contact with the surface of the composite are polarized. The attracting force between the alumina particles and the composite may prevent the particles residing on the surface to be removed during stripping cycle as illustrated in figure 1.

Sample #	J_+ (mA/cm^2)	t_+ (ms)	J_- (mA/cm^2)	t_- (ms)	J_{ave} (mA/cm^2)	ρ_{com} (gm/cm^3)	% Wt	Duty Cycle
20	20	15,000	-40	3,000	10.0	7.2	14	0.6
21	20	22,000	-40	7,000	5.52	6.4	23	0.36

Table 4 Reverse pulse plating. Both samples were first plated with 20 mA/cm^2 direct current for 30 minutes (about 0.2 μm thick), then followed by reverse pulse plating as described in the table.

For this nickel-alumina system, the minimum theoretical density is 5.97 gm/cm^3 assuming identical spherical alumina particles packed next to each other and the space between the spheres is filled with nickel. As the density of the composite approaches this minimum theoretical value, the mechanical properties of the composite degrade. Sample 21 crumpled when a small force was applied, acting similar to an ice cream waffle cone.

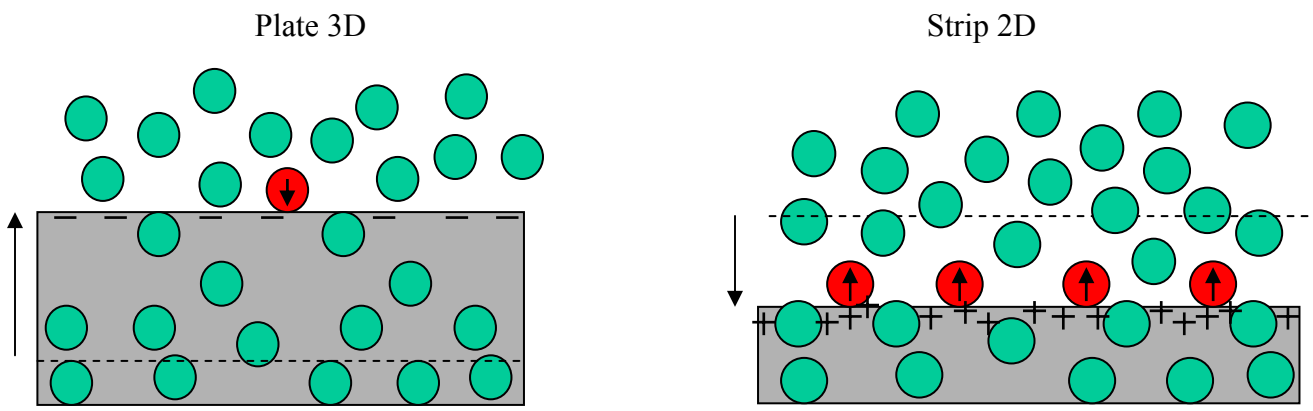

Figure 1 Model for reverse pulsing plating (plate 3D and strip 2D). The left figure shows that particles are integrated into the composite during 3D plating cycle. The right figure shows how the "released" particles remain to be attached to the surface of the composite during the 2D stripping cycle, possibly caused by the interaction between the polarized alumina particles and the substrate. Most of these particles in contact with the surface are re-trapped during the following plating cycle.

Conclusion

With conventional direct current plating method, maximum alumina particle inclusion in the nickel matrix remains about 2% (wt). Periodic pulse plating does not significantly change the results. Pulse reversal plating appears to be a valid method in increasing alumina particle inclusion. Higher particle concentration can be found when the deposit thickness per cycle approaches the particle diameter size, i.e., plating ND and stripping (N-1)D. The lowest composite mass density achieved in this study is 6.4 gm/cm^3, approaching the theoretical minimum 5.97 gm/cm^3.

Acknowledgements

The authors would like to thank William Jones for creating this research opportunity and Jimmy Perkins for his assistance in composite density measurements. This work is funded by NASA/SFFP (2003) program.

References

[1] Yee-Shyi Chang and Jin-Yuan Lee, *Materials Chemistry and Physics*, **20**, pp. 309-321(1988).
[2] V. Peter Greco1 (1988), "Electrocomposites the strengthening of metals with particles or fibers by electrodeposition techniques," American Electroplaters and Surface Finishers Society.
[3] A. Hovestad, L. J. J. Janssen, *J. Appl. Electrochem*, **25**, pp. 519-527 (1995).
[4] E. J. Podlaha and D. Landolt, *J. Electrochem. Soc.,* Vol. **144** (7), pp. L200-2 (1997).
[5] Jean L. Stojak, and Jan B. Talbot, *Journal of the Electrochemical Society*, **146** (12), pp. 4504-4513 (1999).

REPORT DOCUMENTATION PAGE

Form Approved
OMB No. 0704-0188

Public reporting burden for this collection of information is estimated to average 1 hour per response, including the time for reviewing instructions, searching existing data sources, gathering and maintaining the data needed, and completing and reviewing the collection of information. Send comments regarding this burden estimate or any other aspect of this collection of information, including suggestions for reducing this burden, to Washington Headquarters Services, Directorate for Information Operation and Reports, 1215 Jefferson Davis Highway, Suite 1204, Arlington, VA 22202-4302, and to the Office of Management and Budget, Paperwork Reduction Project (0704-0188), Washington, DC 20503

1. AGENCY USE ONLY *(Leave Blank)*

2. REPORT DATE
May 2004

3. REPORT TYPE AND DATES COVERED
Contractor Report

4. TITLE AND SUBTITLE
The 2003 NASA Faculty Fellowship Program Research Reports

5. FUNDING NUMBERS
NAG8–1904

6. AUTHORS
S.K. Nash-Stevenson, G. Karr,* and L.M. Freeman** (Program Directors)
and J. Bland (Compiler and Editor)

7. PERFORMING ORGANIZATION NAMES(S) AND ADDRESS(ES)
The University of Alabama in Huntsville, Huntsville, AL 35899
The University of Alabama, Tuscaloosa, AL 35487

8. PERFORMING ORGANIZATION REPORT NUMBER
M–1117

9. SPONSORING/MONITORING AGENCY NAME(S) AND ADDRESS(ES)
National Aeronautics and Space Administration
Washington, DC 20546–0001

10. SPONSORING/MONITORING AGENCY REPORT NUMBER
NASA/CR—2004–213285

11. SUPPLEMENTARY NOTES
*The University of Alabama in Huntsville; **The University of Alabama
Prepared for the Education Programs Department, Customer and Employee Relations Directorate

12a. DISTRIBUTION/AVAILABILITY STATEMENT
Unclassified-Unlimited
Subject Category 99
Availability: NASA CASI (301) 621–0001

12b. DISTRIBUTION CODE

13. ABSTRACT *(Maximum 200 words)*
For the 39th consecutive year, the NASA Faculty Fellowship Program (NFFP) was conducted at Marshall Space Flight Center. The program was sponsored by NASA Headquarters, Washington, DC, and operated under contract by The University of Alabama in Huntsville. In addition, promotion and applications are managed by the American Society for Engineering Education (ASEE) and assessment is completed by Universities Space Research Association (USRA). The nominal starting and finishing dates for the 10-week program were May 27 through August 1, 2003. The primary objectives of the NASA Faculty Fellowship Program are to: (1) Increase the quality and quantity of research collaborations between NASA and the academic community that contribute to NASA's research objectives; (2) provide research opportunities for college and university faculty that serve to enrich their knowledge base; (3) involve students in cutting-edge science and engineering challenges related to NASA's strategic enterprises, while providing exposure to the methods and practices of real-world research; (4) enhance faculty pedagogy and facilitate interdisciplinary networking; (5) encourage collaborative research and technology transfer with other Government agencies and the private sector; and (6) establish an effective education and outreach activity to foster greater awareness of this program.

14. SUBJECT TERMS
space transportation; science in low gravity; making use of space; materials and processes; structures; dynamics; conceptual design; large space optics manufacturing; thermal control; testing and experimentation; quality engineering; information and electronic systems/aviation; automation and robotics; astrophysics; Earth science; space science; system analysis and integration

15. NUMBER OF PAGES
350

16. PRICE CODE

17. SECURITY CLASSIFICATION OF REPORT
Unclassified

18. SECURITY CLASSIFICATION OF THIS PAGE
Unclassified

19. SECURITY CLASSIFICATION OF ABSTRACT
Unclassified

20. LIMITATION OF ABSTRACT
Unlimited